Scattering properties of ultra-cold chromium atoms

Von der Fakultät Physik der Universität Stuttgart
zur Erlangung der Würde eines Doktors der
Naturwissenschaften (Dr. rer. nat.) genehmigte Abhandlung

Vorgelegt von

Piet O. Schmidt

aus Schwäbisch Hall

Hauptberichter:	Prof. Dr. T. Pfau
Mitberichter:	Prof. Dr. M. Mehring
Tag der Einreichung:	20. Februar 2003
Tag der mündlichen Prüfung:	20. März 2003

Physikalisches Institut der Universität Stuttgart

2003

Contents

Zusammenfassung

In dieser Arbeit präsentiere ich experimentelle Ergebnisse über die Streueigenschaften von ultrakalten Chromatomen. Diese Resultate stellen einen wichtigen Schritt in Richtung eines Bose-Einstein-Kondensats (BEC) mit Chromatomen dar.

Die erstmalige Realisierung eines Bose-Einstein-Kondensats in verdünnten atomaren Gasen im Jahr 1995 [1, 2, 3] hat eine faszinierende Forschungsrichtung eröffnet: das Studium makroskopischer Quantenzustände als eine neue Form der Materie. Eine immer weiter wachsende Zahl an theoretischen und experimentellen Arbeiten wurden seitdem veröffentlicht. Weltweit arbeiten ca. 40 experimentelle Gruppen auf diesem Gebiet, die meisten mit BECs der Alkaliatome Rubidium, Natrium und Lithium. 2001 haben Eric Cornell, Wolfgang Ketterle und Carl Wieman den Nobelpreis in Physik für ihre Leistungen auf diesem Gebiet erhalten [4].

Viele der faszinierenden Eigenschaften von Bose-Einstein-Kondensaten entspringen dem Zusammenspiel von Quantenstatistik und der Wechselwirkung zwischen den Atomen. In allen bislang erzeugten BECs ist dies die isotrope Kontaktwechselwirkung, welche durch s-Wellen Stöße vermittelt wird. Sie hat zu interessanten Effekten, wie akustischen Wellen und Phononen [5, 6, 7] und der Realisierung von Spinor-Kondensaten [8, 9] geführt. Bose-Einstein-Kondensate sind zudem Supraflüssigkeiten [10, 11, 12], in denen quantisierte Wirbel nachgewiesen werden konnten [13, 14, 15, 16].

Kondensate können im Rahmen einer nichtlinearen Schrödingergleichung beschrieben werden, wobei die Nichtlinearität durch die Wechselwirkung hervorgerufen wird. Eine vergleichbare Gleichung beschreibt die Propagation von Licht in einem nichtlinearen Medium. Daher konnten in BECs bekannte Phänomene der nichtlinearen Optik, wie die Vierwellenmischung [17] und die Erzeugung von hellen und dunklen Solitonen [18, 19, 20, 21, 22] beobachtet werden.

Die Stärke der Wechselwirkung in einem Bose-Kondensat ist nicht notwendigerweise festgelegt. In besonderen Fällen können die s-Wellen Streueigenschaften mit Hilfe von Feshbach-Resonanzen durch Anlegen externer Magnetfelder verändert werden [23]. Dies führt zu so dramatischen Effekten, wie der sogenannten “Bosenova” [24, 25]. Wie wir schon an diesen wenigen Beispielen sehen können, tragen Wechsel-

wirkungen massgeblich zur Vielfalt der beobachteten Phänomene in Bose-Einstein-Kondensaten bei.

In den letzten Jahren hat das theoretische Interesse an Wechselwirkungen die über die isotrope Kontaktwechselwirkung hinausgehen zugenommen. Besonders vielversprechend ist die Dipol-Dipol Wechselwirkung [26, 27, 28, 29, 30, 31, 32, 33, 34, 35, 36, 37, 38], da sie im Gegensatz zur Kontaktwechselwirkung langreichweitig und anisotrop ist. So wurden z.B. das Zusammenspiel dieser beiden Wechselwirkungen und ihr Einfluss auf die Eigenschaften eines Kondensats untersucht [31, 35, 39]. Es wurde vorhergesagt, dass in einem eindimensionales Gitter aus dipolaren Atomen ein ferromagnetischer Phasenübergang auftritt [34]. Darüber hinaus gibt es Vorschläge mit permanenten Dipolen einen Quantencomputer zu implementieren [27].

Ähnlich wie bei Feshbach-Resonanzen lässt sich auch die Dipol-Dipol Wechselwirkung durch Anlegen zeitlich veränderlicher Magnetfelder durchstimmen [28]. Dies ermöglicht es die oben genannten Effekte als Funktion der Stärke und des Vorzeichens der Dipol-Dipol Wechselwirkung zu studieren.

Mögliche Realisierungen dieser dipolaren Systeme beinhalten Atome und Moleküle mit einem hohen elektrischen oder magnetischen Dipolmoment. Ein Kandidat mit einem großen magnetischen Moment von 6 Bohr Magnetonen ist atomares Chrom. Die dipolare Wechselwirkung zwischen zwei Chromatomen ist um einen Faktor 36 größer als bei Alkaliatomen. Obwohl die Bose-Einstein-Kondensation von Chrom bislang nicht erreicht wurde, verfolgen weltweit drei Gruppen — uns eingeschlossen — dieses Ziel [40, 41].

Bose-Einstein-Kondensate werden unter Einsatz verschiedener Kühlmechanismen und Fallentypen erzeugt. Üblicherweise beginnt man mit einer magneto-optischen Falle (MOT), in der Atome eingefangen und lasergekühlt werden. Inelastische Kollisionen in Gegenwart von nahresonantem Laserlicht verhindern weitere Kühlung und limitieren die erreichbaren Dichten. Die Atome werden daher in eine Magnetfalle transferiert. Dort werden sie evaporativ bis in das quantenentartete Regime gekühlt. Die genaue Kenntnis der elastischen und inelastischen Stoßeigenschaften der Atome sind nicht nur für die Vorhersage der Eigenschaften des Kondensats unerlässlich, sondern auch für seine Erzeugung. Im Gegensatz zu den Alkaliatomen waren vor dieser Arbeit weder experimentelle noch theoretische Vorhersagen über die ultrakalten Stoßeigenschaften von Chrom bekannt. Diese Arbeit hat wesentlich zum Verständnis dieser Eigenschaften beigetragen.

Abweichend vom üblichen Weg zur Erzeugung eines Bose-Einstein-Kondensats konnten wir aufgrund der speziellen spektroskopischen Eigenschaften und dem hohen magnetischen Moment von Chrom einen kontinuierlichen Lademechanismus entwickeln. In dieser sogenannten CLIP Falle (Continuously Loaded Ioffe-Pritchard Trap) können Atome aus dem angeregten Zustand der magneto-optischen Falle in einen langlebigen metastabilen Zustand zerfallen. Dort sind sie magnetisch gefangen

und vom Licht der MOT entkoppelt. Mit bis zu 2×10^8 Atomen konnten wir in der CLIP Falle mehr als 40 Mal mehr Atome fangen als in der MOT. Zudem erleichtert die direkte Ansammlung der Atome in der Ioffe-Pritchard Magnetfalle die nachfolgenden Präparationsschritte für ultrakalte Atome erheblich. Wir haben detaillierte Messungen zur Temperaturabhängigkeit der Wolke, der gefangenen Atomzahl und der Ladezeitkonstanten für verschiedene Fallenparamter durchgeführt. Wir konnten die beiden dominierenden Verlustmechanismen identifizieren. Ein Modell basierend auf Ratengleichungen erlaubte es uns die entsprechenden Ratenkoeffizienten für diesen Verlustprozess aus den Daten zu bestimmen. In Kollisionen zwischen Atomen im angeregten Zustand der MOT und magnetisch gefangenen Atomen im metastabilen Zustand wird ein Teil der Anregungsenergie in kinetische Energie umgewandelt. Dies führt zu einem Verlust der Atome mit einem Ratenkoeffizienten von $\beta_{ed} = 5 \times 10^{-10} \pm 45$ % cm^3/s. Inelastische Stöße zwischen den magnetisch gefangenen Atomen begrenzen die Lebensdauer der Atome in diesem Zustand. Wir konnten den entsprechenden Ratenkoeffizienten zu $\beta_{dd} = 1.3 \times 10^{-11} \pm 17$ % cm^3/s bestimmen. Dieser recht große Wert verhinderte weitere Experimente in diesem metastabilen Zustand. Daher werden die Atome nach dem Laden durch Rückpumplaser zurück in den Grundzustand transferiert, in dem alle nachfolgenden Experimente stattfinden.

Im nächsten Schritt wird die Magnetfalle komprimiert um die Dichte der Atome zu erhöhen. Dabei steigt jedech ebenso die Temperatur. Durch Dopplerkühlen der Atome in der komprimierten Falle wurde die Temperatur reduziert und damit einhergehend die Dichter weiter gesteigert. Obwohl lediglich ein axialer Kühllaser eingestrahlt wurde, konnte ein signifikanter Kühleffekt in radialer Richtung beobachtet werden. Wir haben ausführliche Untersuchungen zur zeitlichen Entwicklung der Temperatur sowie ihrem stationären Verhalten durchgeführt. Mit Messungen zur Intensitätsabhängigkeit der radialen Temperatur sowie dem Einfluss der optischen Dichte in der Wolke auf diese Temperatur konnten elastische Kollisionen und anharmonisches Mischen der Freiheitsgrade als Kühlmechanismus ausgeschlossen werden. In dem von uns entwickelten Modell führt die hohe optische Dichte der Atomwolke zur Reabsorption von gestreuten Kühlphotonen. Durch die Erweiterung der Doppler-Kühltheorie um diesen Effekt konnte ein theoretisches Modell des radialen Kühlprozesses entwickelt werden. Die Vorhersagen dieses Modells stimmen quantitativ mit den Messergebnissen überein. In axialer Richtung wurden Temperaturen nahe der Dopplertemperatur von $124\,\mu$K erreicht. Die radiale Temperatur war um etwa einen Faktor zwei höher.

Eine weitere Verringerung der Temperatur wurde durch evaporatives Kühlen erreicht. Bei dieser Methode werden Atome mit hoher kinetischer Energie aus der Falle entfernt. Die verbleibenden Atome thermalisieren über elastische Stöße zu einer neuen — tieferen — Gleichgewichtstemperatur. Die Effizienz dieses Kühlmechanismusses hängt wesentlich von den elastischen und inelastischen Streueigenschaften des verwendeten Atoms ab. Für Chrom waren die relevanten Eigenschaf-

ten vor dieser Arbeit unbekannt. Ultrakalte Kollisionen von Grundzustandsatomen werden durch s-Wellen Stöße dominiert. Diese sind durch einen einzigen Parameter, der Streulänge a, charakterisiert. Wir konnten die Temperaturabhängigkeit der elastische Kollisionsrate der beiden Chromisotope ^{52}Cr und ^{50}Cr in einem Relaxationsexperiment bestimmen. Bei dieser Methode wird die Fallengeometrie nach dem evaporativen Kühlen schnell verändert. Dies erzeugt eine anisotrope Temperaturverteilung in der Wolke. Über den zeitlichen Verlauf der von elastischen Stößen vermittelte Relaxation zur Gleichgewichtstemperatur kann auf den Streuquerschnitt geschlossen werden. Der Vergleich mit einer Theorie, die die effektive Reichweite des Potentials beinhaltet, erlaubt es nicht nur den Absolutbetrag der Streulänge, sondern auch ihr Vorzeichen zu ermitteln. Die deka-triplett Streulänge von ^{52}Cr konnten wir zu $a(^{52}\mathrm{Cr}) = 170 \pm 39\,\mathrm{a_0}$ bestimmen, wobei $a_0 = 0.53$Å der Bohr'sche Radius ist. Das Vorzeichen der Streulänge spielt hierbei eine wichtige Rolle, da Kondensate nur bei positiver Streulänge stabil sind. Die geringere natürliche Häufigkeit von ^{50}Cr schränkte den messbaren Temperaturbereich ein. Daher konnten wir in diesem Fall nur den Absolutbetrag der deka-triplett Streulänge von $|a(^{50}\mathrm{Cr})| = 50 \pm 23\,\mathrm{a_0}$ bestimmen.

Unsere Bemühungen ein Bose-Einstein-Kondensat mit Chromatomen durch evaporatives Kühlen in der Magnetfalle zu erreichen, resultierten in einer maximalen Phasenraumdichte von 0.04 ± 0.013, bei einer Temperatur von $370 \pm 52\,\mathrm{nK}$ und mit 1500 ± 260 verbleibenden Atomen, was einer zentralen Dichte von $(6.5 \pm 1.7) \times 10^{11}\,\mathrm{cm^{-3}}$ entspricht. Weiteres Kühlen reduzierte die Phasenraumdichte aufgrund eines erhöhten Verlusts an Atomen durch dipolare Relaxation.

Wir konnten vorläufige Ergebnisse zur Magnetfeldabhängigkeit der dipolaren Relaxationsrate bei einer Temperatur von $300\,\mu$K erzielen. Unsere experimentellen Daten sind in ausgezeichneter Übereinstimmung mit der Theorie. Bei einem magnetischen Offset-Feld von $B_0 = 20\,\mathrm{G}$ erhalten wir einen Ratenkoeffizienten für den Atomzahlverlust von $\beta_{dp} = 10^{11}\,\mathrm{cm^3/s}$. Eine Messung der durch dipolare Relaxation verursachten Heizrate in Atomwolken von ^{52}Cr und ^{50}Cr zeigte vergleichbare Heizraten für beide Isotope. Mit diesen Experimenten konnten wir die Vorhersagen der Theorie bestätigen, dass die dipolare Relaxationsrate unabhängig von den Details des Wechselwirkungspotentials ist, jedoch mit dem magnetischen Offset-Feld und dem Dipolmoment der Atome skaliert. Im Gegensatz dazu hängen die Eigenschaften der elastischen s-Wellen Streuung sensitiv vom Wechselwirkungspotential ab.

Die Ergebnisse dieser Arbeit stellen einen wichtigen Schritt auf dem Weg zu einem Bose-Einstein-Kondensat von Chromatomen dar. Speziell die Kenntnis der elastischen und inelastischen Stoßeigenschaften im Grundzustand erlauben es nun eine erfolgreiche Strategie zu entwickeln.

Ein vielversprechender Ansatz hierzu stellt das Umladen der Atome in eine optische Dipolfalle [42] dar. Dabei werden die Atome im absoluten Grundzustand gefangen,

welcher immun gegenüber dipolaren Verlusten ist. Mit den in dieser Arbeit entwickelten Kühlmethoden können die Atome in einer Magnetfalle vorgekühlt werden. Der große elastische Streuquerschnitt von Chrom sollte effizientes evaporatives Kühlen nach dem Umladen in die Dipol-Falle bis ins quantenentartete Regime erlauben. Dieser Ansatz wird derzeit in unserem Labor experimentell umgesetzt.

Sobald ein Bose-Einstein-Kondensat mit Chrom erzeugt wird, sind eine Reihe interessanter Experimente möglich. So kann z.B. der Einfluss der (einstellbaren) Dipol-Dipol Wechselwirkung auf die Expansion eines Chrom-Kondensats studiert werden [28, 29]. Die starke dipolare Wechselwirkung lässt zudem eine ausreichende Breite der Feshbach-Resonanzen erwarten. Diese könnten dann dazu eingesetzt werden die Kontaktwechselwirkung zu verändern und sogar vollständig zu unterdrücken. In einem solchen System wäre die dipolare Wechselwirkung dominant. Durch Einstellen des Vorzeichens und der Wechselwirkungsstärke könnten die Stabilität und der Kollaps eines derartigen dipolaren Kondensats untersucht werden [31, 33] — komplementär zu den analogen Experimenten in Alkaliatomen, in denen eine attraktive Kontaktwechselwirkung zum Kollaps führt [24].

Wir erwarten, dass die Dipol-Dipol Wechselwirkung in einem Bose-Einstein-Kondensat mit Chromatomen die Vielfalt an Effekten in quantenentarteten Systemen deutlich bereichern wird. Die Kontrolle über sowohl die Kontakt- als auch die Dipol-Dipol Wechselwirkung wird eine ganze Reihe an faszinierenden Experimenten ermöglichen, die zu einer Vertiefung unseres Verständnisses dieser neuen Form von Materie beitragen werden.

Abstract

In this thesis, I present experimental results on the scattering properties of ultra-cold chromium atoms. This represents a significant progress towards a Bose-Einstein condensate with chromium atoms. Deviating from the standard approach for the preparation of ultra-cold atoms, we have devised a continuous loading scheme for a magnetic trap from a magneto-optical trap. Doppler cooling of the atoms in the compressed magnetic trap further reduces the temperature of the cloud and increases its density. Subsequent forced radio-frequency evaporation resulted in a maximum phase-space density of 0.04. Strong dipolar relaxation collisions originating from the large magnetic dipole moment of chromium prevented us from reaching quantum degeneracy. We measured the magnetic field dependence of the dipolar relaxation rate, which was typically on the order of $\beta_{dp} \approx 10^{11}\,\mathrm{cm}^3/\mathrm{s}$, in excellent agreement with theory. Probably the most important parameter for ultra-cold scattering of chromium atoms is the scattering length a. We were able to perform a detailed measurement of the temperature dependence of the elastic collision rate. A comparison of our data with theory allowed us to extract the deca-triplet scattering lengths for the two bosonic chromium isotopes ^{52}Cr and ^{50}Cr. For ^{52}Cr we obtained a value of $a(^{52}\mathrm{Cr}) = 170 \pm 39\,\mathrm{a}_0$ with a positive sign ($a_0 = 0.53$Å is Bohr's radius). The low natural abundance of ^{50}Cr limited the temperature range of our measurement. As a result, we could only deduce the magnitude $|a(^{50}\mathrm{Cr})| = 50 \pm 23\,\mathrm{a}_0$ of the scattering length. Knowing the ultra-cold scattering properties allows now to devise a successful route to a Bose-Einstein condensate with chromium atoms.

Chapter 1

Introduction

In this Chapter I give a brief introduction into the field of Bose-Einstein condensates. The experimental studies presented in this thesis are aimed towards the realization of a Bose-Einstein condensate with chromium atoms.

The first realization of Bose-Einstein condensation (BEC) in dilute atomic gases in the year 1995 [1, 2, 3] has pioneered the exploration of an exciting new form of matter: the macroscopic quantum state. This date marked the emergence of a fascinating new field in atom optics and quantum physics. An ever growing enormous number of theoretical and experimental publications have appeared since then. Around 40 experimental groups are working now in the field, mostly with BECs of the alkali atoms rubidium, sodium and lithium. Besides these elements, atomic hydrogen [43] and recently metastable helium [44, 45], potassium [46] and cesium [25] have been Bose-condensed. In 2001, Eric Cornell, Wolfgang Ketterle and Carl Wieman were awarded the Nobel Price in Physics "for the achievement of Bose-Einstein condensation in dilute gases of alkali atoms, and for early fundamental studies of the properties of the condensates" [4].

The phenomenon of Bose-Einstein condensation was first discussed by Einstein [47] based on the photon statistics invented by Bose [48]. The particle–wave duality in quantum mechanics allows to attribute a wavelength to atoms in a gas, the de Broglie wavelength λ_{dB}. If the particle density n in a gas of atoms is such that the interparticle separation is of the same order of magnitude as the de Broglie wavelength, the particles can no longer be treated as independent. This is the condition for Bose-Einstein condensation, which can be expressed in terms of the phase-space density $\varrho = n\lambda_{\mathrm{dB}}^3 \approx 2.6$. BEC is characterized by the macroscopic population of a single quantum state, described by a macroscopic wavefunction which is the order parameter of the system. In atomic vapors the transition temperature is typically on the order of a few hundred nK at densities between $10^{14} \ldots 10^{15}\,\mathrm{cm}^{-3}$. Comparing this density to typical densities in air ($10^{19}\,\mathrm{cm}^{-3}$) or solids ($10^{23}\,\mathrm{cm}^{-3}$),

demonstrates that we are dealing with a very dilute system. Even under ideal experimental conditions, most Bose-Einstein condensates have a limited lifetime. Ultimately, interactions lead to the formation of molecules which results in the destruction of the BEC and relaxation into the thermodynamically stable regime. It was therefore not clear in the beginning, whether a condensate state existed long enough to be observable at all.

Probably the first BEC occured in liquid helium. Helium is special in that it stays a liquid even for very low temperatures and becomes superfluid below a critical temperature. London was the first to relate the superfluidity in ^{4}He to Bose-Einstein condensation [49]. The strong interactions between the atoms in a liquid result in a small condensate fraction in superfluid helium. BEC in dilute gases occurs in a complementary regime: interactions are weak and almost the whole sample comprising typically $10^4 \ldots 10^6$ atoms is in the condensate state. Despite their weakness, interactions govern the main properties of Bose-Einstein condensates in atomic vapors.

The dominant interaction is the contact interaction arising from s-wave scattering of the atoms. Most of the interesting features of a BEC emerge from the interplay of quantum-statistical effects and the contact interaction. These include elementary excitations like acoustic waves and phonons [5, 6, 7], and the realization of condensate spin mixtures, so-called "spinor-condensates" [8, 9]. Just like liquid helium, Bose condensates are superfluids below the critical temperature [10, 11, 12] in which quantized vortices [13, 14, 15, 16] have been observed.

The macroscopic occupation of a single quantum state is well-known from laser physics. The analogy between the mode of a laser and Bose-Einstein condensates has motivated the realization of atom "lasers" [50, 51, 52, 53] and a coherent amplifier for matter waves [54, 55].

Bose-Einstein condensates can be described in the framework of a nonlinear Schrödinger equation, where the nonlinearity arises from the interactions. In quantum optics, a similar equation governs the propagation of light in a nonlinear medium. Consequently, nonlinear optical phenomena like four-wave mixing [17] and the creation of bright and dark solitons [18, 19, 20, 21, 22] could be observed in a Bose-Einstein condensate.

The interaction in a BEC is not necessarily fixed. In special cases, the s-wave scattering properties of the atomic species can be tuned with an external magnetic field via a Feshbach resonance [23]. This can lead to a dramatic change in the properties of the BEC including its spectacular collapse in a so-called "Bosenova" [24, 25]. As we can see from these examples, interactions between the atoms contribute to the richness of effects in Bose-Einstein condensates.

In recent years, theoretical interest in additional interaction mechanisms beyond the isotropic contact interaction has grown. Especially the dipole-dipole interaction has attracted much interest [26, 27, 28, 29, 30, 31, 32, 33, 34, 35, 36, 37, 38] since

it is long-range and anisotropic — two features the contact interaction lacks. The interplay between contact and dipole-dipole interaction will govern the properties of a Bose-Einstein condensate [35]. Theoretical investigations have shown that the stability and shape of a dipolar BEC is dependent on the shape of the trap [31, 39]. The attractive part of the dipole-dipole interaction can lead to a BCS (Bardeen-Cooper-Shrieffer) type transition in a fermionic quantum gas [26], and may result in a quantum phase transition of a bosonic ultra-cold dipolar gas in an optical lattice [32]. If dipolar atoms are arranged in a one-dimensional optical lattice, a ferromagnetic phase transition is predicted and spontaneous magnetization is expected to occur [56]. Moreover, there are theoretical proposals for realizing a quantum computer with permanent dipole moments [27].

Similar to the Feshbach resonances, the magnitude and sign of the dipole-dipole interaction can be adjusted by applying time varying magnetic fields [28]. This makes it possible to map the dependence of the effects described above on the strength of the dipolar interaction. Obviously, dipole-dipole interactions will further diversify the phenomenons observed in Bose-Einstein condensates.

Possible realizations of such dipolar systems include atoms and molecules that have a large electric dipole moment in an external electric field, and atoms with a large magnetic dipole moment. Several groups have started activities towards cooling and trapping of polar molecules [57, 58, 59]. A candidate with a large magnetic moment of 6 Bohr magnetons is atomic chromium. The dipole-dipole interaction between two chromium atoms is larger by a factor of 36 compared to alkali atoms. Although Bose-Einstein condensation in atomic chromium has not yet been achieved, three groups including us are pursuing this goal [40, 41]. Chromium also has a fermionic isotope, which allows to study quantum statistical effects in a degenerate fermi gas under the influence of dipole-dipole interactions [30, 60, 61, 62, 63, 64, 65].

Typically, Bose-Einstein condensates are produced using a combination of cooling and trapping techniques. The “standard” approach to BEC starts with a magneto-optical trap in which atoms are collected, precooled and trapped. Inelastic collisions in the presence of the near resonant cooling laser light make a transfer to a magnetic or optical-dipole trap necessary. There, the atoms are evaporatively cooled to the quantum degenerate regime. Other approaches employ buffer gas cooling in a cryogenic environment to precool the atoms and load them into a steep magnetic trap, in which evaporative cooling is performed [41, 43].

The knowledge of the elastic and inelastic scattering properties of the atoms is not only essential for predicting the properties of a Bose-Einstein condensate, but also for the optimization of the “route to BEC”. Unlike for the alkali atoms, neither experimental nor helpful theoretical data existed on the ultra-cold scattering properties of chromium. Elastic and inelastic scattering rates for chromium at temperatures exceeding 10 mK have been obtained in a cryogenic trapping experiment [41]. By

virtue of the complexity of atom-atom scattering, this data allows no extrapolation to the ultra-cold regime.

The elastic and inelastic scattering properties are very sensitive to the details of the molecular interaction potential of two colliding atoms. Feshbach resonance spectroscopy has successfully been employed to refine model potentials for the interaction between ^{133}Cs [66, 67], ^{23}Na [68], ^{85}Rb [69] and ^{87}Rb [70]. These model potentials allow an accurate prediction of the elastic s-wave cross-section, position of resonances and also inelastic collision rates. Photoassociation spectroscopy is supposably the most powerful method to obtain information on weakly bound molecular states. Again, model potentials can be refined to fit the experimental data and allow predictions of further scattering properties [71, 72, 73]. Cross-dimensional thermal relaxation of an anisotropic temperature distribution in a trapped cloud of atoms [74] and loss rate measurements of the number of atoms from a finite depth trap [75] provide the most direct access to the elastic and inelastic scattering properties of atoms in a trap, respectively.

In this thesis, I report on the elastic ground state scattering properties of the chromium isotopes ^{52}Cr and ^{50}Cr using the cross-dimensional relaxation method. Preliminary inelastic dipolar relaxation rates are determined from a loss rate measurement. In addition, we have studied the elastic and inelastic collision mechanisms involved in the preparation of our ultra-cold samples.

We have developed a variation of the standard approach. Atoms from the MOT are continuously loaded into a magnetic trap. Subsequent laser cooling further reduces the temperature of the atoms in the compressed magnetic trap. Evaporative cooling allowed us to reach phase-space densities as high as 0.04. Bose-Einstein condensation was prevented by excessive heating and atom loss due to a strong dipolar relaxation rate.

The thesis is organized as follows:

In Chapter 2, I give a summary of the physical and spectroscopic properties of chromium relevant for this work. Chapter 3 provides the theoretical background for the laser cooling and trapping mechanisms employed. Special attention is given to the theory of Doppler cooling, which is extended in Chapter 7 to account for cooling effects of reabsorbed photons. The principles of magnetic trapping are discussed in Chapter 4. I review the different regimes of a Ioffe-Pritchard type magnetic trap and address possible loss mechanisms due to the trap geometry. The technical details of the experimental setups and the data evaluation procedures are presented in Chapter 5. The first step in the preparation of an ultra-cold cloud of chromium atoms is the CLIP (Continuously Loaded Ioffe-Pritchard) trap, which I introduce in Chapter 6. Experimental results on the temperature and the loading efficiency for different trap parameters are presented and compared to a simple model. In the next preparation step, Doppler cooling in a compressed magnetic trap is used to

further reduce the temperature of the cloud. Details of this method are described in Chapter 7. Elastic scattering of photons followed by reabsorption in the optically dense cloud can explain the observed radial cooling, even though the cooling laser beam is only applied along the axial direction. The standard treatment of Doppler cooling is extended to account for this reabsorption cooling. A model based on rate equations is compared with the experimental result. Evaporative cooling is typically the last preparation step for the realization of a BEC. Elastic and inelastic collisions determine the efficiency of this method. Therefore, I give a review on basic scattering theory in Chapter 8. I consider the most prominent features in ultra-cold scattering using the square-well potential as an example. Specialities of atom–atom scattering like e.g. Feshbach resonances and dipolar relaxation are discussed in a separate Section. The Chapter concludes with a description of the evaporative cooling technique. In Chapter 9, I present experimental results on the elastic scattering properties for the two chromium isotopes ^{52}Cr and ^{50}Cr. Theoretical models are fitted to the data and allow us to extract the scattering length for ^{52}Cr and its magnitude for ^{50}Cr. At the end of Chapter 9, I present the results of our effort to achieve Bose-Einstein condensation in atomic chromium via evaporative cooling. Preliminary results on the extraordinarily large dipolar relaxation rate in chromium are shown in Appendix E. The thesis concludes with a summary and future perspectives in Chapter 10.

Chapter 2

Chromium

In this chapter I present the physical, electronic and spectroscopic properties of chromium relevant to this work. A summary of the electronic dipole transitions employed for the laser cooling and trapping techniques is given.

The experiments presented in this thesis are performed with two different bosonic isotopes of the transition metal element chromium. Chromium is a very hard (9 mohs), lustrous, silvery-white metal with a body-centered cubic (bcc) crystalline structure. It has a very high melting and boiling point of around 1850 °C and 2690 °C, respectively. Sublimation under vacuum conditions results in a vapor pressure of 6×10^{-7} mbar at a temperature of 1500 °C [76] — sufficient for an atomic beam experiment. The difficulty of operating a high temperature effusion cell under ultra-high vacuum conditions is eased by the getter capabilities of chromium. The inner wall of the vacuum chamber is continuously coated with a chromium film during operation. Residual gas atoms hitting the coated surfaces stick to it and are buried under the growing chromium film. In titanium sublimation getter pumps, the same mechanism results in typical pumping speeds of several thousand liters per second. In fact, chromium is an even more efficient getter material than titanium [76, 77], but due to its high sublimation temperature not commonly used in getter pumps.

element	mass [au]	abundance [%]	nuclear spin I	statistics
chromium	50	4.35	0^+	boson
	52	83.79	0^+	boson
	53	9.5	$^3/_2{}^+$	fermion
	54	2.36	0^+	boson

Table 2.1: Natural abundance and nuclear spin of stable chromium isotopes.

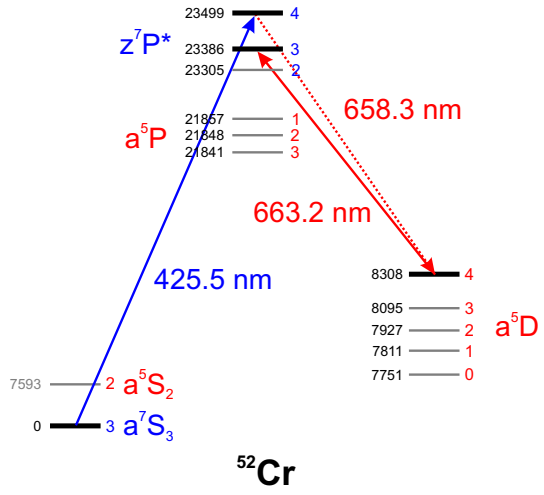

Figure 2.1: Part of the level scheme for chromium (energies not to scale). Shown are the septet (blue) and quintet (red) system for the S, P and D terms up to an energy of 23 500 cm^{-1}. The numbers on the left and right of each level are the energy in wave numbers (cm^{-1}) and the total angular momentum J, respectively. The relevant transitions for cooling (425.5 nm), continuous loading of the magnetic trap (658.3 nm) and repumping (663.2 nm) are indicated by the arrows.

One of the original scopes of this project is the investigation of quantum statistical effects in bosons and fermions. A natural choice are two different isotopes of the same element. In chromium, we have three bosonic and one fermionic isotope. The fermion has $I = 3/2$ nuclear spin, whereas the bosons have none. Table 2.1 summarizes the natural abundance and nuclear spin for the stable chromium isotopes. In the experiments presented in this thesis, we have mainly used ^{52}Cr, but sometimes for comparison also ^{50}Cr.

The spectroscopic properties of chromium are important for the laser cooling experiments presented in Chapter 6 and 7. Figure 2.1 shows the relevant part of the level scheme for bosonic chromium[1]. The corresponding levels for the fermionic isotope ^{53}Cr (not shown) are further split by the hyperfine interaction. We operate the Zeeman-slower and the magneto-optical trap (see Chapter 3) on the strong transition connecting the ground state $^7S_3$ with the excited state $^7P_4$ in the blue at a wavelength of 425.5 nm. The main properties of this transition are summarized in Table 2.2. Atoms in the excited ^{7}P manifold can undergo a transition to the metastable ^{5}D manifold via intercombination lines. The wavelengths of the most important of these transitions are summarized in Table 2.3. Spontaneous de-excitation via the spin forbidden $^5D_4 \leftrightarrow {}^7P_4$ transition is utilized to continuously load atoms into a magnetic trap (see Chapter 6). The atoms accumulate during operation of the

[1]The isotope shifts for the transitions are with a few 100 MHz rather small.

vacuum wavelength	λ	=	$\frac{2\pi}{k}$	=	$425.554\,\mathrm{nm}$
natural linewidth	Γ	=	$\frac{1}{\tau}$	=	$31.5 \times 10^6\,\mathrm{s}^{-1}$
				=	$2\pi \times 5.02\,\mathrm{MHz}$
saturation intensity	I_s	=	$\frac{\pi hc\Gamma}{3\lambda^3}$	=	$8.52\,\mathrm{mW/cm^2}$
absorption cross-section	σ_λ	=	$6\pi\lambda^2$	=	$8.65 \times 10^{-10}\,\mathrm{cm}^2$
Doppler temperature	T_D	=	$\frac{1}{k_\mathrm{B}}\frac{\hbar\Gamma}{2}$	=	$124\,\mu\mathrm{K}$
recoil temperature	T_rec	=	$\frac{1}{k_\mathrm{B}}\frac{(\hbar k)^2}{2m}$	=	$1.02\,\mu\mathrm{K}$
recoil velocity	v_rec	=	$\frac{\hbar k}{m}$	=	$1.80\,\mathrm{cm/s}$

Table 2.2: Properties of the cooling and trapping transition $^7\mathrm{S}_3 \leftrightarrow {}^7\mathrm{P}_4$.

magneto-optical trap in the metastable $^5\mathrm{D}_4$ state. We use a repumper laser on the $^5\mathrm{D}_4 \leftrightarrow {}^7\mathrm{P}_3$ line to pump the atoms back into the ground state, since this transition is faster than the $^5\mathrm{D}_4 \leftrightarrow {}^7\mathrm{P}_4$ transition and disturbing dark state resonances on the latter transition are absent [78].

Atoms in the excited state can also undergo a transition to the $^5\mathrm{D}_3$ state and accumulate there. This occurs on a longer timescale than for the $^5\mathrm{D}_4$ state due to a smaller natural linewidth, as indicated in Table 2.3. Nevertheless we have set up a repumper laser to the $^7\mathrm{P}_3$ state to slightly increase the number of atoms in our magnetic trap.

Prior to our measurements [78], only the natural linewidth of the $^5\mathrm{D}_4 \leftrightarrow {}^7\mathrm{P}_3$ transition was known. It is worthwhile to mention, that the natural linewidths for the intercombination lines starting in the $^7\mathrm{P}_4$ excited state are orders of magnitude smaller than those starting from $^7\mathrm{P}_3$. The reason for this might be a coupling of the $^5\mathrm{P}_3$ to the $^7\mathrm{P}_3$ state, thus allowing the septet state to decay via the $^5\mathrm{P}$ state to the $^5\mathrm{D}$ state. Since a $^5\mathrm{P}_4$ state does not exist, the conservation law for the spin is enforced and the transition rates are small [79].

Most laser cooling and trapping experiments are carried out with alkali metals, that have a rather simple electron configuration with one valence electron. Chromium on the other hand has six valence electrons in a hybridized $[\mathrm{Ar}]3\mathrm{d}^5 4\mathrm{s}^1$ electronic configuration. The alignment of all electron spins leads to a strong magnetic moment in the $^7\mathrm{S}_3$ ground ($6\,\mu_B$) and metastable $^5\mathrm{D}_4$ ($6\,\mu_B$), $^5\mathrm{D}_3$ ($4.5\,\mu_B$) states. This allows us to achieve magnetic traps with a strong confinement (see Chapter 4) as required for evaporative cooling (see Section 9.4.4). Elastic scattering of magnetic dipoles scales with the fourth power of the magnetic moment and is therefore by more than three orders of magnitude stronger than for the alkali metals (see Section 8.6.3). We expect new and fascinating effects in a Bose-Einstein condensate of chromium in which the dipole-dipole force can be the dominant interaction.

isotope	intercombination line	vacuum wavelength	natural linewidth
^{52}Cr	$^5\mathrm{D}_4 \leftrightarrow {}^7\mathrm{P}_4$	658.2740(2) nm [a]	$\Gamma = (127 \pm 14)\,\mathrm{s}^{-1}$ [a]
	$^5\mathrm{D}_4 \leftrightarrow {}^7\mathrm{P}_3$	663.1846(2) nm [a]	$\Gamma = 6000\,\mathrm{s}^{-1}$ [b]
	$^5\mathrm{D}_3 \leftrightarrow {}^7\mathrm{P}_4$	649.1978(2) nm [a]	$\Gamma = (42 \pm 6)\,\mathrm{s}^{-1}$ [a]
	$^5\mathrm{D}_3 \leftrightarrow {}^7\mathrm{P}_3$	653.9727(2) nm [a]	- [c]
^{50}Cr	$^5\mathrm{D}_4 \leftrightarrow {}^7\mathrm{P}_4$	658.2733(2) nm [a]	see above
	$^5\mathrm{D}_4 \leftrightarrow {}^7\mathrm{P}_3$	663.1877(2) nm [d]	see above
	$^5\mathrm{D}_3 \leftrightarrow {}^7\mathrm{P}_4$	653.9764(2) nm [a]	see above

Table 2.3: Vacuum wavelength and natural linewidths of the most important intercombination lines between ^{7}P and ^{5}D for the two isotopes ^{52}Cr and ^{50}Cr.

[a] [78]
[b] [80]
[c] unknown
[d] this work

On the other hand, also inelastic dipolar relaxation collisions scale in a similar way with the dipole moment and prevents us from reaching the quantum degenerate regime in a purely magnetic trap. A far-off resonant optical dipole trap allows storage of the atoms in the absolute ground state of the system and eliminates this loss process. Bose-Einstein condensation of chromium should be possible in such a trap, which is currently being set up.

The number of electrons also has profound consequences on the complexity of ultracold elastic collisions. Two bosonic chromium atoms can collide on 7 different molecular potential curves (see Figure 8.11) that are further split by the Zeeman energy. The mere number of electrons makes accurate *ab initio* calculations of the molecular potentials extremely hard and only one such calculation for the $^{13}\Sigma_g^+$ molecular state is known from the literature [81]. As a result, no theoretical predictions of the scattering properties of chromium exist. The experimental results of this thesis (see Chapter 9 and Appendix E) might allow to construct a more accurate model potential for chromium in the future.

Chapter 3

Optical cooling and trapping techniques

Atom–light interactions are a vast subject which has been studied since the early days of atomic physics. This Chapter gives a brief summary of the most important effects with special emphasis on the laser cooling and trapping techniques. In the first Section I discuss the dipole- and the radiation pressure force acting on an atom in a light field. As an application of these forces, one-dimensional Doppler and polarization gradient cooling are being presented in Sections 3.2-3.4. Finally, I show in Section 3.5 how these techniques can be extended to three dimensions and — combined with a magnetic field — form a magneto-optical trap for neutral atoms.

3.1 Atom–light interaction

Atoms in a monochromatic light field with a frequency tuned close to an atomic resonance frequency experience strong forces and large accelerations which can be used for slowing down the atoms. The force acting on an atom in a light field has two contributions: the conservative dipole force arising from energy shifts of the atomic states in the light field (ac Stark shift) and the dissipative radiation pressure force arising from momentum transfer of scattered photons.

3.1.1 The dipole force

Consider an atom with two internal states: the ground state $|\,g\,\rangle$ and an excited state $|\,e\,\rangle$ which are connected via an optical dipole transition with frequency ω_{atom} and spectral linewidth Γ. The electric field $\vec{E}$ of a quasi-resonant light field with intensity I and frequency ω_{laser} couples to the electric dipole moment $\vec{d}$ of the atom

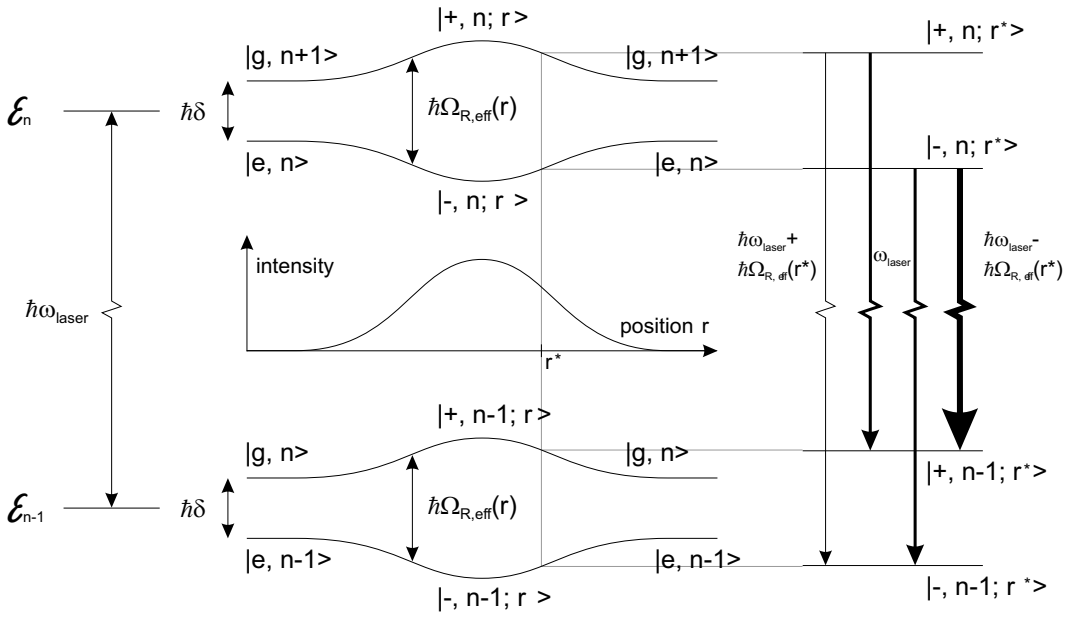

Figure 3.1: Energy diagram of the combined atom–photon system for a blue detuned laser ($\delta > 0$). Left: Energy of the photon field. Middle: Energy shifts of the eigenstates for the atom-photon system across a Gaussian laser beam. Right: Spontaneous emission lines at position r^* with intensities proportional to the line thickness.

giving rise to an interaction energy of $V = -\vec{d} \cdot \vec{E}$. In strong light fields with $I \gtrsim I_s$, where $I_s = \frac{\pi h c \Gamma}{3\lambda^3}$ is the saturation intensity, the ground and excited state of the atom ("bare states") are no longer eigenstates of the Hamiltonian describing the system. The joint system atom–photon is described by a so-called "dressed state" and the number of photons n in the light field. The new eigenstates $|+, n\rangle$ and $|-, n\rangle$ and are superpositions of the bare states $|g\rangle$ and $|e\rangle$ [82]:

$$|+, n\rangle = -\sin\Theta|g\rangle + \cos\Theta|e\rangle \tag{3.1}$$

$$|-, n\rangle = +\cos\Theta|g\rangle + \sin\Theta|e\rangle, \tag{3.2}$$

where $\tan 2\Theta = -\frac{\Omega_R}{\delta}$ is the tangens of the so-called "Stückelberg angle" with the Rabi frequency

$$\Omega_R = |\frac{\vec{d} \cdot \vec{E}}{\hbar}| = \Gamma\sqrt{\frac{I}{2I_s}} \tag{3.3}$$

and the detuning $\delta = \omega_{\text{laser}} - \omega_{\text{atom}}$ of the laser from the atomic resonance. Figure 3.1 shows the energy evolution of the eigenstates across a Gaussian intensity distribution. The energy spectrum can be described as a ladder system with pairs of steps having an energy splitting corresponding to the photon energy of the light field and a

frequency splitting between two dressed states given by the effective Rabi frequency $\Omega_{R,\text{eff}} = \sqrt{\Omega_R^2 + \delta^2}$. The energy shift of the dressed states with respect to the bare states is given by

$$U_{\text{dip}} = \pm \text{sign}(\delta) \frac{\hbar}{2} (\Omega_{R,\text{eff}} - |\delta|), \tag{3.4}$$

where the "+" sign applies for the dressed state adiabatically evolving from the ground state. An intensity gradient in the light field results in the so-called "dipole force" $\vec{F}_{\text{dip}} = -\nabla U_{\text{dip}}$. For a red detuned laser ($\delta < 0$), atoms initially in the ground state are attracted to high electric fields ("high field seekers"), since their electric dipole oscillates in phase with the external field. For a blue detuned laser, a phase shift of π reverses this behaviour: atoms are repelled from the high intensity region ("low field seekers").

By spontaneously emitting a photon, atoms can undergo transitions between the step pairs of the ladder. The corresponding fluorescence spectrum consists of three frequencies ω_{laser} and $\omega_{\text{laser}} \pm \Omega_{R,\text{eff}}$, the so-called Mollow-Triplet [83], with different intensities as shown on the right hand side of Figure 3.1. We will discuss the fluorescence spectrum emitted by an atom in more detail in Appendix A.

The dipole force has many applications in atom optics. In atom lithography, a standing wave light mask can be used to focus a beam of atoms onto a substrate [84]. Focused laser beams can be used as optical traps and optical waveguides for atoms [42]. Several cooling techniques, such as the bichromatic force [85] or polarization gradient cooling in standing wave light fields [86] rely on dipole forces in multi-level atoms.

3.1.2 The radiation pressure force

Each absorption and emission process of a photon is accompanied by a momentum transfer of $\hbar k$ between atom and photon, where $k = \frac{2\pi}{\lambda}$ is the wave number of the laser light. Directed absorption of photons from a laser beam leads to a net force in the direction of the laser beam, since the subsequent spontaneous emission is centro-symmetric and averages to zero for many absorption/emission cylces. The average force acting on an atom is the rate of change in momentum:

$$F_{\text{sc}} = \hbar k \Gamma_{\text{sc}}, \tag{3.5}$$

where we have introduced the scattering rate

$$\Gamma_{\text{sc}} = \frac{\Gamma}{2} \frac{s}{s+1} = \frac{\Gamma}{2} \frac{I/I_s}{(1 + I/I_s + 4\Delta^2/\Gamma^2)} \tag{3.6}$$

with the saturation parameter

$$s = \frac{I/I_s}{(1 + 4\Delta^2/\Gamma^2)} \tag{3.7}$$

and the effective detuning Δ. For $s = 1$, the scattering rate drops to half its maximum value of $\frac{\Gamma}{2}$. The frequency difference between the incident laser beam in the laboratory frame and the atomic transition frequency in the moving frame of the atom, is given by the effective detuning Δ. Depending on the system of consideration, it can have several contributions:

$$\Delta = \delta + kv - \frac{\Delta\mu B}{\hbar}. \tag{3.8}$$

The first term is the laser detuning for an atom at rest. For an atom moving at a velocity v along the direction of a counterpropagating laser beam, the frequency of the laser light is Doppler-shifted by kv (second term). The energy of an atomic state with a magnetic dipole moment μ can be shifted in an external magnetic field (Zeeman effect). The shift in the atomic transition frequency depends on the magnitude of the magnetic field B, and the difference between the magnetic moment of the ground and excited state, $\Delta\mu$ (last term of Equation 3.8). A simple application of the magnetic tuning of the resonance frequency is the Zeeman-slower (see Section 5.2). It is used to produce slow atomic beams by scattering photons from a counterpropagating laser beam. To keep the atoms on resonance with the laser beam during deceleration, either the laser frequency or the atomic resonance frequency has to compensate the change in Doppler shift with decreasing velocity. This can be accomplished by applying a specially designed inhomogeneous magnetic field along the direction of the atomic beam.

In principle, the energy of an atomic state can also be altered with electric fields [87]. The experimental complexity and obstacles to generate the required field strengths compared to magnetic fields have prevented this technique to be widely used in atom optics experiments until recently. In a challenging experiment, Gerald Meijer and coworkers have succeeded in slowing down and trapping dipolar molecules with time-varying electric fields [57, 88].

3.2 Doppler cooling

In the previous section, we have seen that a laser beam can exert an average force on an atom. Due to the irreversibility of the spontaneous emission process, the radiation pressure force is non-conservative and can be used to cool atoms to very low velocities [89]. Consider two red detuned, counterpropagating laser beams incident on an atom

moving along the direction of the laser beams. The net radiation pressure force is the sum of the forces of each laser beam:

$$\begin{aligned} F_{\mathrm{sc}} &= F_{\mathrm{sc}}^{+} + F_{\mathrm{sc}}^{-} && (3.9)\\ &= \hbar k \frac{\Gamma}{2} \left(\frac{{}^{I}/_{I_s}}{1 + {}^{I}/_{I_s} + 4\,{}^{(\delta - kv)^2}/_{\Gamma^2}} - \frac{{}^{I}/_{I_s}}{1 + {}^{I}/_{I_s} + 4\,{}^{(\delta + kv)^2}/_{\Gamma^2}} \right) && (3.10)\\ &\approx \hbar k \frac{\Gamma}{2} \frac{I}{I_s} \frac{kv}{\Gamma} \frac{16\,{}^{\delta}/_{\Gamma}}{1 + 8\,{}^{(\delta^2 + k^2 v^2)}/_{\Gamma^2} + 16\,{}^{(\delta^2 - k^2 v^2)^2}/_{\Gamma^4}}. && (3.11) \end{aligned}$$

For the last step, we have approximated the full expression assuming low saturation (${}^{I}/_{I_s} \ll 1$). We can further simplify the last expression in the limit of low velocity ($|kv| \ll \Gamma$ and $|kv| \ll |\delta|$) and write it as a friction force $F_{\mathrm{sc}} = -\alpha\, v$. The damping coefficient α is given by

$$\alpha = -8\,\hbar k^2 \frac{{}^{\delta}/_{\Gamma}}{(1 + 4{}^{\delta^2}/_{\Gamma^2})^2} \frac{I}{I_s}. \tag{3.12}$$

In the rest frame of the atom, the frequency of the light beam counterpropagating the atomic motion is Doppler-shifted closer to the atomic resonance. As a result, the atom absorbs more light from this beam than from the one copropagating with the atom and is therefore slowed down.

The heating and cooling rates for Doppler cooling are obtained by considering the time evolution of the kinetic energy of a particle under the influence of cooling and heating effects of photon scattering. Let us neglect reabsorption processes for the moment. The atom experiences a cooling power which is proportional to the square of its velocity [90]:

$$\left(\frac{dE}{dt} \right)_{\mathrm{cool}} = Fv = -\alpha v^2. \tag{3.13}$$

This results in an exponential decrease of kinetic energy with a time constant τ_{cool} corresponding to a cooling rate of

$$\frac{1}{\tau_{\mathrm{cool}}} = -\frac{(dE/dt)_{\mathrm{cool}}}{E} = \frac{2\alpha}{m}, \tag{3.14}$$

where m is the mass of the atomic species. Absorption and spontaneous emission lead to a random walk in momentum space, which can be described as a diffusion process $\frac{d(p^2)}{dt} = \chi D_p$, with the diffusion constant $D_p = 2\hbar^2 k^2 \Gamma_{\mathrm{sc}}$. The contribution of absorption and spontaneous emission to momentum diffusion in the direction of observation ($\vec{e}_z$) is given by χ. Absorption from a laser beam propagating along this direction leads to a momentum kick of 1. In a purely one dimensional system, each absorption/emission cylcle yields $\chi = 2$ steps in momentum space. For three dimensional systems, the projection of the emission pattern $P_e(\vartheta, \phi)$ onto the direction of

emission type	$P_e(\vartheta, \phi)$	χ
one-dimensional	1	$1+1$
isotropic	$\frac{1}{4\pi}$	$1+\frac{1}{3}$
linear dipole along $\vec{e}_x$	$\frac{3}{8\pi}(1-\sin^2\vartheta\cos^2\phi)$	$1+\frac{2}{5}$

Table 3.1: Spontaneous emission patterns and corresponding contribution χ to momentum diffusion in $\vec{e}_z$ direction. In this example, the direction of the cooling laser coincides with the direction of observation, therefore absorption always leads to a momentum kick of 1.

interest has to be taken into account[1]

$$\chi = 1 + \int_0^{2\pi} d\phi \int_0^{\pi} d\vartheta \cos^2(\vartheta) P_e(\vartheta, \phi) \sin(\vartheta). \tag{3.15}$$

Table 3.1 summarizes different emission patterns and the resulting χ.

The gain in kinetic energy $\frac{p^2}{2m}$ due to momentum diffusion leads to a heating power which is given by

$$\left(\frac{dE}{dt}\right)_{\text{heat}} = \chi \frac{D_p}{2m}. \tag{3.16}$$

In contrast to the cooling power (Equation 3.13), the heating power is independent of energy, yielding a heating rate of

$$\frac{1}{\tau_{\text{heat}}} = \frac{(dE/dt)_{\text{heat}}}{E_R} = \frac{\chi D_p}{\hbar^2 k^2} = 2\chi\Gamma_{\text{sc}}. \tag{3.17}$$

The kinetic energy evolution of the system converted to temperature is given by the sum of heating and cooling rates:

$$\frac{dT}{dt} = \frac{E_R}{k_{\text{B}}\tau_{\text{heat}}} - \frac{T}{\tau_{\text{cool}}} \tag{3.18}$$

where $E_R = \frac{\hbar^2 k^2}{2m}$ is the recoil energy of the cooling transition and k_{B} Boltzman's constant. The steady state temperature is easily found by setting the left hand side of Equation 3.18 to zero. The minimal temperature is achieved for a detuning of $\delta = -\frac{\Gamma}{2}$ and is called the Doppler temperature T_{D}, which is usually evaluated for a one-dimensional system ($\chi = 2$):

$$k_{\text{B}} T_{\text{D}} = \hbar \frac{\Gamma}{2}. \tag{3.19}$$

[1]The term $\cos^2(\vartheta)$ arises from the projection of p^2 onto the z-direction with $p_z = p\cos(\vartheta)$.

It is worthwhile to note that the Doppler temperature is independent of the cooling light intensity and the mass of the atomic species. For strong cooling transitions, T_{D} is usually around $120\,\mu$K. The fact that it only depends on the linewidth of the cooling transition can be exploited to achieve extremely low temperatures on transitions with a small linewidth [91]. We will extend the standard treatment of Doppler cooling as it has been presented here in Section 7.2 to include reabsorption processes and their contribution to cooling.

3.3 Multi-level atoms

In the context of laser cooling, the term "multi-level atoms" is used for atoms with a Zeeman substructure in the ground and/or excited state which arises from the coupling of the atomic magnetic moment $\vec{\mu}$ to magnetic fields. The levels are characterized by the projection of $\vec{\mu}$ onto the quantization axis (usually given by the direction of an external magnetic field). The z component of this projection is proportional to the magnetic quantum number $m_{_J}$ (or m_F if the atom has hyperfine structure):

$$\mu_z = -m_{_J} g_{_J} \mu_B, \tag{3.20}$$

where μ_B is Bohr's magneton. For simplicity, we will write $\mu = \mu_z$ for the z component of the magnetic moment from now on and use the term "magnetic moment" but mean "projection of the magnetic moment onto the quantization axis" instead. The Landé-factor $g_{_J}$ of an atomic state with quantum numbers L (orbital angular momentum), S (spin) and J (total angular momentum of the atom) is given by

$$g_{_J} = 1 + \frac{J(J+1) + S(S+1) - L(L+1)}{2J(J+1)}. \tag{3.21}$$

For atoms with hyperfine structure, the Landé-factor reads

$$g_F = g_{_J} \frac{F(F+1) + J(J+1) - I(I+1)}{2F(F+1)}, \tag{3.22}$$

where I is the quantum number for the nuclear spin and F for the total angular momentom of the atom.

The magnetic moment of the atom interacts with magnetic fields, resulting in an energy shift

$$\Delta E_{\mathrm{ZS}} = -\vec{\mu} \cdot \vec{B} = g_{_J} m_{_J} \mu_B B. \tag{3.23}$$

This energy shift is frequently expressed in terms of the Larmor precession frequency, which is given by

$$\omega_{\mathrm{L}} = \left| g_{_J} m_{_J} \frac{\mu_B B}{\hbar} \right| \tag{3.24}$$

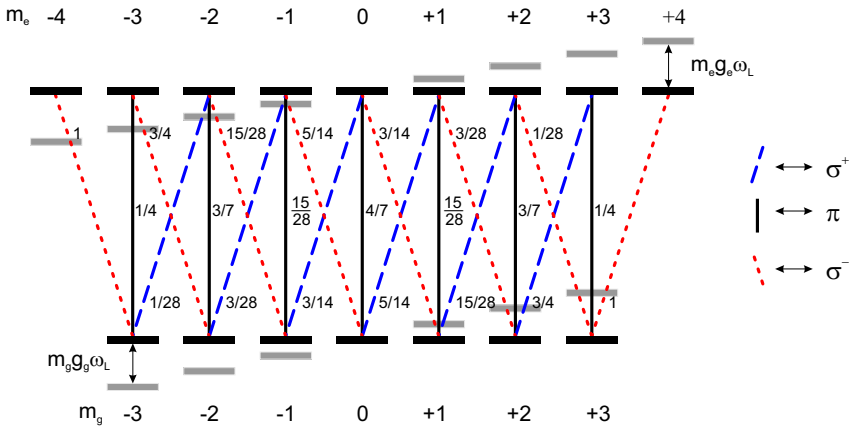

Figure 3.2: Zeeman structure for the $^7S_3 \longleftrightarrow {}^7P_4$ transition in ^{52}Cr. The numbers close to the transition lines are the squares of the Clebsh-Gordan coefficients denoting the coupling strength to σ^+, σ^- and π light.

External magnetic fields can be used to tune the atomic transition frequency (see Equation 3.8) or, in inhomogeneous magnetic fields, to trap the atoms in a magnetostatic trap (see Chapter 4).

Optical dipole transitions between electronic states of an atom have to satisfy the selection rules $\Delta m_J = 0, \pm 1$ arising from angular momentum conservation for a photon having spin 1. In a two-level atom, the coupling constant between ground and excited state is given by the Rabi-frequency Ω_R (Equation 3.3). For multi-level atoms, the addition rule for angular momenta have to be taken into account. This results in additional coupling constants, the squares of the so-called Clebsh-Gordan coefficients [92]. As an example for a multi-level atom, we show in Figure 3.2 the $^7S_3 \longleftrightarrow {}^7P_4$ transition in ^{52}Cr.

3.4 Polarization gradient cooling

First optical cooling experiments of multi-level atoms achieved much lower temperatures than predicted by the Doppler cooling theory [93]. Soon thereafter, a theoretical explanation was found independently by two groups [86, 94]: polarization gradient cooling. We will briefly discuss the basic concepts in the following.

Sub-Doppler cooling mechanisms such as polarization gradient cooling are multi-photon cooling processes of multi-level atoms in a light field with a spatially varying polarization. In contrast to Doppler cooling, the cooling mechanisms do not rely on the Doppler shift, but rather on a motional coupling of the internal state population to the light field. The most commonly used 1D light field configurations consisting of two counterpropagating laser beams are called lin $\perp$ lin and σ^+/σ^-.

In the lin $\perp$ lin configuration, the two laser beams have orthogonal linear polarizations. Along the direction of the laser beams, the polarization of the light field changes from linear–σ^+–linear–σ^- over half an optical wavelength. At this point the Clebsh-Gordan coefficients become important. They determine how strongly the allowed transitions couple to the local light field polarization. Different Clebsh-Gordan coefficients result in different optical potential depths (see Equation 3.4). Optical pumping an atom at rest achieves a steady state population in which the state with the lowest energy (with the strongest coupling to the light field) is populated most. An atom moving in a polarization gradient light field has to climb a potential hill at the cost of kinetic energy, since its atomic substate population does not correspond anymore to the lowest energy configuration of the new polarization. A finite optical pumping time constant allows to maintain this population imbalance resulting in a strong damping force. Since the atom always climbs a potential hill, this cooling mechanism is also called "Sisyphus cooling" in analogy to the Greek mythology. The cooling process is based on the interplay of two time scales: the optical pumping time and the time it takes an atom to move by half an optical wavelength. If the atom is too slow, optical pumping can maintain the steady state population and no damping occurs. If the atom is too fast, the optical potentials average to zero. From these considerations, it is obvious that lin $\perp$ lin cooling is only effective over a small range of velocities corresponding to a Doppler shift of typically one fourth of the linewidth centered around zero velocity. Just as is the case for Doppler cooling, kinetic energy is converted to photon energy by spontaneous emission during the optical pumping process.

The cooling principle is slightly different for the σ^+/σ^- configuration in which the two laser beams are σ^+ and σ^- polarized. This results in a linear polarization everywhere, rotating by 2π over an optical wavelength. If we define our quantization axis always by the direction of the local electric field polarization, only π transitions can be excited and no optical potential gradient exists. Consider an atom with a transition $J = 0 \rightarrow J = 1$ at rest in such a light field configuration. The difference in Clebsh-Gordan coefficients leads to a large population of the $m_J = 0$ state at the expense of the $m_J = \pm 1$ states during optical pumping. For a moving atom, the rotation of the quantization axis given by the local electric field mixes the Zeeman substates. If the atom is moving faster than a typical optical pumping time required to reach steady state, the atomic substate populations for a moving atom lag behind the steady state. The population difference is such, that the atom preferentially absorbs photons from the counterpropagating laser beam. This leads to strong damping forces comparable to the lin $\perp$ lin configuration. For both configurations, the damping coefficient scales linearly with the detuning of the laser beam, whereas the capture velocity is inversely proportional to the detuning. This is in contrast to Doppler cooling which achieves a minimum temperature at a detuning of $-\frac{\Gamma}{2}$. Therefore, the damping forces for sub-Doppler cooling are larger by a factor of $2\frac{|\delta|}{\Gamma}$.

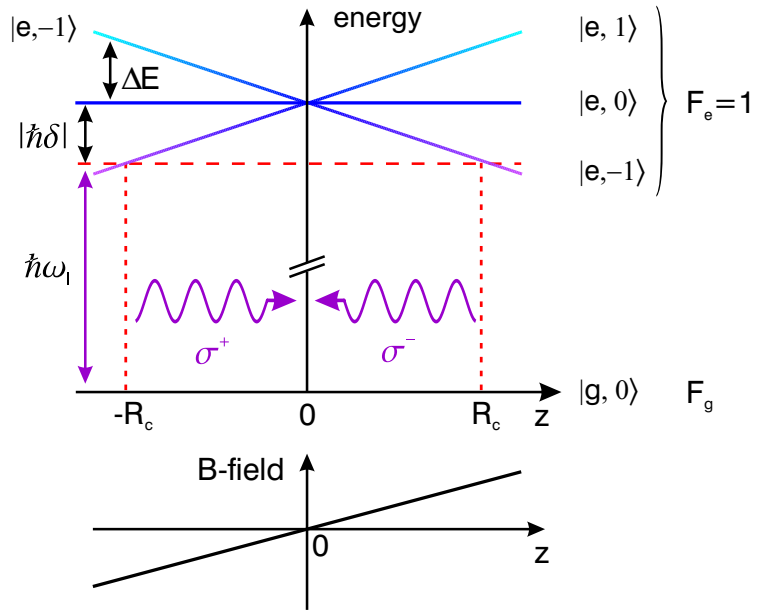

Figure 3.3: One-dimensional principle of operation of a magneto-optical trap. In addition to laser cooling, an atom experiences a restoring force which is directed to the trap center. The energy of the Zeeman substates in the excited state is shifted by the magnetic field gradient in such a way, that the atom comes more into resonance with the beam opposing the displacement from the center of the trap.

Since the photon diffusion constants are comparable, much lower temperatures can be achieved with the polarization gradient cooling mechanisms. The theoretical limit is given by the photon recoil temperature $T_{\mathrm{rec}} = \frac{\hbar^2 k^2}{2mk_{\mathrm{B}}}$. More sophisticated cooling mechanisms can reach even lower temperatures by exploiting internal state coherences to decouple atoms from the light field that are moving at velocities below the recoil velocity or use Raman transitions between spectrally resolved vibrational levels in a trap (see review article by Balykin *et. al.* [95] and references therein).

σ^+/σ^- cooling is most commonly used in magneto-optical trapping schemes, which will be described in the next Section.

3.5 Magneto-optical trap

The cooling mechanisms and light field configurations discussed so far can only slow the atoms down, but are unable to trap them. In general, a trap is characterized by a restoring force which is directed towards the trap center. This can be achieved by breaking the symmetry along the cooling laser beams and thus enabling the atoms to distinguish between the laser beam directions. In a magneto-optical trap (MOT)

the symmetry is broken by a magnetic field gradient with a zero crossing at the center of the trap. The atom can distinguish between the counterpropagating laser beams if they couple to different atomic (Zeeman) levels. Therefore, in general only multi-level atoms, where the cooling laser drives a $F \rightarrow F+1$ transition are suitable for magneto-optical traps. The simplest MOT configuration is shown in Figure 3.3. An atom with a single ground state $|\, g, 0 \,\rangle$ and three excited states $|\, e, 0 \,\rangle$, $|\, e, \pm 1 \,\rangle$ moves in the light field of two counterpropagating σ^+/σ^- polarized laser beams. The magnetic field gradient shifts the energy of the Zeemann substates in the excited state. As a result, an atom moving at small velocity comes more into resonance with the laser beam opposing the displacement from the trap center. This increases the force from that beam acting on the atom. The net force from both laser beams is therefore directed towards the trapping center. In the low intensity ($\frac{I}{I_s} \ll 1$) and low velocity ($|kv| \ll \Gamma$ and $|kv| \ll |\delta|$) limit, the total force acting on an atom is given by

$$F = -\alpha\, v - \kappa_{\mathrm{MOT}} z \qquad \text{with} \tag{3.25}$$

$$\kappa_{\mathrm{MOT}} = -8\Delta\mu B' k \, \frac{\delta/\Gamma}{(1 + 4\delta^2/\Gamma^2)} \, \frac{I}{I_s}, \tag{3.26}$$

where α is the damping constant given by Equation 3.12, κ_{MOT} the spring constant and B' the magnetic field gradient. The volume of the trap is determined by the capture radius R_c, at which the beams become resonant with the atomic transition. Atoms far beyond R_c are heated and expelled from the trap. Magneto-optical traps can capture atoms having a velocity below the capture velocity v_c, which can be approximated by the maximum radiation force and the diameter of the trapping region, $2R_c$:

$$\frac{1}{2}\, m v_c^2 = 2 R_c F_{\mathrm{sc}}. \tag{3.27}$$

Typical values for the capture velocity are between $10\,\mathrm{m/s}$ and $30\,\mathrm{m/s}$.

Extension of this one dimensional magneto-optical trapping scheme in two and three dimensions is easily accomplished. In the standard 3D configuration, a magnetic quadrupole field provides a linear magnetic field gradient along all three axes. Three pairs of σ^+/σ^- polarized laser beams along the same axes cool and trap the atoms. Figure 3.4 shows the two dimensional configuration used in our experiments. A two-dimensional magnetic quadrupole field together with two pairs of σ^+/σ^- polarized laser beams provide cooling and trapping in radial (x, y) direction. Cooling along the axial degree of freedom (z) is accomplished by an additional pair of σ^+ polarized laser beams. In this direction the atoms are only Doppler cooled, since polarization gradient cooling would require a σ^+/σ^- light field configuration, which is not desired in our setup (see Chapter 6).

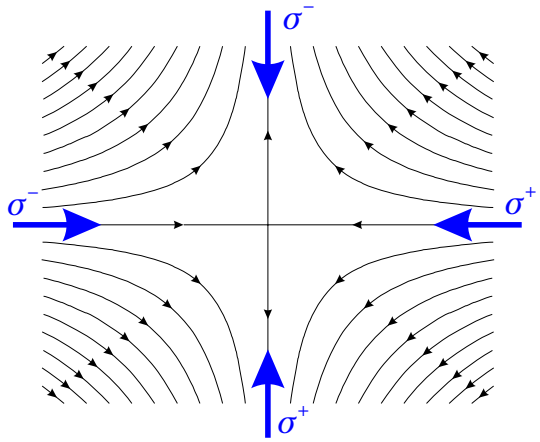

Figure 3.4: Light and magnetic field configuration for a 2D-MOT. Black lines are magnetic field lines, solid arrows denote the direction and polarization of the cooling light.

For an extensive review of the properties of magneto-optical traps, refer to [89] and references therein.

In 3D magneto-optical traps, typically atomic densities on the order of 10^{11} cm^{-3} and atom numbers exceeding 10^10 at temperatures of around 100 μK have been achieved. The ultimate limit in this type of trap are inelastic excited state collisions between atoms in the ground state and atoms excited by the MOT laser. Although many groups have investigated the possibility of the so-called "all-optical Bose-Einstein condensation", in the sense that all cooling steps are performed by optical means, this goal has not been achieved so far. Instead, purely magnetic and lately also far-off resonant optical dipole traps [25, 42, 96, 97] have opened the way to higher densities and colder temperatures by eliminating the near-resonant cooling laser. We will discuss magnetic trapping of neutral atoms in the following Chapter.

Chapter 4

Magnetic trapping

In this Chapter the basic principles of magnetic trapping of neutral atoms are outlined. I will concentrate on the magnetic field configuration of a Ioffe-Pritchard trap, since this trap type is used in the experiments presented in this thesis. Different trapping regimes are discussed and an estimate of Majorana spin-flip losses for very low magnetic offset fields will be given.

4.1 Introduction

Magneto-optical trapping of atoms, as described in the previous Chapter, is a powerful tool for a large variety of atomic physics experiments. Nevertheless, the quest for even colder and denser atomic gases continued. Inelastic loss processes in the presence of near-resonant cooling light limit the density and the achievable temperature in a MOT. Purely magnetic traps together with evaporative cooling (see Section 9.4.4) have led to the realization of Bose-Einstein condensates in dilute atomic gases [1, 2, 3, 98].

We have already seen in Section 3.3, that the Zeeman sublevels experience an energy shift in a magnetic field $\vec{B}$ according to $\Delta E_{\mathrm{ZS}} = -\vec{\mu} \cdot \vec{B} = \mu_z B$, with the projection $\mu_z = \mu = -g_{_J} m_{_J} \mu_B$ of the magnetic moment $\vec{\mu}$ onto the quantization axis along $\vec{B}$. This effect can be used to magneto-statically trap the atoms in an inhomogeneous three-dimensional magnetic field configuration $\vec{B}(\vec{r})$. An atom in such a field configuration is subject to a conservative force $\vec{F}_B(\vec{r}) = \vec{\nabla}(\vec{\mu} \cdot \vec{B}(\vec{r}))$. Depending on the orientation of the projection of the magnetic moment onto the external field, the atoms are either called "high-field seekers"($\vec{\mu}$ parallel to $\vec{B}(\vec{r})$, $g_{_J} m_{_J} < 0$) or "low-field seekers"($\vec{\mu}$ anti-parallel to $\vec{B}(\vec{r})$, $g_{_J} m_{_J} > 0$). Since Maxwell's equations forbid a static magnetic field maximum in free space [99], only low-field seekers can be trapped in a magneto-static trap.

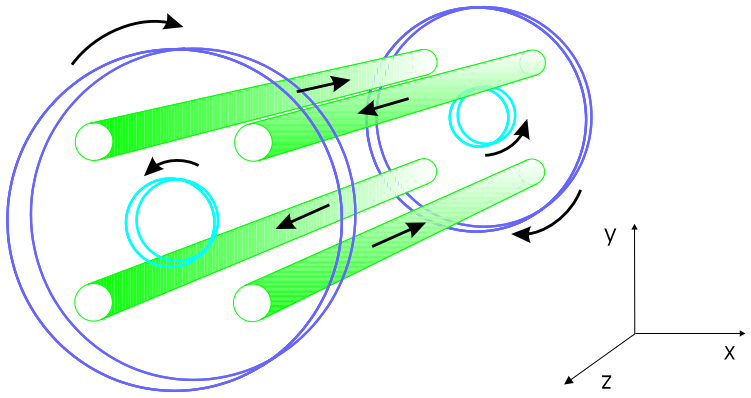

Figure 4.1: The standard Ioffe-Pritchard configuration. Four parallel wires (Ioffe-bars, green) carrying the same current in alternating directions produce a radial 2D quadrupole field. A pair of dipole coils (red) generate a curvature field in axial direction which is compensated at the center of the trap by the homogeneous field of a pair of offset compensation coils (blue).

Purely magnetic traps are usually rather shallow compared to the kinetic energy of thermal atoms, since the interaction between the magnetic moment of an atom and reasonably large magnetic fields is weak. Typically, the atoms need to be precooled to temperatures below 1 mK, which is most commonly achieved with optical cooling techniques (see Chapter 3). So it was not before 1984, when optical cooling techniques had been sufficiently evolved, that neutral atoms could be trapped magnetically [100]. Several magnetic trap configurations have been proposed and implemented [95, 101, 102]. The most widely-used trapping field configuration for storing ultra-cold atoms is of the Ioffe-Pritchard type, which will be discussed in detail in the next Section.

4.2 The Ioffe-Pritchard trap

The Ioffe-Pritchard trap (IP trap) has originally been invented by Ioffe for plasma confinement [103]. Pritchard has adopted the magnetic field configuration to neutral atom trapping [104]. It can be implemented with a wide variety of current carrying wire configurations, including the baseball trap [8], 4-Dee trap [105], QUICK trap [106] and the cloverleaf trap [107]. All these different coil configurations produce to lowest order the same magnetic trapping field. We have implemented our IP trap in the cloverleaf configuration (see Section 5.1). Its trapping potential is easiest derived from the simple setup shown in Figure 4.1. The four Ioffe-bars produce a translationally invariant 2D quadrupole field in the xy-plane (see magnetic field lines in Figure 3.4) which provides radial confinement. Axial confinement is achieved with a

pair of dipole coils (sometimes also called "pinch" coils) which generate a quadratically increasing magnetic "curvature" field along the z direction. The magnetic offset field of the dipole coils at the center of the trap is partially compensated by the homogeneous field of a pair of offset compensation coils. A full evaluation of the Biot-Savart integral for this current configuration to second order in the coordinates yields the magnetic field of the Ioffe-Pritchard trap:

$$\vec{B}(\vec{r}) = \begin{pmatrix} 0 \\ 0 \\ 1 \end{pmatrix} B_0 + \begin{pmatrix} x \\ -y \\ 0 \end{pmatrix} B' + \begin{pmatrix} -xz \\ -yz \\ z^2 - \frac{1}{2}(x^2+y^2) \end{pmatrix} \frac{B''}{2}. \tag{4.1}$$

The field is characterized by the magnetic offset field B_0, the radial gradient B' and the axial curvature B''. In the adiabatic limit (see Section 4.2.4), the magnetic moment of the atom follows the direction of the magnetic trapping field. The trapping potential can then be simplified to $U(\vec{r}) = \mu|\vec{B}(\vec{r})|$, where the magnitude of the magnetic field is given by

$$|\vec{B}(\vec{r})| = B(\vec{r}) = \sqrt{\left[B_0 + \frac{B''}{4}(2z^2 - x^2 - y^2)\right]^2 + \left[B'y + \frac{B''}{2}yz\right]^2 + \left[B'x - \frac{B''}{2}xz\right]^2} \tag{4.2}$$

We have plotted the $B(\vec{r})$ and its gradient for typical trap parameters of $B_0 = 1\,\mathrm{G}$, $B' = 150\,{}^{G}/_{\mathrm{cm}}$ and $B'' = 150\,{}^{G}/_{\mathrm{cm}^2}$ in Figure 4.2. The shape of the trapping potential seen by the atoms depends on the specific trap parameters and the size (i.e. the temperature) of the atomic cloud. We will discuss the stability and different regimes of the trap in the following subsections.

4.2.1 Instability points

One can see from Equation 4.1 that the radial and axial magnetic field components are coupled via the last term. Therefore, the radial field parameters are dependent on the position in z direction. In a pathological situation, the trap can even lose its radial confinement. This occurs in the xy-plane for

$$\begin{aligned} 0 &= \frac{dB(x,0,z)}{dx} \\ &= B''(B''x^2 - 4B_0) + 8B'(B' - B''z). \end{aligned}$$

Keeping only the terms linear in the coordinates (small displacement from the trap center), we obtain the instability points for the radial confinement along the z direction:

$$z_d = \pm\left(\frac{B'}{B''} - \frac{B_0}{2B'}\right). \tag{4.3}$$

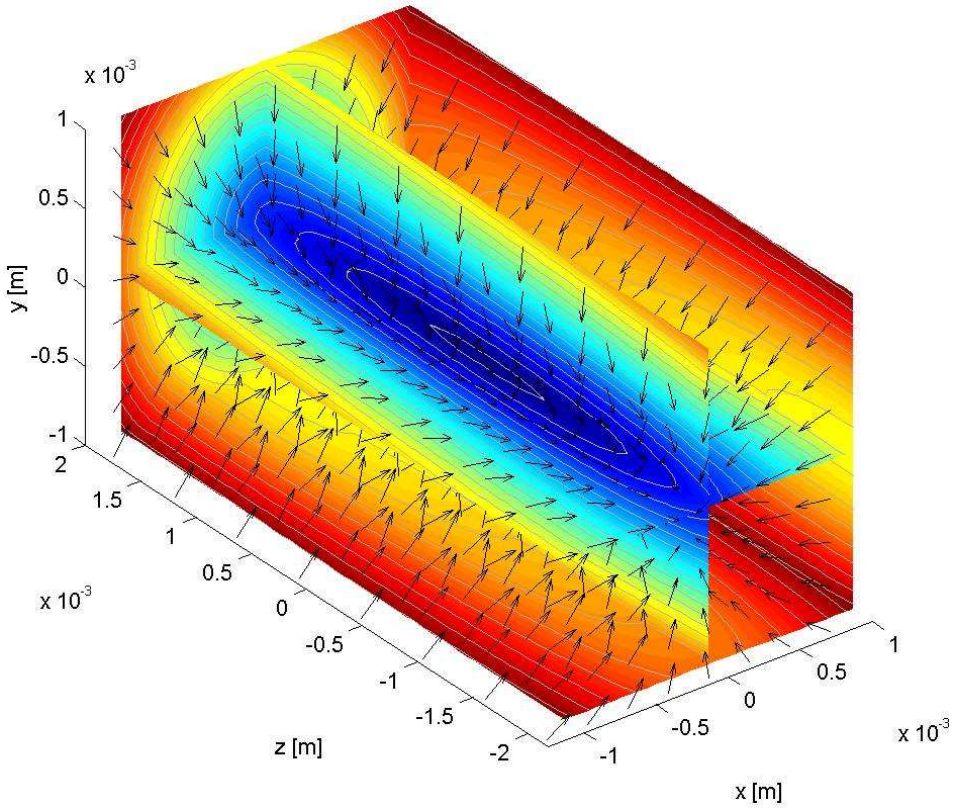

Figure 4.2: Magnetic field of a Ioffe-Pritchard trap. The magnitude of the magnetic field $B(\vec{r})$ is color coded (blue: low magnetic field to red: high magnetic field). The contour lines have a spacing of 1 G. Black arrows show the direction and magnitude (arrow length) of the magnetic field gradient. The magnetic field was calculated according to Equation 4.1 using the following trap parameters: $B_0 = 1\,\mathrm{G}$, $B' = 150\,\mathrm{G/cm}$ and $B'' = 150\,\mathrm{G/cm^2}$.

The trap develops additional minima at four points off center from the trap. These additional minima strongly deform the trap and allow the atoms to occupy a much larger volume, although they are not expelled from the trap. Such a configuration is shown in Figure 4.3. In this regime, images of the atomic cloud exhibit a characteristic x-pattern which we have observed in our experiments.

4.2.2 Harmonic regime

For cold (small) clouds compared to the potential energy at the center of the trap ($\mu B_0 \gg k_\mathrm{B}T$) we can neglect all higher order terms in the coordinates in a series

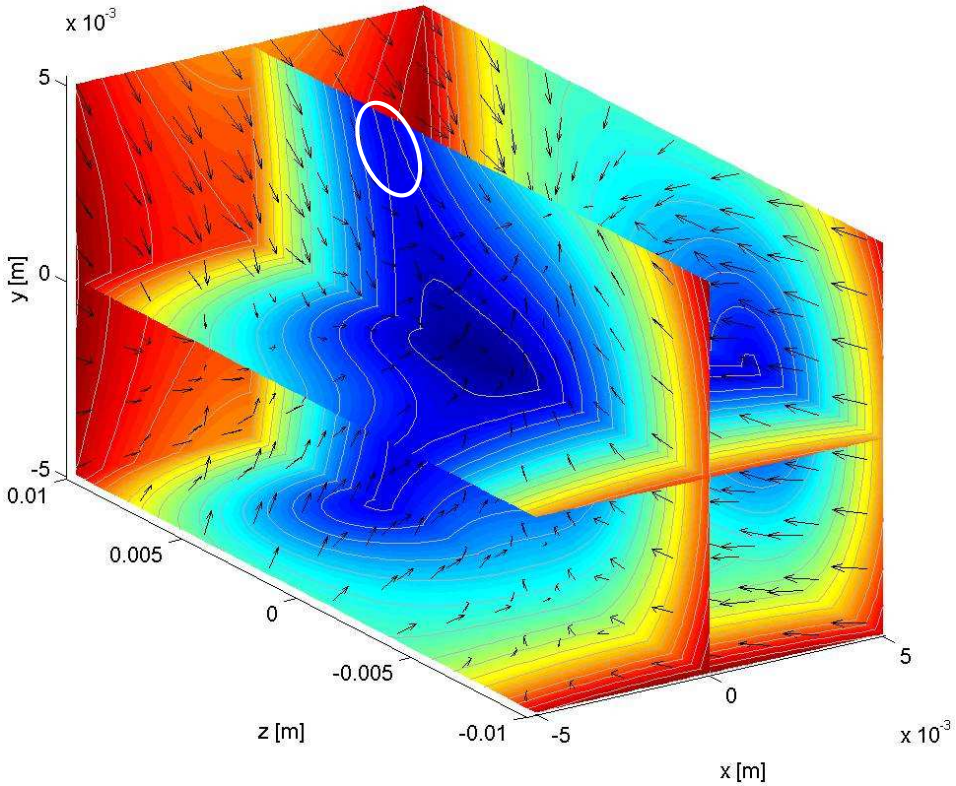

Figure 4.3: Magnetic field of a shallow Ioffe-Pritchard trap. Same trap as in Figure 4.2, except for a radial gradient of $B' = 50\,{}^{G}/_{\mathrm{cm}}$ and a different axis scaling. Note the radial deformation of the trapping field towards the instability points. One of them is marked by a white circle.

expansion of the square root in Equation 4.2. The potential is then given by

$$U_{\mathrm{ht}}(\vec{r}) = \mu \left(B_0 + \frac{1}{2} B_r''(x^2 + y^2) + \frac{1}{2} B'' z^2 \right) \tag{4.4}$$

with

$$B_r'' = \frac{B'^2}{B_0} - \frac{B''}{2}. \tag{4.5}$$

The resulting trapping potential (neglecting gravity) is harmonic in all three dimensions with trap frequencies

$$\omega_x = \omega_y = \sqrt{\frac{B_r'' \mu}{m}} \tag{4.6}$$

$$\omega_z = \sqrt{\frac{B'' \mu}{m}}. \tag{4.7}$$

It is important to note, that the radial trap frequency is sensitive to the magnetic offset field via Equation 4.5. Thus radial compression of the trap can be accomplished by lowering B_0. The atomic motion in a harmonic trap is separable along the principal axes of the trap. Therefore, energy conservation holds in each direction separately.

The density distribution of a thermal cloud of atoms subject to this trapping potential is given by a Gaussian distribution

$$n_{\mathrm{ht}}(\vec{r}) = n_0 \exp\left(-\frac{U_{\mathrm{ht}}(\vec{r})}{k_{\mathrm{B}}T}\right) = n_0 \exp\left(-\frac{x^2}{2\sigma_x^2} - \frac{y^2}{2\sigma_y^2} - \frac{z^2}{2\sigma_z^2}\right), \tag{4.8}$$

where

$$\sigma_x = \sigma_y = \sqrt{\frac{k_{\mathrm{B}}T}{\mu B_r''}} = \frac{1}{\omega_z}\sqrt{\frac{k_{\mathrm{B}}T}{m}} \qquad \text{and} \tag{4.9}$$

$$\sigma_z = \sqrt{\frac{k_{\mathrm{B}}T}{\mu B''}} = \frac{1}{\omega_r}\sqrt{\frac{k_{\mathrm{B}}T}{m}} \tag{4.10}$$

are the $1/\sqrt{e}$ sizes of the distribution. The peak density n_0 of the trap is the ratio between the number of trapped atoms, N, and the occupied volume $V_{\mathrm{ht}} = (2\pi)^{3/2}\sigma_x\sigma_y\sigma_z$. In our experiments, the atoms are usually imaged with a charge-coupled device (CCD) camera along a specific direction. The density distribution (Equation 4.8) has to be integrated along the imaging axis (e.g. the x direction) to obtain the distribution recorded by the camera:

$$\tilde{n}_{\mathrm{ht}}(y,z) = n_0\sqrt{2\pi}\sigma_x \exp\left(-\frac{y^2}{2\sigma_y^2} - \frac{z^2}{2\sigma_z^2}\right). \tag{4.11}$$

Taking the linear potential produced by gravity into account, the position of the density maximum is shifted and the density distribution becomes asymmetric. For the harmonic trap parameters used in our experiments, gravity can safely be neglected.

4.2.3 Linear regime

We can gain further insight into the trapping potential by assuming a low offset field B_0 compared to all other magnetic field components seen by the atoms ($\mu B_0 \ll k_{\mathrm{B}}T$). Neglecting the offset field and keeping only the terms to lowest order in the coordinates, the trap can be approximated by a linear potential in the radial and a harmonic potential in the axial direction. The trapping potential in the linear regime is then given by

$$U_{\mathrm{lt}}(\vec{r}) = \mu\left(B'\sqrt{x^2+y^2} + \frac{1}{2}B''z^2\right). \tag{4.12}$$

It is worthwhile to note, that, in contrast to the harmonic trap, this potential is not separable in the coordinates. As a consequence, the atomic motion in such a trap is not separable and so-called anharmonic mixing between different degrees of freedom occurs. The density distribution in the linear regime is characterized by the $1/e$ length

$$\xi = \frac{k_\mathrm{B}T}{\mu B'} \tag{4.13}$$

in the radial direction and reads

$$n_\mathrm{lt}(\vec{r}) = n_0 \exp\left(-\frac{U_\mathrm{lt}(\vec{r})}{k_\mathrm{B}T}\right) = n_0 \exp\left(-\frac{\sqrt{x^2+y^2}}{\xi} - \frac{z^2}{2\sigma_z^2}\right). \tag{4.14}$$

Integration along the imaging axis yields the density distribution as seen by the camera:

$$\tilde{n}_\mathrm{lt}(y,z) = 2|y|n_0 \exp\left(-\frac{z^2}{2\sigma_z^2}\right) \mathrm{K}_1\left(\frac{|y|}{\xi}\right), \tag{4.15}$$

where $\mathrm{K}_1(x)$ is the modified Bessel function of the second kind of first order.

For very weak radial confinement as used in our CLIP trap (see Chapter 6), gravity has to be taken into account. The radial symmetry is broken by the linear gravitational potential along the y direction. This results in an asymmetric cloud characterized by an additional $1/e$ length

$$\xi_g = \frac{k_\mathrm{B}T}{mg}, \tag{4.16}$$

where $g = 9.81\,\mathrm{m/s^2}$ is earth's acceleration. Gravity does not change the position of the maximum. The full density distribution and the integrated distribution then read

$$n_\mathrm{lt,g}(x,y,z) = n_0 \exp\left(-\frac{\sqrt{x^2+y^2}}{\xi} - \frac{y}{\xi_g} - \frac{z^2}{2\sigma_z^2}\right) \tag{4.17}$$

$$\tilde{n}_\mathrm{lt,g}(y,z) = 2|y|n_0 \left[\exp\left(-\frac{z^2}{2\sigma_z} - \frac{y}{\xi_g}\right) \mathrm{K}_1\left(\frac{|y|}{\xi}\right)\right], \tag{4.18}$$

respectively. In the linear regime, the trap volume has to be determined from a numerical integration of Equation 4.15 or 4.18.

4.2.4 Majorana spin-flip losses

One of the major advantages of a Ioffe-Pritchard trap over the much simpler quadrupole magnetic trap [78, 101] is its finite offset field at the center of the trap.

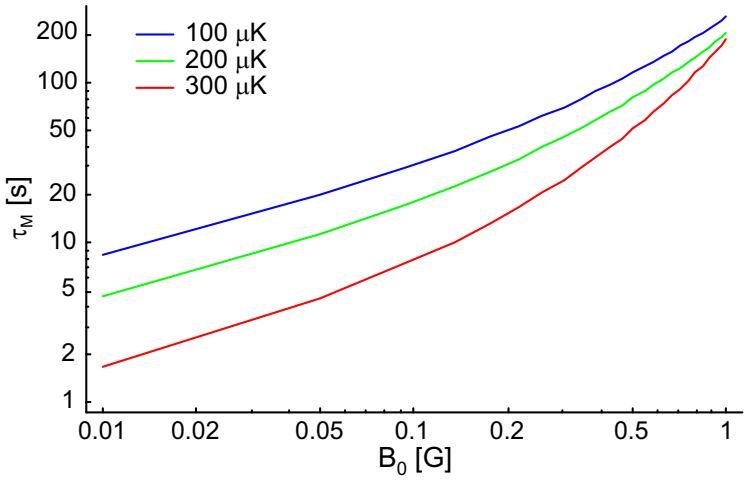

Figure 4.4: Lifetime of an atomic ensemble subject to Majorana spin-flip losses in the CLIP trap for different temperatures.

For vanishing offset field, the Larmor precession frequency $\omega_{\mathrm{L}} = {}^{\mu B_0}/_{\hbar}$ (see Equation 3.24) can become smaller than the oscillation frequency ω_t of the atom in the trap. The spin can no longer adiabatically follow the local magnetic field direction. Motional coupling between different magnetic substates can lead to a spin flip to a high-field seeking state and the atom is ejected from the trap [108]. These so-called Majorana spin-flip losses can be suppressed by providing a magnetic offset field high enough to maintain $\omega_L \gg \omega_t$. Sukumar *et. al.* [109] have derived an expression for the high temperature limit ($k_{\mathrm{B}}T > 2\hbar\omega_t$) of the spin-flip transition rate w for the radial oscillation of an atom in the center of a Ioffe-Pritchard trap:

$$w = \frac{\pi\hbar\omega_t^2}{k_{\mathrm{B}}T} \exp\left(-\frac{\Delta E_{\mathrm{ZS}} + \hbar\omega_t}{k_{\mathrm{B}}T}\right), \tag{4.19}$$

where ΔE_{ZS} is the Zeeman energy released during the spin-flip. For chromium in the $m_{_J} = +3$ state, a transition to the $m_{_J} = +2$ state corresponds to $\Delta E_{\mathrm{ZS}} = 2\mu_B B_0$. Note, that the trap frequency also depends on the offset field via Equation 4.6. Averaging the position dependent spin-flip rate over the density distribution along the z direction yields the inverse lifetime $\tau_M = {}^1/_{<w>}$ of the atomic ensemble in the trap. In Figure 4.4 we have plotted this lifetime vs. the magnetic offset field in the CLIP trap configuration (see Chapter 6: B' =12 ${}^{\mathrm{G}}/_{\mathrm{cm}}$, B'' =11 ${}^{G}/_{\mathrm{cm}^2}$) for different temperatures of the cloud. The rather small radial magnetic field gradients already allow a small offset field of $B_0 = 40\,\mathrm{mG}$ to achieve a lifetime of more than 10 s. It is important to note though, that after compression of the trap to its maximum trapping fields, the Majorana loss rate can be significant. In Figure 4.5 we have plotted the Majorana loss rate for typical trapping parameters of the fully

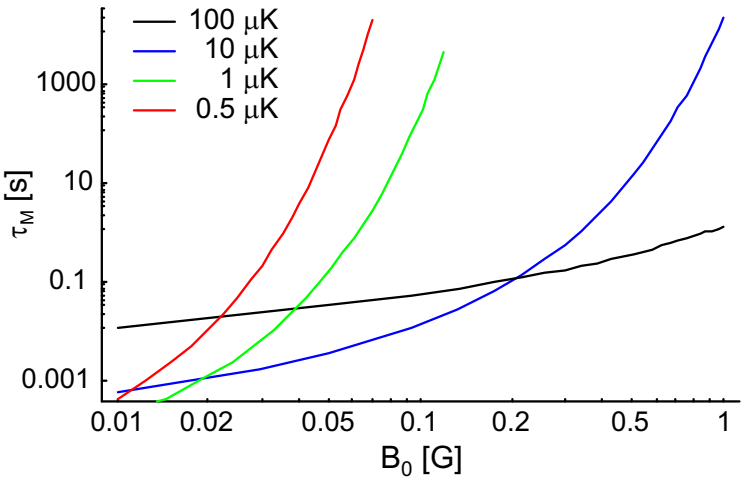

Figure 4.5: Lifetime of an atomic ensemble subject to Majorana spin-flip losses in the fully compressed Ioffe-Pritchard trap for different temperatures.

compressed magnetic trap ($B' = 150\,{}^{G}/_{\mathrm{cm}}$, $B'' = 100\,{}^{G}/_{\mathrm{cm}^2}$). It is obvious from the Figure, that lowering the offset field to values below 1 G is only advisable for rather could clouds. The atoms can be quite hot ($\approx 1\,\mathrm{mK}$) in the compressed trap, therefore the offset field should be lowered only after precooling the atoms. A multi-step sequence, alternating between cooling steps and lowering the offset field, might give the best results. Most experiments in this thesis have been performed at magnetic offset fields on the order of 4 G, for which the Majorana-limited lifetime is on the order of minutes for temperatures around $100\,\mu\mathrm{K}$.

Chapter 5

Experimental setup and methods

In this Chapter I describe the technical details of the experimental setup including magnetic trap, vacuum and laser system as well as the data evaluation procedure. For the experiments presented in this thesis, we have used two separate vacuum systems and magnetic traps, which differ only in minor technical details. I will concentrate here on the description of the first ("old") system, which has been used to perform the measurements for the CLIP trap (Chapter 6), the Doppler cooling (Chapter 7) and the inelastic ground state scattering properties (Appendix E). Where necessary, we will mention variations in the second ("new") system, which has been used to measure the elastic ground state scattering properties of chromium (Chapter 9).

5.1 The cloverleaf magnetic trap

We have implemented a Ioffe-Pritchard trap in the cloverleaf configuration [107]. Our selection was motivationed by the compatibility of the cloverleaf trap with the existing vacuum chamber and the flexible control of the trap parameters, including the possibility to operate the trap at arbitrarily low magnetic offset fields. Another advantage is the excellent mechanical and optical access to the trapped atoms. As a general rule for magnetic traps, all coils need to be as close as possible to the trapping center to provide strong confinement. In a standard IP trap as shown in Figure 4.1, the Ioffe bars need special vacuum chamber designs, e.g. employing glass cells [110] or sophisticated vacuum feed-throughs [111]. In the cloverleaf configuration, the Ioffe bars are replaced by eight so-called "cloverleaf" coils creating a radial 2D quadrupole field. This setup provides a 2π optical and mechanical access in radial direction as shown in Figure 5.2.

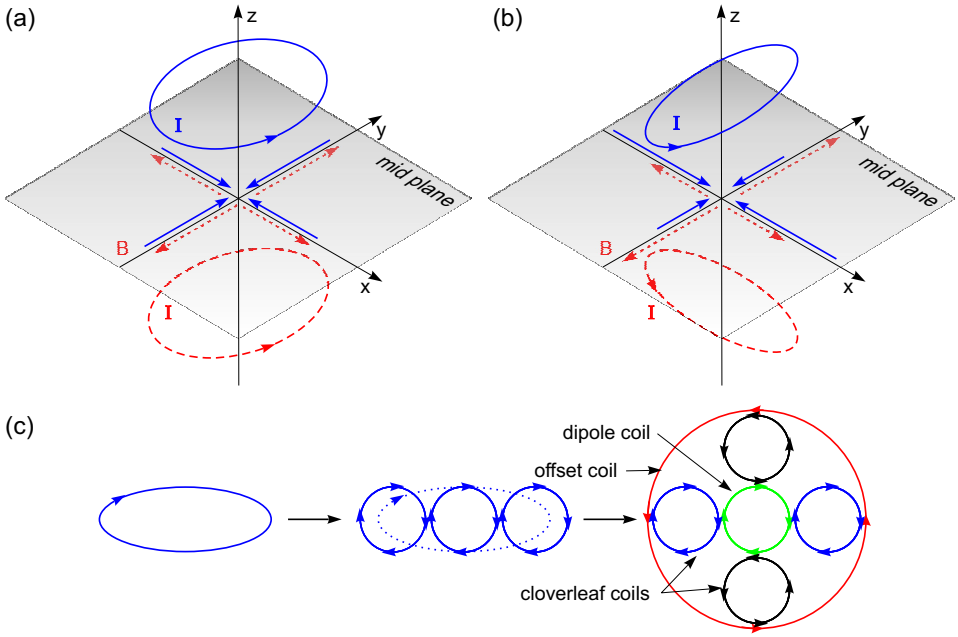

Figure 5.1: Qualitative derivation of the cloverleaf field. The length of the arrows in the mid-plane indicate the magnitde of the magnetic field produced by the corresponding coil having the same color. (a) Two circular coils produce an axial curvature field, but no radial gradient at the center between the coils. (b) Coils that are pinched along two orthogonal directions produce an axial curvature and a radial gradient. (c) Each pinched coil (left) can be substituted by three smaller coils (center): a dipole coil between two gradient coils. Two additional gradient coils (drawn in black) double the radial gradient and form together with an offset coil (drawn in red) one coil package of the cloverleaf trap.

Figure 5.1 illustrates the main principle of the cloverleaf configuration. Consider two circular coils with radius R lying in the xy-plane, separated along the z-direction by a distance $d > R$ as shown in Figure 5.1(a). Both coils produce a magnetic field which is decreasing with increasing distance from the coils. At the center between the two coils the fields add up and yield a quadratically increasing magnetic field along the z axis. Due to symmetry, the radial magnetic field components cancel in the mid-plane between the coils, since they have the same magnitude but opposite sign. This situation changes for the configuration shown in Figure 5.1(b), where the two coils are pinched along orthogonal directions. The magnetic field produced by the long side of the elliptically shaped coils is stronger than that from the short side. Thus, the radial field components of the two coils do not cancel any more and we obtain in addition to the axial curvature a radial magnetic field gradient[1]. Figure 5.1(c)

[1]This is true only for the radial field *components*, not for the gradient of the absolute value of the magnetic field, $|\vec{B}(\vec{r})|$. The strong axial offset field in this configuration makes the trap harmonic

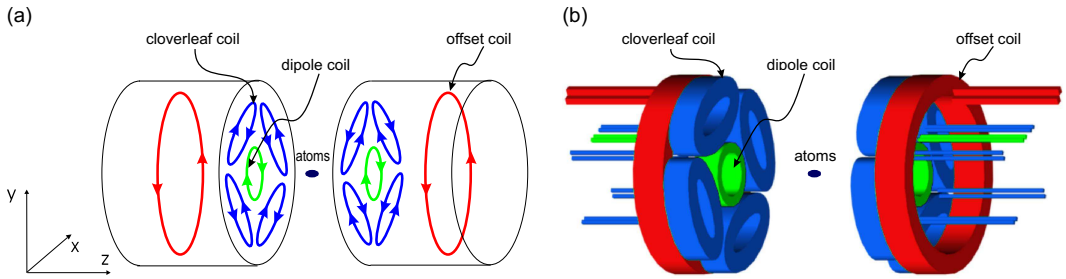

Figure 5.2: Coil setup for the cloverleaf magnetic trap. (a) Sketch of the coil configuration with arrows indicating the direction of the current. (b) Rendered image of the implementation for the new system (to scale). The four cloverleaves (blue) in each coil package surround the dipole coil (green). The offset coil (red) is placed behind the leaves.

shows the evolution of the cloverleaf configuration (right) from one of the pinched coils (left). An additional offset coil compensates the offset field of the dipole coil at the center of the trap. A very nice feature of the cloverleaf trap configuration is the ability to independently control the radial magnetic field gradient, axial curvature and offset field by adjusting the current through the cloverleaf, the dipole and the offset coils, respectively.

Our implementation of the cloverleaf trap is shown in Figure 5.2. Cloverleaf and dipole coils are located in the same plane to achieve maximum radial gradient without sacrifying axial curvature. The offset coils are placed behind the cloverleaves and produce an almost homogeneous field cancelling the field of the dipole coils at the center of the trap. The actual shape of the cloverleaf coils is not circular but rather elliptical to fill the available space most efficiently (see Figure 5.2). We have run a computer simulation of the magnetic fields produced by the coils. The coil shapes and winding patterns were optimized to achieve both, a high curvature *and* a high gradient field under a few technical constraints given by our vacuum system, power dissipation (thermal expansion) and the availability of commercial power supplies and copper tubing. The need for fast current switching times ($\ll 1$ ms) puts a limit on the inductivity and thererfore the number of loops for each coil[2]. Consequently, the coils are made out of a few loops of hollow copper tubing to allow for water cooling. For the cloverleaves (elliptical with half axes 12.5x25.6 mm, 10 layers high and 2 layers thick), we used round copper tubing with an outer diameter of 3 mm and an inner diameter of 1.5 mm. The same tubing was used for the dipole coil (circular with 12.6 mm inner diameter, 10 layers high). The offset coil (cicular with 68 mm

also in the radial direction. Only with an offset compensation field supplied by additional offset coils, a truly linear trap in radial direction can be achieved.

[2]In principle, the ratio of current density vs. power dissipation increases with decreasing wire diameter.

outer diameter, 4 layers high and 3 layers thick) was wound using 4 mm square copper tubing with a wall thickness of 0.5 mm. All copper tubings were isolated prior to winding using Kapton tape[3]. To mechanically fix the position of the coils, they were glued into a tightly fitting plastic form using two component low expansion epoxy glue[4] together with a mechanical support that is used to mount the trap to the vacuum chamber. For fine adjustments of the offset field, we have additional moveable offset coils. They consist of a single circular loop of solid copper with a diameter of 65 mm. Placed on a moveable support behind each coil package and connected in series to the offset coils, these coils allow small corrections to the offset field after installation of the trap.

The coil assemblies are mounted inside two re-entrance windows made out of glass[5], which permit to operate the coils for the trap outside the vacuum while achieving a minimum separation of 37 mm between the cloverleaf coil assemblies. We use a power supply[6] with 16.8 V/300 A for the dipole and offset compensation coils which are connected in series to achieve common mode rejection of current noise. An electronic MOSFET resistor bank in parallel with the offset coils controls the magnetic offset field. In addition, we use compensation coils wound around the chamber for fine tuning the offset field. We achieve an axial curvature of 116 $^{\mathrm{G}}/_{\mathrm{cm}}$ at 300 A current through the coils. The cloverleaves are powered by a separate current supply[7] with 30 V/330 A producing a radial gradient of 150 $^{\mathrm{G}}/_{\mathrm{cm}}$ at 300 A. The measured values agree to within 15 % with the numerical simulation of the trapping fields. Heating of the coils during operation could be reduced to a maximum of 20 °K by temperature stabilized high pressure (12 bar) cooling water which flows through the copper tubing. Fast switching of the trap is accomplished by using IGBT's (Insulated Gate Bipolar Transistor) and a carefully designed free wheeling circuit. We achieve switching times below 50 μs. Residual eddy currents in the steel chamber prolong the magnetic field switching time to around 300 μs.

In the old system, we experienced a severe thermal drift of the magnetic trap. A change in distance of the coil assemblies of only 100 μm results in a change of 0.27 G offset field corresponding to a change in final temperature after radio-frequency induced evaporation (see Section 9.4.4) of almost 40 μK. This inacceptably large drift was probably due to thermal expansion of the brass support of the trap which was mounted to the vacuum chamber. In the new system, the re-entrance windows were made out of steel with a 2.5 cm diameter window melted onto a small tube protruding from the center of the bucket. This design allows the coil assembly to be pressed into the buckets by heavy duty screws. After sufficient warm up time, we

[3] CMC Klebetechnik GmbH
[4] Fa. Lord, 310 A/B
[5] Caburn MDC, also known as "inverted vacuum windows"
[6] Agilent technology, model HP 6682A
[7] Power Ten, model P63D 30330)

observe a drift in the magnetic offset field of less than 10 mG during several hours of operation. With the new trap, we achieve trapping fields of $B' = 200\,\mathrm{G/cm}$ in radial and $B'' = 324\,\mathrm{G/cm^2}$ in axial direction with the same power supplies as above but a different coil geometry adopted to larger re-entrance windows. We observe a rather slow decay (≈ 5 ms) of stray magnetic offset fields after switching off the new trap which is presumably caused by eddy currents in the steel buckets and the copper seals of the vacuum flanges for the re-entrance windows. This effect puts a lower limit on the minimum time-of-flight after which the number of atoms can be extracted accurately from absorption images (see Section 5.5).

Further information on the magnetic trap setup and construction for the old system can be found in Reference [112] and for the new system in Reference [113].

To allow radio-frequency (rf) forced evaporative cooling (see Section 8.14), an additional single-loop coil was attached in front of one cloverleaf coil-package. This low inductance coil is used to couple the radio-frequency into the magnetic trapping region. A 35 W power amplifier[8] connected to this coil was operated at a typical output power between 1 and 5 W. Frequency and amplitude of our frequency source [9] were controlled via analog inputs having a modulation bandwith of 10 kHz. For radio-frequencies exceeding 50 MHz, we used a commercial frequency generator[10].

5.2 The vacuum system

The ultra-high vacuum system (Figure 5.3) consists of two vertically arranged steel chambers connected by a 50 cm long Zeeman slower tube. In the lower oven-chamber chromium is sublimated at temperatures of around 1750 K in a high temperature effusion cell[11]. The cell is resistive heated via tungsten wires. Commercially available chromium granulate is deposited in a CaO stabilized zirconium dioxide crucible[12] which itself is placed inside a tungsten crucible[13]. The combination of two crucibles is necessary, since chromium forms a low-melting alloy with tungsten [76] and the zirconium dioxide crucibles tend to break and react with the tantalum rods holding the crucibles. A 3 mm thick aperture with a hole of 1 mm diameter inside the crucibles collimates the chromium beam. A movable metal plate connected to a stepper-motor-operated mechanical feedthrough allows shutting the atomic beam on and off within 200 ms. The oven chamber is pumped by a two-stage turbo-

[8] ENI, model 440LA
[9] self-made frequency synthesizer based on Analog Devices' model AD-9851
[10] Rohde & Schwarz, model SML-01
[11] VTS J. Schwarz GmbH, model HT-TA-35-10/W (special design)
[12] Haldenwanger, special design
[13] VTS J. Schwarz, model W-T-HTC-UK-802

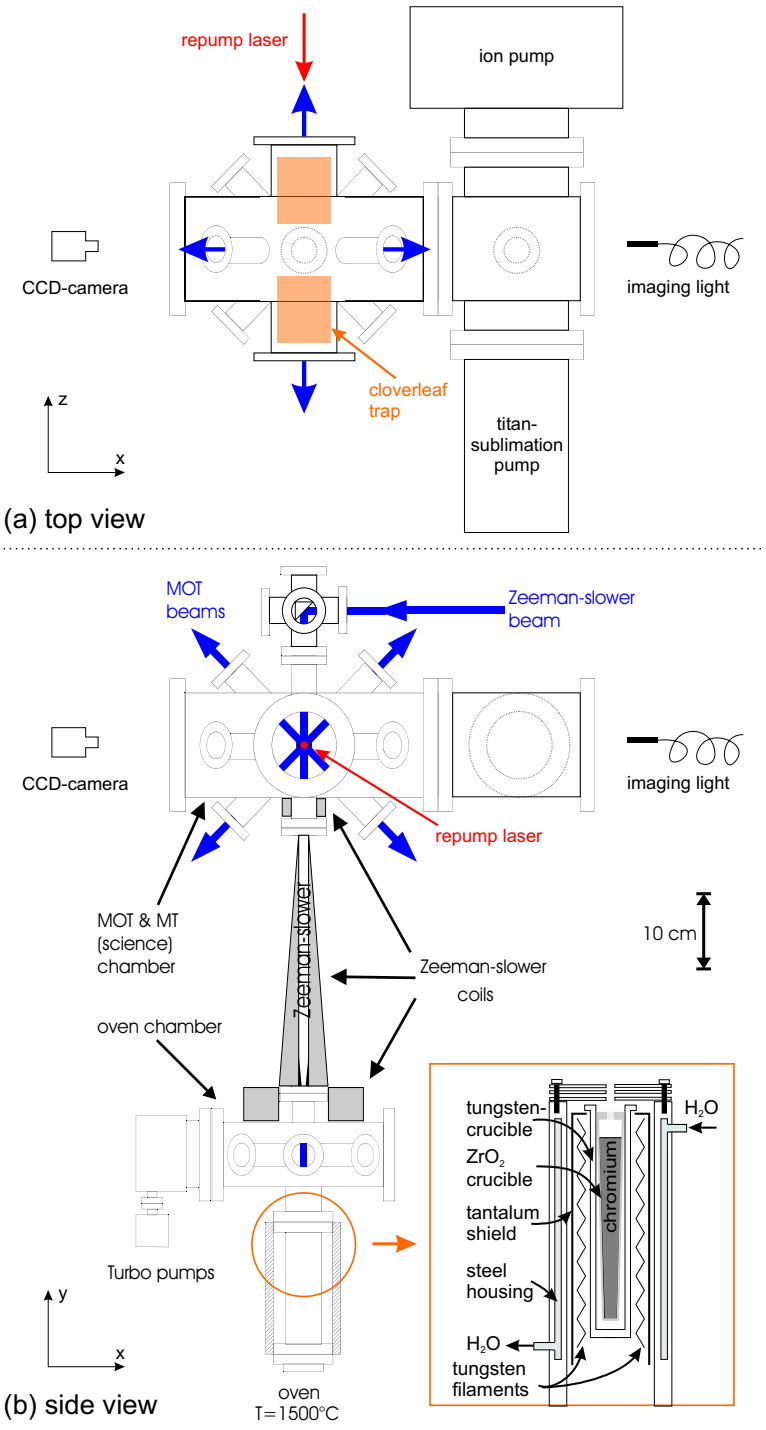

Figure 5.3: Top and side view of the ultra-high vacuum system for preparing ultra-cold samples of chromium atoms in a magnetic trap. Shown are the oven chamber (bottom) connected to the science chamber (top) via the Zeeman-slower. See text for details.

molecular pump assembly[14] to around 10^{-8} mbar. In the new vacuum system a much lower pressure has been achieved by replacing the turbo-molecular pumps by an ion pump[15]. The upper science-chamber is pumped by an ion pump[15] and a Ti:sublimation pump[16] yielding a pressure in the lower 10^{-11} mbar regime. The spin-flip Zeeman-slower [78, 114] is used to slow the atoms down longitudinally on their way from the oven- to the science-chamber. A counterpropagating laser beam is kept into resonance with the decelerating atoms by means of an inhomogeneous magnetic field (see Section 3.1.2) created by an especially designed solenoid wound around the tube. With an inner diameter of 1.5 cm, the Zeeman-slower tube also acts as a differential pumping stage. An additional 7 cm long conical insert inside the lower end of the Zeeman-slower tube further increases the efficiency of the differential pumping stage to maintain a pressure difference between the upper and the lower chamber of more than three orders of magnitude. A 45 °-mirror inside the vacuum on top of the science-chamber reflects the laser light for the Zeeman-slower through the Zeeman-slower tube onto the oven aperture, where the light has a focus. This mirror is being continuously re-coated with chromium by the atomic beam. The reflectivity of a chromium coated mirror for the laser light at 426 nm has been measured to be around 70 %. Several viewports attached to the science-chamber are needed for the laser light of the magneto-optical trap and fluorescence and absorption imaging along the horizontal axis. Two re-entrance vacuum windows made out of glass allow the operation of the cloverleaf coils in the science-chamber outside the vacuum.

5.3 The laser system

5.3.1 Cooling laser

Cooling and trapping is performed on the $^7S_3 \leftrightarrow {}^7P_4$ transition of ^{52}Cr at a wavelength of 425.6 nm. The laser light for this transition is generated by frequency doubling the output of an Ar^+-laser[17] pumped Ti:sapphire-laser[18] in a self-made external, pump beam resonant cavity using a 10 mm long Brewster cut LBO crystal. We obtain 300 mW of blue light at 2 W fundamental input power. Further details on the frequency doubling system can be found in reference [115]. Figure 5.4 shows a schematics of the blue laser system. The laser is actively frequency-stabilized to the cooling transition in the chromium spectrum (beam II). Doppler-free polarization spectroscopy is performed in a chromium gas which is produced by cold gas

[14] Pfeiffer Vacuum, models TMU 260 and TMH 064 with a membrane pump from Vacuumbrand, model MD 4T

[15] Varian, model Plus 75 Diode

[16] Varian, model TSP filament cartridge

[17] Coherent, model Sabre 25 TSM, multi-line visible mode (MLVIS)

[18] Coherent, model MBR 110

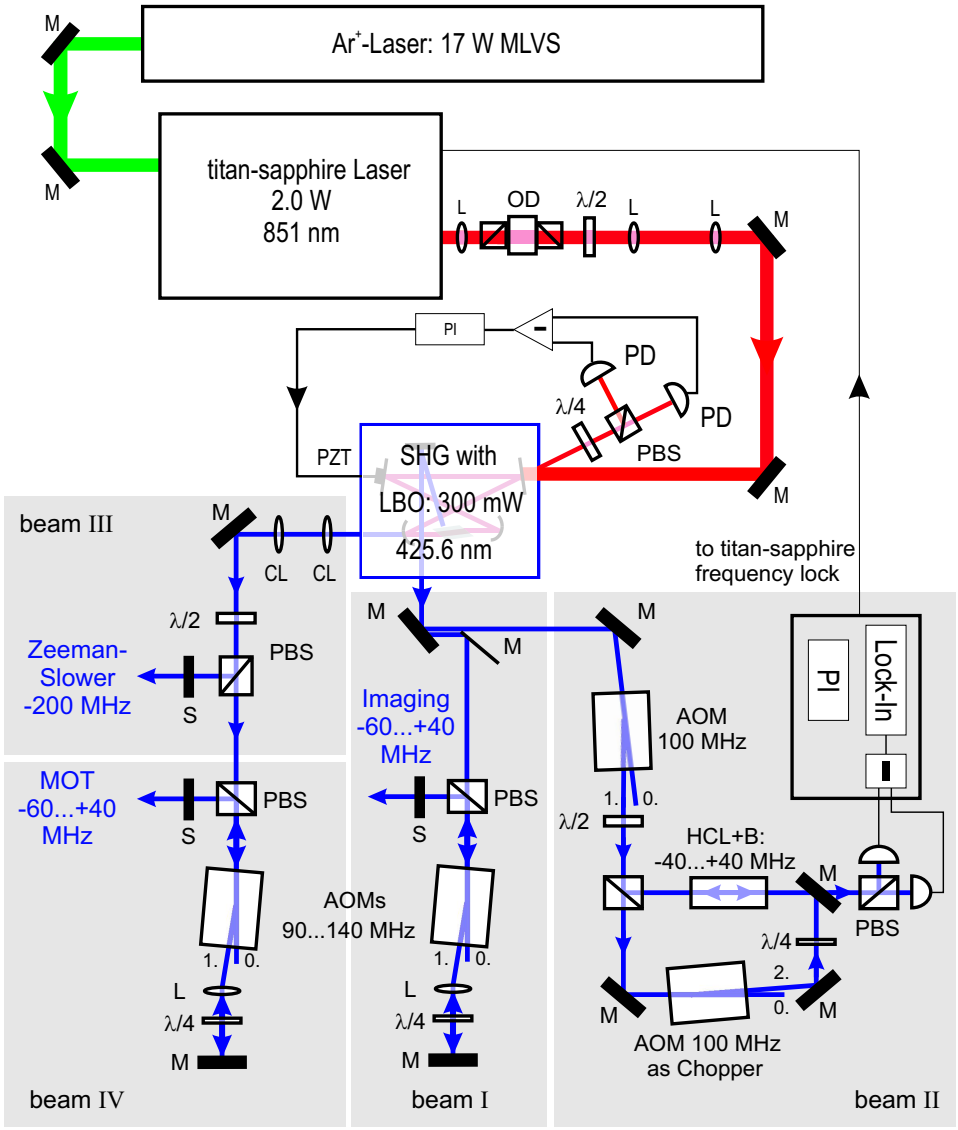

Figure 5.4: Sketch of the setup for the cooling laser system showing laser light generation, frequency stabilization (beam II) and beam preparation for absorption imaging (beam I), Zeeman-slower (beam III) and magneto-optical trap (beam IV). The frequencies of the beams are relative to the atomic resonance. L: lens, OD: optical diode, $\lambda/2$, $\lambda/4$: half and quarter waveplate, respectively, M: mirror, PBS: polarizing beam splitter, PD: photo diode, PI: proportional-integral servo, PZT: piezo transducer, CL: cylindrical lens, S: mechanical shutter, AOM: acousto-optic modulator, HCL: hollow cathode lamp.

discharge in a chromium tube under an argon atmosphere [78]. The resonance frequency of the atoms in the spectroscopy can be fine-tuned by Zeeman-shifting the transition energy with an external magnetic field in the spectroscopy. We achieve a long term frequency stability of around 1 MHz. An additional AOM can be placed into the beam path for the spectroscopy via kinematic mounts. The AOM frequency shifts the light for the spectroscopy by ≈ 150 MHz (not shown). Keeping the lock on the strong ^{52}Cr resonance therefore results in the same frequency shift for the cooling laser, now being resonant with the $^7S_3 \leftrightarrow {}^7P_4$ transition in ^{50}Cr. A frequency tunable and fast switchable laser beam for absorption imaging is obtained by frequency shifting the laser light in a double-pass AOM[19] (beam I) controlled by a VCO (voltage controlled oscillator). We use a single-mode glass fiber to guide the imaging light to the vacuum chamber. This improves the transverse mode quality and beam pointing stability. The light for the spectroscopy and the imaging is obtained from reflections of the blue light at the exit face of the LBO crystal[20]. The main output of the frequency doubling cavity is split between the Zeeman slower (beam III, 120 mW) and the three retroreflected MOT beams (beam IV, 60 mW for all three beams) with an area of 11 mm^2 each. For optimum performance of the MOT, the z beam was adjusted to have less than 10 % of the total MOT intensity. The frequency of the Zeeman-slower beam is fixed to 200 MHz below the atomic resonance by frequency shifting the laser light for the spectroscopy (beam I). As for the imaging light, a double-pass AOM is employed to allow fast switching and frequency shifts of the MOT light by a few linewidths around the atomic resonance without compromising the beam pointing stability. Beams III and IV are steered to the vacuum system using a pair of mirrors for each beam. We found the reproducability of the beam positions sufficient, provided a temperature stability in the laboratory of below 2 K could be achieved. In all experiments reported here, the laser detuning for the MOT beams was set to $-2\Gamma_{eg}$, unless otherwise noted.

5.3.2 Repumping laser

Atoms in the metastable $^5D_4$ and $^5D_3$ states can be transfered to the ground state by exciting them with repumper lasers to the $^7P_3$ state from which they spontaneously decay into the ground state. Figure 5.5 shows a sketch of the experimental setup. A commercial diode laser[21] in the Littrow configuration [116] is tuned to the $^5D_4 \leftrightarrow {}^7P_3$ transition in chromium at a wavelength of 663.2 nm. It provides 5 mW of repumping light in a 2 mm diameter beam. Optionally, the laser power can be

[19] In an AOM in double-pass configuration, the frequency shifted laser beam is retroreflected and passes the AOM twice. This compensates the frequency dependence of the Bragg-angle and shifts the frequency of the laser twice

[20] The Brewster condition for the entrance and exit faces of the crystal is only fulfilled for the pump light.

[21] Toptica, model DL100

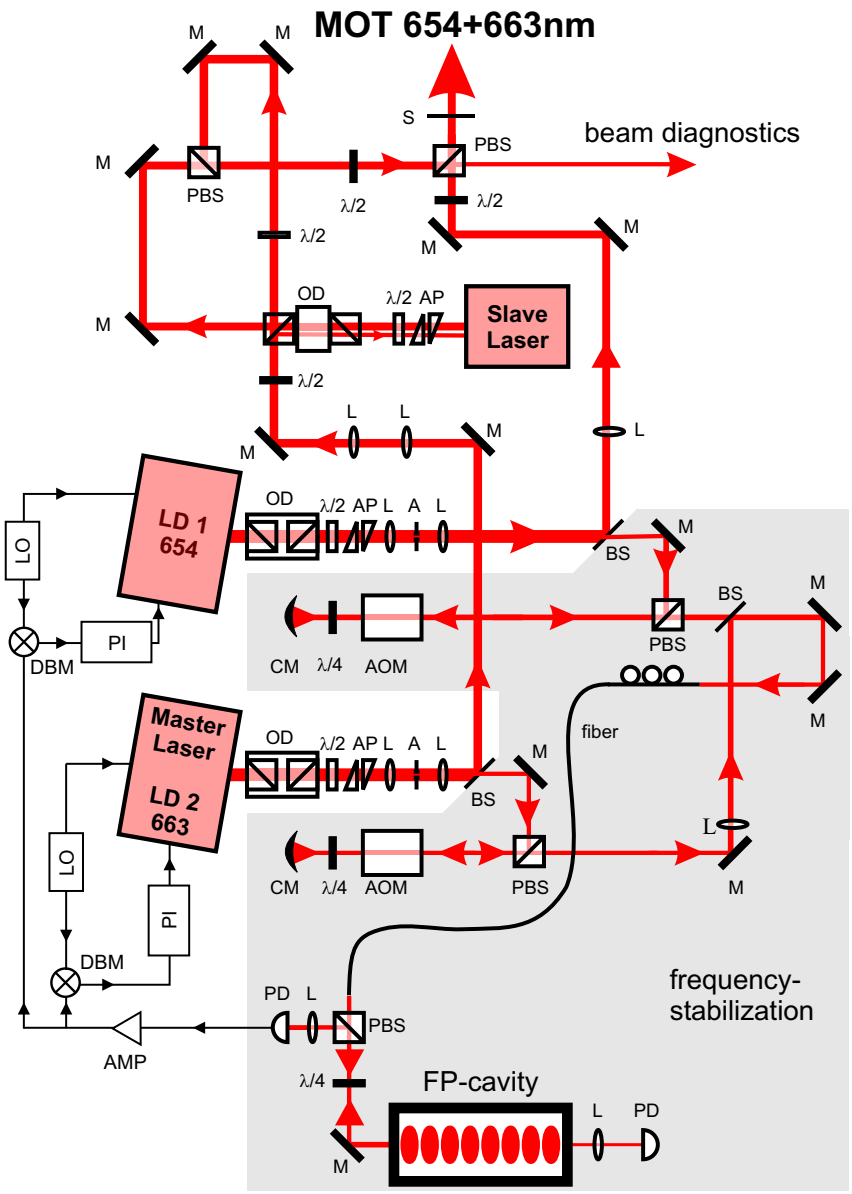

Figure 5.5: Sketch of the setup for the repumping laser system showing both master laser diode systems, the slave system for the 663 nm laser, frequency stabilization and beam preparation. L: lens, OD: optical diode, $\lambda/2$, $\lambda/4$: half and quarter waveplate, M: mirror, CM: curved mirror, PBS: polarizing beam splitter, BS: beam splitter, PD: photo diode, LO: local oscillator, DBM: double balanced mixer, PI: proportional-integral servo, PZT: piezo transducer, CL: cylindrical lens, S: mechanical shutter, AOM: acousto-optic modulator.

increased to 15 mW by injection locking a slave laser diode. A second diode laser system at 654.0 nm serves as repumper for the $^5D_3 \leftrightarrow {}^7P_3$ transition. Both laser frequencies are locked to a mode of an evacuated and temperature stabilized Fabry-Perot reference cavity made of Zerodur and Invar[22] using the Pound-Drever-Hall sideband modulation technique [117]. The laser light for the stabilization cavity can be frequency shifted with double-pass AOMs to coincide with a cavity resonance without altering the output frequency of the lasers for the experiment. We achieve a frequency stability of typically $2\,^{\mathrm{MHz}}/_{\mathrm{hour}}$ dominated by temperature drifts of the Fabry-Perot cavity. Further details on the repumper laser system and the frequency stabilization can be found in reference [118].

5.4 Computer control

Preparation and detection of ultra-cold atoms is a multi-step procedure requiring precise timing of around 24 digital and 8 analog channels. A typical experimental run consists of a sequence of 10-30 steps in which e.g. lasers and currents are shut on or off, the current through the coils of the magnetic trap is ramped, or the power and frequency of the radio-frequency ramp are adjusted. Automation of these steps is a mandatory prerequisite for efficient experiments.

We have implemented our computer control system using cost-effective standard IBM-PC compatible hard- and software. The control computer is equipped with an AMD Athlon 1.2 GHz CPU and a 32 channel digital input/ouput PCI card[23] and an 8 channel, 12 Bit analog output PCI card[24] running under Microsoft Windows 2000. The analog and digital output cards are synchronized via the card specific RTSI-bus and are able to perform clocked pattern generation at a maximum rate of around $75\,^{\mathrm{MBytes}}/_{\mathrm{s}}$. One should avoid generating any traffic other than that for the pattern generation on the PCI bus, since the bandwidth is shared among all components and the very limited size of the onboard buffer does not tolerate a latency exceeding 80 μs. With this system we are able to generate arbitrary digital and analog patterns at a rate of 100 kHz. The digital output signals from the computer are opto-coupled to a 50 Ω driver which can also be controlled manually. The analog output signals for the current supplies are decoupled from the computer using an isolated 1 : 1 amplifier. Most other analog signals are simply rescaled to the range required by the attached device.

The experimental sequences are programmed in a graphical user interface based on LabView[25]. The self-made sequencer software [119] allows to define states of the

[22] both materials have a very low thermal expansion coefficient
[23] National Insturments, model PCI-6533 (DIO-32HS)
[24] National Instruments, model PCI-6713
[25] National Instruments

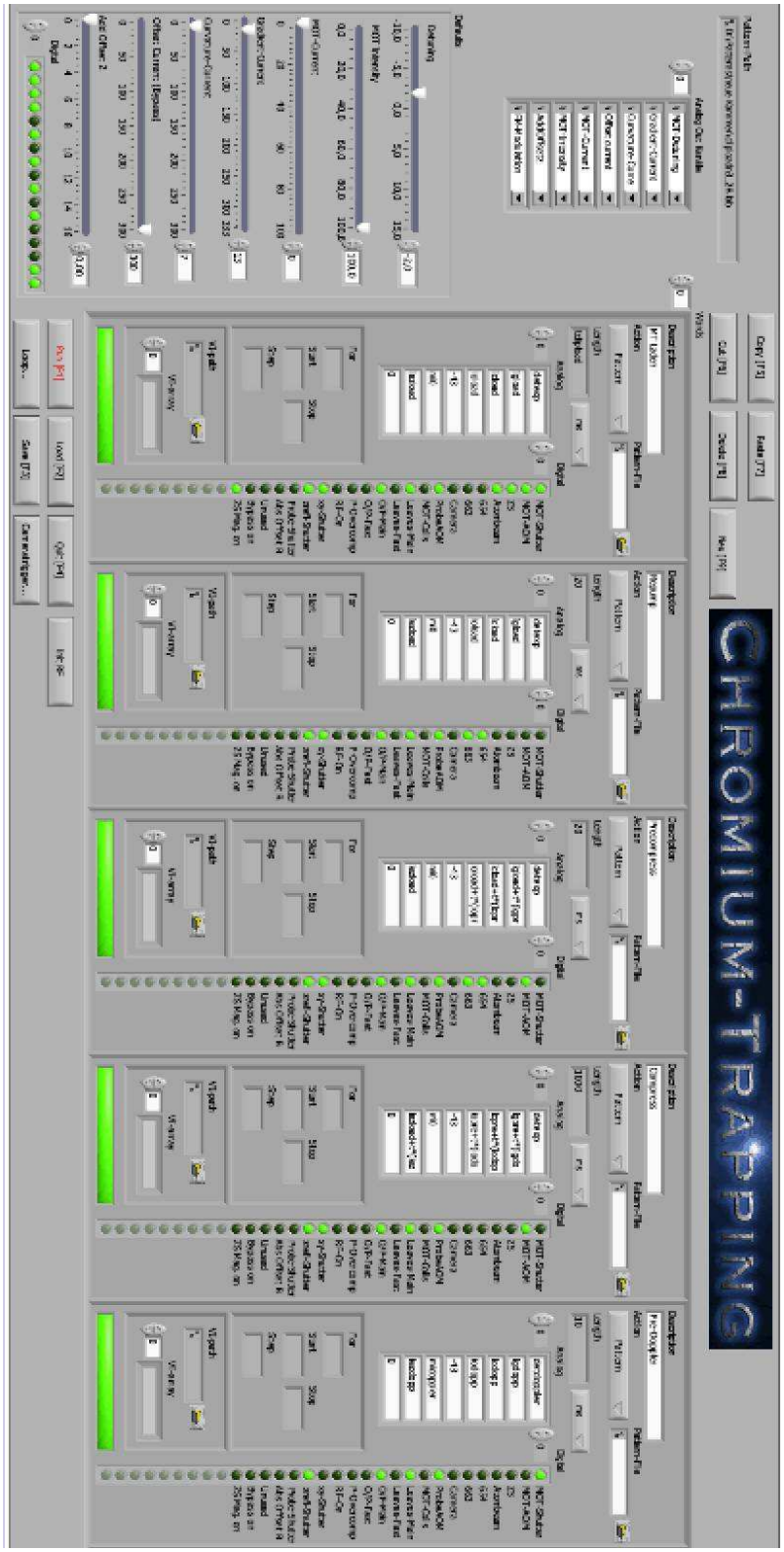

Figure 5.6: Screen shot of the computer control software. The sequence shown is used as a module to load atoms into the CLIP trap (Section 6), compress the trap and perform Doppler cooling (Section 7).

system that last for a specified time until the system advances to the next state. A state is characterized by certain digital and analog ouput patterns. A typical series of states is shown in Figure 5.6. The software allows to program linear and nonlinear analog ramps using standard mathematical functions, loops of sequences and to use external modules of sequences. It is also possible to define constants that can be used within the program. Automatic saving of the sequence file and generation of an information file for the data evaluation software enforces documentation of an experimental run.

5.5 Imaging and data evaluation

All relevant thermodynamic properties of an atomic ensemble can be obtained from images of its density and momentum distribution. In this section we will discuss the different imaging techniques used in this thesis and how the physical properties can be derived from the pictures.

We use a 12 Bit digital progressive scan charge coupled device (CCD) camera[26], connected to a standard IBM-PC compatible computer. A custom-made camera control software based on LabView controls the exposure time of the electronic shutter and saves the pictures to the hard drive. The camera is hardware triggered by one of the digital output channels of the computer control board.

The density regime of the cloud determines the imaging technique to be used. Fluorescence imaging is mostly employed for large and hot clouds with a low optical density. For clouds with a high optical density, absorption imaging is preferrable. We will discuss the different imaging techniques and their applications in the following.

5.5.1 Fluorescence imaging

Fluorescence imaging is based on the collection of near-resonant laser light scattered by the atoms. We use the laser beams for the magneto-optical trap to illuminate the atoms for fluorescence imaging. The different polarizations of the six laser beams yield an approximately unpolarized light field. As a consequence, even a polarized sample of atoms is depolarized (all Zeeman substates are equally populated) after a few optical cycles. Assuming a depolarized cloud in an unpolarized light field, we can include the effects of different polarization coupling constants for multi-level atoms by introducing a mean saturation intensity $<I_s> = {}^{I_s}/_{<\mathrm{CGK}>}$, where $<\mathrm{CGK}>$ is an average over the squares of the Clebsh-Gordan coefficients. For chromium, $<\mathrm{CGK}> = {}^{3}/_{7}$ results in a mean saturation intensity which is larger by a factor of 2.3 compared to the two-level atom saturation intensity [78].

[26] PCO, model PixelFly VGA

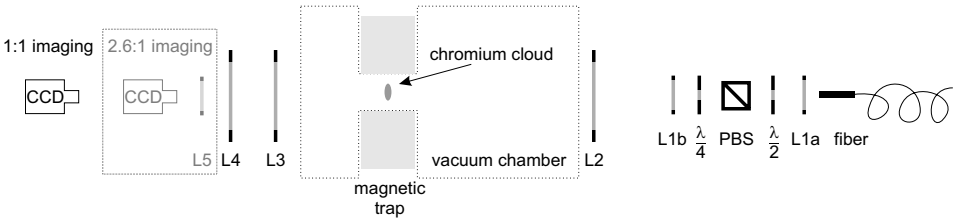

Figure 5.7: Schematic setup for the imaging system (top view). The cloud of atoms is imaged onto a CCD camera using lenses L3-L5 (2.6:1 magnification) or L3-L4 (1:1 magnification). For absorption imaging, blue laser light from a single mode glass fiber (beam I in Figure 5.4) is expanded in a telescope formed by the lenses L1 and L2. Polarization and intensity of the light are adjusted by the half ($\lambda/2$) and quarter ($\lambda/4$) waveplates together with the polarizing beam splitter (PBS).

Atoms scatter light at a rate given by Equation 3.6. For a cloud of atoms with a small optical density, the intensity of the incident light is uniform over the cloud and reabsorption of scattered photons can be neglected. The total photon scattering rate of N atoms is then given by the incoherent sum of all single atom scattering rates $\Gamma_{\mathrm{tot}} = N\Gamma_{\mathrm{sc}}$. For an unpolarized cloud and unpolarized light, the emission pattern of the fluorescence light is isotropic. The solid angle fraction imaged onto the camera determines how much of the fluorescence light is captured by the imaging system. To increase this fraction and thus the signal to noise ratio, lenses with a large diameter d and a small focal length f placed at a small distance (usually corresponding to the focal length) from the cloud, should be used. These efficiency considerations are summarized in the so-called "f-number" $f/\# = f/d$. The spot size[27] of a lens illuminated with a parallel laser beam having a wavelength λ is then given by $\Delta d = 2.44\lambda f/\#$. The corresponding resolving power of an imaging system according to the Rayleigh criterion is $\Delta x = \Delta d/2$.

Figure 5.7 shows the setup of our imaging system. For fluorescence imaging, only the optics left of the vacuum chamber is relevant. The atoms are illuminated by all six MOT beams tuned to the atomic resonance frequency producing an approximately unpolarized light field. We use two 50 mm diameter achromats[28] (L3, L4) with a focal length of 300 mm each in a $2f$—$2f$ imaging system with a magnification of 1. An additional lens with a focal length of 75 mm (L5) can be inserted to yield a magnification (actually a reduction) of 2.6:1. The camera can be moved from the 1:1 imaging position to the 2.6:1 imaging position via kinematic mounts. The optical resolution[29] of the 1:1 imaging system has been measured with a USAF-1951 test target to be 15 μm. It is limited by the 10 μm pixel size of our camera. After the

[27] defined as the diameter of the first order diffraction minimum
[28] Linos Photonics, model 32 2305
[29] distance between two black lines that were just distinguishable

experiments for this thesis, a larger magnification was added resulting in a measured resolution of 6 μm.

A typical experimental sequence for a fluorescence image starts with switching off the trapping field. After an adjustable time-of-flight the camera exposure is started and the MOT laser beams are tuned to the atomic resonance and switched on for an adjustable exposure time, which varies between 100 μs and a few ms. After this fluorescence picture, the atoms are removed from the trapping region and a background picture with the same laser light and exposure time is taken. The background picture is subtracted from the fluorescence picture prior to data evaluation.

Each atom scatters many photons during fluorescence imaging. A diffusion process and imbalances in the counterpropagating laser light intensities lead to a distortion of the shape of the cloud for long exposure times. We found experimentally, that clouds with an original size on the order of 500 μm keep their original shape to within 10 % for exposure times below 500 μs. Smaller clouds or longer exposure times allow only a determination of the number of atoms.

Accurate determination of the number of atoms in the atomic cloud requires precise knowledge of laser light intensity and detuning, the solid angle fraction captured by the imaging system, its transmission and the camera calibration. In the high intensity limit, the scattering rate is to first order independent of the incident light intensity and detuning, since all atoms scatter at a rate of $\frac{\Gamma}{2}$ (see Equation 3.6). The solid angle fraction $d\Omega$ can be obtained from the lens diameter d and distance $f' \gg d$ from the center of the cloud

$$d\Omega = \frac{\pi(d/2)^2}{4\pi f'^2}. \tag{5.1}$$

The transmission of the imaging system can either be measured or estimated from the number of uncoated and anti-reflection coated glass surfaces. We calibrated our CCD camera with a laser beam of known intensity which yielded an efficiency of $9.3 \times 10^{-18}\,\mathrm{Ws/_{pixelcount}}$.

The images recorded by the camera reflect the density distribution of the atoms integrated along the imaging direction. The number of atoms in the cloud can be obtained from the calibrated pixelcounts summed over all pixels. We estimate the accuracy of our atom number determination to around 20 %. This was verified by comparison with absorption images of identically prepared atomic clouds. Where possible, we calibrated the fluorescence images to yield the same number of atoms as absorption images.

In atomic clouds with a high optical density, the intensity of the incident light is significantly reduced when passing through the cloud. This results in an intensity gradient and thus a reduced scattering rate of atoms close to the center. As a consequence, the observed density profile is distorted and the number of atoms

underestimated. Absorption imaging uses exactly this effect to obtain an image of the cloud and thus turns the disadvantage of strong absorption of photons into an advantage.

5.5.2 Absorption imaging

The absorption imaging technique is complementary to fluorescence imaging. Whereas in the latter photons *scattered* from a light beam are recorded, in absorption imaging the photons *remaining* in the illuminating laser beam are used to obtain the density distribution of the cloud. The absorbing cloud casts a shadow which can be recorded with a CCD camera.

It is well known from Beer's law, that the light intensity in a homogenous absorbing medium decreases exponentially with penetration depth x:

$$I(x) = I_0 e^{-OD \cdot x}, \tag{5.2}$$

where OD is the optical density of the medium. For a cloud of two-level atoms, the optical density can easily be derived using the concepts of Chapter 3. In the low intensity limit ($I/I_s \ll 1$), the light power scattered by a two-level atom can be written as

$$P_{\mathrm{sc}} = \frac{\hbar\omega_{\mathrm{laser}}\Gamma}{2} \frac{I/I_s}{1 + 4\delta^2/\Gamma^2} = \sigma_\lambda(\omega_{\mathrm{laser}})\, I, \tag{5.3}$$

with

$$\sigma_\lambda(\omega_{\mathrm{laser}}) = \frac{\sigma_\lambda^0}{1 + 4\delta^2/\Gamma^2}. \tag{5.4}$$

The resonant light scattering cross-section is given by

$$\sigma_\lambda^0 = 6\pi\lambda\!\!\!^{-2} = \frac{\hbar\omega_{\mathrm{atom}}\Gamma}{2I_s}, \tag{5.5}$$

where $\lambda\!\!\!^{-}$ is the transition wavelength divided by 2π. The intensity of light passing along the x direction through a cloud of atoms with density distribution $n(x, y, z)$ is reduced by $dI = -\sigma_\lambda(\omega_{\mathrm{laser}})\, n(x, y, z)\, I\, dx$. Integration yields Beer's law (Equation 5.2), where the exponent of the exponential function is replaced by a position dependent optical density of

$$\tilde{OD}(x, y, z) = -\sigma_\lambda(\omega_{\mathrm{laser}}) \int_{-\infty}^{x} n(x', y, z)\, dx'. \tag{5.6}$$

From the last equation it becomes clear, that the intensity profile of the laser beam after having passed through the cloud contains the information about the integrated

density distribution $n(y, z)$ of the cloud. It can be reconstructed if the intensity profiles of the laser beam before ($I_b(y, z)$) and after ($I_a(y, z)$) passing through the cloud are known:

$$n(y,z) = -\frac{1}{\sigma_\lambda(\omega_{\text{laser}})} \ln \frac{I_a(y,z)}{I_b(y,z)}. \tag{5.7}$$

Integration of this equation yields the total number of atoms. Since the recorded images are divided into descrete pixels, the integration is turned into a summation over all pixels:

$$N = \frac{A}{\sigma_\lambda(\omega_{\text{laser}})} \sum_{\text{pixels}} \ln \frac{I_a(y,z)}{I_b(y,z)}, \tag{5.8}$$

where A is the area in the cloud corresponding to the size of a pixel. In contrast to fluorescence imaging, no camera and transmission calibration nor solid angle measurement is necessary to determine the number of atoms from an absorption image. It only requires a calibration of the magnification, which can be done very accurately. We estimate a systematic uncertainty of around 20 % in the determination of the number of atoms arising mostly from fluctuations of the magnetic field and the imaging laser polarization. Interference fringes in the intensity distribution of the imaging laser limit the detection capability to clouds with an optical density exceeding 5 %.

Figure 5.5 on page 43 shows the experimental setup for absorption imaging. The absorption beam is guided to the vacuum chamber in a single mode glass fiber to improve the mode quality and to reduce beam drifts and vibrations during an imaging sequence. The light is expanded in a telescope consisting of lenses L1a/b ($f = -50\,\text{mm}$) and L2 ($f = 200\,\text{mm}$) to a diameter of approximately 40 mm. The intensity and polarization are adjusted using a half and a quarter waveplate together with a polarizing beam splitter. The cloud of atoms casts a shadow in the absorption beam passing through it. This shadow is projected onto the CCD camera using the same imaging system as for fluorescence imaging. A weak homogeneous magnetic offset field along the direction of the σ^+-polarized absorption beam is used as a support field to keep the atoms aligned. The atoms are optically pumped within a few cycles to the extreme Zeeman-substate $m_J = 3$ from which they can undergo transitions only to $m'_J = 4$ with a Clebsh-Gordan coefficient of 1. They can therefore be treated as ideal two level atoms.

Besides the transverse mode quality of the absorption beam, the spectral properties are important. The spectral width of the imaging light needs to be much smaller than the linewidth of the transition, so that the light scattering cross-section $\sigma_\lambda(\omega_{\text{laser}})$ is the same for all frequency components of the light.

The duration of the absorption imaging light pulse has to be short enough for the atoms to maintain their original density distribution. The diffusion induced by

photon scattering (see Section 3.2) leads to an increase in the size of the cloud. The number of photons contributing to an acceleration along one direction is given by the square root of the total number of scattered photons [120]. In our setup, each atom scatters typically 35 photons during absorption imaging. The atoms are accelerated and travel approximately 5 μm during the 100 μs pulse. This distance is below our resolution limit and can therefore be safely neglected.

An absorption image is obtained by taking a series of three pictures: the dark, bright and background picture. The sequence starts with switching off the trapping fields (usually the currents for the magnetic trap) and simultaneously switching on the magnetic imaging field. After a variable time of flight[30], the absorption light tuned to the atomic resonance frequency in the imaging field is switched on for 100 μs to take the absorption picture. The intensity of the absorption light is adjusted to almost saturate the CCD camera during the 100 μs exposure. It is usually much below the saturation intensity as required for the derivation of Equation 5.3. The atoms are removed from the trapping region before the bright image is taken with the same laser and magnetic field parameters as before. Finally, a background picture is taken with the same camera exposure time as before but no laser light. After background subtraction from the dark and bright pictures, the integrated density distribution of the atoms is obtained according to Equation 5.7.

5.5.3 Intra-trap absorption imaging

Intra-trap absorption imaging can be used to determine the size of the cloud in the magnetic trap. The imaging sequence is the same as for regular absorption imaging, except that the magnetic trapping fields are kept on during imaging and no magnetic support field is switched on. Determining the number of atoms from these pictures is very complicated, since in our magnetic field configuration the atoms cannot be treated as two-level systems anymore. We adjust the polarization of the absorption light to be linear along the z-axis and the magnetic offset field of the trap. Optical pumping distributes the atoms among the magnetic substates at rates which depend on the laser light intensity and the magnetic offset field that Zeeman-shifts the transitions according to Figure 3.2. Additional distortions of the optical density arise from the finite temperature of the cloud and the inhomogeneous magnetic trapping fields. A large (hot) cloud of atoms probes stronger magnetic fields in axial and radial directions leading to position dependent Zeeman-shifts and a rotation of the atomic quantization axis with respect to the π-polarization of the light field. We have modeled the optical pumping process assuming a homogeneous magnetic offset field using rate equations. During a 100 μs long absorption laser pulse, no steady state in the atomic distribution is reached. The effective absorption therefore

[30] Residual magnetic fields generated by eddy currents in the vacuum chamber prevent us from taking pictures for a time-of-flight shorter than 0.5 ms in the old system and 5 ms in the new system.

changes during exposure and is strongly dependent on laser light intensity. We found qualitative agreement with the experimental results, but could not satisfactorily predict a universal scaling factor for the number of atoms. A more sophisticated approach including local magnetic field effects might allow to "deconvolute" the original density distribution from the intra-trap absorption image.

We found observed ratios for the number of atoms from absorption and intra-trap absorption images ranging between 2 and 4, depending on the temperature and density of the cloud. However, the initial size and therefore the temperature of the cloud agreed to within 20 %. In conlusion, intra-trap absorption imaging can be a useful tool to probe the temperature of an atomic ensemble, but can only give approximate atom numbers that need to be calibrated by other imaging techniques.

5.5.4 Data evaluation

The main purpose of the data evaluation is to extract from the CCD camera images the physical properties describing the atomic ensemble. These include number of atoms, density, size, temperature and phase-space density of the atoms.

From CCD camera images, we get the integrated density distribution divided into pixels. Fitting a model distribution (Equations 4.11 or 4.15) to the data yields the size of the cloud $\sigma_{y,z}$ or ξ, the peak density n_0 and the position of the maximum. We use either a full 2D least squares fit to the image or two 1D fits to orthogonal cuts through the center of the cloud along the trap axes. From the rotational symmetry of the cloud in the xy-plane, the full 3D density distribution can be reconstructed. The number of atoms can be derived from the peak density and the size of the cloud,

$$N = n_0 V = (2\pi)^{\frac{3}{2}} n_0 \sigma_x \sigma_y \sigma_z, \tag{5.9}$$

where we have assumed a harmonic trap in the last equality. We found this method more accurate than determining the number of atoms from the calibrated pixelsum of the image as described in the previous Subsections.

There are several ways to obtain the momentum distribution of the cloud which is in thermal equilibrium characterized by the temperature. The most accurate method is to perform a time-of-flight (TOF) experiment in which the atoms are released from the trap and are allowed to expand freely for a specific amount of time. During expansion, the initial *momentum* distribution is transformed into a *density* distribution which is independent of the initial density distribution for long expansion times. Recording the evolution in a series of TOF images allows the reconstruction of the initial momentum distribution, i.e. the temperature of the ensemble. For a cloud in a harmonic trap, the momentum and the density

distribution are Gaussian (Equation 4.8). At a time t after release from the trap, the size of the cloud is given by

$$\sigma(t) = \sqrt{\sigma_0^2 + \frac{k_\mathrm{B}T}{m}\,t^2}, \tag{5.10}$$

where σ_0 is the initial size of the cloud at $t = 0$ and T the temperature. For a harmonic trapping potential, this equation holds for all three directions independently. A fit of this equation to the measured evolution of the cloud size yields the temperature and the initial size in the trap. The temperature can also be obtained from σ_0 and the known trapping potential B'' by means of Equation 4.9 or 4.10. For a well known trapping potential, we can insert the relation between size and temperature in Equation 5.10 and thus reduce the fit parameter to the temperature only:

$$\sigma(t) = \sqrt{\frac{k_\mathrm{B}T}{\mu B''} + \frac{k_\mathrm{B}T}{m}\,t^2}. \tag{5.11}$$

Absorption images are usually taken after a certain time-of-flight to allow the magnetic fields to settle before imaging. The size of the cloud in these images is larger than the initial size according to Equation 5.10. Eliminating the temperature in this Equation by inserting Equation 4.10 and solving for the initial size yields

$$\sigma_0 = \sqrt{\frac{k_\mathrm{B}T}{\mu B''}} = \sqrt{\frac{\sigma(t)^2}{1 + \frac{\mu B''}{m}t^2}}. \tag{5.12}$$

Solving the same Equations for the temperature of the cloud, one obtains

$$T = \frac{\sigma_0^2 \mu B''}{k_\mathrm{B}} = \frac{\sigma(t)^2}{\frac{k_\mathrm{B}}{\mu B''} + \frac{k_\mathrm{B}}{m}t^2}. \tag{5.13}$$

With these formulae, it is possible to derive the temperature and the initial density of the atoms in the trap from a single TOF image, although with less precision. We chose the appropriate method for evaluating the cloud parameters using the most accurately determined values in the specific experiment.

We have developed a data evaluation software based on Matlab[31]. It enables us to perform almost real-time data evaluation during an experimental run. The software implements modules for loading images, standard fitting procedures of the image data and evaluation of the cloud properties from the fit. The methods for determining these properties are controlled by variable flags and switches. All relevant experimental parameters (e.g. camera type and magnification, imaging technique, magnetic trap parameters) are modular and user selectable. Details of the experimental run are read in from a human-readable text file which is usually generated

[31] The Mathworks

by the computer control software. Matlab's flexible script language allows to easily program complex data evaluation procedures using these modules. The plots and results are automatically stored in an encapsulated postscript (eps) file and a binary file, respectively.

Chapter 6

Continuous loading of a Ioffe-Pritchard magnetic trap

In this Chapter I present a novel technique to continuously load atoms from a magneto-optical into a magnetic trap of the Ioffe-Pritchard type. It allows us to accumulate an order of magnitude more atoms than we are able to trap in a chromium magneto-optical trap. In Section 6.2 the continuous loading scheme together with a discussion of the general requirements for the atomic level structure and possible implementations is presented. The rate equation model developed in References [78, 121] for the temperature and the accumulation of magnetically trapped atoms is summarized and extended in Section 6.3. Details of the specific experimental techniques are discussed in Section 6.4. Measurements of the temperature, the number of trapped atoms and the accumulation efficiency in the CLIP trap are presented in Section 6.5 and compared to our model. I conclude this chapter with a discussion of possible applications and extensions of our scheme in Section 6.6. Parts of this chapter have been published in [122].

6.1 Introduction

Cold atomic gases have proven to be a useful tool for a wide variety of fundamental experiments in physics, including Bose-Einstein condensation (BEC) [123] and atom interferometry [124]. The preparation of ultracold atomic samples for experiments in magnetic traps is a challenging task involving multi-step cooling and trapping procedures. The starting point is usually a magneto-optical trap (MOT) (see Section 3.5). Transferring the atoms from the MOT into the magnetic trap (MT) is typically accompanied by a significant loss in atom number. A crucial point of this transfer process is to match the size and position of the atomic cloud in the MOT and the

MT (so called "mode matching") to obtain maximum transfer efficiency and to avoid heating [125].

We present a simple scheme for a **C**ontinuously **L**oaded **I**offe-**P**ritchard ("CLIP") trap, which is directly loaded from a magneto-optical trap. The CLIP trap can serve as a robust source of cold atoms for various atom optics experiments. It significantly simplifies the preparation of cold atomic samples in harmonic magnetic traps and can be implemented for a variety of elements [121, 126]. Accumulation of atoms in the magnetic trap during operation of the MOT removes the need for a separate transfer step and allows to capture more atoms than in the MOT. The latter is especially useful for atomic species like chromium with a large inelastic two-body loss coefficient for excited state collisions [78, 127].

Besides loading a magnetic trap, our scheme could serve as a source for magnetic waveguide experiments. A fully continuous atom laser has been on the wish list of many atomic physicists ever since the successfull formation of a BEC in dilute atomic gases. In one of the most promising schemes [128], a magnetic waveguide is loaded from a MOT and evaporative cooling is performed on a continuous beam of atoms along the waveguide transforming the temporal evolution of evaporation into a spatial evolution. The mode matching of the initial MOT to the magnetic waveguide is a complicated issue [129]. Due to its continuous character, our scheme is an ideal source for this and other magnetic waveguide and atom interferometry [130, 131] experiments.

The CLIP trap is based on our previously reported continuously loaded magnetic quadrupole trap [121]. The new scheme removes the need for a transfer step from a 3D-quadrupole into an IP magnetic trap, thus greatly simplifying the preparation procedure. Another advantage is the possibility to adjust the aspect ratio in the IP trap, thus reducing the influence of the dominant density dependent loss mechanisms [78, 121]. The CLIP trap employs a modified magneto-optical trapping scheme allowing us to operate a MOT and a large volume IP trap overlapped in space and time. Atoms are magnetically trapped in a long-lived metastable state which is decoupled from the MOT light. Transfer between MOT and MT is provided by radiative leakage [121, 132] from the excited state, which is populated by the MOT laser. We have implemented this scheme with atomic chromium, but also the alkaline earth metals and e.g. ytterbium are well suited [126] for that scheme and several groups are working on an implementation [133, 134].

6.2 Continuous loading scheme

The basic principle of the continuous loading scheme presented here has been developed and implemented for chromium in a 3D-quadrupole magnetic trap [121]. In

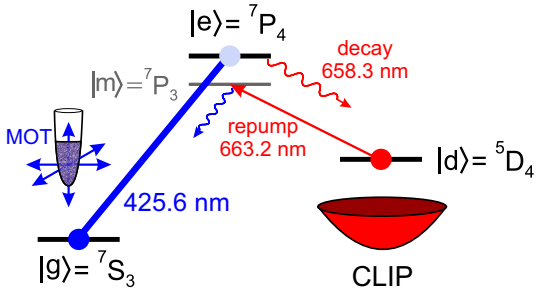

Figure 6.1: CLIP trap loading scheme. Shown are the relevant atomic levels and transitions for the implementation in ^{52}Cr (black lines). The magneto-optical trap is operated by driving the fast transition from $|\,g\,\rangle$ to $|\,e\,\rangle$. Transfer between MOT and CLIP trap is provided by radiative leakage from $|\,e\,\rangle$ to $|\,d\,\rangle$. Repumping the atoms via an intermediate state $|\,m\,\rangle$ (gray lines) allows to transfer the atoms to the ground state.

this chapter we show that the scheme can be extended to magnetic traps of the Ioffe-Pritchard type. We will introduce the concepts of the CLIP trap with chromium. Requirements and possibilities for the implementation with other atomic species will be discussed at the end of this section.

Figure 6.1 shows the principle of operation on a simplified level scheme for ^{52}Cr (see Figure 2.1 for more details). A strong dipole transition with linewidth Γ_{eg} connecting the ground state $|\,g\,\rangle$ and an excited state $|\,e\,\rangle$ allows the operation of a modified magneto-optical trap (see Section 3.5). We employ a light field configuration similar to the 2D$^+$-MOT [135]: two orthogonal pairs of σ^+/σ^--polarized laser beams cool and trap the atoms radially. An additional pair of σ^+-polarized laser beams along the axial direction provides Doppler cooling and very weak confinement due to light pressure forces [136, 137]. The advantage of using this setup rather than a standard 3D-MOT is the compatibility with the magnetic field configuration of the IP trap. For simplicity, in the following we will refer to our configuration as "MOT", although we actually mean the modified setup just described. The radial magnetic field gradient needed for the 2D-MOT is provided by the Ioffe-Pritchard trap (see Section 4.2). The magnetic field configuration for the latter consists in radial direction (x, y) of a 2D-quadrupole with magnetic field gradient B' supporting the atoms against gravity. In axial direction (z), magnetic confinement is provided by a curvature field B'' [138]. Along the same direction, a small magnetic offset field B_0 prevents Majorana spin-flip losses [109].

The cycling transition used for the chromium MOT is not closed. Atoms can undergo spontaneous emission to a long-lived metastable state, denoted $|\,d\,\rangle$ in Figure 6.1, at a rate Γ_{ed}. This radiative leakage is the loading mechanism for the magnetic trap. Atoms in the low field seeking magnetic substates of the $|\,d\,\rangle$-state manifold can be magnetically trapped in the field of the IP trap. While operating the MOT,

atoms spontaneously decay to the metastable level and accumulate in the MT. The branching ratio Γ_{eg}/Γ_{ed} has to be much larger than 1 to provide cooling in the MOT before the atoms are transferred into the MT. In chromium, the branching ratio $\Gamma_{eg}/\Gamma_{ed} \approx 250\,000$ is rather high, thus limiting the loading rate into the CLIP trap (see Section 6.3.1 below). Additional optical pumping to the state $|\,m\,\rangle$ would allow a much higher loading rate due to a branching ratio of only $\Gamma_{mg}/\Gamma_{md} \approx 5200$ and will be implemented in future experiments [139]. Simultaneous operation of a MOT and a MT is only possible if the magnetic field gradient required for magnetic trapping is compatible with the MOT. Chromium with 6 μ_B (Bohr magnetons) is easily supported against gravity for magnetic field gradients around 5-10 G/cm, which are typical gradients for operating a MOT with an atom having a linewidth of $\sim 2\pi \times 5$ MHz.

In general, there are few requirements on the atomic species properties for an implementation of the CLIP trap scheme: (i) The atoms need to be laser-coolable to operate a MOT. (ii) A long-lived magnetically trappable state decoupled from the MOT light must exist. (iii) A dissipative transfer mechanism between MOT and metastable atoms is needed. (iv) The MOT should operate at magnetic field parameters required to trap the metastable atoms.

We will briefly discuss each of these points and possible implementations of the continuous loading scheme for two other atomic species: rubidium as a representative of the alkali metals and strontium for the earth alkali metals.

Requirement (i) seems obvious and is met by most atomic species used in atom optics experiments, although some restrictions may apply (see below). Besides metastable states, also hyperfine states with a sufficiently large separation from the states used for the MOT, should be utilizable to fulfill condition (ii). In ^{87}Rb, where the MOT is usually operated on the $|\,g\,\rangle \mathrel{\hat{=}} {}^5\mathrm{S}_{1/2}$, F=2 $\leftrightarrow {}^5\mathrm{P}_3/2$, F=3 $\mathrel{\hat{=}} |\,e\,\rangle$ transition, the F=1 hyperfine state of the ^{5}S manifold could serve as the magnetic trapping state $|\,m\,\rangle$. Off-resonant excitation of the $^5\mathrm{P}_{3/2}$, F=2 state by the MOT light followed by spontaneous decay to state $|\,m\,\rangle$ serves as the loading mechanism for the magnetic trap (requirement (iii)). The loading rate can be tuned by adjusting the intensity of the MOT laser beams. At this point condition (i) puts a restriction on the actual implementation: a Rb MOT without repumping the atoms from the F=1 to the F=2 manifold has a strongly reduced efficiency. The dark SPOT-MOT [140] solves this problem by surrounding a central spot in the MOT with repumping light. Also, the operation of a MOT at magnetic field gradients required for the magnetic trapping of rubidium having a magnetic moment of 0.5 μ_B in the lower hyperfine state can be a problem (requirement (iv)).

A ^{88}Sr MOT for catching and precooling the atoms is typically operated between the absolute ground state $^1\mathrm{S}_0$, $|\,g\,\rangle$, and the excited state $^1\mathrm{P}_1^0$. As in chromium, this transition is not closed. Nevertheless, 8×10^7 atoms can be trapped in a Sr MOT

even without repump laser [91]. Atoms can spontaneously decay via an intermediate state $^1D_2$ to the long-lived magnetic trap state $^3P_2^0$, $|\, m \,\rangle$ (requirements (ii) and (iii)). Additional decay channels can be closed by repumping lasers. Here, simultaneous operation of a MOT and a MT is assisted by a moderate magnetic moment of $3\mu_B$ and the spectrally broad MOT transition requiring high magnetic field gradients of 50-150 G/cm by itself (requirement (iv)). A more elaborate discussion of this trapping scheme and its variants adopted for ytterbium and other earth alkalis is given in Reference [126].

Requirement (iii) might raise the issue of reabsorption of spontaneously emitted photons by a very dense cloud of already magnetically trapped atoms. In the scheme for chromium presented here, the narrow transition $|\, e \,\rangle \leftrightarrow |\, d \,\rangle$ into the trap state is spectrally broadened by the strong MOT transition $|\, g \,\rangle \leftrightarrow |\, e \,\rangle$. The integral absorption cross section for this spin-forbidden transition to state $|\, e \,\rangle$ is determined by the small transition strength giving rise to a suppression of reabsorption by a factor of Γ_{eg}/Γ_{ed} [78, 141].

6.3 Model

In this section, we want to summarize and extend the model for the continuous loading scheme developed in Reference [121] and adapt it to the Ioffe-Pritchard configuration.

6.3.1 Number of trapped atoms

Loading of the CLIP trap is characterized by a loading rate R, proportional to the number of excited atoms in level $|\, e \,\rangle$, N^*_{MOT}, the decay rate into the metastable level Γ_{ed}, and a transfer efficiency η, giving

$$R = \eta N^*_{\mathrm{MOT}} \Gamma_{ed}. \tag{6.1}$$

The maximum attainable transfer efficiency (i.e. the fraction of atoms in a magnetically trappable low field seeking state) can be estimated using a rate equation model for optical pumping. Its theoretical prediction for chromium atoms in a standard 3D-MOT is around 30% [78]. Similar values have been obtained experimentally in our CLIP trap configuration.

Accumulation of atoms in the MT is limited by loss mechanisms removing magnetically trapped atoms. We have identified two inelastic collision processes as the major loss mechanisms: (i) inelastic collisions between optically excited atoms in the MOT and atoms in the MT, characterized by a rate constant β_{ed}, and (ii) inelastic

collisions between two magnetically trapped atoms with a rate constant[1] β_{dd}. For completeness, we have also included background gas collisions at a rate γ_d, although they are negligible in our setup. The rate equation for the number of atoms in the CLIP trap, N_{MT}, reads

$$\begin{aligned}\frac{\mathrm{d}N_{\mathrm{MT}}}{\mathrm{d}t} &= R - \gamma_d N_{\mathrm{MT}} - \beta_{ed}\int_V n_e(\vec{r})n_d(\vec{r})\mathrm{d}V - 2\beta_{dd}\int_V n_d^2(\vec{r})\mathrm{d}V \\ &= R - (\gamma_d + \gamma_{ed})N_{\mathrm{MT}} - 2\beta_{dd}\frac{N_{\mathrm{MT}}^2}{V_{\mathrm{MT}}} \qquad (6.2)\end{aligned}$$

with

$$\gamma_{ed} = \frac{N_{\mathrm{MOT}}^* \beta_{ed}}{V_{\mathrm{eff}}}, \qquad (6.3)$$

$$V_{\mathrm{eff}} = N_{\mathrm{MOT}}^* N_{\mathrm{MT}} \left(\int_V n_e(\vec{r})n_d(\vec{r})\mathrm{d}V\right)^{-1}, \qquad (6.4)$$

$$V_{\mathrm{MT}} = N_{\mathrm{MT}}^2 \left(\int_V n_d^2(\vec{r})\mathrm{d}V\right)^{-1}. \qquad (6.5)$$

Here we have introduced the loss rate γ_{ed} for collisions between MOT and MT atoms to emphasize that this process is effectively a single-atom loss for magnetically trapped atoms. In these equations, the density of atoms in the MT and in the excited state of the MOT is given by $n_d(\vec{r})$ and $n_e(\vec{r})$, respectively. The size of the effective volume V_{eff} is dominated by the larger of the two volumes V_{MOT} and V_{MT} for the magneto-optical and magnetic trap, respectively. In our experiments with chromium, we find $V_{\mathrm{MOT}} \ll V_{\mathrm{MT}}$, so we can approximate the effective volume with the volume of the CLIP trap $V_{\mathrm{eff}} \approx V_{\mathrm{MT}}$. Then, the steady state solution of Equation 6.2 is given by

$$N_{\mathrm{MT}}^{\infty} = \frac{-(\gamma_d + \gamma_{ed})V_{\mathrm{MT}} + \sqrt{(\gamma_d + \gamma_{ed})^2 V_{\mathrm{MT}}^2 + 8\beta_{dd} R V_{\mathrm{MT}}}}{2\beta_{dd}} \qquad (6.6)$$

Neglecting background gas collisions ($\gamma_d = 0$) and assuming saturation for the MOT transition ($N_{\mathrm{MOT}}^* \approx N_{\mathrm{MOT}}/2$), Equation 6.6 together with Equation 6.3 can be rewritten as an accumulation efficiency κ:

$$\kappa := \frac{N_{\mathrm{MT}}^{\infty}}{N_{\mathrm{MOT}}} = \frac{-\beta_{ed} + \sqrt{\beta_{ed}^2 + 16\beta_{dd} R V_{\mathrm{MT}}/N_{\mathrm{MOT}}^2}}{4\beta_{dd}}. \qquad (6.7)$$

This equation allows an estimate of the number of atoms in the CLIP trap given the number of atoms in the MOT, N_{MOT}, and the inelastic collision properties

[1] Each inelastic collision event removes two atoms from the trap. Therefore the loss rate in the differential equation for the number of atoms in the trap is twice the inelastic collision rate.

β_{ed} and β_{dd}. The inelastic processes limit the achievable density in the magnetic trap (Equation 6.2) and therefore the number of accumulated atoms. Increasing the magnetic trapping volume therefore leads to accumulation of more atoms. This is one of the main advantages of using the Ioffe-Pritchard trap over a 3D-quadrupole trap: independent control of the trapping field parameters in radial and axial direction allows increasing the magnetic trapping volume without degradation of the MOT performance.

After loading the CLIP trap and switching off the MOT, the atoms are still subject to a non-exponential decay given by the inelastic collisions between atoms in the $|\,d\,\rangle$ state. The evolution of the number of atoms can be derived from Equation 6.2 by setting $R = 0$ and $\gamma_{ed} = 0$:

$$N_{\mathrm{MT}}(t) = N_{\mathrm{MT}}^{\infty} \frac{\gamma_d e^{-\gamma_d t}}{\gamma_d + N_{\mathrm{MT}}^{\infty}(1 - e^{-\gamma_d t})\frac{\beta_{dd}}{V_{\mathrm{MT}}}}. \tag{6.8}$$

This equation can be used to independently determine the two-body loss coefficient β_{dd} by measuring the number of atoms and the volume of the cloud for different holding times in the metastable $|\,d\,\rangle$ state.

6.3.2 Temperature

The temperature of the atoms in the magnetic trap is determined by the initial temperature in the MOT (T_{MOT}) and the shape of the trapping potentials [78, 121]. Assuming the MOT to be much smaller than the MT, loading occurs at the center of the magnetic trap where the atoms have only kinetic but no potential energy. In the new trapping potential the initial kinetic energy is distributed between the final kinetic and potential energy according to the Virial theorem. The trapping potential in the CLIP trap is harmonic in axial and linear in radial direction, whereas the MOT is approximately harmonic in all three dimensions. Using the relation $V_f^z = E_f^z$ for the final potential and kinetic energy in z-direction, respectively, and $V_f^r = 2E_f^r$ for the radial direction, we have

$$\frac{3}{2}k_B T_{\mathrm{MOT}} = E_f^z + V_f^z + 2(E_f^r + V_f^r) = \frac{8}{3}E_f = \frac{8}{3}\frac{3}{2}k_B T_{\mathrm{MT}},$$

where E_f is the thermalized kinetic energy in the magnetic trap. Therefore, in an ideal situation, one would expect the atoms in the CLIP trap to have a temperature of $T_{\mathrm{MT}} = \frac{3}{8}T_{\mathrm{MOT}} \approx 0.4 \times T_{\mathrm{MOT}}$. In reality, additional heating increases the temperature. One source of heating is misalignment between MOT and MT due to an imbalance in laser beam intensities. Inelastic processes like dipolar relaxation collisions (see Appendix E) and fine-structure changing collisions can also contribute to heating in the MT.

It is worthwhile mentioning, that it is in fact advantageous to have the atoms in the MT not too cold if a maximum number of atoms is desired, since a hot cloud is less dense and thus allows trapping of more atoms in the presence of density limiting inelastic losses as discussed in the previous section.

6.4 Experimental techniques and data evaluation

A typical experimental sequence starts with loading the CLIP trap from the MOT at a radial gradient of 13 G/cm, an axial curvature of 11 G/cm^2 and an offset field close to zero. After 10 s loading, MOT and Zeeman-Slower lasers are switched off and the repumping laser is switched on for 20 ms to transfer the atoms to the ground state. The magnetic trapping fields are switched off rapidly (< 300 μs) 11 ms after repumping and - in case of absorption imaging - a homogeneous magnetic support field along the imaging axis is switched on. We either image the cloud a few hundred microseconds after switching off the trapping field to obtain the density distribution of the atoms in the trap or after a variable time-of-flight to obtain the temperature.

We probe the atoms using fluorescence and absorption imaging (see Section 5.5) on the strong $|\,g\,\rangle \leftrightarrow |\,e\,\rangle$ transition. After loading, magnetically trapped atoms in the metastable $|\,d\,\rangle$ state are optically pumped to the ground state with the repumping laser. Temperature, shape and Zeeman substate of the polarized atoms are not significantly changed during repumping since only two photons are scattered by every transferred atom and the involved states $^7S_3$ and $^5D_4$ have the same magnetic moment of 6 μ_B. The density profile of the atomic cloud is recorded with a calibrated CCD camera and fitted with the appropriate density distribution assuming thermal equilibrium. For the magneto-optical trap the density distribution is given by a Gaussian with $1/\sqrt{e}$ radius $\sigma_x = \sigma_y$ and σ_z in radial and axial direction, respectively. The density in the magnetic trap is given by a Gaussian distribution in axial (characterized by the $1/\sqrt{e}$ size σ_z^{MT}) and an exponential distribution in radial direction which is modified by gravity along the y-axis (see Equations 4.17 and 4.18). From the fit we extract the volume of the cloud. Typical sizes of the MOT are $\sigma_z \approx 1.3$ mm, $\sigma_{x,y} \approx 0.1$ mm and for the magnetic trap $\sigma_z^{\mathrm{MT}} \approx 2$ mm, $\xi_1 \approx 0.5$ mm and $\xi_2 \approx 1.2$ mm. All measured sizes are well beyond the 20 μm resolution limit of our imaging system. The number of atoms is determined from the integrated fluorescence or absorption recorded by the calibrated CCD camera. The atomic density is then given by the ratio of the number of atoms and the fitted volume.

We assume a polarized sample of atoms in the $m_J = +3$ magnetic substate throughout this Chapter. We have experimentally verified that this assumption is valid by comparing the fitted size of the cloud with the size derived from the known trapping potential and the temperature. The sizes were compatible with a projection of the magnetic moment of $6 \pm 10\%$ μ_B.

Laser beam intensities for the plot in Figure 6.2 are obtained from a measurement of the light power passing through a 1 mm diameter circular aperture with a calibrated photo diode. The loading rate into the magnetic trap has been determined from a measurement in which we loaded the trap for a variable time and recorded the number of atoms accumulated during that time. A linear fit to data up to a loading time of 250 ms yields the loading rate R. We introduce an effective loading time $\tau = N_{\mathrm{MT}}/R$ as a measure for the losses from the trap. Strictly speaking, this definition is only valid for a single-particle loss process. Nevertheless $1/\tau$ is a qualitative measure of the trap loss. More accurately, Equation 6.6 should be used. We measured the temperature of the atomic ensemble by a time-of-flight measurement. In this case, we also fitted the atoms released from the magnetic trap with a gaussian density distribution which gave good results after a few ms time-of-flight.

6.5 Performance of the CLIP trap

In this Section, we present measurements on the temperature and the accumulated number of atoms in the CLIP trap. We compare our experimental results with the model presented in Section 6.3 and give improved numbers for the relevant collisional properties.

6.5.1 Temperature

We have measured the temperature of the magneto-optical and magnetic trap for different light-shift parameters ${}^{(I/I_{\mathrm{sat}})}/_{(|\delta|/\Gamma_{eg})}$, where I is the sum of all six laser beam intensities. We expect a linear increase in the temperature of the MOT with increasing light-shift parameter [142, 143]. In Figure 6.2 we have plotted the radial temperature of the atoms in the MOT and in the CLIP trap. For very low scattering rates at low light-shift parameters, the temperature increases again, since cooling breaks down (not shown). Linear fits to the high temperature tails give slopes of 22 ± 2 and $10 \pm 1 \mu\mathrm{K} \times \Gamma_{eg}/I_{\mathrm{sat}}$ for the MOT and the MT, respectively. The value of 0.46 for the ratio of these slopes is in qualitative agreement with the prediction of 1/3 for the radial temperature from our model as descibed in Section 6.3.2. At very low temperature the measured temperatures fail our model, which is manifested in the intesection of the fitted lines at ${}^{I}/_{|\delta|} > 0$. Possible systematic errors include uncertainties in the laser beam intensity and detuning. Especially at low temperatures, off-center loading of the MT and the finite size of the MOT increase the temperature achieved in the magnetic trap. Furthermore, perfect overlap of MOT and MT is hard to maintain when changing the light force on the atoms by almost an order of magnitude. Additional heating arises from the exothermic two-body loss process limiting the number of accumulated atoms as described in Section 6.3.1.

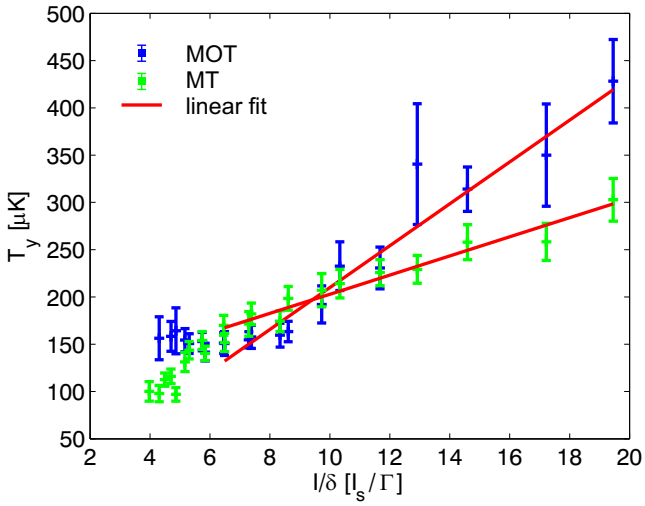

Figure 6.2: Radial temperature of the atoms in the MOT (blue markers) and the CLIP trap (green markers) versus the light-shift parameter. A linear fit (red lines) to the high temperature tails gives a slope of 22 ± 2 and $10 \pm 1\,\mu\mathrm{K} \times \Gamma_{eg}/I_{\mathrm{sat}}$ for the MOT and MT temperature, respectively.

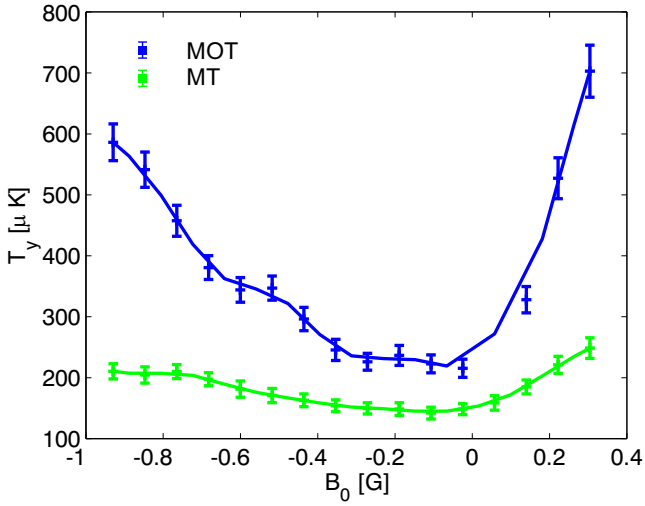

Figure 6.3: Radial temperature of the atoms in the MOT (blue) and MT (green) for different axial magnetic offset fields. The lines are 2-point moving averages to guide the eye.

One of the major advantages of the Ioffe-Pritchard trap over a 3D-quadrupole trap is the finite offset field at the center of the trap, preventing atom loss due to Majorana spin-flips for cold atomic clouds. For the radial trapping parameters in the CLIP trap, an offset field as low as 40 mG reduces the spin-flip rate to below 0.1 1/s (see Section 4.2.4). We observed lifetimes in the $^7S_3$ state of more than 25 s in the CLIP trap even for negative offset fields. Although we are not limited by Majorana spin-flips while loading the CLIP trap, a small positive offset field prevents atom loss during the subsequent compression of the Ioffe-Pritchard trap.

The influence of an axial magnetic field consisting of the small offset field and the curvature field of the magnetic trap on the cooling performance in the MOT is an important aspect [144, 145, 146]. In Figure 6.3 we measured the radial temperature of the MOT and the MT for different axial magnetic offset field strengths. As expected, we observe a temperature minimum around zero magnetic offset field. The number of atoms in the MOT is constant over the range of magnetic fields shown in Figure 6.3. For negative offset fields, the MOT temperature increases only at large magnetic fields, whereas positive offset fields lead to a strong degradation of the cooling efficiency of the MOT. For optimum performance, a magnetic field strength approaching zero results in a temperature close to the minimum achieveable temperature in the MOT, while at the same time preventing Majorana spin-flip losses during subsequent compression of the trap.

In summary, we observed a minimum temperature of 140 μK in the magneto-optical and 100 μK in the magnetic trap for low MOT light intensities and large detunings. An axial offset field close to zero does not degrade the MOT performance. We optimized the loading of our CLIP trap to achieve a maximum number of accumulated atoms at the cost of minimal temperature, thus operating the MOT at high laser light intensities and a detuning of -2Γ. Subsequent repumping to the $^7S_3$ ground state and compression of the IP trap is followed by a Doppler cooling stage which results in a temperature close to the Doppler temperature independent of the initial temperature (see Chapter 7). Using this preparation scheme, the figure of merit for loading the CLIP trap is reduced to the number of atoms, thus greatly simplifying adjustment and daily operation.

6.5.2 Number of atoms

In this section, we present experimental results on the number of atoms accumulated in the CLIP trap as a function of the trap parameters. We show that the steady state number of atoms is very robust against moderate magnetic field variations and demonstrate the advantages of using a Ioffe-Pritchard trap instead of a 3D-quadrupole trap. By determining independently the loading rate into the CLIP trap and the number of trapped atoms in the MOT and the MT, we are able to explain our findings qualitatively. A fit of the model developed in Section 6.3.1

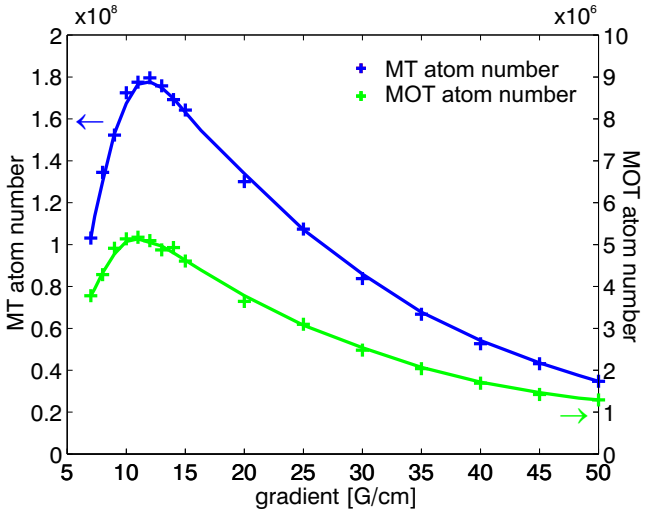

Figure 6.4: Steady state number of atoms in the MOT (blue) and in the CLIP trap (green) for different radial magnetic field gradients. The lines are 3-point moving averages of the data to guide the eye. Note the different scale for the number of atoms in the MOT and in the MT.

to the experimental data results in a more accurate determination of the collision parameters responsible for trap loss than previously reported [121].

In Figure 6.4, we have plotted the number of atoms in the MOT and the steady state number of atoms accumulated in the CLIP trap for various radial field gradients while keeping all other trapping parameters at their optimum values. The measured volume of the magnetic trap decreases almost linearly with increasing gradient from 14×10^{-3} cm^3 to 4×10^{-3} cm^3. Due to an unusually high inelastic excited state collision rate for chromium with a loss coefficient on the order of 10^{-9} cm^3/s [78, 127], the number of atoms in the MOT is density limited to around 5×10^6. The number of atoms in the MT exhibits a maximum around 13 G/cm. To either side, a decrease in atom number coincides with a reduced MOT performance and thus a reduced loading rate (see Equation 6.1). This situation is comparable to changing the gradient of a 3D-quadrupole trap [121]: both, magnetic and magneto-optical trap are affected by a change in gradient. This can be seen more clearly in the loading rate and time measurement presented in Figure 6.5. The loading rate closely follows the number of atoms in the MOT for high gradients and decreases even more steeply for low gradients. This behaviour is an indication for a degradation in loading efficiency due to position mismatch between MOT and MT. The inverse of the effective loading time τ, which takes into account inelastic collisions, is a measure for the loss rate from the magnetic trap (see Section 6.4). Therefore the observed increase in effective loading time for low gradients in Figure 6.5 resembles a decreased loss from the CLIP

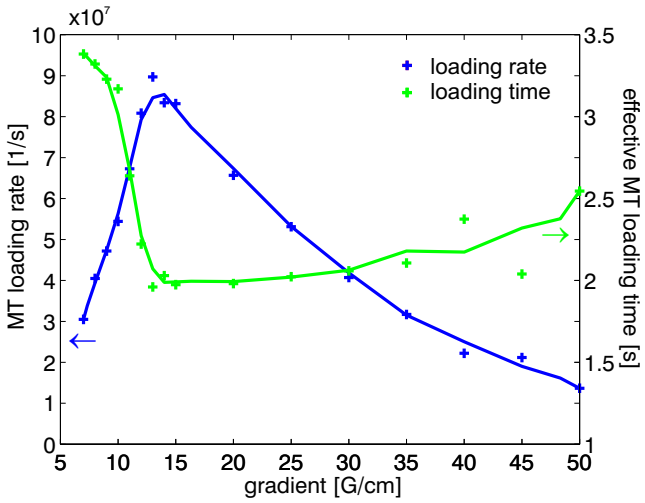

Figure 6.5: Loading rate into the CLIP trap (blue) and effective loading time (green) for different radial magnetic field gradients. The lines are 3-point moving averages of the data to guide the eye.

trap originating from a reduced number of atoms in the MOT and an increase of the trapping volume (see Equations 6.2 and 6.3).

For high gradient fields, we observe a small rise in the effective loading time. At this point the number of atoms in the magnetic trap decreases faster than the trapping volume, thus the density in the CLIP trap decreases. This leads to a slight reduction in the inelastic loss rates and therefore an increase in loading time.

The situation shown in Figures 6.6 and 6.7 is different. Here, we have changed the axial curvature and recorded the number of atoms in the MOT and the CLIP trap as well as the effective loading time and rate. The volume of the magnetic trap is approximately inversely proportional to the applied curvature field, ranging from 14×10^{-3} to 3.9×10^{-3} cm^3 thus covering essentially the same range as for the gradient measurements. For comparison, we have marked in Figure 6.6 the equivalent curvature of a typical 3D-quadrupole trap having a volume corresponding to the volume in the CLIP trap. Whereas in Figure 6.4 the MOT performance is strongly affected by the radial gradient, in Figure 6.6 only a weak dependence of the number of atoms in the MOT on the curvature field is observed (note that the vertical axis scales in both Figures are identical). Consequently, the loading rate in Figure 6.7 is also constant to within 30 %. In this situation, the number of atoms accumulated in the CLIP trap is limited mainly by inelastic loss processes. This becomes evident from the decrease in the effective loading time (i.e. the increase in loss) in the high curvature regime shown in Figure 6.7. At very low curvatures, reduced axial confinement, apparent in the reduced effective loading time, and probably misalignment

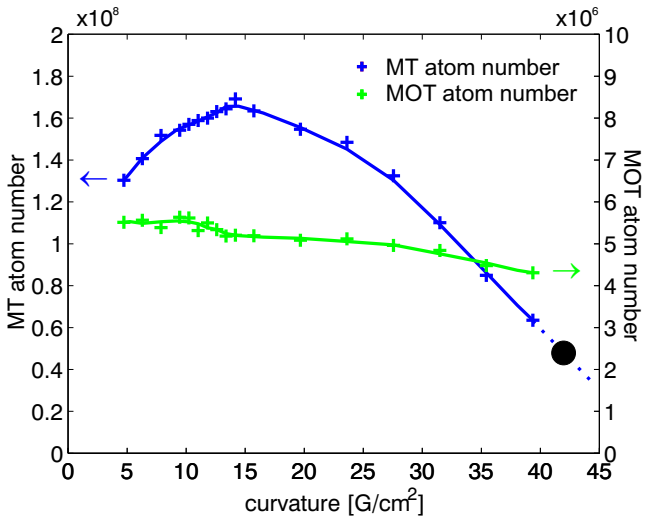

Figure 6.6: Steady state number of atoms in the MOT (blue) and in the CLIP trap (green) for different axial magnetic field curvatures. The filled black circle shows a typical 3D-quadrupole trap having a volume that corresponds to the volume of an IP trap with the indicated curvature. The lines are 3-point moving averages of the data to guide the eye. Note that the vertical scales are identical to Figure 6.4.

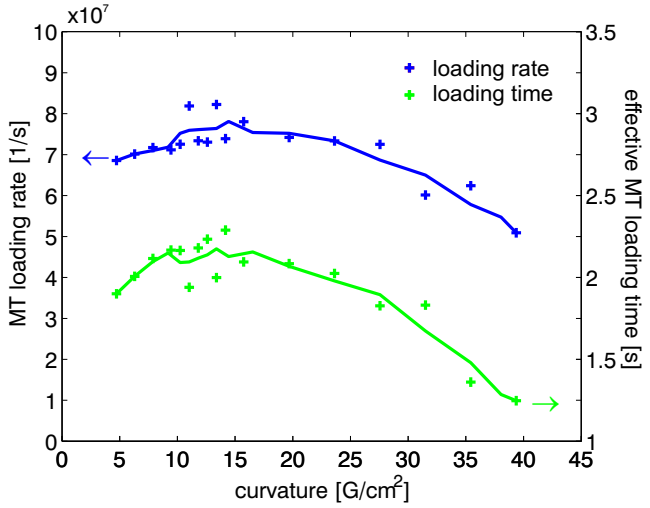

Figure 6.7: Loading rate into the CLIP trap (blue) and effective loading time (red) for different axial magnetic field curvatures. The lines are 3-point moving averages of the data to guide the eye. Note that the vertical scales are identical to Figure 6.5.

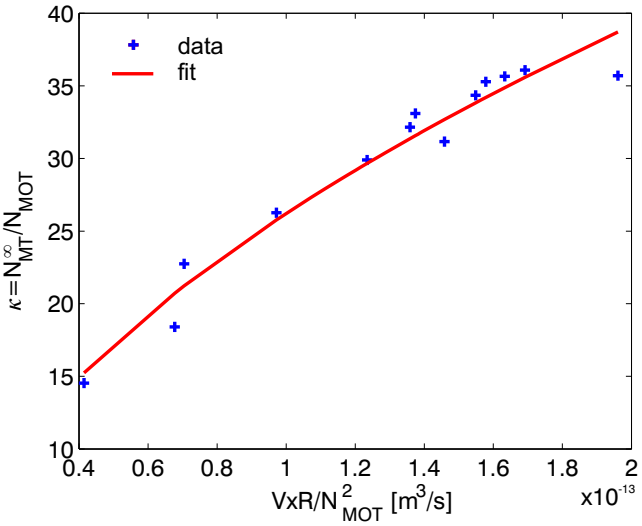

Figure 6.8: Accumulation efficiency into the CLIP trap versus transfer rate divided by the density of excited MOT atoms. The line is a least squares fit to the data.

between MOT and MT, noticeable in a slightly reduced loading rate, are responsible for a lower number of atoms in the CLIP trap. More accurate alignment of the MOT at low curvature fields should allow a constant loading rate at its maximum value even at low curvature fields. Such a configuration would be useful for continuous loading of a magnetic waveguide.

We achieved a maximum number of 2×10^8 atoms in the CLIP trap at a loading rate of 10^8 atoms/s for optimum trapping parameters of $B' = 12.5$ G/cm for the radial gradient, $B'' = 10.5$ G/cm^2 for the axial curvature and an axial offset field close to zero. This is about three times the number of atoms trapped previously in a 3D-quadrupole trap under comparable loading conditions.

The data presented in Figures 6.5 and 6.7 indicates that the effective loading time is limited to around 2 s due to inelastic collisions. We have determined the magnitude of the two major loss mechanisms by fitting the simplified rate equation model from Equation 6.7 to the gradient and curvature data from Figures 6.4 and 6.6. The result is shown in Figure 6.8, where we have plotted the accumulation efficiency $\kappa = N_{\mathrm{MT}}/N_{\mathrm{MOT}}$ versus $RV_{\mathrm{MT}}/N^2_{\mathrm{MOT}}$. The line is a least squares fit of Equation 6.7 to the data with β_{dd} and β_{ed} as fitting parameters. For the fit we have neglected the low gradient and curvature data points in which other loss mechanisms dominate. Since both loss rates scale with the volume of the magnetic trap, the fitting parameters are strongly correlated resulting in the large statistical uncertainty for each parameter. We obtain $\beta_{ed} = 6 \times 10^{-10} \pm 45$ % cm^3/s for inelastic collisions between MOT atoms in the excited state and magnetically trapped atoms and

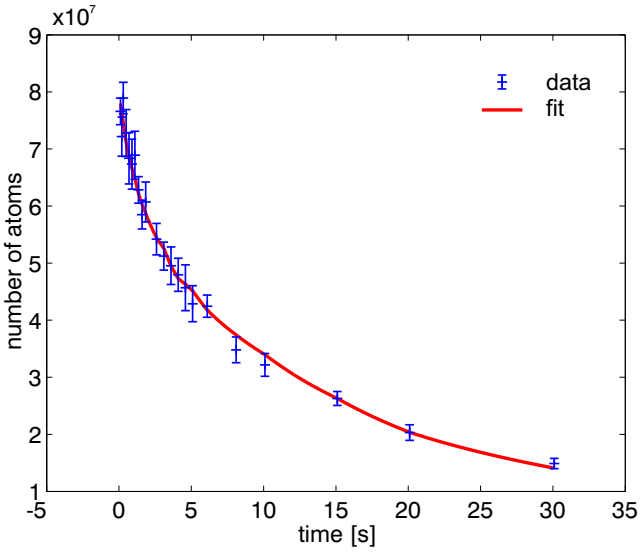

Figure 6.9: Number of atoms remaining in the CLIP trap after a certain holding time. The fit of Equation 6.8 with $\gamma_{ed} = 0$ to the data yields a two-body loss coefficient of $\beta_{dd} = 3.8 \times 10^{-11} \pm 10$ % cm^3/s.

$\beta_{dd} = 1.3 \times 10^{-11} \pm 17$ % cm^3/s for inelastic collisions between atoms in the CLIP trap. The two inelastic processes lead to loss rates of the same order of magnitude in Equation 6.2. Systematic errors, mainly from the determination of the densities, reduce the accuracy of the given values to within a factor of 2. These more accurate results improve the order of magnitude rates reported previously [121]. An independent measurement of β_{dd} was performed by observing the decay of magnetically trapped atoms in the ^{5}D$_4$ state and fitting the evolution of the number of atoms given by Equation 6.8 under single- and two-atom loss processes to the data. We have included the volume of the cloud for each data point in the fit function, since the volume increases during the measurement due to heating by the exoergodic inelastic collision process and selective removal of the coldest atoms near the center of the cloud. The single-body loss rate γ_d is dominated by collisions with the fast chromium atoms in our atomic beam. It was determined in a seperate measurement to approximately 30 s. The experimental situation in the decay measurement is different from the accumulation measurement, where only the steady state atom number is recorded. Other processes not included in our model, like e.g. dipolar relaxation (see Appendix E) and variations in temperature and magnetic substate distribution of the cloud during the decay process make a comparison difficult. Nevertheless, the obtained value of $\beta_{dd} = 3.8 \times 10^{-11} \pm 10$ % cm^3/s is close to the value from the fit to the accumulation efficiency.

6.6 Conclusion

We have presented a continuous optical loading scheme for ultracold atoms from a magneto-optical trap into a Ioffe-Pritchard magnetic trap. We achieved temperatures below 100 μK, a loading rate of up to 10^8 atoms/s and 2×10^8 atoms accumulated in the magnetic trap in our implementation for chromium atoms. The loading rate is limited by the small number of atoms trappable in a chromium MOT [78, 127] and the small decay rate Γ_{ed} into the metastable trap state. We plan to increase the loading rate by optically pumping the atoms via another fine structure level of the excited state that has a higher decay rate into the trap state. Two major loss mechanisms limit the number of atoms in the magnetic trap: inelastic collisions among excited state atoms in the MOT and magnetically trapped atoms and inelastic collisions between atoms in the magnetic trap [121]. We have presented a model for the steady state number of atoms in the magnetic trap that is in good agreement with our experimental data. From a fit of the model to the data we could determine the loss rates for the two inelastic density limiting processes to be $\beta_{ed} = 6 \times 10^{-10} \pm 45$ % cm^3/s and $\beta_{dd} = 1.3 \times 10^{-11} \pm 17$ % cm^3/s for collisions between MOT and MT atoms and between MT atoms, respectively. Independent control of the radial and axial trapping fields in the Ioffe-Pritchard trap allowed us to accumulate more atoms in the MT by increasing the volume of the trap without losing confinement or deteriorating MOT performance. The inelastic loss in the metastable trap state in chromium requires repumping the atoms to the ground state for subsequent experiments.

We use the CLIP trap loading scheme as a starting point for further cooling sequences which will be discussed in the following Chapters.

Our experiments at low axial confinement (Figures 6.6, 6.7) show that continuous loading of a magnetic waveguide should be possible. In that case, slightly tilting the trap would allow the atoms to escape the trapping region resulting in a continuous flux exceeding 10^8 magnetically trapped ultracold atoms per second in the case of chromium.

Another possibility of accumulating orders of magnitudes more atoms would be to extend the Ioffe-Pritchard configuration. For example the combination of a tilted magnetic waveguide with magnetic or optical endcaps could serve as a large volume accumulation reservoir and prolong the loading time[2]

The continuously loaded Ioffe-Pritchard trap presented here is not limited to chromium. Atoms like e.g. the earth alkalis and ytterbium with a large natural

[2]Such a reservoir could be loaded until the atoms return to the loading position due to the conservative character of the guiding potentials. However, the available loading time can be increased by employing anharmonic guiding potentials where pseudo-chaotic motion and anharmonic mixing can significantly increase the return time of the atoms.

linewidth allow high gradients for operating the MOT, thus enabling magnetic trapping at the same time. Besides this feature, the earth alkalis have a level structure which is especially well suited for the continuous loading scheme presented here or variations of it [126].

Chapter 7

Doppler cooling of an optically dense cloud of magnetically trapped atoms

Doppler cooling of magnetically trapped atoms is used to further increase the phase-space density of our atomic ensemble. In contrast to previous experiments [147, 148, 149], we observe efficient cooling in all three dimensions by applying a one dimensional optical molasses. Our findings can be quantitatively explained by taking into account the cooling effects of reabsorbed photons. In Section 7.2, I present and discuss a theoretical model for Doppler cooling in a magnetic trap in the presence of reabsorption. Experimental results on the dynamics and steady state properties of the cooling process are presented in Section 7.4. I conclude with a discussion of our results in Section 7.5. Excerpts of this chapter have been published in [150].

7.1 Introduction

Since the advent of laser cooling of neutral atoms more than 20 years ago, this method has been extensively studied [90] and widely used for a variety of atoms and applications. Ultimately, laser cooling followed by evaporative cooling [151] allowed the creation of a Bose–Einstein condensate (BEC) of neutral atoms [123, 152, 153].

In almost all BEC experiments atoms are caught in a magneto–optical trap. After sub-Doppler molasses cooling [154] and polarization of the sample by optical pumping, the atoms are typically transferred into a magnetic trap [123, 152, 153] or, as has been recently demonstrated, into an optical [96] trap. The ensuing evaporative cooling process requires both, a high initial density to provide a reasonably large elastic collision rate, and a large number of atoms, since most atoms are removed

from the trap during evaporation. The figure of merit for efficient evaporative cooling is the initial phase space density of the atomic cloud. Therefore, all laser cooling and polarization steps have to be optimized carefully, to keep the temperature of the atoms low and the number of atoms high, thus maximizing the phase space density in the final trap.

Alternative approaches for reaching high phase space densities include gray molasses [155], 3D Raman sideband cooling in optical lattices [156, 157] and cooling on a spin-forbidden transition close to the recoil limit [91]. Using these techniques, atomic samples with a phase space density close to degeneracy have been loaded into optical dipole traps [97, 158] and ultimately Bose-Einstein condensation of cesium could be achieved [25].

Sub-Doppler cooling schemes for atoms in magnetic traps have been proposed by Pritchard and Ketterle [159] and Newbury *et al.* [160]. In the latter setup very low temperatures of $1.5\,\mu$K corresponding to 4 recoil energies have been achieved in a weak magnetic trap for low atomic densities.

In this Chapter, we present a robust Doppler cooling scheme in an external trap which is applicable to most laser-coolable atomic species. Our scheme is particularly well suited for optically dense samples and reduces the figure of merit for evaporative cooling to the number of atoms transferred into the trap regardless of temperature.

Free-space one-dimensional Doppler cooling is usually performed in a standing wave light field created by two counterpropagating laser beams with a frequency below the atomic transition frequency. Cooling is based on preferential absorption of photons from the laser beam opposing the direction of motion of the atom. Subsequent spontaneous emission is centrally symmetric and does not change the mean momentum of the atom. Doppler cooling of polarized atoms in a magnetic trap has been proposed for atomic hydrogen [161] and experimentally realized for sodium [147], hydrogen [149] and lithium [148]. In Reference [147] one-dimensional Doppler cooling of an optically thin cloud of sodium atoms in a magnetic trap was performed. The atoms were treated as a two level system since a very high magnetic offset field ($B_0 \approx 1\,500\,\mathrm{G}$) spectroscopically resolved the Zeeman substates. Cooling of the motional degrees of freedom orthogonal to the laser beams was provided by anharmonic mixing in the trapping potential. Due to a long mixing time compared to the cooling time, the achieved temperature was ten times the Doppler temperature for sodium. In Reference [149] single-beam pulsed Doppler cooling was performed on a dense sample of magnetically trapped hydrogen atoms. Thermalization of the cloud was accomplished by elastic collisions between the atoms. Cooling was limited to approximately five times the Doppler temperature due to limited laser power and additional heating rates.

The main advantage of the cooling technique presented here is, that it combines three-dimensional temperatures close to the Doppler-limit with the cooling of dense

samples. In our experiment, one-dimensional optical molasses cools the cloud of atoms in the axial direction down to the Doppler limit (see Section 3.2). Cooling in the radial directions, orthogonal to the laser beams, can be explained by reabsorption of spontaneously emitted photons by the optically dense cloud. To our knowledge, reabsorption has so far been treated only as a density-limiting mechanism which comes along with heating of the atomic sample [162, 163, 164, 165, 166, 167, 168]. Here, we focus on the cooling aspects of scattered and reabsorbed photons in a trapped polarized atomic sample.

We show that the atoms in the magnetic trap remain polarized during the cooling process and practically no atoms are lost, provided the magnetic substructure is spectrally resolved. We are able to cool chromium atoms in a magnetic trap from ≈ 1 mK to a mean temperature of 240 μK, corresponding to an increase in phase space density by a factor of 80. We have studied the dynamics of the cooling process as well as the steady state temperature for various cooling parameters. The experimental results can be explained with a simple model based on rate equations for the temperature.

7.2 Theory

7.2.1 Rate Equations

In this section, we present a simple model based on rate equations. Although we assume cooling in a magnetic trap here, the scheme is universal to all kinds of traps, provided cooling is compatible with the trap and the quantization axis of the atoms is independent of the position of the atoms in the trap.

Consider a cloud of spin-polarized atoms with mass m and magnetic moment μ confined in an axially symmetric harmonic magnetic trap with trapping potential $V(x,y,z) = \mu(B_x'' x^2/2 + B_y'' y^2/2 + B_z'' z^2/2 + B_0)$ (see Section 4.2).

$B_x'' = B_y''$ and B_z'' are the magnetic field curvatures in the radial (x, y) and axial (z) direction, respectively, and B_0 is a homogeneous offset field along the axial direction. We assume that the corresponding trap frequencies $\omega_{x,y,z} = \sqrt{\mu B_{x,y,z}''/m}$ are much smaller than the Larmor precession frequency at the center of the trap $\omega_L = \mu B_0/\hbar$, ensuring that the atoms stay spin polarized and no spin flip losses occur [109].

Doppler cooling is performed on an electric dipole transition that couples a long-lived ground state with total angular momentum J to a short-lived excited state with angular momentum J', such that[1] $J' = J + 1$. We also assume the corresponding Landé factors g_J and $g_{J'}$ to have the same sign, which we choose to be positive for

[1] In principle the same argument holds for a $J' = J$ transition for simplicity we will concentrate on the situation above.

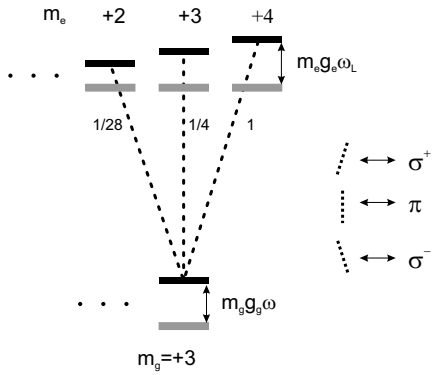

Figure 7.1: Part of the Zeeman substructure of ^{52}Cr as an example of a $J \rightarrow J+1$ transition. See Figure 3.2 for the full substructure. The numbers next to the transitions are the squares of the Clebsch-Gordan coefficients.

our example. The atoms are polarized in the "weak field seeking"state $m_J = J$ and have a magnetic moment of $\mu = m_J g_J \mu_B$, where μ_B is Bohr's magneton.

Cooling is carried out in a σ^+/σ^+-standing wave created by two laser beams propagating along the axial direction with intensity I and detuning δ. For a spin-polarized sample of atoms in a magnetic trap, the quality of the polarization of the cooling light is important. No depolarizing transitions $m_J \rightarrow m_J, m_J - 1$ can occur for perfectly polarized σ^+-light propagating along the quantization axis of the atoms in a homogeneous magnetic field. For imperfect polarization, the cooling light can also drive depolarizing transitions which cause loss of atoms. In the configuration described above, the Zeeman-splitting due to the finite offset field B_0 reduces the scattering rates R_{dep} of unwanted depolarizing transitions with respect to the rate R_{pol} of the cooling transition $m_J \rightarrow m_J + 1$:

$$R_{\mathrm{dep}} = \frac{\Gamma}{2} \frac{2C_3^3 I/I_s}{1 + 4\Delta_{dep}^2/\Gamma^2} \ll \frac{\Gamma}{2} \frac{2C_3^4 I/I_s}{1 + 4\Delta_{pol}^2/\Gamma^2} = R_{\mathrm{pol}}, \tag{7.1}$$

where $\Delta = \Delta_{\mathrm{pol}}$ and Δ_{dep} are the effective detunings between the laser and the atomic transition frequency in a magnetic field and C_i^j is the square of the Clebsch-Gordan coefficient for the transition from state $m_g = i$ to $m_e = j$. In Figure 7.1 this effect is illustrated for the $J = 3 \rightarrow J = 4$ transition that connects the ground state $^7S_3$ to the excited state $^7P_4$ in ^{52}Cr (see Chapter 2 for details). A full treatment of optical pumping in an arbitrary light field, taking into account all excited and ground state levels, gives the steady state population of each ground state for a given magnetic field. Assuming a polarization quality of 1:10, a detuning of $\Delta = -0.5\,\Gamma$ for the polarizing transition and allowing for an atom loss of less than 1% during the cooling process, we find for the case of chromium a necessary offset field of $B_0 \geq 9$ G and for rubidium of $B_0 \geq 12$ G.

Following the common treatment of free-space Doppler cooling as presented in Section 3.2, rate equations for the temporal evolution of the temperature for the axial (z) and radial (y) degrees of freedom are readily obtained:

$$\frac{dT_z}{dt} = \frac{2T_{\rm rec}}{\tau_z^{heat}} - \frac{T_z}{\tau_z^{cool}} \tag{7.2}$$

$$\frac{dT_y}{dt} = \frac{2T_{\rm rec}}{\tau_y^{heat}} - \frac{T_y}{\tau_y^{cool}}, \tag{7.3}$$

where $T_{\rm rec}$ is the recoil energy of the cooling transition with wave number k. Usually, the heating and cooling time constants are derived by considering the random walk in momentum space due to spontaneous emission and the net cooling effect of scattered photons from the two counterpropagating laser beams. In an optically dense sample reabsorption of photons has to be taken into account. Previously, reabsorption has mainly been discussed as a reason for density limitations and density-dependent heating in magneto-optical traps [163, 164, 167] and in the context of sub-recoil cooling [162]. In our model, we emphasize cooling effects of reabsorbed photons which can be substantial for polarized atoms confined in an external trapping potential.

We show in Appendix A.1, that the photon energy after a scattering event in the low intensity limit is only slightly shifted. Therefore scattered photons have essentially the same detuning as the cooling laser beams. The emission pattern of σ^+ polarized light with respect to the quantization axis is proportional to $(1+\cos^2\vartheta)^2$, as derived in Appendix A.2. For our calculations, we use the axial direction parallel to the laser beam as our quantization axis. The contribution of the reabsorbed photons to cooling of the radial and axial directions depends on the projection of their wave vector $\vec{k}$ onto these directions. The effective intensity $I_{z,y}^{\rm eff}$ of the cooling photons is proportional to the incident laser light intensity $2I$ with a proportionality factor $\kappa_{z,y}$ which primarily depends on the optical density $OD_{z,y}$ in these directions:

$$I_{z,y}^{\rm eff} = 2I \times \kappa_{z,y} \sim 2I \times \kappa_{z,y}^{*} \times OD_{z,y} \tag{7.4}$$

To simplifiy the calculations, we assume only a single scattering/reabsorption process. The coefficients κ are then obtained by averaging the intensity scattered by a volume element dV_0 over the normalized density distribution, taking into account absorption of the incident light, the projection of the k-vectors onto the direction of interest and the angular dependence of the σ^+ polarized fraction of the emitted light. We derive in Appendix B the following expressions for the coefficients:

$$\kappa_y = \int_V dV_0 \int_V \sin^2\vartheta \, dr \, d\vartheta \, d\phi \; \kappa_0(\vec{r}_0, r, \vartheta, \phi) \, |\sin\phi| \tag{7.5}$$

$$\kappa_z = \int_V dV_0 \int_V \sin\vartheta \, dr \, d\vartheta \, d\phi \; \kappa_0(\vec{r}_0, r, \vartheta, \phi) \, |\cos\vartheta|, \tag{7.6}$$

with

$$\kappa_0(\vec{r}_0, r, \vartheta, \phi) = \frac{3\,P_{\rm sc}(\vec{r}_0)}{32\pi I_0}(1+\cos^2\vartheta)^2\, n(\vec{r}_0)\, n(\vec{r}_0, r, \vartheta, \phi). \tag{7.7}$$

Here, $P_{\rm sc}(\vec{r}_0)$ is the light power scattered by an atom at position $\vec{r}_0$ in the cloud, $n(\vec{r}_0)$ the atomic density distribution and $n(\vec{r}_0, r, \vartheta, \phi)$ the density distribution in spherical coordinates relative to $\vec{r}_0$.

In a simple picture, $\kappa_{z,y}$ can be interpreted as the effective number of photons that contribute to cooling in the corresponding directions originating from a single photon absorbed from the laser light. The total number of reabsorption/emission cycles for an incident photon is given by

$$\kappa = \int_V dV_0 \int_V \sin\vartheta\, dr\, d\vartheta\, d\phi\ \kappa_0(\vec{r}_0, r, \vartheta, \phi). \tag{7.8}$$

For the derivation of these quantities, we have assumed the incident laser light intensity to be constant across the cloud of atoms. Absorption of photons creates an intensity gradient across the cloud which is included in the expression for the scattered power.

If the effects of reabsorbed photons are included the cooling rates become

$$\frac{1}{\tau_z^{cool}} = -\Gamma\frac{32(1+\kappa_z)2\,(I/I_s)\,\Delta/\Gamma}{(1+4\Delta^2/\Gamma^2)^2}\frac{k_{\rm B}T_{\rm rec}}{\hbar\Gamma} \tag{7.9}$$

$$\frac{1}{\tau_y^{cool}} = -\Gamma\frac{32\kappa_y 2\,(I/I_s)\,\Delta/\Gamma}{(1+4\Delta^2/\Gamma^2)^2}\frac{k_{\rm B}T_{\rm rec}}{\hbar\Gamma}. \tag{7.10}$$

In the axial and radial direction the total cooling light intensity reads $I_z^{\rm tot} = 2I + I_z^{\rm eff} = 2I(1+\kappa_z)$ and $I_y^{\rm tot} = I_y^{\rm eff} = 2I\kappa_y$, respectively.

For the derivation of the heating rates, we have to take into account directed reabsorption of $\kappa_{z,y}$ photons and spontaneous emission of $(\kappa+1)$ photons for each photon absorbed from the cooling laser beams:

$$\frac{1}{\tau_z^{heat}} = [(1+\kappa_z) + \frac{2}{5}(1+\kappa)]\frac{2I/I_s}{1+4\Delta^2/\Gamma^2}\Gamma \tag{7.11}$$

$$\frac{1}{\tau_y^{heat}} = [\kappa_y + \frac{3}{10}(1+\kappa)]\frac{2I/I_s}{1+4\Delta^2/\Gamma^2}\Gamma \tag{7.12}$$

The first term on the right hand side of Equation 7.11 accounts for the first absorption of a photon from the laser beams (1) and the subsequent reabsorptions in z direction (κ_z). The second term corresponds to the contribution of the first ($2/5$) photon to heating in z direction according to the emission pattern of σ^+ polarized light and all subsequent emissions from reabsorbed photons ($2/5\kappa$). In the heating

rate in the y direction (Equation 7.12), the first absorption momentum kick is absent and the radiation pattern of emitted photons has a statistical weight of $3/10$ instead of $2/5$.

In this model we have neglected additional loss and heating processes, like e.g. radiative escape [169] and radiation trapping [167]. The influence of these additional effects will be discussed in the experimental part of this Chapter.

7.2.2 Discussion of the Model

Steady State

For simplicity we assume the coefficients $\kappa_{z,y}$ to be time independent. This is justified for the evaluation of the steady state parameters of the cooling process. The dynamics of the cooling process can be described only qualitatively within this model, since the optical density will change during cooling and therefore the number of reabsorbed photons increases.

The steady state temperatures are readily derived from Equations 7.2, 7.3 to be

$$T_z^\infty = 2T_{\mathrm{rec}}\frac{\tau_z^{cool}}{\tau_z^{heat}} = \frac{1+\kappa_z+\frac{2}{5}(1+\kappa)}{1+\kappa_z}\frac{T_D}{2} \tag{7.13}$$

$$T_y^\infty = 2T_{\mathrm{rec}}\frac{\tau_y^{cool}}{\tau_y^{heat}} = \frac{\kappa_y+\frac{3}{10}(1+\kappa)}{\kappa_y}\frac{T_D}{2}, \tag{7.14}$$

where T_D is the Doppler temperature defined by Equation 3.19. These minimum temperatures are found at a detuning of $\Delta = -1/2$, in agreement with free space Doppler cooling [90]. It is worthwhile to mention that in this configuration in absence of reabsorption (i.e. $\kappa_{z,y} = \kappa = 0$) the 1D temperature in the axial direction

$$T_z^{\min} = \frac{7}{10}T_D \tag{7.15}$$

is smaller than what is usually called the 1D Doppler temperature. The reason is easily seen: in the 1D model photons can be absorbed and emitted only along the axial direction. In a 3D model with 1D cooling, photons can be emitted into the radial degrees of freedom according to the dipole radiation pattern. These degrees of freedom take up photon recoil heating and therefore reduce the heating rate in the axial direction. In this situation the radial energy grows without limit.

If we now include reabsorption, the situation changes. Whereas reabsorption only in the axial direction ($\kappa_z > 0$) changes the cooling rate but not the steady state temperature, reabsorption in the radial direction ($\kappa_y > 0$) provides a cooling effect, that establishes a radial steady state temperature (Equation 7.14). The magnitude of this temperature is determined by the ratio of heating to cooling photons.

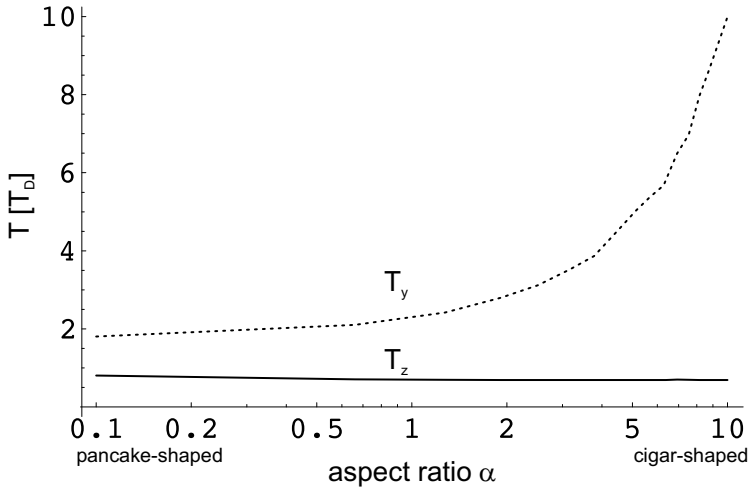

Figure 7.2: Temperatures in the axial (z) and radial (y) direction as a function of trap aspect ratio for $N = 10^8$ atoms and a peak density of $n_0 = 5 \times 10^{10}$ cm^{-3}.

Experimentally, it is not possible to independently change κ_y, κ_z and κ. They depend via Equations 7.6 and 7.8 on the shape of the trapped cloud. In Figure 7.2 we show an example, where we have integrated these equations for different aspect ratios $\alpha = \sigma_z/\sigma_y$ to calculate the steady state temperatures. The aspect ratio has no influence on the axial temperature, since cooling is dominated by photons scattered directly from the laser beams. Most photons are scattered close to the surface of an optically dense cloud. Therefore, we observe a decreasing temperature towards a pancake-shaped cloud for which more photons are scattered and reabsorbed in radial direction than for a cigar-shaped cloud. Doppler temperature in all directions could be achieved with a larger number of atoms in the trap. The ultimate phase-space density attainable in such a system depends on the Doppler temperature and the inelastic collisional properties of the atomic species used. In laser cooling experiments, the highest reachable densities correspond to the cubed inverse transition wavelength, i.e. $10^{12} \ldots 10^{13}$ cm^3.

Dynamics

The transient evolution of the temperature in the radial and axial direction can be approximated by the well known solution of Equations 7.2, 7.3:

$$T_{z,y}(t) = T^{\infty}_{z,y} + (T^{0}_{z,y} - T^{\infty}_{z,y}) \exp(-\frac{t}{\tau^{cool}_{z,y}}) \tag{7.16}$$

where $T^0_{z,y}$ are the initial temperatures of the cloud in the axial and radial direction. Depending on the initial temperatures and the steady state temperatures Equations

7.13, 7.14, either Doppler cooling ($T^{\infty}_{z,y} < T^{0}_{z,y}$) or Doppler heating ($T^{\infty}_{z,y} > T^{0}_{z,y}$) occurs. However, since the atoms are oscillating in a harmonic trap, cooling preferentially occurs close to the trap minimum where the velocity of the atoms is highest. Therefore the cooling rates can not be higher than approximately one quarter of the trap oscillation period $t_{z,y}$.

According to Equations 7.9, 7.10 the time constants τ_z^{cool}, τ_y^{cool} depend on the number of scattered cooling photons. This can provide a test for the reabsorption model. If cooling in the radial direction originated from elastic scattering [149] or anharmonic mixing by the trapping potential [147], one would expect an intensity independent relaxation towards an equilibrium temperature, provided $\tau_z^{cool} \ll \tau_y^{cool}$, while our model explicitly requires an intensity dependence of τ_y^{cool}

We have already mentioned in the previous section that the effective intensity of reabsorbed photons will change during the cooling process. We will now discuss the dynamical effects on the relevant parameters $\kappa_{z,y}$. From Figure 7.2 and Equation 7.13 we deduce a weak dependence of the axial steady state temperature on reabsorbed photons. In this regime cooling in the axial direction is dominated by the real laser beams and we can assume T_z to be unperturbed from its minimum value $T_z^{\min}$. In contrast, radial cooling strongly depends on the reabsorbed photons, therefore we have to take into account how κ_y changes with time. As cooling in the z-direction starts, the cloud shrinks according to $\sigma_z = \sqrt{k_B T_z/\mu B_z''}$. This will increase the optical density in the radial direction and thus the number of reabsorbed photons according to Equation 7.4 and

$$OD_y \propto \frac{1}{\sigma_z \sigma_y} \propto \kappa_y.$$

As a result, the radial steady state temperature is reduced, since it depends on the effective number of reabsorbed photons (Equation 7.14). The same argument holds for the size of the cloud in the radial direction. During radial cooling σ_y shrinks and we arrive at an even lower T_y^{∞}. In actual experiments this nonlinear effect is less pronounced and will be neglected.

7.3 Experimental techniques and data evaluation

In our experiment, we continuously load typically 10^8 chromium atoms in the low field seeking $|j = 3, m_{_J} = 3>$ magnetic substate into a weak Ioffe-Pritchard trap as described in the previous Chapter. In the compressed cigar-shaped trap with a nearly harmonic trapping potential in all three dimensions, we have an axial and a radial curvature of $B_z'' = 110$ G/cm^2 and $B_y'' = 750$ G/cm^2, respectively. This corresponds to trapping frequencies for chromium $\mu = 6\mu_B$ of $\omega_x = \omega_y = 2\pi \times 110$ Hz and $\omega_z = 2\pi \times 42$ Hz. We use a rather high offset field of $B_0 = 28$ G to assure sufficient

harmonicity in all directions. During compression the atoms are adiabatically heated to a temperature of 1 mK at a peak density of $0.4 - 1 \times 10^{10}$ cm^{-3}. In this trap we perform one-dimensional Doppler cooling on the $^7S_3 \leftrightarrow {}^7P_4$ transition in ^{52}Cr with a retroreflected σ^+-polarized beam along the axial direction of the trap. The laser frequency is tuned to 7 Γ above the unperturbed transition frequency corresponding to an effective detuning of approximately $-0.8\,\Gamma$ for a nonmoving atom placed at the minimum of the magnetic field in the center of the trap. This value was optimized with respect to minimum temperature in all directions. The mean intensity of the ≈ 1 cm diameter beam as seen by the ≈ 2 mm diameter cloud was measured to be $4 \times 10^{-3}\ I_{sat}$ using a 1 mm diameter pinhole in front of a calibrated photodiode. The atomic ensemble is detected by absorption imaging using a 12 Bit CCD camera. The resulting optical density profile of the cloud is fitted with two orthogonal Gaussian profiles meeting at the center of the cloud as descibed in Section 5.5. The number of atoms is extracted from this fit using the peak optical density and the size. We perform time-of-flight (TOF) sequences to obtain the temperature in the axial and radial direction. Densities are derived using the size of the cloud in the trap obtained from the time-of-flight fit and the number of atoms. The error bars shown in the figures are the square root of the diagonal elements of the covariance matrix for the fitting parameters obtained from a least square fit. No systematic errors have been included, unless otherwise noted.

7.4 Experimental Results

7.4.1 Dynamics

In this section, we present experimental results on the dynamics of the cooling process. In Figure 7.3 we have plotted the temperature of the cloud in the axial (z) and radial (y) direction after a variable cooling time. We start in both directions with a temperature of approximately 1 mK. In the axial (cooling laser beam) direction we see a fast decrease in temperature. But also in the radial direction, where no laser beam is applied, cooling is observed on a short timescale. The initial decrease in temperature is well fitted by an exponential decay in both cases (see inset in Figure 7.3), as is expected from Equation 7.16. The cooling time constants derived from the fit are $\tau_y^{cool} \approx 50$ ms and $\tau_z^{cool} \approx 10$ ms, corresponding to the fastest possible cooling time of $2\pi/4\omega_z$. In fact, we have never observed axial cooling time constants significantly lower than 10 ms. The minimum steady state temperatures in Figure 7.3 are $T_y^\infty = 334 \pm 7\ \mu$K and $T_z^\infty = 124 \pm 3\ \mu$K, corresponding to 2.7 and 1 times the 1D Doppler temperature of $T_D = 124\mu$K. Due to density dependent heating effects in the light field [127, 132], the minimum axial temperature of $T_z^{\min} \approx 90\mu$K is not reached. Figure 7.4 shows the evolution of the number of atoms and the phase space density during the cooling in a double logarithmic plot to resolve the fast initial

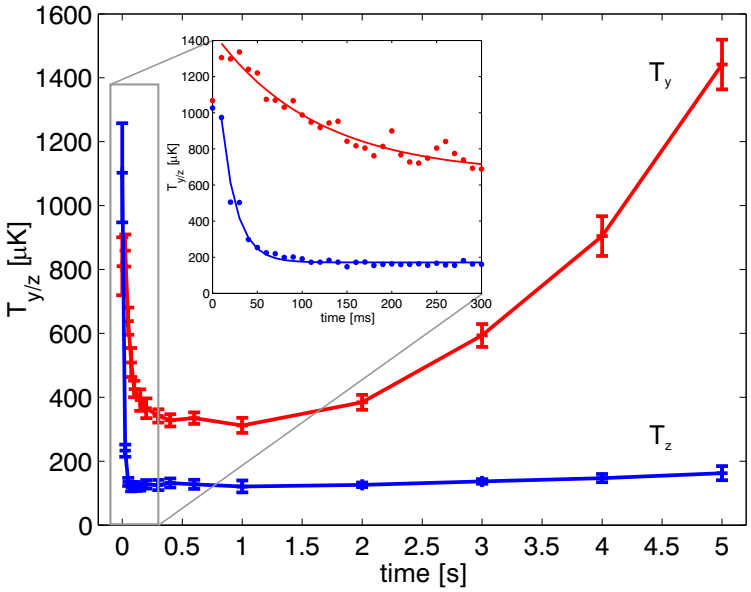

Figure 7.3: Typical evolution of the temperatures in the axial (z) and radial (y) direction as a function of cooling time. The intensity of the cooling laser was 4×10^{-3} I_{sat}. The inset shows another measurement with finer resolution of the initial decrease in temperature. The lines in the inset are least square fits of an exponential decay to the data with a typical uncertainty in the time constants of below 10 %.

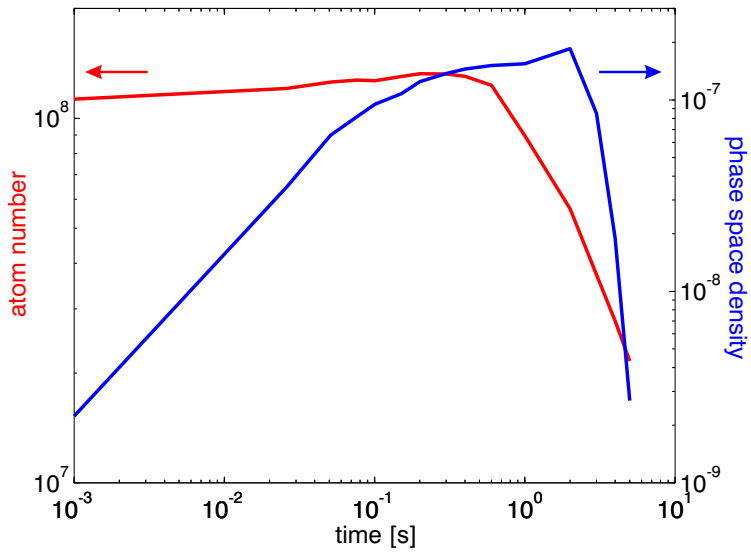

Figure 7.4: Evolution of the number of atoms and the phase space density for the same data set as shown in Figure 7.3. The statistical error in the data of 20 % has been omitted for clarity.

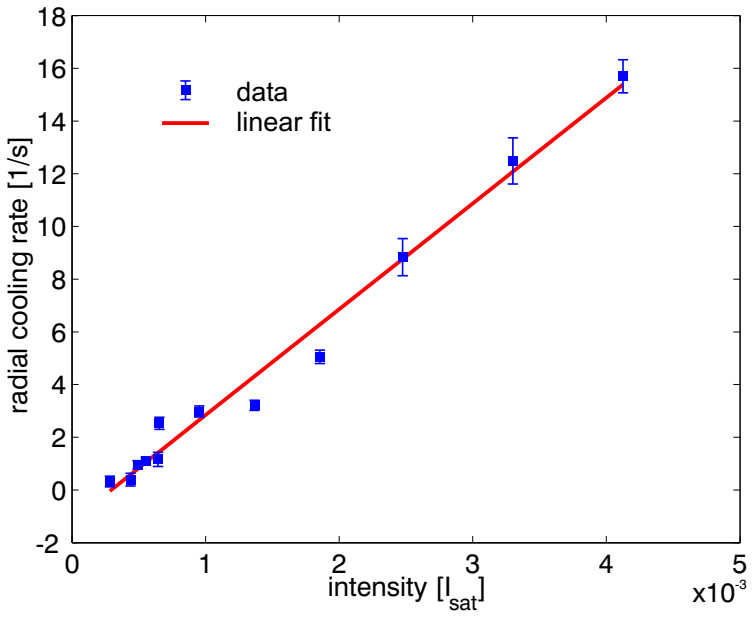

Figure 7.5: Radial cooling rate $1/\tau_y^{cool}$ as a function of measured single beam cooling light intensity. The corresponding cooling rates in the axial direction are larger by a factor of at least 5 for each data point.

dynamics. The number of atoms stays constant within experimental uncertainty beyond 300 ms at which time the steady state temperature is reached. We gain more than a factor of 80 in phase space density and increase at the same time the peak density by more than one order of magnitude from 0.4×10^{10} to 5.6×10^{10} cm^{-3}.

In the experiment shown in Figures 7.3 and 7.4, we continued cooling after reaching steady state. Figure 7.4 shows a strong reduction in the number of atoms for cooling times longer than 500 ms. Atoms are lost from the trap presumably by radiative escape or fine structure changing collisions [121, 169] in the cooling light. At the same time the temperature increases in the radial direction, whereas it stays constant in the axial direction. This is evidence for a density dependent cooling effect in the radial direction. A lower number of atoms results in a reduced optical density and, according to Equation 7.14, to a higher steady state temperature T_y^∞. We will come back to this effect in the discussion of the steady state results.

We have already pointed out in Section 7.2.2 that the cooling rate of the radial degrees of freedom via anharmonic mixing or elastic collisions between the atoms should be independent of cooling light intensity, provided cooling in the axial direction is much faster. In Figure 7.5 the results of a cooling experiment with different cooling light intensities are plotted. For each data point we have performed an experiment analogous to Figure 7.3 and fitted the initial exponential decay of the

temperature to obtain the cooling rate. The corresponding rate constant for the axial direction has been verified to be larger by at least a factor of five for each data point. One can clearly see a linear dependence of the radial cooling rate on light intensity, ruling out anharmonic mixing or elastic collisions as the major cooling mechanism. We have also performed an experiment in which we stopped cooling after the axial direction reached steady state, thus producing a highly anisotropic temperature distribution. The subsequent cross-dimensional relaxation of the temperatures, driven by elastic ground state collisions, occurred on a much longer timescale than the observed cooling time constants when the light was on.

Increasing the laser intensity beyond the values shown in Figure 7.5 results in a strong distortion of the cloud due to light pressure forces and intensity imbalance between the two counterpropagating cooling beams. This causes parasitic heating and increases the achievable temperatures.

From the slope of the linear fit to the data in Figure 7.5 we can extract $\kappa_y = 0.0069$ for a detuning of $\Delta = -0.8\Gamma$ according to Equation 7.10. To compare this experimentally determined value with theory, we have integrated Equation 7.5 using the steady state density distribution with a cloud size of $\sigma_z = 700\mu$m and $\sigma_y = 410\mu$m. The theoretical result of $\kappa_y = 0.046$ is larger by more than a factor 6. If absorption of the scattered intensity inside the cloud is taken into account in Equation 7.5, the result reduces to $\kappa_y = 0.028$ or 4 times the experimental value. This deviation may arise from a change in κ_y originating from an increase in the optical density during cooling. From our experimental data we extract an average cooling rate, which is systematically lower than the steady state value.

7.4.2 Steady State Temperatures

In this section, we present experiments that elucidate the different effects influencing the steady state temperature and compare them to theory.

In the simplified model used to derive the steady state temperatures in the axial and radial direction given by Equations 7.13 and 7.14, the latter are independent of cooling light intensity, since both, the heating rate $1/\tau_{z,y}^{heat}$ and the cooling rate $1/\tau_{z,y}^{cool}$ are linear in intensity. Accounting for an additional constant heating rate R in the differential equation (7.3), the steady state temperature is now intensity dependent and for a detuning of $\Delta = -0.5\Gamma$ becomes

$$T_y^\infty = \frac{\left(\kappa_y + \frac{3}{10}(1+\kappa) + \frac{R}{k_B T_{\rm rec}\Gamma I/I_s}\right)}{\kappa_y}\frac{T_D}{2}. \tag{7.17}$$

In Figure 7.6 we have plotted the measured steady state temperature T_y^∞ for different cooling light intensities. The fit to Equation 7.17 using the measured detuning of $\Delta = -0.8\Gamma$ and $\kappa = 0.16$ calculated from Equation 7.8, gives $\kappa_y = 0.1 \pm 0.002$ and

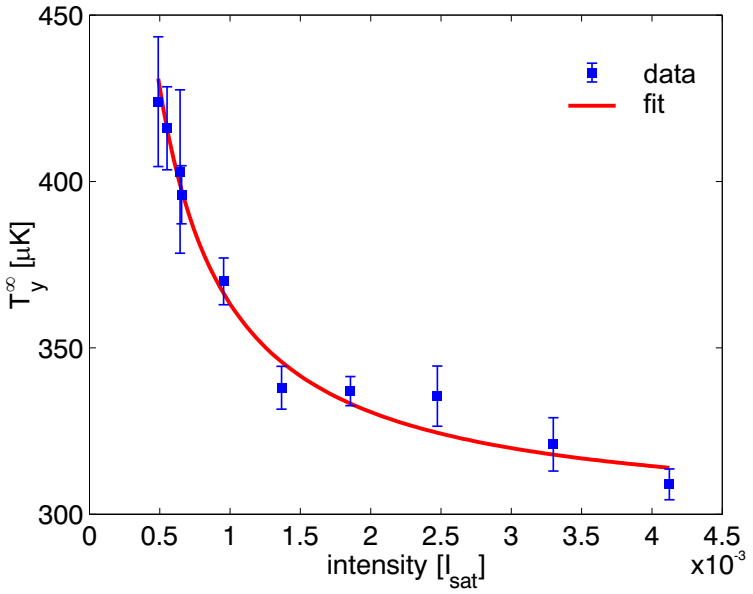

Figure 7.6: Radial steady state temperature as a function of cooling light intensity. The data is fitted by Equation 7.17. The data is from the same experimental run as in Figure 7.5.

$R = 2.4 \times 10^{-26} \pm 10\%$ Js^{-1}. This result agrees well with the integrated value for $\kappa_y = 0.07$ obtained from Equation 7.5. We can also estimate a minimum radial temperature of $T_y^\infty \approx 300\mu$K from Figure 7.6, which is in good agreement with the predicted value using Equation 7.14 (see Figure 7.2) of $T_y^\infty = 2.6T_D \approx 320\mu$K. Although the calculated temperature (neglecting multiple scattering events) is higher than the measured one, we expect the additional, intensity independent heating mechanism to slightly increase the minimum temperature. We have identified this mechanism to be a strong dipolar relaxation process in chromium which will be discussed in Appendix E.

We have already seen in Figure 7.3 that the steady state temperature in the radial direction depends on the number of atoms in the cloud (the temperature increases when the number of atoms decreases at longer cooling times). To elucidate this effect more quantitatively we have performed an experiment in which we cool down the atoms to steady state as described before. In a second "cooling"stage we reduce the cooling laser intensity to 1.6×10^{-3} I_s to slow down the loss of atoms. After different cooling times, we measure the temperature and the optical density in the radial direction. The result is plotted in Figure 7.7 as a function of optical density in the radial direction. We observe a decrease in temperature with increasing optical density. The effective number of reabsorbed radial and total cooling photons, κ_y and κ, respectively, are to lowest order linearly proportional to the optical density OD_y

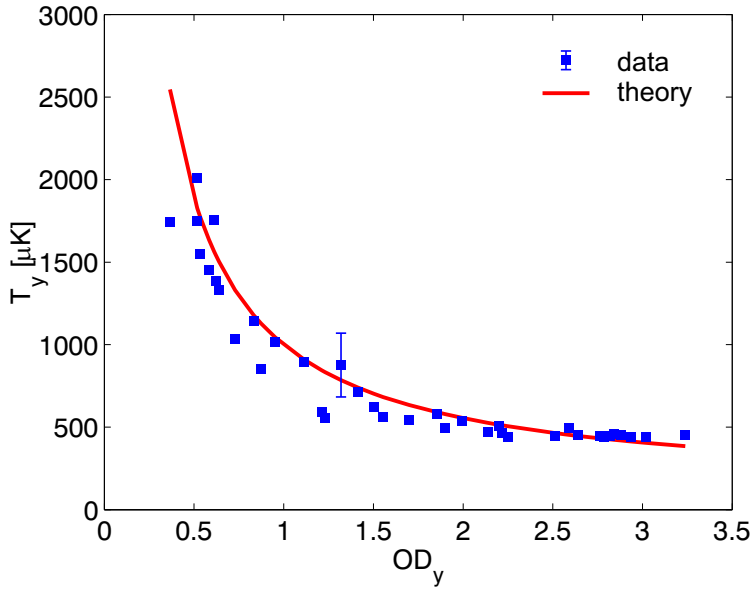

Figure 7.7: Steady state temperature in the radial direction as a function of optical density (OD) in this direction. The error bar resembles the typical error from the temperature fit to the time of flight data. The theory curve is a plot of Equation 7.18 using the results of the fit from Figure 7.6.

(Equation 7.4). Introducing two new constants, $\kappa_y^* = \kappa_y/OD_y$ and $\kappa^* = \kappa/OD_y$, the steady state temperature reads

$$T_y^\infty = \frac{\left(\kappa_y^* \times OD_y + \frac{3}{10}(1 + \kappa^* \times OD_y) + \frac{R}{k_B T_{rec} \Gamma I/I_s}\right)}{\kappa_y^* \times OD_y} \frac{T_D}{2}. \tag{7.18}$$

This equation is plotted as a solid line in Figure 7.7 using the results for R and κ_y (normalized to steady state optical density of 4.5) from the fit to the data in Figure 7.6. The agreement with the experimental data is surprisingly good, since κ_y and κ are not strictly linear in the optical density (see Equations 7.5, 7.8) and the heating rate depends on temperature and density.

7.5 Conclusion

We have presented a general Doppler cooling technique which works for optically dense, trapped atomic samples. In experiments with magnetically trapped Chromium atoms we have achieved an increase in phase space density by two orders of magnitude. To explain our experimental results, in particular the fast and efficient three-dimensional cooling in a one-dimensional molasses, we have developed a

model which takes into account the radial cooling due to reabsorption of scattered photons. Our experimental findings for the intensity-dependence of the cooling rate and the steady-state temperature agree well with the theoretical considerations. We could exclude thermalization effects via elastic collisions or anharmonic mixing as the origin of the radial cooling we observe. Optimum radial cooling is observed for pancake shaped trap configurations and the radial cooling efficiency increases with the radial optical density.

Our technique should be applicable to most atomic species which can be laser-cooled provided that a moderate magnetic offset-field (e.g. $B_0 = 15$ G for ^{87}Rb) is applied to prevent depolarization of the sample. Implementation of this technique in a BEC experiment could simplify the initial laser cooling stages, since Doppler cooling in the trap reduces the figure of merit for loading of the trap to the number of atoms transferred into the trap regardless of temperature. Due to the low light intensities needed to cool the atoms, our method might also be applicable to magnetically trapped atoms in a cryogenic environment [41, 170]. In our experiment, the achieved phase space density for chromium already provides good starting conditions for evaporation and only excessive atom loss and heating due to dipolar relaxation (see Appendix E) in the consecutive evaporation stage prevented us from reaching quantum degeneracy. In conclusion, we have shown that Doppler-cooling applied in a magnetic trap serves as a technique for preparing ultra-cold magnetically trapped atoms. We observe that high optical densities in the cloud improve the cooling efficiency by reabsorption of scattered photons.

Chapter 8

Basic collision theory

In this Chapter I introduce the basic concepts of collision theory with main emphasis on cold and ultra-cold collisions. I do not intend to give a full derivation of the theoretical formalism but rather stress the — sometimes less precise — underlying physical pictures and interpretations. To understand the dynamics of an ultra-cold trapped atomic ensemble, it is necessary to be acquainted with the features of low energy scattering. After an introduction, various scattering features with a square-well as a model potential are discussed. In Section 8.6, I address the specialities of atom-atom collisions arising from their internal structure. The last Section gives a short introduction in the theory of evaporative cooling.

8.1 Introduction

8.1.1 Terms and definitions

We will consider the non-relativistic collision process between two distinguishable quantum particles interacting via a finite-range[1] skalar potential $V(\vec{r}_1, \vec{r}_2)$. Effects of identical particle scattering will be discussed in Section 8.1.3. It is convenient to treat the scattering process in the center of mass system, thus transforming a two particle problem into two single particle problems. The center of mass motion of the two particles is unaffected by the collision process, whereas the relative motion describes the scattering of a single particle with reduced mass $m_\mu = \frac{m_1 m_2}{m_1+m_2}$ on the potential $V(\vec{r}_1 - \vec{r}_2) = V(\vec{r})$. The kinetics of the scattering process is characterized by either the initial momentum $\vec{p}$, wave vector $\vec{k} = \vec{p}/\hbar$ or its magnitude $k = |\vec{k}|$, velocity $\vec{v}$, kinetic energy $E = \frac{\vec{p}^2}{2m_\mu}$ or corresponding temperature $T = E/k_\mathrm{B}$ of the reduced mass in the center of mass frame[2].

[1] We will specify the term "finite-range"more stringently below.

[2] We will use these quantities synonymously.

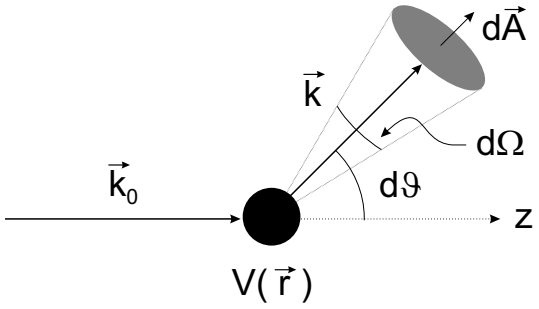

Figure 8.1: Basic scattering problem: an incident plane wave with wavevector $\vec{k}_0$ is scattered by a potential $V(\vec{r})$. The scattered wave is detected in the shaded area $d\vec{A}$ along a direction $\vec{k}$ under the solid angle $d\Omega$.

In quantum mechanics, particles are usually described as wavepackets. We assume the wavepackets of the scatterers to be very broad in position space and to have a well defined momentum (i.e. energy) in momentum space according to Heisenberg's uncertainty relation. The superposition principle of quantum mechanics allows to decompose the wavepackets into an arbitrary set of wave functions. We will choose the plane wave approach in the position representation here. In principle, collision theory can be treated in a very general but abstract way in the framework of the Lippmann-Schwinger equation (see e.g. [171] or [172]), which is an integral equation for the formal solution of the scattering problem. The plane-wave approach presented here simplifies calculations and allows to gain more insight into the physical properties of the scattering process.

The simplified scattering problem is sketched in Figure 8.1. An incident plane wave with wavevector $\vec{k}_0$ is scattered by a potential $V(\vec{r})$. The scattering of the plane wave is described by the time independent Schrödinger equation

$$\left[\frac{\hat{\vec{p}}^2}{2m_\mu} + V(\vec{r})\right]\phi(\vec{r}) = E\phi(\vec{r}), \tag{8.1}$$

where $\hat{\vec{p}}$ is the momentum operator and E the total energy. The stationary solution has two components: the incident plane wave $\phi_0(\vec{r})$ and an outbound scattered wave $\phi_s(\vec{r})$:

$$\phi(\vec{r}) = \phi_0(\vec{r}) + \phi_s(\vec{r}). \tag{8.2}$$

The Ansatz for the scattered wave in the far field is given by a spherical wave with wavevector k modulated by the angle-dependent scattering amplitude $f(\vartheta, \phi)$:

$$\phi_s(\vec{r}) \xrightarrow[\vec{r}\to\infty]{} f(\vartheta,\phi)\frac{e^{ikr}}{r}. \tag{8.3}$$

Elastic scattering requires energy conservation, i.e. $k = |\vec{k}_0|$.

The main goal of scattering theory is to derive an expression for the scattering cross-section σ_{tot}. It tells us how many scattering events per unit time and incident particle flux take place. A detector (depicted by the area $d\vec{A}$ in Figure 8.1), on the other hand, usually can only observe a fraction of the total scattered wave. This leads to the definition of the differential scattering cross-section

$$d\sigma(E, \vartheta, \phi) = |f(E, \vartheta, \phi)|^2 d\Omega, \tag{8.4}$$

which is a measure for scattering probability of a single particle into the solid angle $d\Omega$ normalized to the incident particle current density. Integration of Equation 8.4 yields the total scattering cross-section

$$\sigma_{\text{tot}}(E) = \int |f(E, \vartheta, \phi)|^2 d\Omega \tag{8.5}$$

All the information about the collision process can therefore be obained from the scattering amplitude.

It is very instructive to relate the quantum mechanical with the classical description of the scattering process. In a classical picture of a contact (billiard ball) scattering potential, the particles scattered away from the incident wave result in a shadow cast by the potential. In the quantum description of the problem, this shadow emerges as a consequence of the destructive interference of the incident and scattered wave. From these considerations, one can qualitatively understand the optical theorem

$$\sigma_{\text{tot}}(E) = \frac{4\pi}{k} \text{Im} f(E, \vartheta = 0). \tag{8.6}$$

The imaginary part of the forward ($\vartheta = 0$) scattering amplitude is responsible for this destructive interference.

Besides the energy conserving elastic collisions, also exothermic inelastic or even reactive collisions can take place. The concept of collision "channels" has been introduced to account for a change in the properties of the colliding particles. A channel is a possible mode of fragmentation of the composite system (particle 1 + particle 2) during the collision. Elastic collisions always involve a single channel, since entrance and exit channel of the collision are identical. Inelastic collisions usually involve a change in the internal state of one or both particles. Each possible final state of the pair of particles denotes a collision channel, which can be characterized by a set of quantum numbers describing the internal states. A channel is *open*, if the corresponding collision process is allowed by all applicable conservation laws and *closed* if not. Interactions between open and closed channels can lead to interesting effects, like e.g. Feshbach resonances (see Section 8.6.2).

8.1.2 Partial wave decomposition

For central potentials $V(r)$ that depend only on the distance r between the particles, the partial wave decomposition has proven to be a very useful method — especially in the low energy limit, where only a few partial waves contribute to the scattering amplitude. For such a potential, the Hamiltonian in Equation 8.1 commutes with the angular momentum operator and the projection operator of the angular momentum onto the z axis. The angular part of the Schrödinger equation is therefore solved by the spherical harmonic functions which further simplify to the Legendre polynomials $P_\ell(\cos\vartheta)$ if we take into account the azimuthal symmetry of the problem. The partial wave expansion for the wave function

$$\phi(\vec{r}) = \sum_{\ell=0}^{\infty} \frac{u_\ell(r)}{r} P_\ell(\cos\vartheta) \tag{8.7}$$

results in a Schrödinger equation for the radial wave function $u_\ell(r)$:

$$\frac{\hbar^2}{2m_\mu} u_\ell''(r) + [E - V_{\text{eff}}(r)]\, u_\ell''(r) = 0, \tag{8.8}$$

where the double prime ($''$) denotes the second derivative with respect to the radial coordinate. The effective potential in spherical coordinates is given by

$$V_{\text{eff}}(r) = \left[V(r) + \frac{\hbar^2 \ell(\ell+1)}{2m_\mu r^2} \right]. \tag{8.9}$$

The centrifugal term accounts for the rotational energy of the system. This "centrifugal barrier" is responsible for the threshold laws discussed in Section 8.3. The total "potential" energy is given by the effective potential. For a free particle ($V(r) = 0$), Equation 8.8 is similar to the spherical Bessel differential equation. The solution for the full scattering problem satisfying the boundary conditions[3] can be divided into two regions: the interaction region ($V(r) \neq 0$) and the far field ($V(r) = 0$). The far-field solution has the same structure as the free particle solution. Therefore, the difference between scattering and free space solution in the $r \to \infty$ limit can only be a phase shift δ_ℓ. This phase shift is determined by the boundary conditions connecting the interaction with the far-field solution. The dependence of the scattering amplitude on this phase shift is obtained by performing a partial wave expansion of the incoming plane wave $\phi_0(\vec{r})$ in Equation 8.2 and comparing the coefficients of Equations 8.7 and 8.2 in the $r \to \infty$ limit. We obtain for the scattering amplitude

[3] The boundary conditions for physically meaningful solutions require them to be regular and finite everywhere. Only attractive potentials vanishing faster than r^{-2} for $r \to \infty$ can be treated in this formalism.

the following general $r \to \infty$ expression:

$$f(k,\vartheta) = \frac{1}{2ki}\sum_{\ell}(2\ell+1)\left(e^{2i\delta_\ell(k)}-1\right)P_\ell(\cos\vartheta) \tag{8.10}$$

$$= \frac{1}{k}\sum_{\ell}(2\ell+1)e^{i\delta_\ell(k)}\sin\delta_\ell(k)P_\ell(\cos\vartheta), \tag{8.11}$$

where $\delta_\ell(k)$ is the collisional phase shift of the ℓth partial wave, which is explicitly dependent on the collision energy via the wave number $k = \sqrt{2mE}/\hbar$. Integration of Equation 8.4 yields the total scattering cross-section $\sigma_{\text{tot}}(k)$ and the cross-sections for each partial wave, $\sigma_\ell(k)$:

$$\sigma_{\text{tot}}(k) = \frac{4\pi}{k^2}\sum_{\ell}(2\ell+1)\sin^2\delta_\ell(k) = \frac{4\pi}{k^2}\sum_{\ell}\sigma_\ell(k). \tag{8.12}$$

The maximum contribution of a specific partial wave to the total cross-section is reached in the so called *unitarity limit* ($\sin^2\delta_\ell = 1$) and increases with angular momentum according to

$$\sigma_\ell = \frac{4\pi(2\ell+1)}{k^2}. \tag{8.13}$$

Comparing the scattering amplitude in forward direction, $f(k,\vartheta=0)$ with Equation 8.12, directly yields the optical theorem given in Equation 8.6.

We can derive another useful functional form of the $\ell = 0$ (s-wave) scattering amplitude. From Equation 8.10, we obtain the following relations

$$f_0(k) = \frac{1}{k}e^{i\delta_0(k)}\sin\delta_0(k) \tag{8.14}$$

$$\Longrightarrow \text{Im}\frac{1}{f_0(k)} = -k \tag{8.15}$$

$$\Longrightarrow \text{Re}\frac{1}{f_0(k)} = k\cot\delta_0(k). \tag{8.16}$$

From the last two equations it follows immediately that the s-wave scattering amplitude can be written as[4]

$$f_0(k) = \frac{1}{g_0(k) - ik}, \tag{8.17}$$

where we have defined the function $g_0(k) = k\cot\delta_0(k)$. We will use this expression for the scattering amplitude to derive the energy dependence of the s-wave scattering cross-section in Section 8.5.3.

[4] A thorough treatment shows that the validity of this equation is not limited to s-waves [173].

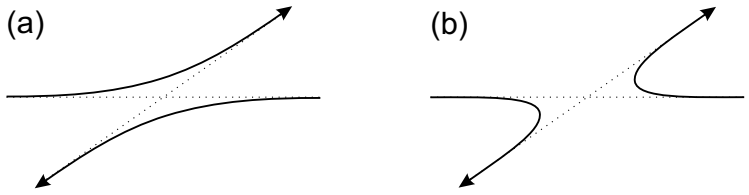

Figure 8.2: Scattering of identical particles. For indistinguishable particles, the scattering events shown in (a) and (b) are described by the same (anti-)symmetrized wave function

We have now reduced the solution of a specific scattering problem to the determination of the corresponding partial wave phase shifts $\delta_\ell(k)$. It can be shown (see Section 8.3) that in the low energy limit $k \to 0$ (threshold scattering), all higher order partial wave cross-sections vanish, except for the spherically symmetric s-wave scattering amplitude $f_0 = -a$ with the cross-section $\sigma_0(k \to 0) = 4\pi a^2$, where a is called the scattering length. Ensembles in which scattering is governed by s-waves will be discussed in more detail in Section 8.5.

The effect of the scattering potential on the phase shift can be understood in terms of a simple optical analog: the incoming wave is represented by a light wave with a wavelength λ and the potential by a transparent material with a refractive index n_r. An attractive potential reduces the wavelength of the incoming particle corresponding to a refractive index of $n_r > 1$. The scattered wave is *retarded* ($\delta_\ell < 0$) with respect to the unscattered wave. For a repulsive potential, the scattered wave is advanced ($\delta_\ell > 0$), corresponding to $n_r < 1$.

8.1.3 Identical particles

Particles in the same internal quantum state are indistinguishable. It is therefore impossible to determine which particle scatters and which is the scatterer (see Figure 8.2). This is accounted for by considering both events in the (anti-)symmetrized wave function. Interchange of particles ($\vec{r} \to -\vec{r}$, $r \to r$, $\vartheta \to \pi - \vartheta$, $\phi \to \pi + \phi$) can either reverse the sign of the wave function for fermions having half integral spin, or leave it untouched for bosons having integral spin. (Anti-)symmetrization of the scattered wave (Equation 8.3) assuming a central potential yields

$$\phi_s(\vec{r}) \xrightarrow[\vec{r}\to\infty]{} [f(\vartheta) \pm f(\pi - \vartheta)] \frac{e^{ikr}}{r}, \tag{8.18}$$

where the plus sign applies for bosons and the minus sign for fermions. The detector cannot distinguish between the identical particles, so both processes depicted in

Figure 8.2 lead to a "click". The differential cross-section is therefore defined by

$$d\sigma(\vartheta) = |f(\vartheta) \pm f(\pi - \vartheta)|^2 d\Omega \tag{8.19}$$

$$= |f(\vartheta)|^2 + |f(\pi - \vartheta)|^2 \pm 2\mathrm{Re}\left[f(\vartheta) f^*(\pi - \vartheta)\right] d\Omega, \tag{8.20}$$

where the star (*) denotes complex conjugate. The last term in this equation is a quantum mechanical interference which vanishes in the classical limit. However, it has important consequences for low energy scattering. In the case of bosons, all odd partial waves interfere destructively, whereas for fermions all even partial waves vanish due to the symmetry properties of the Legendre polynomials. Collisions between identical fermions "freeze out" in the limit $k \to 0$. The total scattering cross-section is obtained by integrating over one half sphere to conserve the number of particles (detection at $\vec{r}* = -\vec{r}$ would yield the same number of "clicks" as observation at $\vec{r}$, thus counting the same event twice). It is worthwhile to mention, that the quantum mechanical s-wave scattering cross-section in the low temperature limit is $\sigma_0 = 8\pi a^2$ and thus twice as large as for distinguishable particles and four times as large as for classical particles. The difference between quantum mechanical and classical result is the interference term in the scattering amplitude which also leads to the optical theorem. Classically, particles are only scattered away from the incident beam. Quantum mechanical scattering has two contributions: a scattered wave corresponding to classical scattering, plus a destructive interference term of the scattered wave with the incident wave responsible for the "shadow" in the beam cast by the scattering potential. These two terms have the same magnitude and double the quantum mechanical cross-section with respect to the classical. The number of collision events (in which two atoms collide) per unit volume per unit time in a gas of density n is given by $<\sigma(E)v>_{\mathrm{th}} n^2/2$ (omitting the factor $1/2$ would count the pairs twice), where $<\ldots>$ denotes thermal averaging (see Appendix C).

In the following we will continue to assume distinguishable particles if not otherwise noted. The corresponding cross-sections and rates for identical particles are larger by a factor of 2.

8.2 Scattering by a square-well potential

In this section, we will discuss low energy scattering of a particle by a square-well potential. Most results obtained here can easily be adopted to other, more realistic potentials as far as they fall off more rapidly than r^{-2} for large r. We will therefore use it as an example to illustrate the general features of low energy collisions.

Consider a three-dimensional attractive square-well potential having a width r_0 and a depth V_0 as sketched in Figure 8.3. The square well can support N_b bound states,

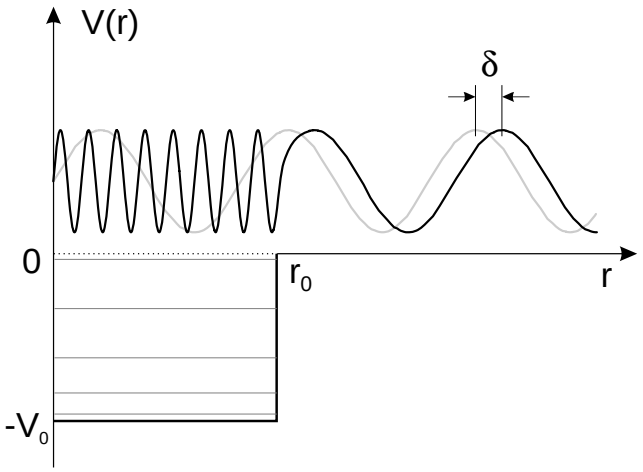

Figure 8.3: Scattering by a square-well potential of depth $-V_0$ and width r_0. The position of bound states are indicated by the gray lines inside the well. The stationary solution of the scattering wave is represented by the black wave, whereas the solution in the absence of the potential is given by the gray wave. The waves have a phaseshift δ modulo 2π, as indicated.

where N_b is given by [172, Ch. 9.2.5]

$$N_b = \text{Ceil}\left[\frac{1}{\pi}\sqrt{\frac{2m_\mu V_0 r_0^2}{\hbar^2}} - \frac{1}{2}\right]. \tag{8.21}$$

The function Ceil$[x]$ returns the next integer greater than or equal to x. The first bound state has an energy of

$$U_b = \frac{\pi^2\hbar^2}{8m_\mu r_0^2}. \tag{8.22}$$

A bound state is characterized by the fact that half the wavelength corresponding to the eigenfunction of this state equals an integer multiple of the effective square well width. Due to the exponential decay of the wavefunction into the classically forbidden region, the effective width can be up to twice as large compared to the actual width [174]. In this regime, the Bohr-Sommerfeld quantization condition is given by $n\lambda_b/4 = r_0$, where n is a positive integer. This can be generalized for arbitrary potentials using the WKB (Wenzel-Crames-Brioullin) quantization condition $\Phi(E) = (N_b + 1/4)\pi$, where the phase integral $\Phi(E)$ between the inner and outer classical turning points r_1 and r_2, respectively, is defined as [175]

$$\Phi(E) = \int_{r_1}^{r_2} k(E)dr. \tag{8.23}$$

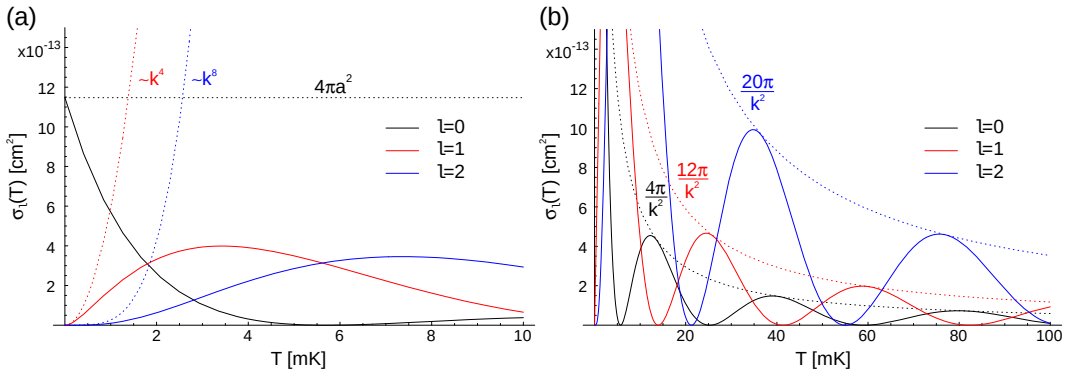

Figure 8.4: Temperature dependence of the $\ell = 0, 1, 2$ scattering cross-sections for a square well potential of width $r = 50\,a_0$ ($a_0 = 0.53$Å is Bohr's radius) and depth $V_0 = V_{N_b=100} + 5$ (see Equation 8.21). (a) Low temperature regime. The dotted lines indicate the low temperature limits of the cross-sections. $\ell > 0$ partial waves vanish as $k^{4\ell}$, whereas the s-wave scattering cross-section reaches a constant value of $4\pi a^2$. (b) Medium temperature regime. The dotted lines indicate the unitarity limit (Equation 8.13) for the different partial waves. The cross-sections oscillate between zero and the unitarity limit.

The stationary solution of the free particle problem ($V(r) = 0$) obtained from Equation 8.8 is given by a linear combination of spherical Bessel $j_\ell(z)$ and von Neumann functions $n_\ell(z)$ (symbolized by the gray wave in Figure 8.3). Inside the potential ($r < r_0$), the only regular solution is the spherical Bessel function, whereas on the outside ($r > r_0$) we get the same structure as in the absence of the potential. The inside and outside wave functions have to meet the boundary condition requiring the continuity of the logarithmic derivative of the wave functions at $r = r_0$. The asymptotic ($r \to \infty$) phase shift between the unperturbed und the scattered solution determines is a direct consequence of this boundary condition. It determines the partial wave cross-section according to Equation 8.12 and is given by

$$\tan\delta_\ell = \frac{k j'_\ell(kr_0) j_\ell(k_0 r_0) - k_0 j'_\ell(k_0 r_0) j_\ell(kr_0)}{k n'_\ell(kr_0) j_\ell(k_0 r_0) - k_0 j\prime_\ell(k_0 r_0) n_\ell(kr_0)}, \tag{8.24}$$

where $k^2 = \frac{2m_\mu}{\hbar^2}E$ is the square of the wave vector outside and $k_0^2 = k^2 + \lambda_0^2$ with $\lambda_0^2 = \frac{2m_\mu}{\hbar^2}V_0$ inside the potential well. We have plotted in Figure 8.4 the exact solution (Equation 8.24) for the temperature[5] dependence of the $\ell = 0, 1, 2$ partial wave cross-sections. The most prominent feature is the oscillation of the scattering cross-sections between zero and the corresponding unitarity limit with temperature. This behaviour is termed the "Ramsauer-Townsend effect" [171, Ch.

[5] We assume a well defined collision energy instead of a thermal energy distribution, but use the temperature as a measure for the kinetic energy. For an atomic ensemble close to thermal equilibrium, thermal averaging of the collision cross-section has to be performed (see Appendix C).

4.3] and can easily be understood in terms of the scattering phase. Each time the incident particle energy is such that an integer multiple of half the wavelength fits inside the potential region, no scattering occurs. In that case, the solutions for the wave with and without potential have an integer phase shift of π and the scattering cross-section vanishes. In between, the phase shift attains odd multiples of $\pi/2$ which corresponds to unitarity scattering (see Equation 8.13).

8.3 Scattering close to threshold

The partial wave expansion is only useful, if we can limit ourselves to the evaluation of only a few phase shifts. A simple classical argument shows, that this is true for low energy scattering. The angular momentum of a particle scattered at a central potential is given by $|\vec{L}| = b\sqrt{2m_\mu E} = \text{const}$, where b is the impact parameter. Scattering requires the particle to penetrate the potential having a range of r_0, thus $|\vec{L}| \leq r_0\sqrt{2m_\mu E}$. The analogous quantum mechanical expression yields an upper limit for the angular momentum involved in the scattering process:

$$\ell \leq \sqrt{\ell(\ell+1)} \leq \frac{1}{\hbar} r_0 \sqrt{2m_\mu E} = k r_0. \tag{8.25}$$

The physics behind this behaviour is easily seen: the centrifugal barrier term in Equation 8.9 scales quadratically with the angular momentum. Thus, collisions involving a high angular momentum have to provide sufficient rotational energy to probe the scattering potential at all. An exception to this behaviour are shape resonances discussed in Section 8.4.

The onset of quantum threshold scattering for a $-C_s/r^s$ potential with $s \geq 3$ is related to the breakdown of the semiclassical WKB approximation for the connection between the external $r > r_q$ and the internal $r < r_q$ wavefunction below a characteristic energy E_q [176]

$$E_q = \frac{\hbar^2}{m_\mu}\left[\left(2\frac{s+1}{3}\right)^{2s}\left(\frac{s-2}{6s}\right)^{s}\left(\frac{2s+2}{s-2}\cdot\frac{\hbar^2}{m_\mu C_s}\right)^{2}\right]^{\frac{1}{s-2}} \tag{8.26}$$

$$r_q = \left(\frac{27s}{4(s+1)^3}\cdot\frac{m_\mu C_s}{\hbar^2}\right)^{\frac{1}{s-2}}. \tag{8.27}$$

In the WKB approach, the potential is linearized around the turning points which results in an energy independent reflection phase of $\pi/2$. The breakdown occurs at an energy for which the de Broglie wavelength λ_{dB} of the incoming wave varies strongly when entering the potential region: $\frac{d\lambda_{\mathrm{dB}}(E,r)}{dr} \gtrsim 1$. The linearization of the potential is no longer valid and thus the phase shift upon reflection deviates from $\pi/2$ and

becomes energy dependent, which marks the onset of quantum threshold behaviour [175].

The height and position of the centrifugal barrier of the effective potential (Equation 8.9) can be related to the characteristic threshold energy E_q and is given for a van der Waals potential with $s = 6$ by

$$E_c(\ell) = 0.0193 E_q \left[\ell(\ell+1)\right]^{\frac{3}{2}} \tag{8.28}$$

$$r_c(\ell) = 2.67 \frac{r_q}{\sqrt[4]{\ell(\ell+1)}}. \tag{8.29}$$

The particle can enter the interaction region for a kinetic energy $E = \frac{3}{2} k_\mathrm{B} T$ exceeding the centrifugal barrier height $E_c(\ell)$. The corresponding $\ell = 2$ and $\ell = 4$ threshold temperatures for bosonic chromium assuming $C_6 \approx 1300$ a.u. (see Appendix D) are $T_{l=2} \approx 1.1$ mK and $T_{l=4} \approx 6.8$ mK, respectively, and thus far above any temperature we observe in our trapped atomic ensembles.

The contribution of the higher order partial waves for low collision energies can be obtained by approximating the solution for the phase shifts for the square well potential (Equation 8.24) in the $kr_0 \ll 1$ limit:

$$\tan \delta_\ell = \frac{2\ell+1}{[(2\ell+1)!!]^2} (kr_0)^{2\ell+1} P_\ell^*(k_0 r_0), \qquad \text{with} \tag{8.30}$$

$$P_\ell^*(k_0 r_0) = \left(\frac{\ell j_\ell(z) - z j_\ell'(z)}{(\ell+1) j_\ell(z) + z j_\ell'(z)} \right)_{z = k_0 r_0}. \tag{8.31}$$

Provided the term abbreviated by P_ℓ^* behaves reasonably (see next Section), we can immediately deduce a $k^{2\ell+1}$ dependence of the scattering phase. Therefore, the cross-sections for partial waves with $\ell > 0$ vanish for decreasing energy as $1/k^{4\ell}$ (Wigner threshold law). On the contrary, the s-wave cross-section remains at a constant value of $\sigma_0 = 4\pi a^2$ (see Figure 8.4 (a)). It can be shown [173, §132], that this behaviour is quite general, provided the scattering potential vanishes faster than $1/r^{2\ell+3}$. An important exception from this is the dipole-dipole interaction, which will be discussed in Section 8.6.3.

The Wigner threshold law has been verified experimentally for p-waves collisions in an ensemble of fermionic ^{40}K atoms [177].

8.4 Shape resonances

We have seen in the previous section that higher partial waves ($\ell > 0$) do not significantly contribute to the low energy scattering cross-section below a certain threshold

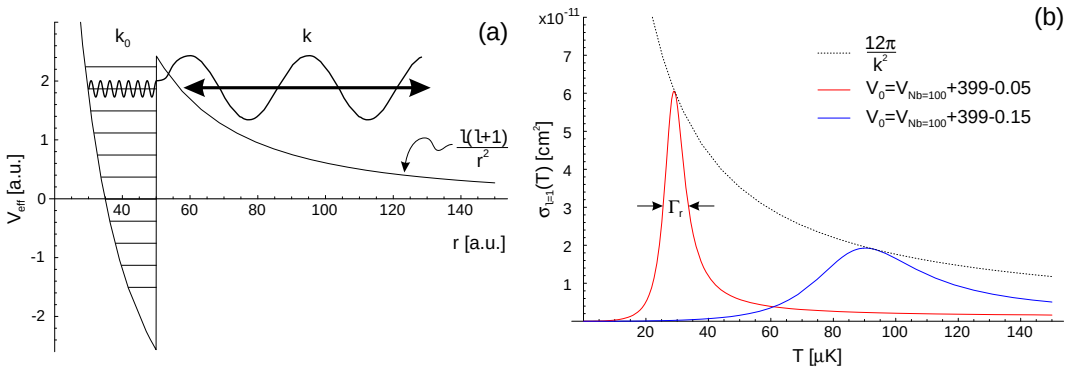

Figure 8.5: Shape resonance for the $\ell > 1$ partial waves in a square well potential. (a) Sketch of the effective potential (Equation 8.9) including the centrifugal barrier (vertical scale exaggerated). The scattering wave k can tunnel through the centrifugal barrier, provided the scattering energy is resonant with a bound level inside the centrifugal barrier. (b) $\ell = 1$ partial wave scattering cross-sections for a square well potential with a low energy shape resonance. The two curves show the influence of a slight change in potential depth, which is given in units of the first bound state energy U_b (Equation 8.22).

(height of the centrifugal barrier), provided the term defined in Equation 8.31 behaves reasonably. An exception from this is the occurence of a *shape resonance*, when the denominator of Equation 8.31 vanishes at a certain energy E_r and $\tan\delta_\ell$ diverges. For a narrow, deep square well potential this energy can be derived from

$$k_0 r_0 - \frac{\pi}{2}\ell \approx \left(n + \frac{1}{2}\right)\pi, \quad \text{with} \quad k_0^2 = \frac{2m_\mu}{\hbar^2}(E_r + V_0) \tag{8.32}$$

where n is a positive integer. The same equation describes the energy E_r of a quasi-bound state with orbital angular momentum ℓ inside the centrifugal barrier. Apparently, higher order partial waves can tunnel through the barrier and couple resonantly to these states as sketched in Figure 8.5 (a). The scattered particle can spend a significant amount of time inside the centrifugal barrier, which results in a large scattering probability.

The energy dependence of the cross-section close to the resonance energy can be obtained from a Taylor expansion of the denominator of Equation 8.31 and assuming $E \approx E_r$. Defining

$$\Gamma_r = \Gamma(E_r) = \frac{(kr_0)^{2\ell+1}}{[(2\ell-1)!!]^2}\left(\frac{2\hbar^2}{mr_0^2}\right), \tag{8.33}$$

we can derive from Equation 8.30 the *Breit-Wigner formula* for resonance scattering:

$$\sigma_\ell = \frac{4\pi(2\ell+1)}{k^2}\frac{\Gamma_r^2}{4(E-E_r)^2+\Gamma_r^2}. \tag{8.34}$$

The scattering cross-section has a Lorentzian lineshape with a resonance half width given by Γ_r. On resonance, it reaches its unitarity value (Equation 8.13). The width of the resonance (Equation 8.33) scales like $E_r^{\ell+1/2}$. This can be understood from the lifetime $\tau \approx \hbar/\Gamma_r$ of the metastable quasi-bound state: the lower E_r, the thicker the centrifugal barrier and the longer the lifetime. This behaviour is illustrated in Figure 8.5 (b), where we have plotted the $\ell = 1$ shape resonance for two slightly different potential depths. Close to the resonance at $T = 30\,\mu$K and $T = 90\,\mu$K the $\ell = 1$ cross-section dominates the scattering process, although the centrifugal barrier for both potentials has a height of 1.4 mK. As we can see from the Figure, already minor changes in the scattering potential can have profound consequences on the position and width of the resonance. It is this sensitivity to the shape of the potential that gave these resonances their name.

Shape resonances can also play an important role in inelastic collisions of atoms. The atoms spend a long time close together inside the centrifugal barrier. Spin-orbit or hyperfine interactions during that time can lead to an enhancement of dipolar relaxation collisions which will be discussed in more detail in Section 8.6.3.

Shape resonances in cold atomic collisions have been observed for p-waves in fermionic ^{40}K in a cross-dimensional relaxation experiment [177], and in d-waves for ^{87}Rb [178] and ^{39}K [179, 180] by photoassociation spectroscopy.

8.5 Elastic s-wave collisions

We have seen in Section 8.3 that all partial wave cross-sections vanish — in the absence of resonances — as the collision energy approaches zero, except for the s-wave cross-section. We will again use the results from the square-well potential to develop the general features of s-wave scattering, most of which have equivalents for other scattering potentials.

8.5.1 The scattering length

From Equation 8.12, we immediately obtain the s-wave scattering cross-section

$$\sigma_0(k) = \frac{4\pi}{k^2} \sin^2 \delta_0(k). \tag{8.35}$$

The full solution for the phase shifts of the square-well scattering problem (Equation 8.24) can be further simplified for s-waves to

$$\delta_0(k) = \arctan\left(\frac{k \tan k_0 r_0}{k_0}\right) - k r_0. \tag{8.36}$$

For vanishing collision energy ($k_0 \to \lambda_0$) and with the definition of the scattering length as

$$a = -\lim_{k\to 0} \frac{\tan\delta_0(k)}{k} \tag{8.37}$$

$$\underset{\text{square well}}{=} \left[1 - \frac{\tan\lambda_0 r_0}{\lambda_0 r_0}\right] r_0, \tag{8.38}$$

the phase shift is

$$\delta_0(k) = \arctan\left[k(r_0 - a)\right] - kr_0. \tag{8.39}$$

Far away from any resonances, a does not diverge [$k_0 r_0 \neq (N_b + 1/2)\pi$, where N_b is an integer], the arctan() can be replaced by its argument and we simply get for the scattering phase (modulo π)

$$\delta_0(k) \approx -ka. \tag{8.40}$$

In this case, the s-wave cross-section (Equation 8.35) is to first order independent of collision energy

$$\sigma_0 = 4\pi a^2. \tag{8.41}$$

We will see in Section 8.5.3, that information on the temperature dependence of the s-wave cross-section can be obtained from an effective range expansion which gives higher order terms in the collision energy. The scattering length a can be positive or negative and is typically on the order of the range of the interaction potential. For collisions between neutral atoms, it is on the order of $100\,a_0$, where a_0=0.53 Å is Bohr's radius. A geometrical interpretation of the scattering length can be obtained by considering the scattered wave function which has the asymptotic form $u_0 \sim \sin(kr + \delta_0)$. In the zero temperature limit and for $r \to 0$, this can be further simplified to $u_0 \sim \pm k(r - a)$ by replacing $\sin(x)$ with its argument and using Equation 8.40. Therfore, the scattering length marks the intersection of the tangent on the asymptotic wavefunction [the argument of $\sin(x)$] with the r-axis. Figure 8.6 shows some examples for threshold ($k \to 0$) wave functions and their tangents (dashed lines) for slightly different potentials resulting in a negative, zero and positive scattering length (from top to bottom).

8.5.2 Zero energy resonances

In the previous subsection we have obtained a low energy expression for the scattering cross-section under the assumption that the scattering length does not diverge. We will now drop this limitation and analyze the behaviour of the phase and the

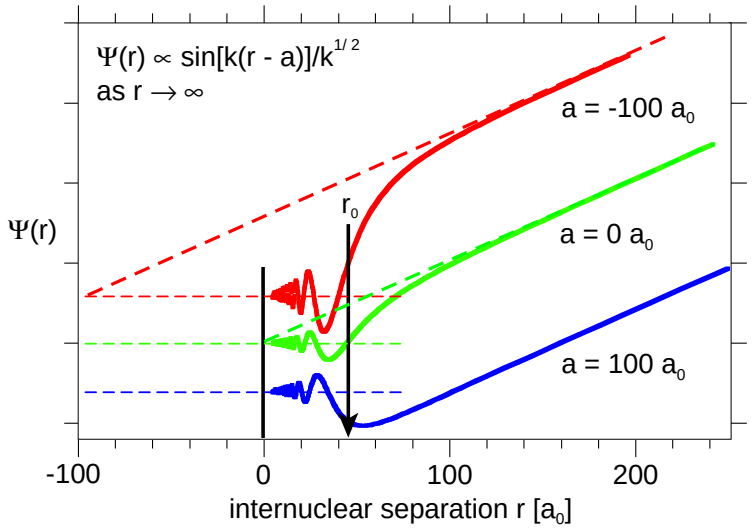

Figure 8.6: Wave functions for slightly different potentials resulting in a negative, zero and positive scattering length a (top to bottom, vertically displaced for clarity). From: [181].

cross-section for different potential depths. We are free to choose $\delta_0 = 0$ for $V_0 = 0$. Increasing the potential depth starting from zero, the scattering length a (Equation 8.38) decreases from 0 to minus infinity[6] as we approach

$$\lambda_0 r_0 = \left(N_b + \frac{1}{2}\right)\pi, \tag{8.42}$$

where N_b is an integer. We immediately see that this is equivalent to the condition for the existence of the first bound level inside the square well (Equation 8.21). In that case the zero energy scattering phase (Equation 8.39) is $\delta_0 = \pi/2$ resulting in a pole in the scattering length and a divergence in the scattering cross-section (Equation 8.41): we observe a zero energy resonance (see Figure 8.7). Just before the condition 8.42 is reached, the scattering length is large and negative and the potential is said to have a *virtual* state. The scattering length has a pole with a change in sign as a new bound state enters the square well. The zero energy scattering phase is zero if no bound state exists, $\pi/2$ as it appears, and π for slightly deeper potentials (see Figure 8.7 (b)). As we further increase the potential depth, the scattering phase remains at π until the potential can support the next bound state and the phase jumps to $3\pi/2$. In summary, the zero energy phase for a potential supporting N_b bound states is

$$\lim_{k\to 0} \delta_0(k) \quad = \quad N_b\pi, \tag{8.43}$$

[6] $\lim_{x\to 0} \frac{\tan x}{x} = 1 + \frac{x^2}{3} + \mathcal{O}(x^4)$

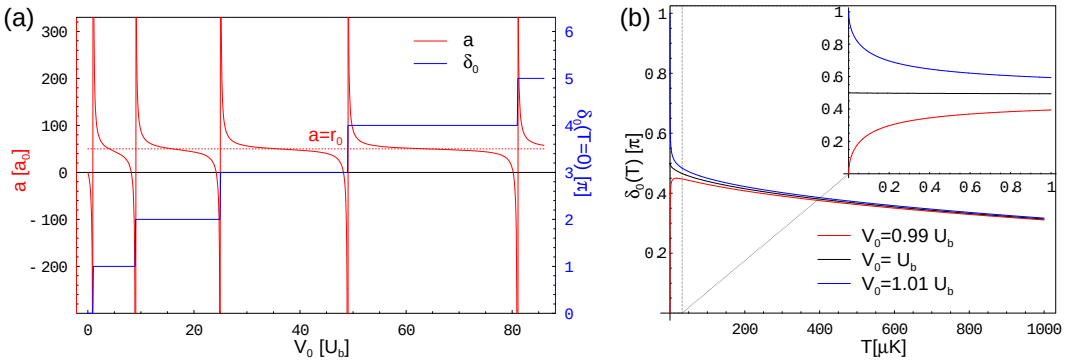

Figure 8.7: (a) Scattering length (red line, left axis) and scattering phase (blue line, right axis) in the zero temperature limit for different potential depths (scaled to the number of bound states the potential can support, Equation 8.21). The dotted line indicates the average scattering length. (b) Energy dependence of the phase shift for a potential which has a virtual state (red line), for which the first bound state just enters (black line) and which supports a single bound state (blue line).

except at a potential depth for which the next $(N_b + 1)$ bound state enters, where it takes the value

$$\lim_{k\to 0} \delta_0(k) \quad = \quad \left(N_b + \frac{1}{2}\right)\pi. \tag{8.44}$$

The last two equations are an example of the more general *Levinson's* theorem [171] which is valid for a wide range of potentials.

The coincidence between a zero energy resonance and a new bound state entering the square well has a simple geometrical meaning: a bound level exists, if an integer multiple of the wavelength inside the potential ($^{2\pi}/_{k_0}$) exactly fits the effective potential range. The incident wave is in the $k \to 0$ limit in resonance with this level which greatly enhances the interaction and thus the scattering cross-section.

This behaviour can be observed in Figure 8.7, where we have plotted the scattering length and the scattering phase for increasing potential depths. The corresponding cross-section in the zero temperature limit is simply given by Equation 8.41. We also note that the scattering length is most of the time positive and coincides with the potential range r_0. One can show that for a truncated $^1/_{r^6}$ potential (see Section 8.6.1), there is a 75 % probability for a random potential depth to have a positive scattering length [182].

8.5.3 Effective range expansion

We are especially interested in the temperature dependence of the s-wave scattering cross-section in the low temperature ($ka \ll 1$) regime. Equation 8.41 is the zero

order approximation of the scattering cross-section for $T \to 0$. More information on the temperature dependence can be obtained from the effective range expansion of the scattering amplitude [171, 173]. Starting point is the scattering amplitude in the form of Equation 8.17. It can be shown that $g_0(k) = k \cot \delta_0(k)$ is analytical over a wide range of collision energies provided the potential $V(r)$ vanishes sufficiently fast[7]. For small collision energies, we can therefore expand $g_0(k)$ in even powers of k

$$g_0(k) \approx c_0 + c_1 k^2 + \cdots . \tag{8.45}$$

Comparing this expansion with the definition of the scattering length (Equation 8.37), we find for the first expansion coefficient $c_0 = -1/a$. For a square well potential, we know the exact solution for the phase shift (Equation 8.36) and perform the series expansion analytically:

$$k \cot \delta_0(k) = -\frac{1}{a} + \frac{1}{2} r_e k^2 + \cdots , \tag{8.46}$$

where the *effective range* r_e is given by

$$r_e = r_0 - \frac{r_0^3}{3a^2} - \frac{1}{\lambda_0^2 a} \approx r_0 - \frac{r_0^3}{3a^2}. \tag{8.47}$$

For the last approximation, we have assumed a sufficiently deep potential $\left(\frac{2m_\mu V_0}{\hbar^2}\, a \gg 1\right)$. The effective range equals the width of the square well exactly at a zero energy resonance. In Figure 8.8, we have plotted the effective range together with the scattering length for increasing potential depth. One can see that the effective range diverges for $a \to 0$.

In a simplistic picture, the term ka gives the phase shift between the scattered and the incoming wave. The effective range expansion term $\frac{1}{2}k^2 a r_e$ is then a second order correction to this phase shift, reducing or enlarging the "effective width" of the potential.

A more general expression can be obtained from the analytical properties of the $k \to 0$ solutions $u_0^2(r)$ and $v_0^2(r)$ of the radial Equation 8.8 with and without the scattering potential, respectively. The effective range is then given by

$$r_e = 2 \int_0^\infty \left[v_0^2(r) - u_0^2(r) \right] dr. \tag{8.48}$$

The numerical factor in front of the integral has been chosen such that the square-well potential solution $r_e = r_0$ is reproduced. The effective range expansion is valid provided the energy dependent term satisfies $\frac{1}{2}k^2 a r_e \ll 1$.

[7] The effective range expansion can be performed for any potential vanishing faster than $1/r^5$ [183].

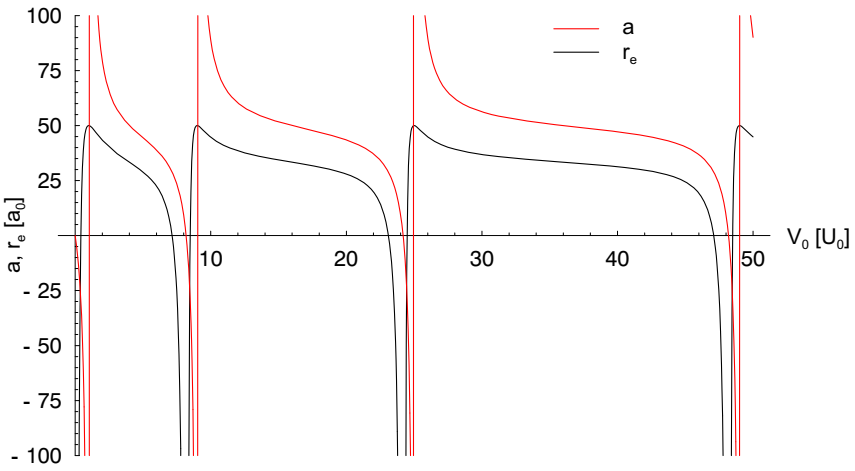

Figure 8.8: Effective range and scattering length (in units of a_0) for an increasing potential depth (in units of U_0) of a square-well. The effective range diverges for vanishing scattering length. The scattering length diverges when a new bound state enters the potential. The effective range equals the width of the square well exactly at these zero energy resonances.

Using Equations 8.17 and 8.5 we obtain the low temperature energy dependence of the s-wave scattering cross-section in the effective range expansion

$$\sigma_0^{(2)}(k) \quad = \quad \frac{4\pi a^2}{k^2a^2 + (\frac{1}{2}k^2 r_e a - 1)^2}. \tag{8.49}$$

Keeping only the first term in the expansion (Equation 8.46) yields a lower order approximation

$$\sigma_0^{(1)}(k) \quad \approx \quad \frac{4\pi a^2}{k^2a^2 + 1}. \tag{8.50}$$

For very large scattering lengths, i.e. close to a zero energy resonance (see Section 8.5.2), the cross-section approaches its unitarity value given by Equation 8.13. The effective range approximation is especially useful for scattering close to such a resonance. In Figure 8.9(a) the exact solution of the scattering cross-section $\sigma_0(T)$ for a square well potential (Equations 8.36 together with 8.35) is compared with $\sigma_0^{(2)}(k)$ and $\sigma_0^{(1)}(k)$ for positive and negative scattering lengths. Obviously, the inclusion of the effective range provides a much better agreement than the first order approximation, although the expansion term ($\frac{1}{2}k^2 r_e a \gg 1$) is beyond its validity for temperatures above 500 μK. The inset shows the high temperature region. We note two important points: i) Neither approximation reproduces the oscillations in the cross-section (Ramsauer-Townsend effect, see Section 8.2). ii) The s-wave scattering

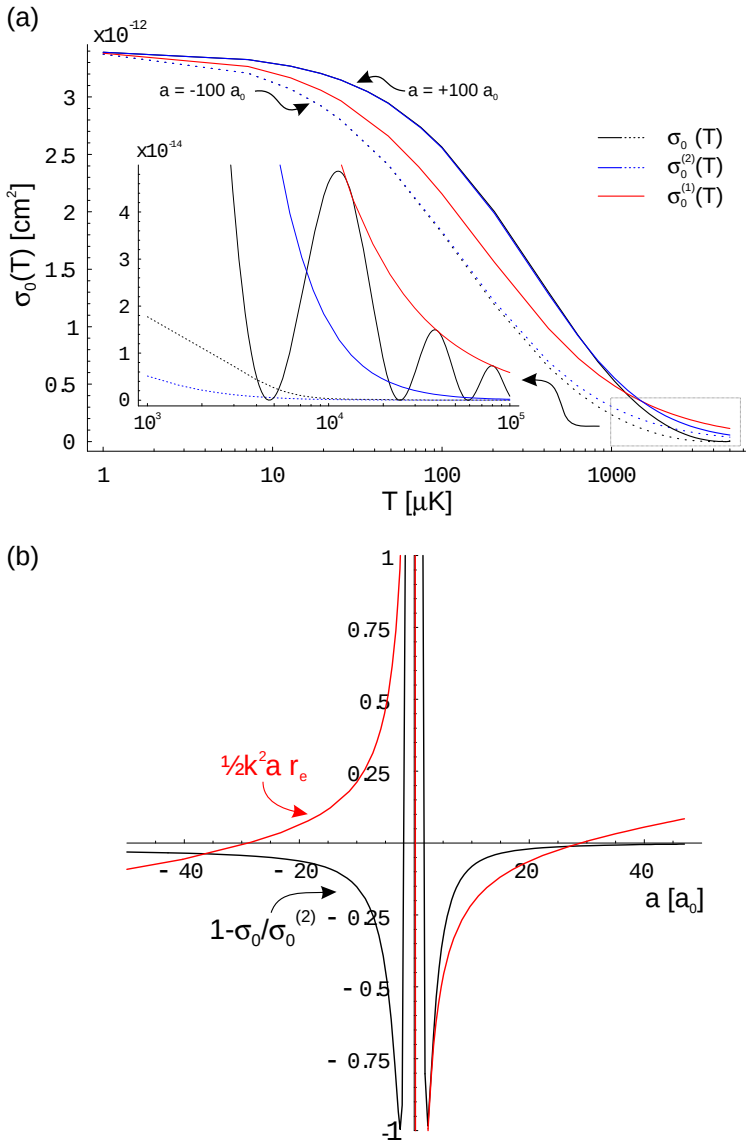

Figure 8.9: (a) Comparison between the temperature dependence of the effective range and low order approximations Equations 8.49 (blue) and 8.50 (red) for the s-wave cross-section and the full solution $\sigma_0(T)$ (black). The solid lines correspond to a scattering length of $a = 100\,\mathrm{a_0}$ and the dotted lines for $a = -100\,\mathrm{a_0}$. The effective range has been determined from Equation 8.47 to be $r_0 = 45.8\,\mathrm{a_0}$. The inset shows a blow-up of the high temperature region. (b) Deviation $1 - \sigma_0/\sigma_0^{(2)}$ of the effective range approximation from the exact cross-section (black line) and magnitude of the effective range expansion term versus the scattering length for a fixed temperature of $200\,\mu$K. We assume a square-well potential with a width of $r_0 = 50\,\mathrm{a_0}$ and a potential depth of $V_0 \approx 40000\,\mathrm{U_0}$.

cross-section for a negative scattering length vanishes much faster than the unitarity limit for high temperature.

Figure 8.9(b) shows the dependence of the relative deviation of the effective range approximation from the exact cross-section on the scattering length (i.e. potential depth) for a fixed temperature of 200 μK. The effective range approximation clearly fails for $r_e \gg a$. On the other hand, it agrees very well close to a zero energy resonance ($a \to \pm\infty$) although the effective range expansion term $\frac{1}{2}k^2 r_e a \gg 1$. We will come back to this point in Chapter 9, where we compare experimental data with theory.

For van der Waals interaction potentials $-C_6/r^6$, the effective range is not a free parameter but related to the scattering length and the C_6 coefficient in the following way:

$$\begin{aligned} r_e = &\quad \frac{\sqrt{2\gamma}}{3}\left[\frac{\Gamma\left(\frac{1}{4}\right)}{\Gamma\left(\frac{3}{4}\right)} - 2\frac{\sqrt{2\gamma}}{a} + \frac{\Gamma\left(\frac{3}{4}\right)}{\Gamma\left(\frac{1}{4}\right)}\frac{4\gamma}{a^2}\right] \\ \approx &\quad \sqrt{\gamma}\left(1.395 - 1.333\frac{\sqrt{\gamma}}{a} + 0.637\frac{\gamma}{a^2}\right), \end{aligned} \tag{8.51}$$

where $\gamma = \sqrt{2m_\mu C_6}/\hbar$, $\Gamma(x)$ is the Gamma function and r_e, a and C_6 are given in atomic unit. This relation has been established analytically using a semi-classical approximation [184] and, independently, using a quantum-defect theory approach [185]. A plot of the effective range versus the scattering length for a C_6 coefficient of 1300 a_0 is shown in Figure 9.3 on page 124.

In the context of zero-energy resonances in Section 8.5.2, we have already discussed the influence of the last bound state on the scattering cross-section. A resonance occurs when the potential can just support a new bound state. In that case, the denominator of Equation 8.17 equals to zero. We can use this condition as the definition for the position of the last bound state with binding energy E_B^* and relate it to the scattering length and the effective range [171, Chap. 11]:

$$E_B^* = -\frac{\hbar^2}{2m_\mu}\left|\frac{1 \pm \sqrt{1 - 2\frac{r_e}{a}}}{r_e}\right|^2. \tag{8.52}$$

8.5.4 The contact interaction

In the previous subsections we have seen that the interaction between two atoms is governed by s-wave collisions which are characterized by the scattering length. In a Bose-Einstein condensate, millions of atoms interact with each other. It is now a well-known concept from theoretical physics (e.g. the Hartree-Fock approach), that these many particle interactions can be simplified in the zero temperature limit

to an effective interaction or *contact interaction*, sometimes also called a pseudo potential. In this regime, the thermal de Broglie wavelength is on the order of the inter-particle separation and much larger than the potential range. Therefore, the atoms "probe" an effective interaction integrated over many particles. The mean field concept has proven to be very successful and describes many features of Bose-Einstein condensates. It is given by $V(\vec{r}) = g\delta(\vec{r})$, where $\vec{r}$ is the particle separation and

$$g = \frac{4\pi\hbar^2 a}{m}. \tag{8.53}$$

is the coupling constant [186]. The stationary Schrödinger equation including particle interactions becomes nonlinear and is called the *Gross-Pitaevskii equation* (GPE)

$$\left[-\frac{\hbar^2}{2m}\nabla^2 + V_{\text{trap}}(\vec{r}) + g|\Psi(\vec{r})|^2\right]\Psi(\vec{r}) = i\hbar\frac{\partial}{\partial t}\Psi(\vec{r}), \tag{8.54}$$

where $\Psi(\vec{r})$ is the condensate wavefunction. It is important to note that the scattering length appears linearly and not squared as for the scattering cross-section. This has major consequences: a positive scattering length results in an effective repulsion of the atoms[8], whereas a negative scattering length leads to attraction and eventually a collapse of the BEC. Nevertheless, a BEC with attractive interactions can exist in a trap for a limited particle number due to the quantum repulsion in the trapping potential[9] and has been observed for ^{7}Li which has a negative scattering length [98, 187].

For condensates with a large number of atoms, the internal interaction dominates over the kinetic energy term in the GPE. In the Thomas-Fermi approximation, the latter is being neglected. The shape of the condensate in this approximation resembles the trapping potential, i.e. for a harmonic trap an ellipsoid. The half axes of this ellipsoid are the Thomas-Fermi radii

$$R_i^2 = \frac{2g}{m\omega_i^2}n = \frac{8\pi\hbar^2 a}{m^2\omega_i^2}n, \tag{8.55}$$

where n is the mean density and ω_i the trap frequency in direction i.

[8] The system is trying to minimize the interaction term by reducing the density given by $|\Psi(\vec{r})|^2$.

[9] The harmonic oscillator ground state in the trap has a certain size assoziated with it. The system is trying to maintain this size leading to quantum repulsion.

8.6 Atomic ground state collisions

8.6.1 Interaction potential

The interaction between two colliding atoms of the same species is very complex. Nevertheless, relatively simple Born-Oppenheimer[10] potentials with a limited set of free parameters have proven to describe the scattering process to a very good accuracy. The dominant interactions can be roughly divided into two regimes, which cross-over around the internuclear distance for which the potential depth is comparable to the hyperfine interaction[11]. For alkali metals this distance is roughly $r_c \sim 20\,\mathrm{a_0}$ [188]. In the inner region the electron clouds overlap and the strong exchange interaction dominates. If the valence electrons are in the same electronic and spin state (triplet state for alkali atoms with a single electron), Pauli's exclusion principle leads to a strong repulsion of the atoms. If they are not (singlet state), the covalent binding energy results in a strong attraction. The difference between the potential minima are of the order of the binding energy of the corresponding molecule. This effect can be observed from the triplet and singlet molecular potentials of ^{87}Rb shown in Figure 8.10. For very small internuclear separations, the exchange interaction of the inner shell electrons and the coulomb interaction result in a strongly repulsive potential.

For large separations $r \gtrsim 20\,\mathrm{a_0}$, the dominant interaction arises from induced fluctuations of the electron clouds which interact via induced electric multipole moments with each other. This dispersion interaction has the form

$$V_{\mathrm{disp}}(r) = -\frac{C_6}{r^6} - \frac{C_8}{r^8} - \frac{C_{10}}{r^{10}}, \tag{8.56}$$

in which the dominant term $-\frac{C_6}{r^6}$ is called the *van der Waals* dispersion term. It is a consequence of the induced dipole-dipole interactions of the electronic clouds. The higher order terms in the interaction potential are ususally small compared to the van der Waals term and will be neglected here.

For many applications, it is sufficient to use a model potential consisting of the van der Waals term and an exponential repulsion for $r \leq r_c$ [189]:

$$V(r) = \frac{1}{2} B r^{\alpha} e^{-\beta r} - V_{\mathrm{disp}} \times \left(\Theta(r - r_c) + \Theta(r_c - r) e^{-(r_c/r - 1)^2} \right), \tag{8.57}$$

where $\Theta(x)$ is the Theta-function and B, α and β are element specific parameters. The radius r_c is used to parametrize the short-distance behaviour of the repulsive

[10] The nuclear and electronic motion is being treated independently. Due to the large mass ratio the electrons "adiabatically" follow the nuclear motions. To obtain the Born-Oppenheimer potential, the electronic eigenenergies are being calculated for every nuclear separation.

[11] At this distance the recoupling from atomic to molecular states takes place. This distance might be much smaller for atoms without hyperfine structure, for which the much larger finestructure splitting is to be compared with the interaction potential.

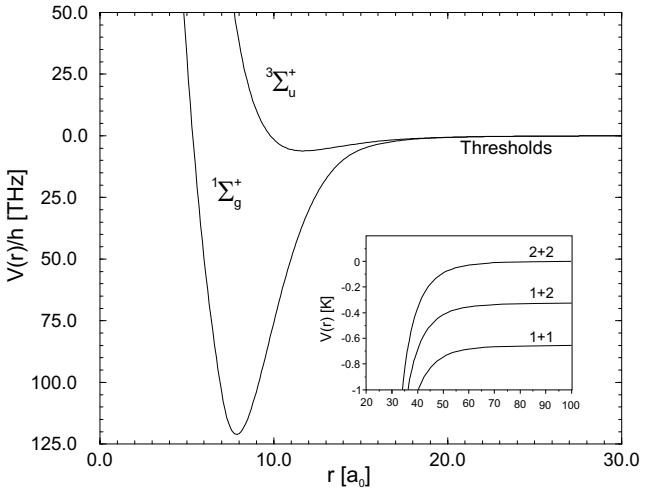

Figure 8.10: The ground state molecular potentials for Rb_2. The full figure shows the potentials on the range of chemical bonding. The inset shows a vertical enlargement at long range in which the hyperfine structure is resolved. The upper two potentials in the inset correlate with the $^3\Sigma_u^+$ molecular state (from: [73]).

part of the exact interaction potential, i.e. to obtain the same number of bound states as in the real potential. This truncated $1/r^6$ potential shows all features of cold atomic ground state collisions with neutral atoms.

We have learned in the previous sections that the position of the last bound (or virtual) state has profound consequences on the scattering properties. We have also seen that its position is extremely sensitive to slightest changes in the interaction potential. From spectroscopic measurements, one can obtain relatively precise information about the position of low-lying bound states in the singlet potential. This provides an accurate determination of the repulsive part of the potential. The structure of the bound states close to the dissociation limit, on the other hand, is determined by the dispersion potential [190]. It is a most formidable task for a theoretical physicist to construct model potentials for the interaction between two neutral atoms. The coefficients for these model potentials are usually not know to the precision required to determine the exact position of the last bound state, and therefore the scattering length. Experimental results on the ultra-cold scattering properties of atoms are usually used to fit the model patameters. Especially Feshbach resonance spectroscopy [66, 67, 68, 70, 191] and photoassociation spectroscopy [71, 72, 73] have proved to be powerful experimental methods to obtain data from which extremely accurate model potentials can be constructed.

For chromium, no such data is available up to now. There is one *ab inito* calculation of the chromium dimer molecular potential curves [81]. The result of this calculation

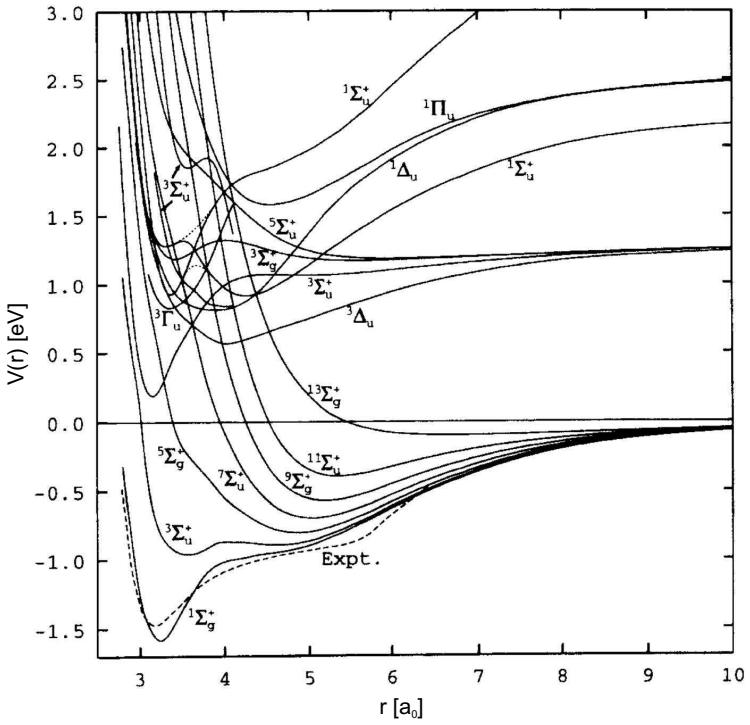

Figure 8.11: Molecular potential curves for the chromium dimer. From: [81].

is shown in Figure 8.11. We are scattering on the $^{13}\Sigma_g^+$ potential curve which adiabatically corresponds to the $(m_J = +3, m_J = +3)$ and $(m_J = -3, m_J = -3)$ atomic states. The accuracy of such calculations is not sufficient to predict the scattering length. In principle, it might allow to extract an approximate C_6 coefficient from the long range slope of the potential. Unfortunately, no data is available for internuclear distances exceeding $10\,a_0$. We have therefore used several other methods to obtain a C_6 coefficient for chromium. They are described in Appendix D.

8.6.2 Feshbach resonances

We have already discussed resonance phenomena in Sections 8.4 and 8.5.2. The properties of these resonances are fixed by the scattering potential. A Feshbach resonance on the other hand, is a multi-channel resonance that can be tuned via an external (usually a magnetic) field. The resonance occurs if the bound state of a closed channel[12] comes into resonance with the threshold energy of the open entrance channel.

[12] A channel is closed, if the total (kinetic and internal) energy of the colliding particles is lower than the internal energy for the collision on the closed channel.

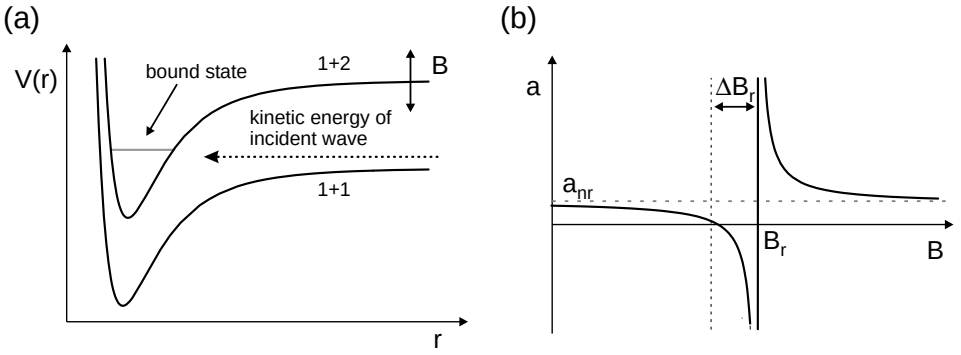

Figure 8.12: (a) A magnetic field shifts the $1+1$ and $1+2$ molecular potentials with respect to each other. A Feshbach resonance occurs, if a bound state of the closed $1+2$ potential comes into resonance with the kinetic energy of the incident wave. (b) Variation of the scattering length with the magnetic field close to a Feshbach resonance according to Equation 8.60.

In ultra-cold atomic collisions, the involved channels are usually molecular potentials of a hyperfine manifold. As an example, we have shown in Figure 8.12 the molecular potentials for two fictitious atoms having a nuclear spin $I = 3/2$, an electron spin $s = 1/2$ and an electronic angular momentum $\ell = 0$ each. The total angular momentum of such an atom can be $f = 1$ or $f = 2$. For two atoms colliding on the channel $\alpha = 1{+}1$, the $1{+}2$ and $2{+}2$ channels are closed. Magnetic shifting[13] of the molecular potentials allows to bring a bound state of channel $\beta = 1+2$ (gray line in the inset of Figure 8.10) in resonance with the threshold energy of the entrance channel. The hyperfine interaction between two atoms couples molecular potentials of the same electron configuration (m, ℓ). Therefore, the atoms can undergo a Landau-Zener type transition from one molecular potential to the other, mediated by the hyperfine interaction. In that case, the bound state of channel $1+2$ can decay into the continuum of the $1+1$ channel and is therefore a quasi-bound metastable state with a certain lifetime $\tau = \frac{\hbar}{\Gamma_{r\alpha}}$, with

$$\Gamma_{r\alpha} = 2\pi \left| \langle \, \phi_\beta \, | \, V_{\beta\alpha} \, | \, \phi_\alpha \, \rangle \right|^2_{E=E_r} , \tag{8.58}$$

where ϕ_α and ϕ_β are the scattering wave function and the normalized bound state wavefunction, respectively. The resonance can decay to several exit channel states α', including inelastic channels. The resonance mediated cross-section between entrance channel α and exit channel α' is then given by a Breit-Wigner type formula (see Equation 8.34 and [192]),

$$\sigma_{\alpha'\alpha} = \frac{4\pi}{k_\alpha^2} \frac{\Gamma_{r\alpha'}\Gamma_{r\alpha}}{4(E - \Delta_{r\alpha})^2 + \Gamma_r^2}, \tag{8.59}$$

[13] relative shifting of the potentials requires the magnetic moment of the involved channels to be different

where $\Gamma_r = \sum_\alpha \Gamma_{r\alpha}$ is the total resonance width. The detuning $\Delta_{r\alpha} = E_r - E_\alpha - s_{r\alpha}$ includes a possible energy shift $s_{r\alpha}$ of the bound state due to the interaction.

The properties of a Bose-Einstein condensate are dominated by the s-wave scattering length. Tuning this parameter allows to dramatically change its behaviour. Close to a Feshbach resonance, one can approximately write the scattering length as [193]

$$a_{FB}(B) = a_{nr}\left(1 - \frac{\Delta B_r}{B - B_r}\right), \tag{8.60}$$

where B_r is the magnetic field for which the resonance occurs and ΔB_r is its width. Provided the width of the resonance is sufficiently broad, the scattering length can be tuned to any desired value between $-\infty$ and $+\infty$ by adjusting the external magnetic field.

Tuning the scattering length close to a Feshbach resonance enables many fascinating experiments with ultra-cold atoms [23], including the coherent formation of molecules [194] in ^{85}Rb. Several groups [195, 196] are working on Feshbach resonances in fermionic ^{6}Li. Tuning the scattering length to large negative values results in a strong attraction between the atoms which might lead to a BCS (Bardeen-Cooper-Shrieffer) transition in a degenerate Fermi gas [197].

Bosonic chromium has no nuclear spin and therefore no hyperfine structure. Magnetic trapping is performed in the low field seeking state $m_J = 3$ in the $^7S_3$ electronic state. The molecular potential of two atoms in this state has the highest energy of all Zeeman potentials in a weak magnetic field (see Section 8.6.1). As a consequence, no closed channels and therefore no Feshbach resonances exist. The situation changes for atoms in the high field seeking state. Its energy can be lowered in a magnetic field with respect to all other states, making these molecular potentials to closed channels with respect to the entrance channel. Magnetic field shifting of the potentials might allow to observe Feshbach resonances in the high-field seeking state of chromium. This would allow to tune the s-wave interaction to any desired value. For chromium, the coupling mechanism between different molecular potentials is the spin-spin dipole interaction. In alkali atoms this interaction is rather weak compared to the hyperfine interaction and therefore leads to very narrow Feshbach resonances [191]. The large magnetic moment in chromium is expected to result in much broader Feshbach resonances. Trapping the atoms for such an experiment requires an optical dipole trap, since the atoms in that state would be expellend from a static magnetic trap. A similar experiment, in which coupling between different Zeeman states is involved, has been performed with ^{133}Cs in an optical dipole trap [191, 198].

8.6.3 Elastic and inelastic Dipole-Dipole scattering

The static magnetic dipole-dipole interaction is vanishingly small for alkali atoms with a magnetic moment of typically one μ_B (Bohr magneton). However, for

chromium with a magnetic moment of $6\,\mu_B$, dipole-dipole interactions are stronger by a factor of 36 and can therefore have an influence on the scattering and mean field properties of an ultra-cold gas.

The dipole-dipole interaction potential between two magnetic moments $\vec{\mu}_1$ and $\vec{\mu}_2$ separated by a distance r is given by

$$V_{\mathrm{dpdp}}(\vec{r}) = \frac{\mu_0}{4\pi r^3}\left[\vec{\mu}_1\vec{\mu}_2 - 3(\vec{\mu}_1\vec{n})(\vec{\mu}_2\vec{n})\right], \tag{8.61}$$

where μ_0 is the magnetic induction constant and $\vec{n} = \vec{r}/r$. In contrast to the isotropic contact interaction, this potential is long range ($1/r^3$ dependence) and due to the second term – anisotropic. The potential is attractive for two magnetic moments separated along the direction of their polarization, and repulsive for a separation perpendicular to it. The interaction strength for a maximally attractive configuration is twice as large as for the repulsive one. The average of Equation 8.61 over all interaction angles is 0. Therefore, the isotropic s-wave scattering cross-section vanishes identically [192]. The anisotropy of the interaction can be exploited to tune the elastic scattering cross-section. With a proper choice of experimental parameters, the magnetic dipoles can adiabatically follow a rotating external magnetic field ("spinning field"). The angle under which the dipoles rotate with respect to the rotation axis is called the "spinning-angle". The time-averaged interaction depends on this angle and can be tuned from positive to zero and even negative values [28]. This technique is well known from NMR experiments.

The long range character prevents the scattering cross-sections for higher partial waves from "freezing out" at low collision energy, since the Wigner threshold law holds only for potentials vanishing faster than $1/r^3$ for large r (see Section 8.3).

Besides elastic scattering, the dipole-dipole interaction can also lead to inelastic scattering: one or both atoms flip their spin and the Zeeman-energy is converted into kinetic energy. This inelastic process is called "dipolar relaxation" and results in loss of atoms from a magnetic trap (spin-flip to an untrapped state) and heating of the atomic sample. Only single $\Delta m_J = 1$ and double $\Delta m_J = 2$ spin-flips are possible in first order pertubation theory. Total angular momentum is conserved, since internal angular momentum is transfered to motional angular momentum. Dipolar relaxation collisions are different from the so-called "spin relaxation" or "purifying" collisions in which atoms in different m_J states exchange internal angular momentum. Subsequent collisions between two atoms in magnetic substates $m_J < J$ lead to untrapped atoms with $m_J \leq 0$ and polarized atoms with $m_J = J$. The rate constants for spin relaxation and dipolar relaxation collisions in alkali atoms are typically on the order of $\beta_{sr} \sim 10^{-11}\,\mathrm{cm^3/s}$ and $\beta_{dp} \sim 10^{-14}\,\mathrm{cm^3/s}$, respectively.

The scattering cross-sections for elastic and inelastic dipole-dipole scattering can be estimated by means of the first Born approximation[14]. Reference [78] outlines the

[14] In the first Born approximation the scattering amplitude $f(\vartheta)$ is basically given by the Fourier

procedure for the calculation of the elastic and inelastic scattering cross-sections for two atoms interacting *only* via the dipole-dipole interaction. Stefano Giovanazzi [199] has recalculated the cross-sections using a different symmetrization. We will summarize his results here. The cross-sections corresponding to no (σ_0), a single (σ_1) and a double (σ_2) spin-flip during the collision are given by:

$$\sigma_{dp}^0 = \frac{16\pi\tilde{a}^2}{45}\left[1 \pm h(1)\right] \tag{8.62}$$

$$\sigma_{dp}^1 = \frac{8\pi\tilde{a}^2}{15}\frac{k_f}{k_i}\frac{1}{J}\left[1 \pm h(k_f/k_i)\right] \tag{8.63}$$

$$\sigma_{dp}^2 = \frac{8\pi\tilde{a}^2}{15}\frac{k_f}{k_i}\frac{1}{J^2}\left[1 \pm h(k_f/k_i)\right], \tag{8.64}$$

with

$$h(x) = -\frac{1}{2} - \frac{3}{8}\frac{(1-x^2)^2}{x(1+x^2)}\log\left[\frac{(1-x)^2}{(1+x)^2}\right] \tag{8.65}$$

where the "+" sign holds for boson and the "-" sign for fermions, J denotes the total internal angular momentum of a single atom and $h(x)$ represents the ratio of the exchange contribution to the direct one. An effective scattering length for dipole-dipole scattering [200] can be defined by

$$\tilde{a} = \frac{\mu_0\mu^2 m_\mu}{4\pi\hbar^2}, \tag{8.66}$$

where μ is the magnetic moment of a single atom and m_μ is the reduced mass. This quantity is useful for comparing the contribution of dipole-dipole scattering to elastic collisions with the ordinary s-wave scattering. The cross-sections are already averaged over all possible orientations of the initial ($\vec{k}_i$) and final ($\vec{k}_f$) wavevectors with respect to the quantization axis given by the magnetic field direction. The factor $\frac{k_f}{k_i} = \sqrt{1 + \frac{2m_\mu\Delta E}{\hbar^2 k_i^2}}$ is the ratio between final and initial momentum. It accounts for the different density of states in the initial and final state. ΔE is the Zeeman energy released in the spin-flip collision, and is given by $\Delta E = 2\mu_B B$ and $\Delta E = 4\mu_B B$ for a single and double spin-flip collision between bosonic chromium atoms, respectively. It is clear that neglecting all other molecular interactions is a simplification of the scattering process. Nevertheless, it is expected — in the absence of resonances — that the cross-sections calculated in first order perturbation theory provide a good approximation. The resulting inelastic rate constant for chromium atoms is on the order of $\beta_{dp} \sim 10^{-11}\,\mathrm{cm}^3/\mathrm{s}$. This is almost three orders of magnitude larger than for alkali atoms and is a direct consequence of the high magnetic moment of $\mu = 6\mu_B$ in chromium.

transform of the interaction potential.

Dipolar relaxation is not limited to magnetic interaction. Also electric dipoles of e.g. polar molecules are subject to this relaxation mechanism. The huge dipole moments in these systems can lead to significant loss in electrostatic traps.

It is worthwhile to note that the correct physical quantity to describe dipolar relaxations depends on the details of the experimental situation. For large offset fields and low temperatures, dipolar relaxation is described by a rate coefficient β_{dp}. In the contrary case of low offset field and high temperature, the inelastic cross-section σ_{dp} is meaningful (see Appendix C.3).

We have discussed here the dipolar relaxation mediated by the long range spin-dipole–spin-dipole interaction. It is dominant in a region where the recoupling between atomic and molecular states takes place. Close to the inner turning point the electron orbitals overlap and the second order spin-orbit interaction [201, 202] dominates the relaxation process. Our model does not account for this additional contribution. Nevertheless, it can be of similar magnitude but different sign, thus either reducing or further increasing the total relaxation rate.

We will discuss the consequences of the large dipolar relaxation rate for evaporative cooling chromium atoms in a magnetic trap in Section 9.4.4 and present preliminary results of the measured relaxation rate in Appendix E.

8.6.4 Three-body recombination

Most Bose-Einstein condensates have a limited lifetime. They exist as a metastable state in the phase diagram of the substance used. Ultimately, three-body recombination will lead to the formation of bound molecules, a precursor to the solid state phase which is the thermodynamically stable state at the temperatures and densities encountered in a BEC. Energy and momentum conservation requires three atoms to collide to form a molecule. Two atoms form a weakly bound molecule and the third takes up the excess binding energy of the molecule. The rate constants for this process depend strongly on the details of the interaction potential. Nevertheless, for the recombination to a weakly bound s level, a universal event rate constant $\alpha_{rec} = 3.9\hbar a^4/m$, where a is the scattering length, can be found [203]. Three-body recombination plays a role only for very dense samples, since the rate constants are typically very small ($\alpha_{rec} \sim 10^{-27}\,\mathrm{cm}^6/\mathrm{s}$), but the loss rate scales with the third power of the density. In the experiments presented in this thesis, three-body recombination can be neglected.

8.7 Evaporative cooling

Evaporative cooling is a powerful technique to cool atomic ensembles below the critical temperature for Bose-Einstein condensation. It has been adopted to trapped

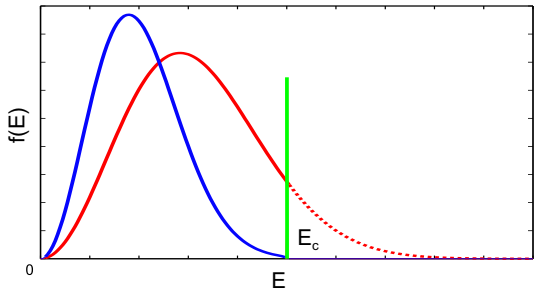

Figure 8.13: Principle of evaporative cooling: atoms with a kinetic energy exceeding E_c are removed from the sample (red curve). The remaining atoms thermalize to a lower temperature (blue curve).

atoms for the first time by Hess *et. al.* [204]. In the meantime this technique is widely used and has been extensively studied [151, 205, 206, to mention just a few].

The principle is the same as for a steaming cup of coffee or tea cooling down: the most energetic atoms are allowed to escape taking with them more than the average kinetic energy in the sample. The remaining atoms thermalize via elastic collisions to a lower temperature. We have sketched in Figure 8.13 the truncated Maxwell-Boltzmann distribution of a cloud of atoms. Atoms with a kinetic energy exceeding the cut-off energy E_c escape from the sample. The remaining atoms thermalize to a lower temperature via elastic collisions. This technique can be implemented in a variety of ways. Lowering the trap depth is a method which has proven to be very efficient in cryogenic magnetic trapping experiments [41, 204] and optical dipole traps [207, 208]. The most frequently used method is radio-frequency (rf) induced evaporative cooling. The principle is shown in Figure 8.14. Atoms in a low-field seeking magnetic substate ($m_{_J} = 1$) can undergo transitions to the untrapped $m_{_J} = -1$ state in the presence of radio-frequency field with frequency $\omega_{\rm rf}$. The magnetic field at which this occurs is given by the resonance condition $\Delta\omega_{\rm L} = \omega_{\rm rf}$, where $\Delta\omega_{\rm L}$ is the frequency difference between two magnetic substates:

$$|g_{_J}\mu_B B(\vec{r})| = \hbar\omega_{\rm rf}. \tag{8.67}$$

Strong coupling results in the adiabatic potentials shown in Figure 8.14(b). The cut-off energy for the atoms is given by the difference between the energy corresponding to the trap bottom (B_0) and the cut-off magnetic field:

$$E_c = |m_{_J}|\,\hbar\,(\omega_{\rm rf} - \omega_{\rm rf0}), \tag{8.68}$$

where $\omega_{\rm rf0} = |g_{_J}\mu_B B_0/\hbar|$ is the resonance frequency at the trap minimum.

The figure of merit for the overall efficiency of evaporative cooling is the steady state cut-off parameter $\eta = E_c/k_{\rm B}T$. Very efficient evaporative cooling is characterized

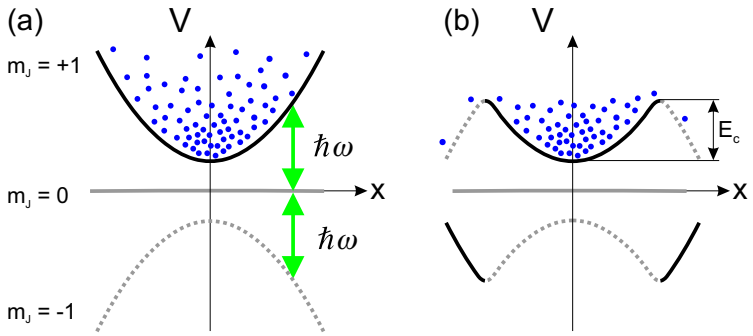

Figure 8.14: (a) Trapping potentials for atoms with $J = 1$. Radio-frequency drives transitions to the untrapped magnetic substate $m_J = -1$. (b) Adiabatic potential curves for a strong rf drive. Atoms that have a kinetic energy exceeding E_c can leave the trap.

by a high η. Applying the so-called "rf-knife" at a single frequency is not sufficient for reaching quantum degeneracy. In forced evaporative cooling, the rf-frequency follows the decreasing temperature of the cloud. During forced evaporation, the cut-off parameter η is kept at its optimum value. Evaporative cooling increases the phase-space density at the expense of the number of atoms left in the sample. Additional trap loss is caused by inelastic processes that can also heat the sample ("bad collisions"). The elastic collisions between atoms, on the other hand, lead to thermalization and therefore determine the cooling speed ("good collisions"). As a rule of thumb, the good to bad collision ratio has to be much larger than 100. If the scattering properties of the atomic species are well known, an optimum route to quantum degeneracy can be devised [151]. We have plotted the good/bad collision ratio in Figure 8.15 versus the temperature for different offset fields. We used the theoretical results (Equations 8.63, 8.64) for the dipolar relaxation rate from Section 8.6.3 and use the low order expression Equation 8.50 for the elastic cross-section assuming a scattering length of $a = 170\,\mathrm{a_0}$ (see next Chapter). Whereas the elastic scattering rate vanishes in the zero energy limit, the inelastic rate approaches a constant value which depends on the offset field. Therefore, the good/bad ratio also tends to zero. Only very small magnetic offset fields $B_0 \ll 0.1\,\mathrm{G}$ allow a sufficiently large good to bad collision ratio even at low temperature. Typical offset fields in evaporative cooling experiments are on the order of 1 G. The technical requirements to achieve a stable magnetic offset field of below 0.1 G are very demanding. A more sophisticated model including three-body recombination and background gas losses in addition to the elastic and dipolar relaxation collisions showed, that Bose-Einstein condensation of chromium in a magnetic trap requires sophisticated cooling and compression sequences, not achievable with our current setup [209].

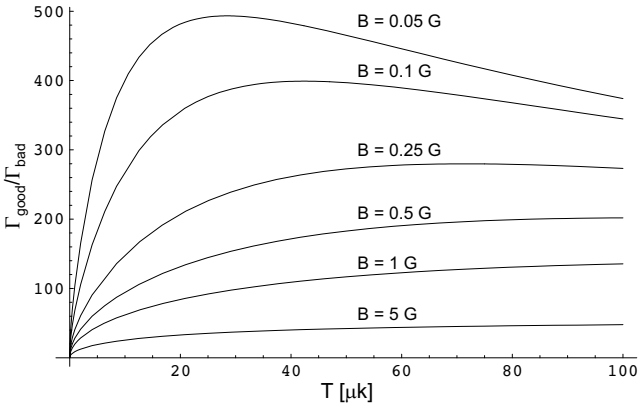

Figure 8.15: Temperature and magnetic field dependence of the good to bad collision ratio for chromium atoms. The elastic collision rate has been obtained from a thermal average of Equation 8.50 and the inelastic rate from a thermal average of the sum of Equations 8.63 and 8.64.

Chapter 9

Elastic collisions

In this chapter I present experimental results on the temperature dependence of the elastic collision rate for the chromium isotopes ^{52}Cr and ^{50}Cr. In Section 9.1 I give a short overview over previously performed relaxation experiments on the ultracold elastic scattering properties of alkali metals. Section 9.2 briefly describes the experimental procedure and data evaluation. The results are presented in Section 9.4 and compared with theory. I conclude in Section 9.5.

9.1 Introduction

We have already pointed out the importance of the scattering length for the properties of ultra-cold atomic gases. It usually dominates the interaction in a Bose-Einstein condensate (see Section 8.5.4) and together with the inelastic rate coefficients, it determines the efficiency of evaporative cooling (see Section 8.7).

Up to now, only the elastic scattering lengths for alkali metals, hydrogen and metastable helium have been determined experimentally. Several different methods have been successfully employed to perform this task. One of the probably most accurate methods is photo-association spectroscopy [71, 73]. During the collision process, two colliding ground state atoms are excited with a photoassociation laser to a bound state of the molecular potential which corresponds to one atom in the ground and one atom in the excited state. The excitation rate depends critically on the Franck-Condon factors (overlap of the initial and final wave functions at the excitation distance). In the highly excited states of the molecular potential, the magnitude of the wavefunction is peaked around the classical turning points. The slow variation of the wavefunction in the ground state can be mapped out by recording the rates for different excited molecular states with known resonance energy. From this map of the wavefunction, the scattering length can be directly deduced.

Another very accurate method is Feshbach resonance spectroscopy. Knowing the magnetic field dependence of Feshbach resonances for various hyperfine states allows to construct an accurate model potential from which the scattering length can be obtained [66, 67, 70].

Once a Bose-Einstein condensate has been created, the scattering length can be deduced from the measured density and Thoms-Fermi radius (Equation 8.55). The main uncertainty in this measurement stems from the difficulty in determining the density accurately. For negative scattering lengths, the condensate is stable only below a critical number of atoms. From this stability criterion, a value for the (negative) scattering length can be obtained.

The method used in our experiments relies on the characteristic temperature dependence of the elastic s-wave cross-section. By recording the relaxation of an anisotropic temperature distribution in an atomic cloud towards equilibrium, we obtain a relaxation time constant which can be translated into a scattering cross-section if the particle density is known. Monroe *et. al.* [74] performed such cross-dimensional relaxation experiment for spin-polarized ^{133}Cs in the $F = 3$, $m_F = -3$ state for the first time. Since then, this technique has been used to determine the ultra-cold scattering properties of cesium [210, 211], the rubidium isotopes [69, 212, 213], sodium [214], and potassium [215, 216], to mention just a few.

In all of these experiments, only the scattering cross-section, i.e. the magnitude of the scattering length could be determined, but not its sign. We have made an effort to measure the temperature dependence of the elastic cross-section for $J = 3$, $m_J = 3$ ^{52}Cr atoms over two orders of magnitude ranging from 5 to 500 μK. Comparing our data to the theoretical prediction for the temperature dependence of the s-wave cross-section in the effective range approximation, we obtain evidence for a large and positive scattering length for ^{52}Cr. The same experiment performed with ^{50}Cr over a smaller temperature range yields a much smaller scattering length, but does not allow to extract its sign.

The threshold for d- and p-waves in binary chromium collisions are $T_{\ell=2} \approx 1.8\,\mathrm{mK}$ and $T_{\ell=4} \approx 11\,\mathrm{mK}$ (see Section 8.3). With the exception of shape resonances, we do not expect significant contribution from d- or higher partial waves in the measured temperature regime.

9.2 Experimental procedure and data evaluation

9.2.1 Sample preparation

We prepare a magnetically trapped cold cloud of chromium atoms using our CLIP trap loading procedure described in Chapter 6 with subsequent Doppler cooling in the compressed magnetic trap as presented in Chapter 7. After Doppler cooling, we

relax the trap radially and compress it axially by reducing the magnetic offset field to 4 G, yielding trap frequencies of $\omega_r = \omega_x = \omega_y = 2\pi \times 124\,\mathrm{Hz}$ and $\omega_z = 2\pi \times 72.6\,\mathrm{Hz}$ in the radial and axial direction, respectively. In this trap, the atoms are further cooled via forced radio-frequency evaporative cooling (see Section 9.4.4). We adjust the temperature of our sample by choosing different end frequencies of the rf ramp. A typical result is shown in Figure 9.8. The evaporation ramp consists of several linear frequency ramps. The total duration is rather long ($\approx 6\,\mathrm{s}$ for the lowest temperatures) to obtain a cloud which is close to thermal equilibrium after evaporation. A 25 ms linear ramp of the magnetic offset field from 4 to 1.75 G increases the radial trapping frequencies to $\omega_r = 2\pi \times 207\,\mathrm{Hz}$. This adiabatic compression results in an anisotropic temperature distribution $T^i_{r,z}$ of the atoms in the trap, since the time scale for the modification of the trap is much faster than the mean time between collisions. Elastic collisions lead to a relaxation to the new steady state temperature $T^f = T^f_r = T^f_z = (2T^i_r + T^i_z)/3$ if no additional heating is present. After a variable thermalization time ranging from 10 ms to 2 s, an intra-trap absorption image as described in Section 5.5.3 is taken to obtain the spatial distribution of the atoms in the trap. A full 2-dimensional fit of Equation 4.11 to the density distribution yields the $1/\sqrt{e}$ sizes σ_r and σ_z of the cloud in the radial and axial direction, respectively. Assuming thermal equilibrium along the three principal axes, we obtain the temperature in radial and axial direction from the corresponding sizes of the cloud using Equations 4.9 and 4.10. As already discussed in Section 5.5.3, this imaging method does not yield the accurate number of atoms in the cloud due to Zeeman shifts and optical pumping. Also, the size of the cloud can be slightly distorted for the same reasons. Nevertheless, it can be used to observe *relative* changes in the size of the cloud, as required for a relaxation experiment.

In the real experimental situation, inelastic processes, dominated by dipolar relaxation (see Section 8.6.3), lead to atom loss and heating. Especially at very low temperatures, this process results in a significant decrease of the density during the thermal relaxation. We account for this effect by employing the time rescaling method of Hopkins *et. al.* [211], which we develop in the following. The relaxation rate $\Gamma_{\mathrm{rel}}(t)$ is in general time dependent via the density. The differential equation of the temperature relaxation is then given by

$$\frac{d\Delta T(t)}{dt} = -\Gamma_{\mathrm{rel}}(t)\Delta T(t), \tag{9.1}$$

where $\Delta T(t) = T_r - T_z$ is the temperature difference between the radial and axial temperature. The solution is easily obtained using the initial condition $\Delta T(0) = \Delta T_0$:

$$\Delta T(t) = \Delta T_0\, e^{-\int_0^t \Gamma_{\mathrm{rel}}(t')\,dt'}. \tag{9.2}$$

The time dependence of the relaxation rate arises from the density $n(t)$, which usually decreases during a relaxation measurement. Inserting $\Gamma_{\rm rel}(t) \propto n(t)$ in Equation 9.2, we obtain

$$\Delta T(t^*) = \Delta T_0 \, e^{-\Gamma_{\rm rel}(0) t^*}, \tag{9.3}$$

where the rescaled time t^* is given by

$$t^*(t) = \frac{1}{n(0)} \int_0^t n(t') \, dt'. \tag{9.4}$$

An exponential fit to $\Delta T(t)$ yields a relaxation time constant $\tau_{\rm rel}$. We have verified that the relaxation time constant is inversely proportional to the density of the cloud, ruling out anharmonic mixing.

We deliberately prepared a rather low number of atoms ranging between 3×10^5 and 2×10^7 atoms for the highest and lowest temperature, respectively, to obtain relaxation time constants on the order of 200 ms. The peak density is typically on the order of 3×10^{11} cm^{-3}. Faster relaxation times conflict with the speed at which we are able to ramp the magnetic fields. Figure 9.1 shows a typical relaxation measurement for a cloud with a mean temperature of $\bar{T}(t) = (2T_r(t) + T_z(t))/3 \approx 42\,\mu$K. We have plotted the evolution of the mean temperature in the inset. A slight increase in temperature for long thermalization times can be attributed to dipolar relaxation collisions. This heating can be significant for very low temperatures and partially mask the relaxation effect. For the exponential fit, we use only data points whose mean temperature does not significantly exceed the initial temperature.

The density and temperature of the cloud are obtained from a separate time-of-flight measurement using absorption imaging (see Section 5.5.2). The atoms are prepared in exactly the same way as in the corresponding relaxation experiment for a fixed relaxation time of $t = 100$ ms. From a measurement of the trap frequencies we know the trap parameters to within a few percent. We can therefore use Equation 5.11 to fit the data with the temperature as the only fit parameter. Figure 9.2 shows a typical TOF measurement corresponding to the thermalization data in Figure 9.1.

Altough the temperatures obtained from the TOF and the intra-trap measurement usually agree to within $\approx 10\,\%$, we always used the more accurate TOF result for the temperature. The density was deduced from an average over the fitted number of atoms from each TOF picture and the initial size of the cloud obtained from the TOF fit.

9.3 Relaxation and collision rates

The elastic collision rate $\Gamma_{\rm coll}$ in an ultra-cold cloud of atoms is given by

$$\Gamma_{\rm coll} = \bar{n}(t) < \sigma(v) v >_{\rm therm}, \tag{9.5}$$

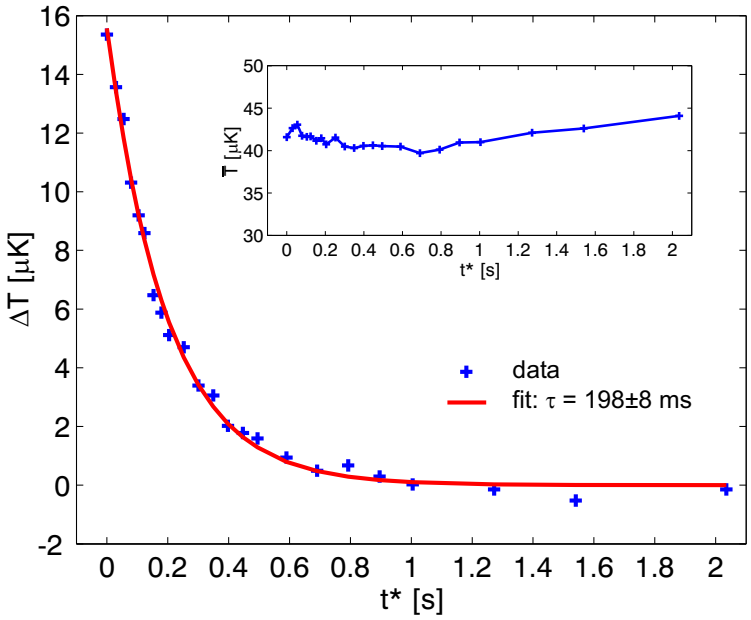

Figure 9.1: Thermal relaxation versus rescaled time of a cloud of ^{52}Cr atoms in a magnetic trap after an abrupt change of the radial trap frequency from $\omega_r = 2\pi \times 124\,\mathrm{Hz}$ to $\omega_r = 2\pi \times 207\,\mathrm{Hz}$. The line is an exponential fit to the data. The inset shows the evolution of the mean temperature of the cloud.

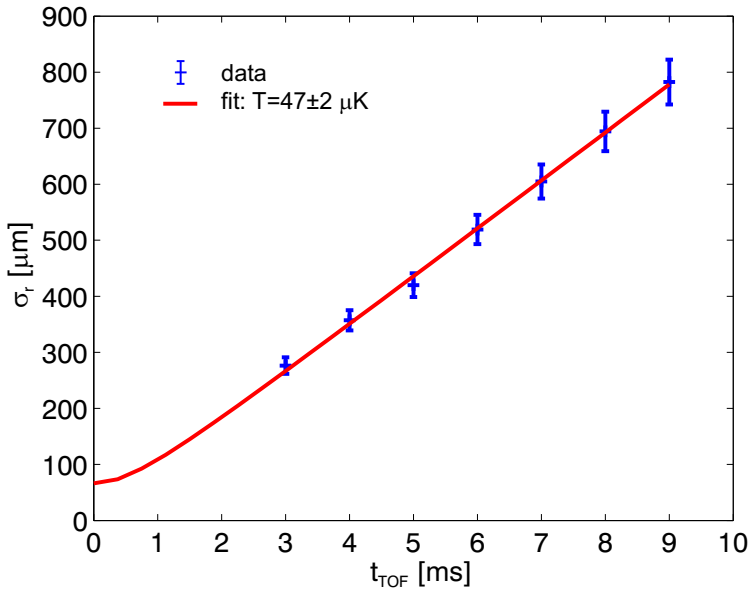

Figure 9.2: Time-of-flight measurement for the data set shown in Figure 9.1. The line is a fit of Equation 5.11 to the data with $T = 47 \pm 2\,\mu\mathrm{K}$.

where $\sigma(v)$ is the velocity dependent s-wave elastic cross-section, $<\cdot>_{\mathrm{therm}}$ denotes thermal averaging (see Appendix C) and $\bar{n} = \int n^2(\vec{r})dV / \int n(\vec{r})dV$ is the mean density. In a harmonic trap the latter can be related to the peak density n_0 by $\bar{n} = {}^{n_0}/\sqrt{8}$. A limited redistribution of energy in the collision process requires each atom to scatter more than once before the cloud reaches thermal equilibrium. The relaxation rate for this thermalization process can be related to the collision rate by $\Gamma_{\mathrm{coll}} = \alpha\Gamma_{\mathrm{rel}}$, where α is in general a temperature dependent factor. In Monte-Carlo simulations $\alpha = 2.7$ has been determined for a temperature independent elastic cross-section [74, 210, 217]. This value seems to be universal for all atomic species and independent of details of the trapping parameters. Analytical [160, 218] solutions of the Boltzmann equation confirmed this result. For a temperature dependent cross-section $\sigma \sim {}^1/_T$, more than 2.7 collisions are needed for thermalization. Scattering preferentially occurs at low collision energies which contribute less to thermalization. From Monte-Carlo simulations $\alpha = 10.7$ was deduced [210], and a somewhat smaller value of $\alpha \approx 8$ from the analytical treatment [218]. The transition from the temperature-dependent to the temperature-independent regime depends on the characteristic temperature of the elastic cross-section (see Equation 8.50) $T_0 = \frac{\hbar^2}{k_{\mathrm{B}} m a^2}$. Although most of the data presented here is below this temperature of $T_0 \approx 150\,\mu\mathrm{K}$ for ^{52}Cr, we are in an intermediate regime where the temperature dependence of α can be significant. We therefore use the analytical result for the relaxation rate from [218] to analyze our data. It is given by

$$\Gamma_{\mathrm{rel}}(T) = \frac{1}{2.65}\,\frac{\bar{n}\,\bar{v}_r}{6(k_{\mathrm{B}}T)^4}\int_0^\infty \sigma_0(E)\,E^3\,e^{-\frac{E}{k_{\mathrm{B}}T}}\,dE = \bar{n}{<}\sigma_0(E)\cdot v\cdot F(E){>}. \quad (9.6)$$

The second equality defines the shorthand notation in which the function $F(E)$ transforms the thermal average over the elastic collision rate into that over a thermal relaxation rate. We will compare different approximations and limits of the s-wave elastic cross-section with our data. The most detailed information can be obtained from the effective range approximation (see Section 8.5.3) of the cross-section[1]:

$$\sigma_0^{(2)}(a, r_e, E) = \frac{8\pi a^2}{a^2k^2 + (\frac{1}{2}k^2 r_e a - 1)^2}, \quad (9.7)$$

where $k^2 = mE/\hbar^2$ is the square of the relative wave vector, m the chromium mass, a the scattering length and r_e the effective range of the potential. The latter can be derived from the scattering length and the C_6 coefficient using Equation 8.51. In Figure 9.3(a) we have plotted the effective range for ^{52}Cr assuming C_6 =1300 a.u. versus the scattering length. Since the effective range is related to the inverse of the scattering length, it diverges for $a \to 0$. The effective range approximation

[1] the cross-section is larger by a factor of 2 compared to Equation 8.50 due to identical particle effects (see Section 8.1.3)

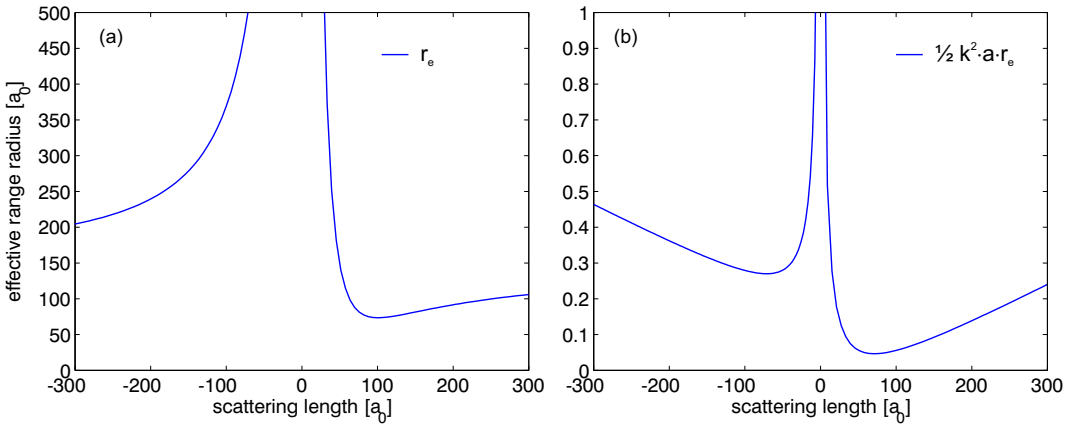

Figure 9.3: (a) Effective range r_e as a function of the scattering length a for a collision energy of $E = k_\mathrm{B} 100\,\mu\mathrm{K}$. The effective range diverges for vanishing scattering length. In this regime the approximation fails. Close to a scattering resonance (a diverges), the effective range approaches a constant value. (b) Second order expansion coefficient of the scattering phase for $T = 100\,\mu\mathrm{K}$. Usually, the effective range approximation requires $\frac{1}{2}k^2 a r_e \ll 1$ (see text).

(truncation of the expansion of the scattering phase in Equation 8.46 after the k^2 term) requires $\frac{1}{2}k^2 a r_e \ll 1$. We have plotted this term for ^{52}Cr and a temperature of $T = 100\,\mu\mathrm{K}$ in Figure 9.3 (b). For vanishing or negative scattering lengths, r_e and thus the expansion term are large. From our discussion of the validity of the effective range expansion in Section 8.5.3 it is clear that it is very difficult to judge at which point the effective range approximation fails. A large expansion term does not necessarily lead to a strong deviation from the exact cross-section. Comparing the effective range approximation with the exact solution for a square-well potential led us to a rule of thumb stating that the requirement $\frac{1}{2}k^2 a r_e \ll 1$ is sufficient as long as the effective range does not exceed the scattering length.

Using only the first order term of the expansion in Equation 8.46 yields a lower order approximation for the temperature dependence of the scattering cross section:

$$\sigma_0^{(1)}(a, E) = \frac{8\pi a^2}{k^2 a^2 + 1}. \tag{9.8}$$

This approximation connects the correct low temperature behaviour of the exact cross-section with the high temperature limit. The zero energy limit for the s-wave scattering cross-section (see Equation 8.41) is given by

$$\sigma_0^{(0)}(a) = 8\pi a^2 \tag{9.9}$$

and is independent of collision energy. For very large collision energies it oscillates between zero and a temperature dependent maximum value (see Figure 8.4) given

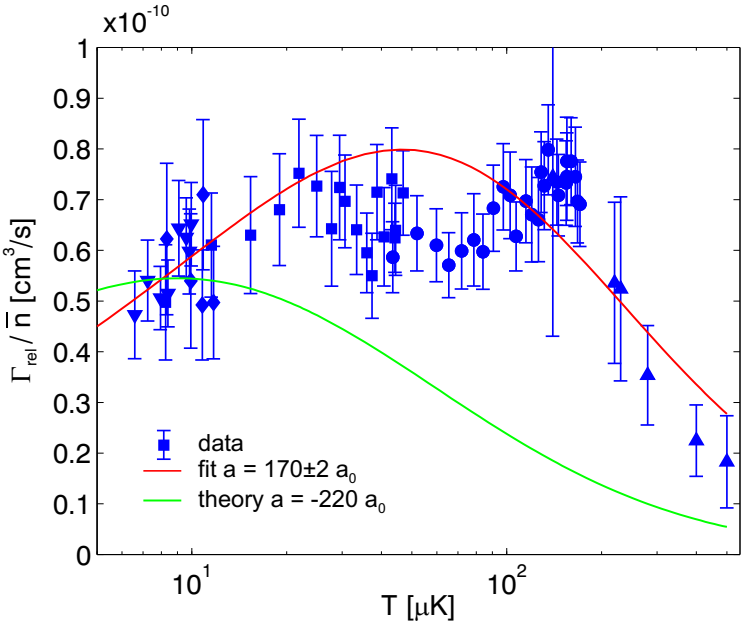

Figure 9.4: Temperature dependence of the density normalized relaxation rate for ^{52}Cr. The red line is a fit of Equation 9.6 which results in a positive scattering length of $a = 170 \pm 2a_0$. The green line corresponds to a negative scattering length of $a = -220a_0$. The error bars are derived from statistical and calibration uncertainties. Data from different experimental runs are labeled by the plot symbols.

by the unitarity limit

$$\sigma_0^{(u)}(E) = \frac{8\pi}{k^2}. \tag{9.10}$$

In this regime s-wave scattering is independent of the details of the interaction potential. We will discuss the different approximations and their validity in the next Section.

9.4 Results

9.4.1 Deca-triplet scattering length of ^{52}Cr

We have performed relaxation rate measurements for ultra-cold ^{52}Cr covering a temperature range of almost two orders of magnitude. The main result is shown in Figure 9.4 where we have plotted the density normalized relaxation rate $\Gamma_{\rm rel}/\bar{n}$ versus the mean temperature. The data is a compilation from 5 different experimental runs, each run indicated by a different plot symbol. The highest temperature data points

(upward pointing triangles) have been obtained in a completely different vacuum system and a different magnetic trap setup ("old system", see Chapter 5). Also, the data evaluation differs slightly: the relaxation curve has been determined from a full time-of-flight sequence for each relaxation time. We observe excellent agreement between this and the rest of the data sets in the overlap region, indicating good reproducability.

Two theory curves are plotted with the data. The red line is a fit of Equation 9.6 to the data points below $25\,\mu$K using the effective range scattering cross-section $\sigma_0^{(2)}(a, r_e, E)$ with $C_6 = 1300\,$a.u. which results in an $r_e = 86\,\mathrm{a_0}$ and a scattering length of $a = 170 \pm 3\,\mathrm{a_0}$, where $a_0 = 0.53$Å is Bohr's radius. This curve is in good agreement with the measured relaxation rates for low- ($\lesssim 25\,\mu$K) and high-temperatures ($\gtrsim 100\,\mu$K). In the intermediate temperature range we observe a small deviation of the measured relaxation rates from the theoretical prediction. The reason for this discrepancy remains unclear. A more sophisticated theoretical analysis based on a multi-channel quantum defect treatment of the scattering process using model potentials for chromium molecules might give further insights into the details of ultra-cold chromium collisions and might help to resolve this issue.

The green line is a plot of Equation 9.6 assuming a negative scattering length. A scattering length of $a = -220\,\mathrm{a_0}$, resulting in an effective range $r_e = 229\,\mathrm{a_0}$, has been chosen to achieve best agreement with the lowest temperature relaxation data. It is obvious from the plot that the assumption of a negative scattering length is incompatible with our relaxation data. For the interpretation of the theory curves, the validity of the effective range expansion has to be considered. From the plot of the second order term $\frac{1}{2}k^2 r_e a$ for a temperature of $100\,\mu$K in Figure 9.3, one can deduce[2] that the effective range expansion for $a = 170\,\mathrm{a_0}$ is valid for temperatures $< 450\,\mu$K. Assuming a negative scattering length, the large effective range limits the validity to temperatures $< 130\,\mu$K.

To show the qualitative difference between positive and negative scattering length more clearly, we have plotted in Figure 9.5 the effective elastic cross-section (see Equation C.9

$$\sigma_{\mathrm{eff}}(T) := \frac{2.65\,\Gamma_{\mathrm{rel}}(T)}{\bar{n}\,\bar{v}_r}, \tag{9.11}$$

where $\bar{v}_r = \sqrt{\frac{8k_{\mathrm{B}}T}{\pi m_\mu}}$ is the relative thermal velocity. The effective range expansion term is smaller than 0.1 for $a = 170\,\mathrm{a_0}$ and smaller than 0.4 for $a = -220\,\mathrm{a_0}$ over the shown temperature range. We therefore assume the effective range approximation to be valid under these experimental conditions. The effective cross-section assuming a negative scattering length has a much steeper slope in the low temperature regime as compared to assuming a positive one. This is a direct consequence of the minus

[2] The expansion term scales linearly with energy.

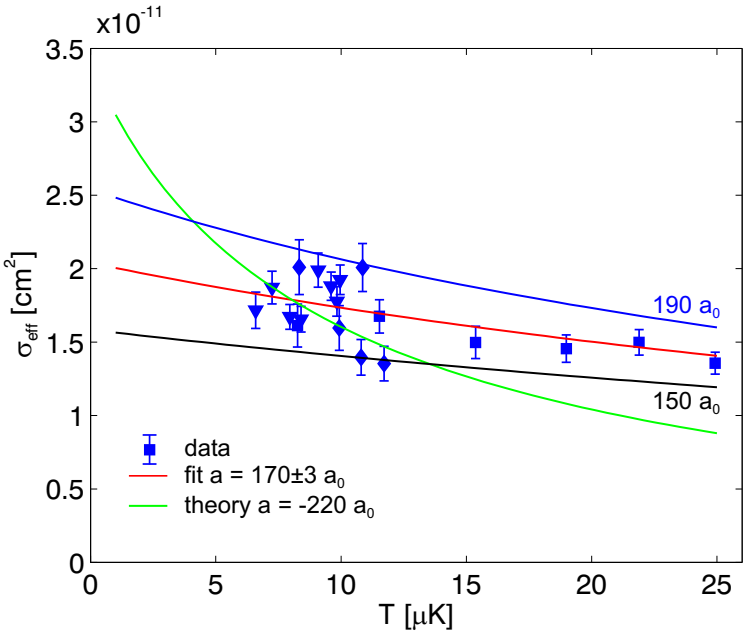

Figure 9.5: Temperature dependence of the effective elastic cross-section of ^{52}Cr for $T \to 0$. The data has been obtained from Figure 9.4 using Equation 9.11. The lines are theory curves derived in the same way for $a = 140$, 170 and $190\,a_0$ along with a negative scattering length of $a = -220\,a_0$.

sign in the denominator of Equation 9.7. As a result, the shape of cross-sections and relaxation rates for negative a is always distinct from positive scattering lengths. The fit for $a > 0$ clearly shows very good agreement with the measured cross-sections in contrast to the $a = -220\,a_0$ curve. We have therefore strong evidence for a positive scattering length. Our data is compatible with a scattering length of $a = 170 \pm 20\,a_0$. The main source of systematic errors in these types of experiments is the uncertainty of around 20 % in determining the density of the atomic cloud. Including this systematic error, we arrive at our final result of $a_{52}^{dt} = 170 \pm 39\,a_0$ for the deca-triplet scattering length of ^{52}Cr.

9.4.2 Comparison between different regimes of the elastic cross-section

Many different approximations have been used for analysing cross-dimensional relaxation data [74, 210, 213]. To our knowledge, we have implemented for the first time the analytical result of [218] for the temperature dependence of the relaxation rate.

We have plotted in Figure 9.6 various limits and approximations of the thermally

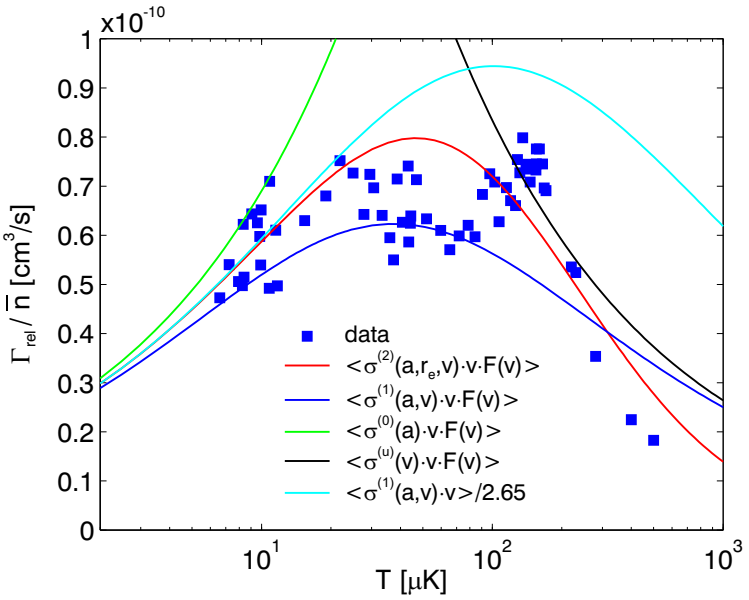

Figure 9.6: Different approximations and limits of the relaxation rate as defined by Equations 9.7-9.10 (see text for more details). The function $F(v)$ incorporates the energy dependence of the cross-dimensional relaxation process. $< \cdots >$ denotes thermal averaging.

averaged relaxation rate together with the data obtained for ^{52}Cr. The green curve corresponds to the relaxation rate for the temperature independent cross-section in the $T \to 0$ limit given by Equation 9.9. It diverges for increasing temperature since the thermal velocity increases without limit. The opposit limit for high temperatures is given by the unitarity cross-section Equation 9.10 (black curve). As discussed in the previous Subsection, the low order approximation given by Equation 9.8 (dark blue curve) interpolates between these limits. We have also plotted the thermal average of the density normalized *elastic collision* rate in this approximation divided by a constant factor of $\alpha = 2.65$ to convert it into a relaxation rate. This has been the most frequently used approximation in analysing relaxation data. As we can see from the plot, the assumption of a temperature independent factor of $\alpha = 2.65$ is valid up to a few tens of micro Kelvins (light blue curve). The red curve is the best fit of the thermal averaged effective range approximation for the elastic cross-section (Equation 9.7) which we have already shown in Figure 9.4. As expected from our discussion of a square well potential in Section 8.5.3 it interpolates the oscillation of the s-wave elasic cross-section between zero and the unitarity limit for high temperature (see also the inset in Figure 8.9(a)). It is noteworthy that our data does not exceed the unitarity limit. This is an indication that no severe error in the determination of the atomic density in the trap has been made.

In conlusion, we have verified that the theoretical prediction for the relaxation rate

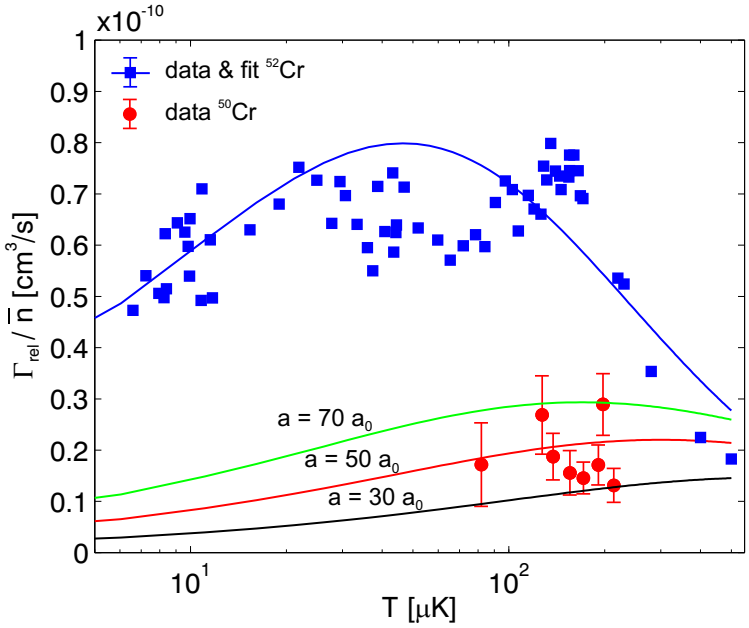

Figure 9.7: Density normalize cross-dimensional relaxation rates for ^{52}Cr (blue squares) and ^{50}Cr (red circles). The blue line is the fit from Figure 9.4 to the data for ^{52}Cr. The black, red and green line are plots of $< \sigma^{(1)}(v,a)vF(v) >$ with $a = 30\,a_0$, $50\,a_0$ and $70\,a_0$, respectively.

using the elastic cross-section in the effective range approximation yields the best overall agreement with the measured data.

9.4.3 Deca-triplet scattering length of ^{50}Cr

The knowledge of the scattering lengths for two different isotopes of the same atomic species with the same nuclear spin can give further insights into the vibrational structure of the topmost bound levels of the involved molecular potentials. Scattering length and effective range can be used to determine the energy of the last bound level close to the dissociation limit via Equation 8.52. From semi-classical quantization formulas [175, 190, 219], information on the slope of the molecular potential can be obtained.

We have therefore performed relaxation measurements for the chromium isotope ^{50}Cr, which is a boson and also has zero nuclear spin. In Figure 9.7 we have plotted the results of the relaxation experiment for ^{50}Cr (red circles) and included for comparision the previously shown data for ^{52}Cr (blue squares). Obviously, the density normalized relaxation rates for ^{52}Cr are much smaller than those for ^{52}Cr. We have

plotted the theoretical relaxation rates according to the low order approximation[3] of the elastic cross-section (Equation 9.8) for three different scattering lengths: $a = 30$, 50 and $70\,a_0$ (from bottom to top). Comparing these theory curves with the data points, we derive an approximate value for the ^{50}Cr deca-triplet scattering length of $|a_{50}^{dt}| = 50 \pm 23\,a_0$, where we have again assumed a systematic uncertainty on the order of 20 %. Theoretical studies have shown, that there is a 75 % probability of finding a positive scattering length for a random potential depth [182]. Especially a "normal" scattering length of around $50\,a_0$ might indicate a positive sign.

Owing to the low natural abundance of only 4.4 %, we were unable to prepare significantly more than 7×10^6 atoms at the highest measured temperature even though we operated the oven at an elevated temperature of 1625 °C. Dipolar relaxation rates on the same order of magnitude as for ^{52}Cr but a much smaller elastic collision cross-section resulted in a rather poor good/bad collision ratio making evaporative cooling inefficient (see Appendix E). This prevented us from achieving higher densities and lower temperatures for the relaxation measurement. Ultimately, our lowest temperature data were limited by the signal to noise ratio of our detection system.

Since we have used exactly the same techniques for both chromium isotopes, systematic errors should affect the results for the scattering lengths in the same way. A more sophisticated theoretical model for ^{52}Cr collisions could significantly reduce the systematic uncertainty and would at the same time improve the prediction for the ^{50}Cr cross-sections.

9.4.4 Evaporative cooling

The rather large scattering length for ^{52}Cr is very promising for efficient evaporative cooling. In Section 8.6.3 we have already mentioned that the disturbing influence of dipolar relaxation collisions can be minimized with a small magnetic offset field. We have therefore performed an experiment in which we increased the phase-space density by forced radio-frequency evaporative cooling (see Section 8.7) at a very low magnetic offset field. We prepared a cloud of atoms as described in Section 9.2. After Doppler cooling, we lowered the trap bottom to an offset field of $B_0 \approx 140\,\mathrm{mG}$ and reduced the radial and axial trap parameters to trap frequencies of 500 Hz and 42 Hz in radial and axial direction, respectively. Subsequently, the atoms were cooled down using a radio-frequency ramp consisting of eight consecutive linear frequency sweeps, each optimized to yield the maximum gain in phase-space density per atom number loss. Figure 9.8 shows the phase-space density for different intermediate frequencies of the fully optimized ramp resulting in a different number of remaining atoms. We achieved a maximum phase-space density of 0.04 ± 0.013 at a temperature

[3] The effective range theory fails in this temperature regime due to the small scattering length and the large effective range of $r_e \approx 150\,a_0$.

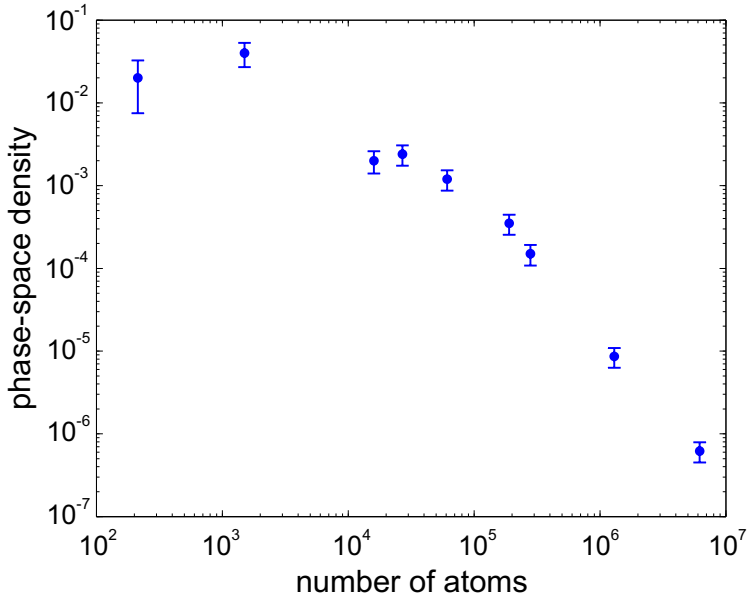

Figure 9.8: Phase-space density versus remaining number of atoms at different intermediate evaporative cooling steps.

of $370 \pm 52\,\mathrm{nK}$ and a peak density of $(6.5 \pm 1.7) \times 10^{11}\,\mathrm{cm}^{-3}$. At that point, two orders of magnitude away from quantum degeneracy, we had only 1500 ± 260 atoms left in the trap. Further cooling did not increase the phase-space density, since the loss in density outweighed the reduction in temperature. This has been confirmed by a more detailed study of the high phase-space density region. As already mentioned in Section 8.6.3, the high magnetic moment in chromium leads to a large dipolar relaxation rate. This inelastic process limits the efficiency of evaporative cooling especially in the low temperature region (see also Figure 8.15). Preliminary results on the dipolar relaxation rate for chromium isotopes in the low-field seeking magnetic substate are presented in Appendix E.

9.5 Conclusion

Cross-dimensional relaxation measurements over a temperature range of almost two orders of magnitude have been presented. Comparing the lowest temperature (5-25 μK) data with theoretical predictions for the thermally averaged relaxation rates in the effective range approximation allowed us to determine the deca-triplet scattering length of ^{52}Cr in the $J = 3$, $m_j = 3$ magnetic substate to $a_{52}^{dt} = 170 \pm 39\,\mathrm{a_0}$. Assuming the effective range expansion to be valid in this regime, we have a strong indication for a positive scattering length. From relaxation data for ^{50}Cr, we deduce

a deca-triplet scattering length of $|a_{50}^{dt}| = 50 \pm 23\,\mathrm{a_0}$ in the $J = 3$, $m_j = 3$ magnetic substate with a high probability of having a positive sign.

We hope that the experimental data presented here inspires and encourages theoretical investigations in the scattering properties of chromium atoms. Together with *ab initio* calculations of the molecular potentials of neutral chromium dimers [81], model potentials for a multi-channel quantum defect formalism could be constructed. Such a calculation would not only aid in explaining the elastic but also the inelastic properties of scattering in the $J = 3$, $m_J = 3$ state. Of special interest are also the scattering properties in the ($m_J = -3$, $m_J = -3$) channel, which is not only immune against inelastic dipolar relaxation collisions, but is also expected to exhibit magnetically tunable Feshbach resonance. Experiments towards Bose-Einstein condensation of chromium in this state using an optical dipole trap are underway.

Chapter 10

Summary and perspectives

In this Chapter I give a summary of the results presented in this thesis and discuss their consequence for future investigations. Prospects for exciting experiments with a Bose-Einstein condensate of chromium atoms conclude the Chapter.

10.1 Summary

The properties of Bose-Einstein condensates with alkali atoms are governed by the isotropic contact interaction arising from s-wave scattering. Chromium on the other hand, has a large magnetic dipole moment which can lead to a significant dipole-dipole interaction in a chromium BEC. In contrast to the contact interaction, the dipole-dipole interaction is anisotropic and long-range. These features are expected to alter the properties of a BEC and may lead to new phenomena.

In this thesis I have presented experimental results of the scattering properties of ultra-cold chromium atoms. This represents a significant progress towards a Bose-Einstein condensate with chromium atoms. Deviating from the standard approach for the preparation of ultra-cold atoms, we have devised a continuous loading scheme for a magnetic trap from a magneto-optical trap. Doppler cooling of the atoms in the magnetic trap further reduces the temperature of the cloud. Subsequent forced radio-frequency evaporation resulted in a maximum phase-space density of 0.04. Strong dipolar relaxation collisions originating from the large magnetic dipole moment of chromium prevented us from reaching quantum degeneracy. We measured the magnetic field dependence of the dipolar relaxation rate which was typically on the order of $\beta_{dp} = 10^{11}\,\mathrm{cm}^3/\mathrm{s}$, in excellent agreement with theory. Probably the most important parameter for ultra-cold scattering of chromium atoms is the scattering length. We were able to perform a detailed measurement of the temperature dependence of the elastic collision rate. Comparison with theory allowed us to extract $a(^{52}\mathrm{Cr}) = 170 \pm 39\,\mathrm{a}_0$ for the scattering length of ^{52}Cr ($a_0 = 0.53$Å is

Bohr's radius). For ^{50}Cr we determined the magnitude of the scattering length to be $|a(^{50}\mathrm{Cr})| = 50 \pm 23\,\mathrm{a}_0$.

The thesis began with an introduction of the main characteristics of chromium relevant for this work, with special emphasis on the spectroscopic properties. In Chapters 3 and 4, I presented the basic theoretical concepts for laser cooling and trapping and purely magnetic trapping of atoms. A detailed description of the experimental apparatus was given in Chapter 5. I outlined the design of the cloverleaf magnetic trap, vacuum chamber and the cooling and repumping laser system. The computer control of the experiment together with the imaging techniques for the atomic cloud and the data evaluation procedure have also been addressed.

The specific spectroscopic properties of chromium together with its high magnetic moment allowed us to devise a continuous loading scheme of a Ioffe-Pritchard trap from a MOT. I introduced this so-called CLIP trap scheme in Chapter 6. Atoms in the excited state of the MOT can undergo a transition to a long-lived metastable state, where they are magnetically trapped and decoupled from the MOT laser light. With 2×10^8 atoms in the CLIP trap, we were able to accumulate up to 40 times more atoms than were captured in the MOT. Furthermore, the direct accumulation of the atoms in a Ioffe-Pritchard magnetic trap greatly simplifies the subsequent preparation process for an ultra-cold sample. I presented a detailed study of the temperature, number of atoms and the effective loading time constants for various trap geometries. We identified two major loss mechanisms from the CLIP trap. A model based on rate equations allowed us to extract the corresponding event rate coefficients for the inelastic processes from our data. In collisions between excited atoms from the MOT and magnetically trapped atoms, part of the excitation energy is converted into kinetic energy, leading to a loss of atoms with a rate coefficient of $\beta_{ed} = 5 \times 10^{-10} \pm 45$ % cm^3/s. Inelastic collisions between magnetically trapped atoms in the metastable state limit the lifetime of atoms in this state. We determined the corresponding rate coefficient to be $\beta_{dd} = 1.3 \times 10^{-11} \pm 17$ % cm^3/s. This rather large value prevented us from using the metastable state for subsequent experiments. Therefore the atoms are optically pumped back into the electronic ground state after loading for further experiments.

Subsequent compression of the magnetic trap increases the density of the atomic sample, but also their temperature. In Chapter 7 I presented a simple technique to cool the magnetically trapped atoms via one-dimensional Doppler cooling without significant atom loss or depolarization. Though only an axial cooling laser beam was applied, we observed cooling also in the radial direction. I presented detailed studies of the dynamical evolution and steady-state temperature of the Doppler cooled cloud. With measurements of the intensity and optical density dependence of the radial cooling rate, we could rule out anharmonic mixing and elastic collisions as the source of the radial cooling. In our model, the high optical density of the atomic cloud leads to reabsorption of scattered cooling photons. Including this effect

in the standard treatment of Doppler cooling, we could qualitatively explain our experimental findings. We observed temperatures close to the Doppler temperature of $124\,\mu$K in axial, and approximately a factor of two higher in radial direction.

Further cooling of the atoms was performed via radio-frequency induced evaporative cooling. This method is based on the selective removal of the most energetic atoms. Elastic collisions thermalize the remaining atoms to a lower temperature. The efficiency of this cooling mechanism is strongly dependent on the elastic and inelastic scattering properties of the atoms. Since these properties were unknown for chromium prior to this work, I introduced the basic concepts of ultra-cold scattering theory in Chapter 8. Using the square-well as a model potential, I could illustrate the most prominent features of low energy scattering. S-wave scattering, characterized by the scattering length a, is dominant in this regime. I also addressed the special features of atom-atom scattering, including Feshbach resonances, elastic and inelastic dipole-dipole scattering and three-body recombination. A brief description of the evaporative cooling technique was given at the end of the Chapter.

Experimental results on the elastic ground state properties of the two bosonic chromium isotopes ^{52}Cr and ^{50}Cr were presented in Chapter 9. We determined the elastic collision rate over a temperature range of almost two orders of magnitude in a cross-dimensional relaxation experiment. In this method the trap geometry is changed rapidly after evaporative cooling of the atoms. This creates an anisotropic temperature distribution. From the collision-driven relaxation towards the new equilibrium temperature, the elastic scattering cross-section could be determined. Comparing the data to an effective range theory allowed us to not only determine the magnitude of the s-wave scattering length, but also its sign. For ^{52}Cr, we found a scattering length of $a(^{52}\mathrm{Cr}) = 170 \pm 39\,\mathrm{a_0}$. The low natural abundance of ^{50}Cr restricted the measurement of the relaxation rates to a smaller range at higher temperature. Therefore, only the magnitude of the scattering length could be determined: $|a(^{50}\mathrm{Cr})| = 50 \pm 23\,\mathrm{a_0}$. We also presented the results of our efforts to achieve Bose-Einstein condensation via evaporative cooling. A maximum phase-space density of 0.04 ± 0.013 at a temperature of $370 \pm 52\,$nK and with 1500 ± 260 remaining atoms corresponding to a peak density of $(6.5 \pm 1.7) \times 10^{11}\,\mathrm{cm}^{-3}$ was achieved. Further cooling did not increase the phase-space density due an increased trap loss originating from dipolar relaxation collisions.

Preliminary results on the magnetic field dependence of the rate constants for dipolar relaxation collisions at a temperature of $300\,\mu$K were presented in Appendix E. We find excellent agreement between our experimental data and theory. At a magnetic offset field of $B_0 = 20\,\mathrm{G}$, we obtain a loss rate coefficient of $\beta_{dp} = 10^{11}\,\mathrm{cm}^3/\mathrm{s}$. A measurement of the dipolar relaxation induced heating rates in atomic clouds of ^{52}Cr and ^{50}Cr showed comparable heating rates for both isotopes. Therefore, we could confirm with this experiment the theoretical prediction that dipolar relaxation collisions are independent of the details of the interaction potential but rather scale

with the magnetic offset field and the magnetic moment. This is in contrast to elastic s-wave scattering which sensitively depends on the interaction potential.

The results of this work represent an important step towards a Bose-Einstein condensate with atomic chromium. Especially the knowledge of elastic and inelastic ground state scattering properties allow now to devise a successful route to BEC with chromium.

10.2 Perspectives

The strong dipolar relaxation rate in magnetically trapped chromium in the low-field seeking state prevented us from reaching the quantum degenerate regime. In an optical dipole trap [42], the atoms can be trapped in the high-field seeking magnetic substate which is the absolute ground state of the system. Energy conservation suppresses dipolar relaxation from this state. A promising implementation of this concept would start by preparing an ultra-cold cloud of chromium atoms using the methods developed in this thesis. Radio-frequency induced evaporative cooling to a temperature of around $10\,\mu$K in the magnetic trap prepares the atoms for the transfer into the optical dipole trap. The latter consists of two crossed, horizontally aligned, far-off resonant laser beams from a fiber laser, tightly focussed onto the center of the magnetic trap. The atoms are transfered from the magnetic into the dipole trap and then into the high field seeking magnetic substate, thus eliminating dipolar relaxation. Assuming an adiabatic transfer, we can estimate a density of around $10^{13}\,\mathrm{cm}^{-3}$ and a temperature of $50\,\mu$K in the dipole trap. Evaporation is then achieved by slowly lowering the potential of the optical trap. The large elastic scattering cross-section in chromium determined in this work, facilitates efficient evaporative cooling. We estimate an initial elastic collision rate of $21\,1/\mathrm{s}$. Experiments towards a chromium BEC in an optical dipole trap implementing this scheme are currently underway.

Once BEC in chromium has been achieved, many fascinating experiments are possible. The influence of the dipole-dipole interaction is probably most easily observable in a ballistic expansion experiment [29]. Tuning the dipole-dipole interaction with magnetic spinning techniques [28] allows to change the aspect ratio of the expanding cloud. Further investigation of dipolar effects in a BEC requires a reduction of the contact interaction arising from s-wave scattering. Magnetic tuning of the scattering length via a Feshbach resonance in the optically trapped high field seeking magnetic substate might allow to diminish or even completely cancel the contact interaction as has been shown in a cesium BEC [25]. It is expected, that the strong dipole-dipole interaction results in sufficiently broad Feshbach resonances in chromium. Investigation of the positions and widths of these Feshbach resonances also contributes to the knowledge of the molecular interaction potentials in a chromium dimer. Together

with the scattering properties determined in this thesis, accurate model potentials could be constructed that aid in further understanding the ultra-cold scattering properties of chromium atoms.

In a system with vanishing contact interaction, the influence of dipolar interactions on the ground state wave-function as well as the stability and collapse of the condensate can be explored [31, 33] by tuning the dipole-dipole interaction [28]. These experiments would be complementary to the investigation of the collapse of a BEC under the influence of an attractive contact interaction [24, 220].

A periodic array of dipolar condensates, e.g. in an optical lattice, allows to investigate several solid-state physics effects in a very "clean" and controllable model system. Ferromagnetism [34] and macroscopic spin tunneling [221] are expected to be observable in such studies.

Sympathetic cooling of the fermionic isotope ^{53}Cr into the quantum degenerate regime constitutes another fascinating direction of investigation. In a first step, its ultra-cold scattering properties need to be explored, using the experimental techniques developed in this work. So far, dipolar interactions in fermionic systems have only been touched theoretically. One can only guess what interesting effects lie in wait here to be discovered.

We expect, that the dipole-dipole interaction in degenerate quantum gases of chromium atoms will significantly enrich the variety of effects observable in such systems. The ability to tune both, the contact and the dipole-dipole interaction, will enable a whole series of exciting experimental investigations in Bose-Einstein condensates that contribute to our understanding of this new form of matter.

Appendix A

Light scattered by a single atom

We have already discussed in Chapter 3 the effects of light scattering on the motion of an atom. In this Appendix, we are interestend in the polarization and spectral properties of the scattered light. Reabsorption of the scattered photons can lead to cooling effects as discussed in Chapter 7.

A.1 Spectral properties

In general, scattered light from a single atom at rest exhibits two distinct contributions: a coherent part, I_{coh}, arising from the mean dipole oscillating in phase with the driving field and an incoherent part, I_{incoh}, originating from fluctuations of the atomic dipole [83, 222]. The frequency spectrum of the coherent part (also known as Rayleigh peak) is identical to the driving laser field of the incident beam, with a mean steady state intensity

$$< I_{\text{coh}} > \propto \frac{s}{(1+s)^2}, \tag{A.1}$$

where s is the saturation parameter as defined by Equation 3.7. The frequency spectrum of the incoherent part is far more complicated and depends on the intensity and detuning Δ given by Equation 3.8. In general, the spectrum of the incoherent part consists of at most three components which can have different frequencies and spectral widths. We will discuss a few limiting cases in the following. For resonance scattering ($\Delta = 0$) in the low intensity limit ($\Omega_R \ll \Gamma$), the incoherent spectrum consists of three components having the same laser frequency $\omega_{\text{laser}} = \omega_{\text{atom}}$ and linewdiths of $\Gamma/2$ and Γ for the first two and the last component, respectively. For low intensity off-resonant scattering ($|\omega_{\text{laser}} - \omega_{\text{atom}}| \gg \Omega_R, \Gamma$, the spectrum consists of a line at the excitation frequency ω_{laser} with a linewidth of 2Γ and two sidebands with a linewidth of $\Gamma/2$ located at $\omega_{\text{laser}} \pm \Delta\Gamma$. In the high intensity limit for

resonance scattering, the well known Mollow-Triplet [83] emerges with a resonant line having a linewidth of Γ and two sidebands at $\omega_{\text{atom}} \pm \Omega_R$ with a linewidth of $3\Gamma/2$. All frequency components differing from the incident laser frequency involve multi-photon processes. The total intensity of the incoherent contribution to the fluorescence spectrum is given by

$$< I_{\text{incoh}} > \propto \frac{s^2}{(1+s)^2}. \tag{A.2}$$

As a consequence of energy conservation, the frequency weighted integrated spectrum of the scattered and the incident light are equal. This is no longer true for atomic ensembles in which collisions play a role. An additional component at the atomic transition frequency with the linewidth of the transition arises at the expense of the elastic component. The energy difference $\hbar\omega_{\text{atom}} - \hbar\omega_{\text{laser}}$ to shift the frequency of the photon is provided by the collision partner.

In our system, the mean time between two collisions $\tau \approx 1\,\text{s}$ is much larger than the excited state lifetime $1/\Gamma \approx 30\,\text{ns}$ of the atoms. Therefore we can safely neglect the influence of collisions on the fluorescence spectrum. The intensity ratio between coherent and incoherent contribution to the spectrum is $\frac{<I_{\text{coh}}>}{<I_{\text{incoh}}>} = \frac{1}{s}$. Since the saturation parameter for the Doppler-cooling light in our experiment is on the order of $s = 1\,\%$, we can also neglect the incoherent contribution to the fluorescence spectrum.

For a moving atom, the Doppler shift of the photon frequency and momentum and energy conservation during the scattering process have to be taken into account. The classical treatment of the elastic scattering of a photon by a moving atom gives a maximum frequency shift for the photon of

$$\Delta\omega = -4\,\omega_{\text{rec}} - 2\,\vec{v}\cdot\vec{k}, \tag{A.3}$$

where $\vec{v}$ is the velocity of the atom and $\vec{k}$ is the wavevector of the photon. The total frequency shift has to be smaller than the laser detuning of $\Delta \approx -0.5\,\Gamma$ for Doppler cooling by reabsorption to be efficient. The first term on the right hand side of Equation A.3 is the recoil shift $4\,\omega_{\text{rec}} \approx 0.02\,\Gamma$, which is small compared to the atomic linewidth. The second term arises from the Doppler shift, which is on the order of $2\,\vec{v}\cdot\vec{k} \approx 0.2\,\Gamma$ at Doppler temperature. On average, more photons are scattered by atoms counterpropagating the cooling laser ($\vec{v} = -|v|\cdot\vec{e}_z$). Therefore, the Doppler shift increases the energy of the scattered photon towards the atomic resonance. From these considerations it becomes clear, that the Doppler shift of the scattered photon limits the efficiency of reabsorption cooling to a few scattering events.

A.2 Polarization properties

In our model, all atoms are polarized along the quantization axis in z-direction and can only absorb light which is σ^+ polarized with respect to this quantization axis (see next section). The scattering atom can be modeled by two oscillating dipoles oriented along the x and y direction having a phase shift of π with respect to each other. The near field complex electric field vector in cartesian coordinates is given by

$$\vec{\epsilon}_1 = \frac{1}{\sqrt{2}} \begin{pmatrix} -1 \\ -i \\ 0 \end{pmatrix}_{xyz} . \tag{A.4}$$

Here we have used the transformation rules for electric fields between the $\sigma^+/\pi/\sigma^-$-basis and cartesian coordinates:

$$\begin{pmatrix} \epsilon^x \\ \epsilon^y \\ \epsilon^z \end{pmatrix}_{xyz} = \frac{1}{\sqrt{2}} \begin{pmatrix} 1 & 0 & -1 \\ -i & 0 & -i \\ 0 & \sqrt{2} & 0 \end{pmatrix} \begin{pmatrix} \epsilon^- \\ \epsilon^\pi \\ \epsilon^+ \end{pmatrix}_{-\pi+} , \tag{A.5}$$

and

$$\begin{pmatrix} \epsilon^- \\ \epsilon^\pi \\ \epsilon^+ \end{pmatrix}_{-\pi+} = \frac{1}{\sqrt{2}} \begin{pmatrix} 1 & i & 0 \\ 0 & 0 & 1 \\ -1 & i & 0 \end{pmatrix} \begin{pmatrix} \epsilon^x \\ \epsilon^y \\ \epsilon^z \end{pmatrix}_{xyz} . \tag{A.6}$$

To obtain the electric field components of the light propagating in the direction of the unit vector $\vec{r}$, we have to project the electric field onto two orthogonal unit vectors $\vec{s}_1$, $\vec{s}_2$, that form a mutually orthogonal tripod with $\vec{r}$. One choice of vectors is the following:

$$\vec{r} = \begin{pmatrix} \cos\phi \sin\vartheta \\ \sin\phi \sin\vartheta \\ \cos\vartheta \end{pmatrix}_{xyz}, \quad \vec{s}_1 = \begin{pmatrix} \sin\phi \\ -\cos\phi \\ 0 \end{pmatrix}_{xyz}, \quad \vec{s}_2 = \begin{pmatrix} \cos\vartheta \cos\phi \\ \cos\vartheta \sin\phi \\ -\sin\vartheta \end{pmatrix}_{xyz}. \tag{A.7}$$

The propagating electric field $\vec{\epsilon}_2$ in cartesian coordinates is then given by

$$\vec{\epsilon}_2 = (\vec{\epsilon}_1 \cdot \vec{s}_1)\vec{s}_1 + (\vec{\epsilon}_1 \cdot \vec{s}_2)\vec{s}_2 \tag{A.8}$$

$$= \frac{1}{\sqrt{2}} \begin{pmatrix} e^{i\phi} \cos\phi \sin^2\vartheta - 1 \\ e^{i\phi} \sin\phi \sin^2\vartheta \\ e^{i\phi} \cos\vartheta \sin\vartheta \end{pmatrix}_{xyz} . \tag{A.9}$$

Only the σ^+ component with respect to the quantization axis in z-direction of the field $\vec{\epsilon}_2$ can be absorbed by the polarized atoms. Transforming $\vec{\epsilon}_2$ back into the $\sigma^+/\pi/\sigma^-$-basis gives

$$\vec{\epsilon}_2 = \begin{pmatrix} \frac{1}{2}e^{2i\phi}\sin^2\vartheta \\ \frac{1}{\sqrt{2}}e^{i\phi}\cos\vartheta\sin\vartheta \\ \frac{1}{2}(1+\cos^2\vartheta) \end{pmatrix}_{-\pi+} . \tag{A.10}$$

From the σ^+ component of $\vec{\epsilon}_2$, we obtain the normalized angular distribution for the scattered light that can be reabsorbed by polarized atoms:

$$\frac{\mathrm{d}P_{\mathrm{sp}}(\vartheta)}{\mathrm{d}\Omega} = \frac{3}{32\pi}(1+\cos^2\vartheta)^2 \tag{A.11}$$

In summary, the light scattered by the atoms has the same spectral width as the incident laser light, but is slightly shifted closer to the atomic resonance by the Doppler shift. The angular distribution of the σ^+-component of the emitted light with respect to the quantization axis is given by Equation A.11.

Appendix B

Effective intensity coefficients

In this Appendix, we sketch the derivation of the proportionality constants $\kappa_{y,z}$ between effective $I_{\text{eff}}^{y,z}$ and incident laser intensity I_0 used in Chapter 7. The effective intensity arises from scattering of photons from a laser beam into all directions. The light can be reabsorbed by other atoms in the cloud and is treated in the Doppler cooling theory as if originating from a separate light source. We will take only a single scattering/reabsorption event into account. Figure B.1 shows a sketch of the model. Let us consider a single monochromatic laser beam with homogeneous intensity I_0 (approximation for a beam size much larger than the diameter of the cloud) propagating along the axial direction. In brief, we derive the intensity scattered by a point source at $\vec{r}_0 = (x_0, y_0, z_0)$ as seen by an atom located at $\vec{r}_1 = (x_1, y_1, z_1)$. Averaging over all positions $\vec{r}_0$ and $\vec{r}_1$ and taking into account only the projection of the emitted intensity onto the direction of interest, we obtain numerical values for the coefficients κ_y, κ_z.

We start by evaluating the intensity of the incident laser beam as seen by an atom at

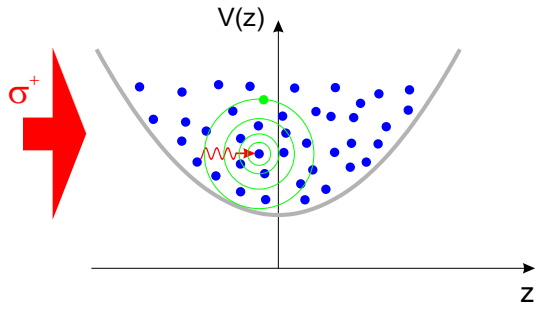

Figure B.1: Illustration of the reabsorption process. A photon (red wavy arrow) from the incident laser beam is scattered by an atom. The scattered wave (green) is absorbed by another atom according the the emission pattern and absorption probability.

position $\vec{r}$. Scattering of light in the cloud with Gaussian density distribution $n(\vec{r})$ results in a spatially varying intensity gradient given by the following expression:

$$I_{\mathrm{inc}}(\vec{r}) = I_0 \exp\left\{-\sigma_\lambda \int_{-\infty}^{z} n(x,y,z')\mathrm{d}z'\right\} \tag{B.1}$$

$$= I_0 \exp\left\{-\sigma_\lambda \frac{N_0}{4\pi\sigma_y^2} \exp\left[-\frac{x^2}{2\sigma_x^2} - \frac{y^2}{2\sigma_z^2}\right]\right. \tag{B.2}$$

$$\left. \times \left[1 + \mathrm{Erf}\left(\frac{z_0}{\sqrt{2}\sigma_z}\right)\right]\right\}, \tag{B.3}$$

where $\mathrm{Erf}(\cdot)$ is the error function, N_0 the number of atoms and σ_x, σ_y and σ_z are the $1/\sqrt{e}$ radii of the cloud in the x, y and z direction, respectively. In the low intensity limit, the light power P_{sc} scattered by an atom is proportional to the incident intensity of the light:

$$P_{\mathrm{sc}}(\vec{r}) = \frac{\hbar\omega\Gamma}{2} \frac{I_{\mathrm{inc}}(x,y,z)/I_s}{1 + 4(\Delta/\Gamma)^2} = \sigma_\lambda \frac{I_{\mathrm{inc}}(x,y,z)}{1 + 4(\Delta/\Gamma)^2}, \tag{B.4}$$

where $\sigma_\lambda = 6\pi\lambda^2$ is the resonant scattering cross-section and λ the wavelength of the transition. Each atoms acts as a point source emitting the scattered power according to the dipole radiation pattern with the intensity falling off as $1/r^2$ with distance r from the source. We must only take into account the fraction of the light that can be reabsorbed by the polarized atoms. The angular distribution is then given by Equation A.11. The intensity at point $\vec{r}_1$ emitted from a volume element $\mathrm{d}V_0$ at position $\vec{r}_0$ is given by

$$\mathrm{d}I_{\mathrm{sc}}(\vec{r}_0, \vec{r}_1) = \frac{3P_{\mathrm{sc}}(\vec{r}_0)}{32\pi|\vec{r}_1 - \vec{r}_0|^2}(1 + \cos^2\vartheta_e)^2 n(\vec{r}_0)\mathrm{d}V_0, \tag{B.5}$$

where $\cos\vartheta_e = \frac{(z_1 - z_0)}{|\vec{r}_1 - \vec{r}_0|}$ is the cosine of the azimuth angle of emission with respect to the quantization axis. The total intensity of the scattered light at position $\vec{r}_1$ is obtained by integrating Equation B.5 over all scattering volume elements $\mathrm{d}V_0$. Weighting this result with the normalized density distribution and integrating over all final positions $\vec{r}_1$ yields the mean intensity. κ is the proportionality constant between the laser intensity I_0 and the mean intensity of light scattered into any direction. It is given by

$$\kappa = \int_V \mathrm{d}V_0 \int_V \mathrm{d}V_1 \, \frac{\mathrm{d}I_{\mathrm{sc}}(\vec{r}_0, \vec{r}_1)}{I_0} \, \frac{n(\vec{r}_1)}{N_0}. \tag{B.6}$$

Similarly, the contribution of the scattered intensity to an effective intensity in the y and z direction is obtained by projecting the emitted intensity onto these direction.

The effective intensity coefficients for these directions then read

$$\kappa_y = \int_V \mathrm{d}V_0 \int_V \mathrm{d}V_1 \, \frac{\mathrm{d}I_{\mathrm{sc}}(\vec{r}_0, \vec{r}_1)}{I_0} \, \frac{n(\vec{r}_1)}{N_0} |\sin\vartheta_e| \, |\sin\phi_e| \tag{B.7}$$

$$\kappa_z = \int_V \mathrm{d}V_0 \int_V \mathrm{d}V_1 \, \frac{\mathrm{d}I_{\mathrm{sc}}(\vec{r}_0, \vec{r}_1)}{I_0} \, \frac{n(\vec{r}_1)}{N_0} |\cos\vartheta_e|, \tag{B.8}$$

where $\sin\phi_e = \sqrt{1 - \frac{(x_1 - x_0)^2}{|\vec{r}_1 - \vec{r}_0|^2}}$ is the sine of the polar angle of emission with respect to the quantization axis. Although no analytic result can be found, numerical integration of these Equations yield coefficients that can be compared with experimental results.

Appendix C

Thermal averaging of rates and cross-sections

The collision process between two atoms is conveniently described in the center of mass reference system. The important physical quantities in the scattering process have no explicit dependence on the center of mass coordinates nor momentas. Therefore, the center of mass evolution is trivial and will be neglected below. The normalized Maxwell-Boltzmann distribution for the relative velocity $\vec{v}_r$ is given by

$$f(\vec{v}_r, T)\,\mathrm{d}^3 v_r = \left(\frac{m}{\pi k_\mathrm{B} T}\right)^{\frac{3}{2}} e^{-\frac{m_\mu \vec{v}_r^2}{2k_\mathrm{B}T}}\,\mathrm{d}^3 v_r \tag{C.1}$$

where $m_\mu = \frac{m_1 m_2}{(m_1+m_2)}$ is the reduced mass. We can write the distribution in polar coordinates with $v_r = |\vec{v_r}|$ and, assuming a spherically symmetric scattering problem (s-wave scattering), integrate the angular part and obtain

$$f(v_r, T)\,\mathrm{d}v_r = \frac{1}{\sqrt{4\pi}} \left(\frac{m}{k_\mathrm{B} T}\right)^{\frac{3}{2}} v_r^2\, e^{-\frac{m_\mu v_r^2}{2k_\mathrm{B}T}}\,\mathrm{d}v_r \tag{C.2}$$

$$f(E, T)\,\mathrm{d}E = 2\sqrt{\frac{1}{\pi}}\,(k_\mathrm{B} T)^{-\frac{3}{2}}\,\sqrt{E}\, e^{-\frac{E}{k_\mathrm{B}T}}\,\mathrm{d}E. \tag{C.3}$$

In Equation C.3 we have transformed the distribution to collision energies.

C.1 Elastic collision rates

The thermal average of the density normalized event rate for elastic collisions is given by $<\sigma\, v_r>_{\rm th}$, or in integral form

$$<\sigma\, v_r>_{\rm th} = \int_0^\infty \sigma(E)\sqrt{\frac{2E}{m_\mu}}\, f(E,T)\,{\rm d}E \tag{C.4}$$

$$= 2\sqrt{\frac{2}{3\pi m_\mu}}\,(k_{\rm B}T)^{-\frac{3}{2}} \int_0^\infty \sigma(E)\, E\, e^{-\frac{E}{k_{\rm B}T}}\,{\rm d}E. \tag{C.5}$$

We can define an effective thermally averaged elastic cross-section in the following way:

$$\sigma_{\rm eff}(T) := \frac{<\sigma\, v_r>_{\rm th}}{\bar{v}_r} = (k_{\rm B}T)^{-2} \int_0^\infty \sigma(E)\, E\, e^{-\frac{E}{k_{\rm B}T}}\,{\rm d}E, \tag{C.6}$$

where $\bar{v}_r = \sqrt{\frac{8k_{\rm B}T}{\pi m_\mu}}$ is the relative thermal velocity.

C.2 Thermal relaxation rates

A cloud of atoms with an anisotropic temperature distribution thermalizes to a uniform steady state temperature at a relaxation rate $\Gamma_{\rm rel}$. We denote the number of collision events per atom required to thermalize the cloud as $\alpha(T)$. It is in general temperature and cross-section dependent. Kavoulakis *et. al.* [218] have solved the Boltzmann equation for the thermal relaxation of a trapped cloud of atoms analytically. We will present here their main result, which has been used to fit the relaxation data for ^{52}Cr and ^{50}Cr in Chapter 9. Their solution for the temperature dependence of the thermal relaxation rate for a general form of the elastic cross-section using a simple trial function for the variational ansatz is given by

$$\Gamma_{\rm rel}(T) = \frac{2}{5}\,\frac{\bar{n}\,\bar{v}_r}{6(k_{\rm B}T)^4} \int_0^\infty \sigma(E)\, E^3\, e^{-\frac{E}{k_{\rm B}T}}\, dE, \tag{C.7}$$

where

$$\bar{n} = \frac{\int n^2(\vec{r})dV}{\int n(\vec{r})dV} = \frac{n_0}{\sqrt{8}} \tag{C.8}$$

is the density weighted density or mean density of the atoms in the trap. The second equality hold for a cloud with peak density n_0 in a harmonic trapping potential. Besides some constant factors, Equation C.7 differs from Equation C.5 only in the power of the energy in the integral. An improved trial function results in a 6 % correction of the numerical factors ($2/5 = 1/2.5$ has to be replaced by $1/2.65$).

Again, we can define an effective cross-section for which we include a constant $\alpha = 2.65$ to obtain the elastic cross-section rather than the relaxation cross-section[1]:

$$\sigma_{\text{eff}}(T) := \frac{2.65\,\Gamma_{\text{rel}}(T)}{\bar{n}\,\bar{v}_r} = \frac{1}{6\,(k_{\text{B}}T)^4}\int_0^\infty \sigma(E)\,E^3\,e^{-\frac{E}{k_{\text{B}}T}}\,dE. \tag{C.9}$$

For a constant cross-section σ, this equation reduces to $\sigma_{\text{eff}} = \sigma$. For more general cross-sections, Equation C.9 has to be evaluated numerically.

C.3 Inelastic rates

Inelastic collision cross-sections typically contain a factor of k_f/k_i, where k_i and k_f are the initial and final wavenumber of the collision, respectively. This factor is a result of Fermi's golden rule, stating that the transition probability is proportional to the density of final states. The event rate for inelastic collisions is again given by a thermal average: $\Gamma_{\text{inel}} = \bar{n} < \sigma_{\text{inel}}(v) v >_{\text{th}}$. It is therefore advantageous to have a physical quantity that is independent of temperature, thus eliminating the need to perform this average. If the release in energy ΔE by the inelastic collision is much larger than the initial kinetic energy, the ratio $\frac{k_f}{k_i} \approx \sqrt{\frac{2\Delta E}{m_\mu}}\frac{1}{v}$ becomes inversely proportional to the velocity. In this case, the rate constant $\beta_{\text{inel}} = \sigma_{\text{inel}}(\bar{v}_r)\bar{v}_r$ is independent of velocity and the event rate can be written as $\Gamma_{\text{inel}} = \bar{n}\,\beta_{\text{inel}}$. If on the other hand the energy release is small compared to the initial kinetic energy, $k_f/k_i \approx 1$ and the useful physical quantity is the velocity independent inelastic cross-section σ_{inel}. The event rate is then given by $\Gamma_{\text{inel}} = \bar{n}\,\sigma_{\text{inel}}\bar{v}_r$.

For example, dipolar relaxation in alkali atoms in the upper hyperfine state typically releases the hyperfine energy, which is always much higher than the initial kinetic energy in these experiments. In chromium, the magnetic field dependent Zeeman energy is released, which can be on the order of the initial kinetic energy. In that case, the full thermal averaging has to be performed and no temperature independent quantity exists.

[1] The choice of $\alpha = 2.65$ restricts the validity of σ_{eff} to low temperatures.

Appendix D

The C_6 coefficient for chromium

There are several ways to obtain an approximate C_6 coefficient. One possibility is to extract it from *ab inito* calculations of the molecular potentials. The lack of data prevents this method for chromium (see Section 8.6.1).

The C_6 coefficient can also be related to the polarizability α of an atom via the following approximate expression [223]:

$$C_6 \approx \frac{3}{4}\frac{4\pi\epsilon_0}{ea_0^5}E_{\text{ion}}\alpha^2, \tag{D.1}$$

where E_{ion} is the first ionization energy in eV and α in units of[1] Å^3 to obtain C_6 in atomic units[2]. The reason is easily seen: the polarizability is a measure for the electric dipole moment of an atom under the influence of an electric field. The C_6 coefficient arises from the interaction of fluctuating dipole moments and is therefore proportional to the square of the polarizability. The formula above has proven to be accurate to within few 10%. For chromium with a static polarizability of $11.6\,\text{Å}^3$, we get $C_6 \approx 1140$ a.u.

An exact expression for the C_6 coefficient can be obtained from a more detailed analysis of the contributions of the dipole transitions to the polarizability. It can be written as a sum over the oscillator strengths of all dipole transitions starting from the ground state. The C_6 coefficient in atomic units can then be expressed as the sum over all pair products of the oscillator strength f_{n0} connecting the ground state with an excited state n [223]:

$$C_6 = \frac{3}{2}\sum_{n,n'}\frac{f_{n0}f_{n'0}}{(E_n - E_0)(E_{n'} - E_0)(E_n + E_{n'} - 2E_0)} \tag{D.2}$$

[1] $\alpha[SI] = 4\pi\epsilon_0\alpha[\text{Å}^3] \times 10^{-30}$, where ϵ_0 is the dielectric constant

[2] $C_6[SI] = C_6[a.u.]\frac{e^2a_0^5}{4\pi\epsilon_0}$, where e is the charge of the electron and a_0 is Bohr's radius

where E_n and E_0 are the energies in atomic units[3] of the excited and the ground state, respectively. We have calculated $C_6 \approx 541$ a.u. for chromium, using all transitions available from the NIST database of atomic line spectra [80].

Along a similar line of thought, an approximate expression for C_6 can be obtained. The polarizability can be related to the C_6 coefficient by taking into account the effective number of electrons, N_{eff} involved in the interaction. For two atoms of the same species, it is given by [224, 225]

$$C_{6,\text{eff}} = K\alpha^2\sqrt{\frac{N_{\text{eff}}}{4\alpha}}, \tag{D.3}$$

where α is the static polarizability of the atom in Å^3 and $K = 13.14$ is a coefficient to obtain C_6 in atomic units. N_{eff} can be approximated using an empirical interpolation formula

$$N_{\text{eff}} = N_{\text{ext}} + \left(1 - \frac{N_{\text{ext}}}{N_{\text{int}}}\right)\left(\frac{N_{\text{int}}}{N_{\text{tot}}}\right)^2 N_{\text{ext}}, \tag{D.4}$$

where N_{int} and N_{ext} are the numbers of total inner and valence electrons, respectively, and $N_{\text{tot}} = N_{\text{int}} + N_{\text{ext}}$. For transition elements of the first half of the d-periods like chromium, the similarity between s and d electrons leads to a slight modification of $N_{\text{eff}} = N_s + 0.6N_d$, where N_s and N_d are the number of s and d electrons, respectively. For chromium, we have $N_{\text{tot}} = 24$ and $N_{\text{eff}} = 6.22$, resulting in $C_6 \approx 1300$ a.u. This C_6 coefficient contains also contributions from higher multipole interactions[4]

In summary, we have used three different ways to obtain an approximate C_6 coefficient for chromium. Equation D.1 is known to yield only a very crude estimate of the C_6 coefficient, whereas the semi-empirical approach (Equation D.3 is believed to be accurate to within a few percents. Both values differ by only 13%, making $C_6 = 1300$ for chromium a good choice. The difference to the number obtained from the oscillator strengths lies probably in the incomplete knowledge of all transitions, especially in the x-ray regime. An indication for this is the failure of the Thomas-Reiche-Kuhn sum rule [223], which states, that the sum over all oscillator strengths equals the number of electrons in the atom. For chromium we have evaluated this sum to be ≈ 1.16 in clear disagreement to the number of electrons. The situation seems to be different for the alkali metals, for which the main contribution to C_6 coefficient comes from the single valence electron. The main transitions for this electron has an oscillator strength of approximately 1. Evaluation of Equation D.2 using this single transition yields a C_6 coefficient, which is in good agreement with experimental and theoretical data.

[3] for a transition wavelength λ, $E_n - E_0 = \frac{hc}{\lambda}\frac{1}{E_H}$, where $E_H \approx 4.36 \times 10^{-18}$ is the Hartree energy

[4] Note added: The isolated C_6 coefficient is approximately 20 % smaller than the effective C_6 determined here [226]. The results of our analysis of the elastic scattering properties in Chapter 9 are not affected by this discrepancy.

Appendix E

Preliminary results on dipolar relaxation collisions

Evaporative cooling of chromium atoms in a magnetic trap is limited by an extraordinarily large dipolar relaxation rate. In this Appendix I present preliminary results on the dipolar relaxation rate constants for two bosonic chromium isotopes as discussed theoretically in Section 8.6.3.

In alkali atoms in the upper hyperfine state, dipolar relaxation changes the hyperfine state of one or both atoms releasing the hyperfine energy corresponding to a temperature of approximately 0.25 K for each atom. Therefore, dipolar relaxation immediately results in atom loss from the trap. In chromium, only the Zeeman energy $\Delta E_{ZS} = 2\mu_B B$, corresponding to a temperature of 500μK for a magnetic offset field of $B = 8\,\mathrm{G}$ is released in a single spin-flip transition. The atoms, then in the $m_J = 2$ magnetic substate, are still trapped together with the $m_J = 3$ atoms. The Zeeman energy is distributed between the collision partners. The two possible relaxation processes

$$(m_J = 3, m_J = 3) \rightarrow (m_J = 3, m_J = 2) + \Delta E_{ZS} \tag{E.1}$$

$$(m_J = 3, m_J = 3) \rightarrow (m_J = 2, m_J = 2) + 2\Delta E_{ZS} \tag{E.2}$$

produce either an energetic $m_J = 3$ and an energetic $m_J = 2$ atom or a pair of hot $m_J = 2$ atoms. The mixture of magnetic substates and kinetic energies makes the interpretation of images of such clouds extremely diffcult.

From these considerations, we devised a technique which allows us to unambiguously measure the dipolar loss rate. We use a radio-frequency shield to selectively remove energetic atoms in the $m_J = 3$ and $m_J = 2$ magnetic substates, as shown in Figure E.1. Using this technique, we can turn the dipolar relaxation in chromium into a real loss process. The frequency of the rf-shield has to be adjusted to sufficiently

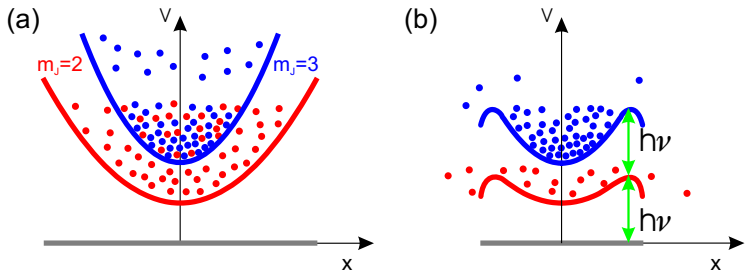

Figure E.1: Measurement principle for dipolar relaxation collisions in chromium. (a) Dipolar relaxation populates the $m_J = 2$ magnetic substate. Atom pairs undergoing a double (single) spin-flip have an additional kinetic energy of $2\Delta E_{ZS}$ (ΔE_{ZS}), corresponding to (half) the energy difference between the $m_J = 2$ and $m_J = 3$ potentials in the magnetic trap. (b) Applying a radio-frequency shield allows to selectively remove the $m_J = 2$ atoms and hot $m_J = 3$ atoms, thus turning dipolar relaxation into a loss process. For simplicity, we have neglected the $m_J = 1$ magnetic substate in the drawing of the potentials.

high frequencies, such that the initial $m_J = 3$ cloud is not significantly evaporatively cooled. Otherwise, evaporative cooling of the initial cloud would lead to additional loss. Consequently, the gain in kinetic energy in the relaxation process needs to be sufficiently large to have the atoms removed by such a rf-shield. From these consideration it becomes clear that this method is only applicable for offset fields $B_0 \gg k_{\mathrm{B}}T/2\mu_B$, where T is the initial temperature of the cloud.

The differential equation governing the decay of the number of atoms (N) from the trap is given by:

$$\frac{\mathrm{d}N}{\mathrm{d}t} = -\gamma_{bg}N - 2\beta_{dp}\frac{N^2}{\bar{V}}, \tag{E.3}$$

where γ_{bg} is the loss rate due to collisions with the background gas, β_{dp} is the event rate[1] for dipolar relaxation collisions and $\bar{V} = \sqrt{8}(2\pi)^{3/2}\sigma_x\sigma_y\sigma_z$ is the mean volume of the atomic cloud having a Gaussian density distribution with $1/\sqrt{e}$ sizes σ_x, σ_y and σ_z. The well-known solution to this differential equation is

$$N(t) = N_0\frac{\gamma_{bg}\, e^{-\gamma_{bg}t}}{\gamma_{bg} + N_0\frac{2\beta_{dp}}{\bar{V}}\left(1 - e^{-\gamma_{bg}t}\right)}, \tag{E.4}$$

where N_0 is the initial number of atoms in the trap.

We have performed a series of measurements in which we recorded $N(t)$ for different magnetic offset fields. A typical experimental sequence starts with the preparation of a cold cloud of atoms using our CLIP trap loading scheme and subsequent

[1] The factor of 2 accounts for the fact that each dipolar relaxation event removes two atoms from the trap.

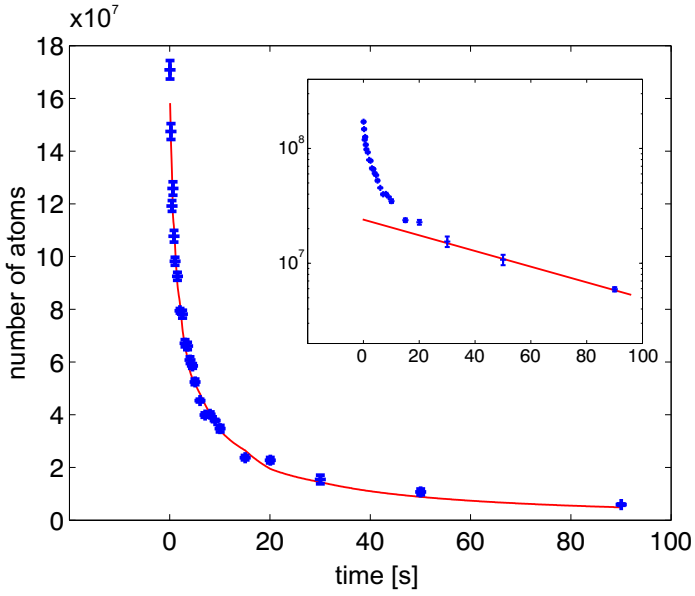

Figure E.2: Decay of the number of atoms due to dipolar relaxation. The blue line is a fit of Equation E.2 to the data, yielding $\beta_{dp} = 1.54 \pm 0.06 \times 10^{-11}\,\mathrm{cm}^3/\mathrm{s}$. The inset shows a logarithmic plot of the data together with a purely exponential decay curve (red line).

Doppler cooling in the magnetic trap as described in Chapters 6 and 7. Performing Doppler cooling already at the desired magnetic offset field assures that the initial temperature of the cloud is approximately the same for all offset fields. After the Doppler cooling stage, the radio-frequency shield is applied and the atomic ensemble is allowed to evolve in the trap for a variable time. The number of remaining atoms is determined from a fluorescence image with an exposure time of 200 μs, taken after 3 ms time-of-flight. The initial density distribution and volume are retrieved from the known trapping parameters via Equation 5.12. An example of such a decay curve is shown in Figure E.2. The red line is a fit of Equation E.4 to the data using a background gas collision rate[2] of $\gamma_{bg} = \frac{1}{300\,\mathrm{s}}$. The latter has been obtained from a separate measurement with a low density atomic cloud. The fit parameters were the inital number of atoms N_0 and the event rate β_{dp} for dipolar relaxation.

We have performed the same measurement for four different magnetic offset fields: 11, 25, 38 and 52 G. The radio-frequency shield was adjusted to corresponded to a cut-off temperature of approximately 3 mK (see Equation 8.68). We have determined the evolution of the temperature of the atoms in a separate measurement using a time-of-flight sequence. The initial temperature in radial direction was typically around $275 \pm 25\,\mu$K. Directly after Doppler cooling, the axial direction is typically

[2]The fit is not sensitive to exact value of this parameter.

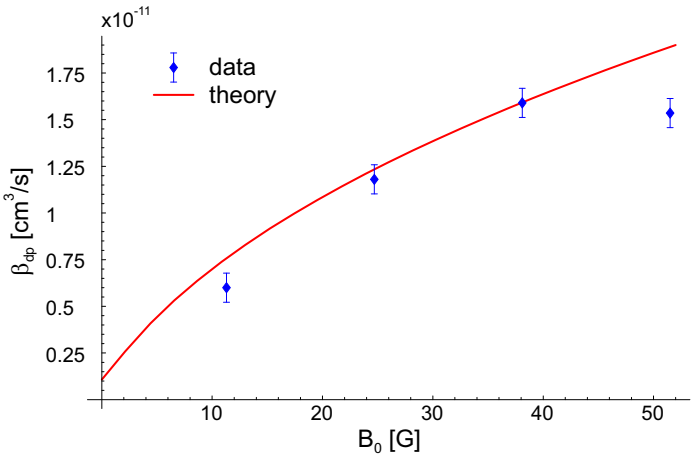

Figure E.3: Magnetic field dependence of the dipolar relaxation rate coefficicent. The blue line is a plot of Equation E.5 with no fit parameter.

close to the Doppler limit. Elastic collisions thermalize the cloud, visible in a rapid increase in the axial temperature. In addition, we observe significant heating during the evolution of the atomic sample in the trap. The increased volume due to the heating was accounted for in the fit. Effects due to the temperature dependence of the inelastic collisional properties are small and have been ignored.

The resulting event rate coefficients β_{dp} for dipolar relaxation as a function of the magnetic offset field are shown in Figure E.3. The red line is a plot of the thermalized theoretical event rate without any adjustable parameters obtained from Equations 8.63 and 8.64 according to

$$<(\sigma_{dp}^1 + \sigma_{dp}^2) \cdot v_r>. \tag{E.5}$$

The agreement with the experimental data is remarkable. We assume a 20 % uncertainty in the number of atoms in addition to the error bars in Figure E.3 which have been obtained from the fit. This agreement is evidence for the validity of the simple theory presented in Section 8.6.3 in the considered regime.

The main result of the theory is the independence of dipolar relaxations from details of the molecular interaction. We have confirmed this conclusion for large magnetic moments by comparing the heating of the atomic cloud due to dipolar relaxation for the two isotopes ^{52}Cr and ^{50}Cr. The result is shown in Figure E.4 where we have plotted the temperature evolution of the clouds, derived from their radial sizes σ_y via Equation 5.13. The upper curve shows a typical measurement for ^{52}Cr with a high initial density of $10^{11}\,\mathrm{cm}^{-3}$. Strong heating with an initial rate of more than $100\,\mu$K/s is observed. Due to the lower natural abundance of ^{50}Cr, we are only able to achieve densities on the order of $10^{10}\,\mathrm{cm}^{-3}$. Comparing the heating rates for ^{50}Cr

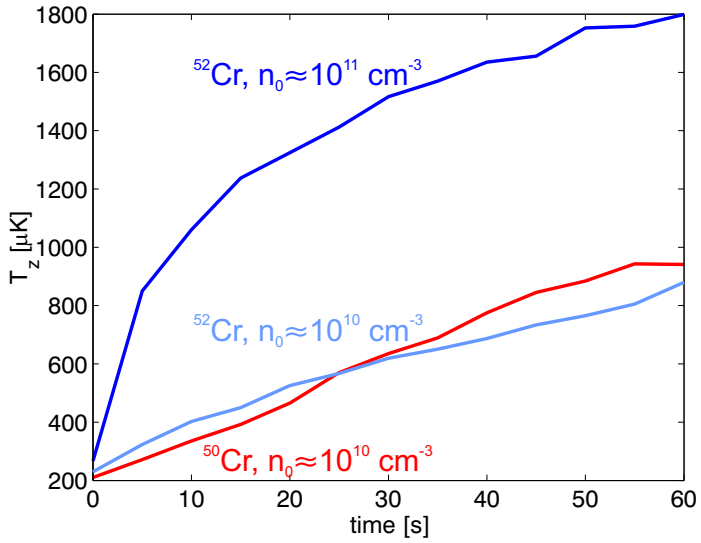

Figure E.4: Heating due to dipolar relaxation for ^{52}Cr and ^{50}Cr. Both isotopes show the same heating for comparable initial density of atoms in the cloud.

with a cloud of ^{52}Cr atoms at comparable densities, we find the same heating for both atomic species. Since the elastic scattering properties of ^{52}Cr and ^{50}Cr are very different (see Chapter 9), we can conclude that the dipolar relaxation rate for chromium is independent of the details of the scattering potential. It rather depends on the magnetic offset field and the magnetic moment of the atomic species. For chromium, we find a typical rate coefficient of $\beta_{dp} = 10^{-11}\,\mathrm{cm}^3/\mathrm{s}$ at a magnetic offset field of $B_0 = 20\,\mathrm{G}$.

This result is especially important for experiments aimed towards electrostatic trapping of large samples of polar molecules [57]. The large dipole-dipole interaction[3] between these molecules will lead to a dramatic rise in the dipolar relaxation rate as the density increases.

Dipolar relaxation can be suppressed by trapping the atoms or molecules in the strong field seeking state which is the absolute ground state of the system and therefore immune against dipolar relaxation. This can be realized in an optical dipole trap [42]. The success of this technique has been demonstrated with Bose-Einstein condensation of atomic cesium [25]. Cesium in the weak field seeking states has resisted all efforts to achieve BEC due to extraordinarily large loss rates [210, 227]. Analogous to cesium, optical trapping of atomic chromium in the high field seeking state should permit to achieve Bose-Einstein condensation.

[3]The electronic dipole-dipole interaction for typical dipole moments of 1 Debeye is four orders of magnitude larger than the magnetic dipole-dipole interaction for magnetic moments of $1\,\mu_B$.

Bibliography

[1] M. Anderson, J. Ensher, M. Matthews, C. Wieman, and E. Cornell, *Observation of Bose-Einstein Condensation in a Dilute Atomic Vapor*, Science **269**, 198 (1995).

[2] C. Bradley, C. Sackett, J. Tollett, and R. Hulet, *Evidence of Bose-Einstein Condensation in an Atomic Gas with Attractive Interactions*, Phys. Rev. Lett. **75**, 1687 (1995), *ibid.* **79**, 1170 (1997).

[3] K. Davis, M.-O. Mewes, M. Andrews, N. van Druten, D. Durfee, D. Kurn, and W. Ketterle, *Bose-Einstein Condensation in a Gas of Sodium Atoms*, Phys. Rev. Lett. **75**, 3969 (1995).

[4] The Royal Swedish Academy of Sciences, *Nobel Prize in Physics for 2001*, http://www.nobel.se/physics/laureates/2001/press.html (2001).

[5] M.-O. Mewes, M. Andrews, N. van Druten, D. Kurn, D. Durfee, C. Townsend, and W. Ketterle, *Collective Excitations of a Bose-Einstein Condensate in a Magnetic Trap*, Phys. Rev. Lett. **77**, 988 (1996).

[6] D. Stamper-Kurn, A. Chikkatur, A. Görlitz, S. Inouye, S. Gupta, D. Pritchard, and W. Ketterle, *Excitation of Phonons in a Bose-Einstein Condensate by Light Scattering*, Phys. Rev. Lett. **83**, 2876 (1999).

[7] D. Stamper-Kurn, H.-J. Miesner, S. Inouye, M. Andrews, and W. Ketterle, *Collisionless and Hydrodynamic Excitations of a Bose-Einstein Condensate*, Phys. Rev. Lett. **81**, 500 (1998).

[8] C. Myatt, E. Burt, R. Ghrist, E. Cornell, and C. Wieman, *Production of Two Overlapping Bose-Einstein Condensates by Sympathetic Cooling*, Phys. Rev. Lett. **78**, 586 (1997).

[9] J. Stenger, S. Inouye, D. Stamper-Kurn, H.-J. Miesner, A. Chikkatur, and W. Ketterle, *Spin domains in ground-state Bose-Einstein condensates*, Nature **396**, 345 (1999).

[10] A. P. Chikkatur, A. Görlitz, D. M. Stamper-Kurn, S. Inouye, S. Gupta, and W. Ketterle, *Suppresion and Enhancement of Impurity Scattering in a Bose-Einstein Condensate*, Phys. Rev. Lett. **85**, 483 (2000).

[11] O. M. Maragò, S. A. Hopkins, J. Arlt, E. Hodby, G. Hechenblaikner, and C. J. Foot, *Observation of the Scissors Mode and Evidence of Superfluidity of a Trapped Bose-Einstein Condensed Gas*, Phys. Rev. Lett. **84**, 2056 (2000).

[12] C. Raman, M. Köhl, R. Onofrio, D. Durfee, C. Kuklewicz, Z. Hadzibabic, and W. Ketterle, *Evidence for a Critical Velocity in a Bose-Einstein Condensed Gas*, Phys. Rev. Lett. **83**, 2502 (1999).

[13] J. R. Abo-Shaeer, C. Raman, J. M. Vogels, and W. Ketterle, *Observation of Vortex Lattices in Bose-Einstein Condensates*, Science **292**, 476–479 (2001).

[14] S. Inouye, S. Gupta, T. Rosenband, A. Chikkatur, A. Görlitz, T. Gustavson, A. Leanhardt, D. Pritchard, and W. Ketterle, *Observation of Vortex Phase Singularities in Bose-Einstein Condensates*, Phys. Rev. Lett. **87**, 080402 (2001).

[15] K. Madison, F. Chevy, W. Wohlleben, and J. Dalibard, *Vortex Formation in a Stirred Bose-Einstein Condensate*, Phys. Rev. Lett. **84**, 806 (2000).

[16] M. Matthews, B. Anderson, P. Haljan, D. Hall, C. Wieman, and E. Cornell, *Vortices in a Bose-Einstein Condensate*, Phys. Rev. Lett. **83**, 2498 (1999).

[17] L. Deng, E. Hagley, J. Wen, M. Trippenbach, Y. Band, P. Julienne, J. Simsarian, K. Helmerson, S. Rolston, and W. Phillips, *Four-wave mixing with matter waves*, Nature **398**, 218 (1999).

[18] B. Anderson, P. Haljan, C. Regal, D. Feder, L. Collins, C. Clark, and E. Cornell, *Watching Dark Solitons Decay into Vortex Rings in a Bose-Einstein Condensate*, Phys. Rev. Lett. **86**, 2926 (2001).

[19] S. Burger, K. Bongs, S. Dettmer, W. Ertmer, K. Sengstock, A. Sanpera, G. Shlyapnikov, and M. Lewenstein, *Dark Solitons in Bose-Einstein Condensates*, Phys. Rev. Lett. **83**, 5198 (1999).

[20] S. Burger, L. Carr, P. Öhberg, K. Sengstock, and A. Sanpera, *Generation and interaction of solitons in Bose-Einstein condensates*, Phys. Rev. A **65**, 043611 (2002).

[21] J. Denschlag, J. Simsarian, D. Feder, C. W. Clark, L. Collins, J. Cubizolles, L. Deng, E. Hagley, K. Helmerson, W. Reinhardt, S. Rolston, B. Schneider, and W. Phillips, *Generating Solitons by Phase Engineering of a Bose-Einstein Condensate*, Science **287**, 97 (2000).

[22] K. E. Strecker, G. B. Partridge, A. G. Truscott, and R. G. Hulet, *Formation and propagation of matter-wave soliton trains*, Nature **417**, 150 (2002).

[23] S. Inouye, M. Andrews, J. Stenger, H.-J. Miesner, D. Stamper-Kurn, and W. Ketterle, *Observation of Feshbach resonances in a Bose-Einstein condensate*, Nature **392**, 151 (1998).

[24] J. Roberts, N. Claussen, S. Cornish, E. Donley, E. Cornell, and C. Wieman, *Controlled Collapse of a Bose-Einstein Condensate*, Phys. Rev. Lett. **86**, 4211 (2001).

[25] T. Weber, J. Herbig, M. Mark, H.-C. Nägerl, and R. Grimm, *Bose-Einstein Condensation of Cesium*, Science **299**, 232–235 (2003).

[26] M. A. Baranov, M. S. Mar'enko, V. S. Rychkov, and G. V. Shlyapnikov, *Superfluid paring in a polarized dipolar Fermi gas*, arXiv: cond-mat/0109437 (2002).

[27] D. DeMille, *Quantum Computation with Trapped Polar molecules*, Phys. Rev. Lett. **88**, 067901 (2002).

[28] S. Giovanazzi, A. Görlitz, and T. Pfau, *Tuning the Dipolar Interaction in Quantum Gases*, Phys. Rev. Lett. **89**, 130401 (2002).

[29] S. Giovanazzi, A. Görlitz, and T. Pfau, *Ballistic expansion of a dipolar condensate*, J. Opt. B: Quantum Semiclass. Opt. **5**, S208–S211 (2003).

[30] K. Góral, B.-G. Englert, and K. Rzążewski, *Semiclassical theory of trapped fermionic dipoles*, Phys. Rev. A **63**, 033606 (2001).

[31] K. Góral, K. Rzążewski, and T. Pfau, *Bose-Einstein condensation with magnetic dipole-dipole forces*, Phys. Rev. A **61**, 051601(R) (2000).

[32] K. Góral, L. Santos, and M. Lewenstein, *Quantum Phases of Dipolar Bosons in Optical Lattices*, Phys. Rev. Lett. **88**, 170406 (2002).

[33] J.-P. Martikainen, M. Mackie, and K.-A. Suominen, *Comment on 'Bose-Einstein condensation with magnetic dipole-dipole forces'*, Phys. Rev. A **64**, 037601 (2001).

[34] H. Pu, W. Zhang, and P. Meystre, *Ferromagnetism in a Lattice of Bose-Einstein Condensates*, Phys. Rev. Lett. **87**, 140405 (2001).

[35] L. Santos, G. Shlyapnikov, P. Zoller, and M. Lewenstein, *Bose-Einstein Condensation in Trapped Dipolar Gases*, Phys. Rev. Lett. **85**, 1791 (2000).

[36] L. Santos, G. V. Shlyapnikov, P. Zoller, and M. Lewenstein, *Erratum: Bose-Einstein Condensation in Trapped Dipolar Gases [Phys. Rev. Lett. **85**, 1791 (2000)]*, Phys. Rev. Lett. **88**, 139904 (2002).

[37] S. Yi and L. You, *Trapped condensates of atoms with dipole interactions*, Phys. Rev. A **63**, 053607 (2001).

[38] W. Zhang, H. Pu, C. Search, and P. Meystre, *Spin Waves in a Bose-Einstein-Condensed Atomic Spin Chain*, Phys. Rev. Lett. **88**, 060401 (2002).

[39] K. Góral and L. Santos, *Ground state and elementary excitations of single and binary Bose-Einstein condensates of trapped dipolar gases*, Phys. Rev. A **66**, 023613 (2002).

[40] A. Peters, private communication (2000).

[41] J. D. Weinstein, R. deCarvalho, C. I. Hancox, and J. M. Doyle, *Evaporative cooling of atomic chromium*, Phys. Rev. A **65**, 021604 (2002).

[42] R. Grimm, M. Weidemüller, and Y. B. Ovchinnikov, *Optical dipole traps for neutral atoms*, Advances in Atomic, Molecular, and Optical Physics **42**, 95–170 (2000).

[43] D. G. Fried, T. C. Killian, L. Willmann, D. Landhuis, S. C. Moss, D. Kleppner, and T. J. Greytak, *Bose-Einstein Condensation of Atomic Hydrogen*, Phys. Rev. Lett. **81**, 3811 (1998).

[44] A. Robert, O. Sirjean, A. Browaeys, J. Poupard, S. Nowak, D. Boiron, and C. W. A. Aspect, *A Bose–Einstein Condensate of Metastable Atoms*, Science **292**, 461–464 (2001).

[45] F. P. D. Santos, J. Léonard, J. Wang, C. J. Barrelet, F. Perales, E. Rasel, C. S. Unnikrishnan, M. Leduc, and C. Cohen-Tannoudji, *Bose-Einstein Condensation of Metastable Helium*, Phys. Rev. Lett. **86**, 3459–3462 (2001).

[46] G. Modugno, G. Ferrari, G. Roati, R. J. Brecha, A. Simoni, and M. Inguscio, *Bose-Einstein Condensation of Potassium Atoms by Sympathetic Cooling*, Science **294**, 1320–1322 (2001).

[47] A. Einstein, *Quantentheorie des idealen einatomigen Gases*, Sitzber. Kgl. Preuss. Akad. Wiss. **1925**, 3–14 (1925).

[48] N. S. Bose, *Plancks Gesetz und Lichtquantenhypothese*, Z. Phys. **26**, 178 (1924).

[49] F. London, *The λ-phenomenon of Liquid Helium and the Bose-Einstein Degeneracy*, Nature **141**, 643 (1938).

[50] B. Anderson and M. Kasevich, *Macroscopic Quantum Interference from Atomic Tunnel Arrays*, Science **282**, 1686 (1998).

[51] I. Bloch, T. W. Hänsch, and T. Esslinger, *Atom Laser with a cw Output Coupler*, Phys. Rev. Lett. **82**, 3008 (1999).

[52] E. Hagley, L. Deng, M. Kozuma, J. Wen, K. Helmerson, S. Rolston, and W. Phillips, *A Well-Collimated Quasi-Continuous Atom Laser*, Science **283**, 1706 (1999).

[53] M.-O. Mewes, M. Andrews, D. Kurn, D. Durfee, C. Townsend, and W. Ketterle, *Output Coupler for Bose-Einstein Condensed Atoms*, Phys. Rev. Lett. **78**, 582 (1997).

[54] S. Inouye, T. Pfau, S. Gupta, A. Chikkatur, A. Görlitz, D. Pritchard, and W. Ketterle, *Phase-coherent amplification of atomic matter waves*, Nature **402**, 641 (1999).

[55] M. Kozuma, Y. Suzuki, Y. Torji, T. Sugiura, T. Kuga, E. W. Hagley, and L. Deng, *Phase–Coherent Amplification of Matter Waves*, Science **286**, 2309 (1999).

[56] H. Pu, S. Raghavan, and N. Bigelow, *Creation of topological states in spinor condensates*, Phys. Rev. A **63**, 063603 (2001).

[57] H. L. Bethlem, F. M. H. C. Giel Berden, R. T. Jongma, and A. J. A. van Roij Gerard Meijer, *Electrostatic trapping of ammonia molecules*, Nature **406**, 491–494 (2001).

[58] S. Rangwala, T. Junglen, T. Rieger, P. Pinkse, and G. Rempe, *A continuous source of translationally cold dipolar molecules* (2003), arXiv: physics/0209041.

[59] J. Ye, private communication (2002).

[60] T. Busch, J. R. Anglin, J. I. Cirac, and P. Zoller, *Inhibition of spontaneous emission in Fermi gases*, Europhys. Lett. **44**, 755–760 (1998).

[61] D. Butts and D. Rokhsar, *Trapped Fermi gases*, Phys. Rev. A **55**, 4346 (1997).

[62] K. Mølmer, *Bose Condensates and Fermi Gases at Zero Temperature*, Phys. Rev. Lett. **80**, 1804 (1998).

[63] M. Moore and P. Meystre, *Atomic Four-Wave Mixing: Fermions versus Bosons*, Phys. Rev. Lett. **86**, 4199 (2001).

[64] J. Oliva, *Ground-state density profile of the weakly interacting Bose and Fermi gases confined in an arbitrary potential well*, Phys. Rev. B **38**, 8811 (1988).

[65] H. T. C. Stoof and M. Houbiers, *Condensed matter physics with trapped atomic Fermi gases*, in *Proceedings of the International School of Physics - Enrico Fermi*, edited by M. Inguscio, S. Stringari, and C. Wieman, p. 537 (IOS Press, 1999).

[66] C. Chin, V. Vuletic, A. J. Kerman, and S. Chu, *High Resolution Feshbach Spectroscopy of Cesium*, Phys. Rev. Lett. **85**, 2717–2720 (2000).

[67] P. J. Leo, C. J. Williams, and P. S. Julienne, *Collision Properties of Ultracold ^{133}Cs Atoms*, Phys. Rev. Lett. **85**, 2721–2724 (2000).

[68] T. Laue, E. Tiesinga, C. Samuelis, H. Knöckel, and E. Tiemann, *Magnetic-field imaging of weakly bound levels of the ground-state Na_2 dimer*, Phys. Rev. A **65**, 023412 (2002).

[69] J. Roberts, N. Claussen, J. P. Burke, Jr., C. H. Greene, E. Cornell, and C. Wieman, *Resonant Magnetic Field Control of Elastic Scattering of Cold ^{85}Rb*, Phys. Rev. Lett. **81**, 5109 (1998).

[70] A. Marte, T. Volz, J. Schuster, S. Dürr, G. Rempe, E. G. M. van Kempen, and B. J. Verhaar, *Feshbach Resonances in Rubidium 87: Precision Measurement and Analysis*, Phys. Rev. Lett. **89**, 283202 (2002).

[71] D. Heinzen, *Ultracold atomic interactions*, in *Proceedings of the International School of Physics - Enrico Fermi*, edited by M. Inguscio, S. Stringari, and C. Wieman, p. 351 (IOS Press, 1999).

[72] C. Samuelis, E. Tiesinga, T. Laue, M. Elbs, H. Knöckel, and E. Tiemann, *Cold atomic collisions studied by molecular spectroscopy*, Phys. Rev. A **63**, 012710 (2001).

[73] J. Weiner, V. S. Bagnato, S. Zilio, and P. S. Julienne, *Experiments and theory in cold and ultracold collisions*, Rev. Mod. Phys. **71**, 1–85 (1999).

[74] C. Monroe, E. Cornell, C. Sackett, C. Myatt, and C. Wieman, *Measurement of Cs-Cs Elastic Scattering at $T = 30\mu K$*, Phys. Rev. Lett. **70**, 414 (1993).

[75] J. Roberts, N. Claussen, S. Cornish, and C. Wieman, *Magnetic Field Dependence of Ultracold Inelastic Collisions near a Feshbach Resonance*, Phys. Rev. Lett. **85**, 728 (2000).

[76] H. Sully and E. Brandes, *Metallurgy of The Rarer Metals-1, Chromium* (London Butterworths, 1967), 2 edn.

[77] S. Nakada, M. Yamaguchi, M. Yamamoto, and H. Ishimaru, *Electron beam evaporator constructed from aluminum alloy and the gettering effect of chromium films.*, J. of Vac. Sci. Tech. A **12**, 1631 (1994).

[78] J. Stuhler, *Kontinuierliches Laden einer Magnetfalle mit lasergekühlten Chromatomen*, Phd thesis, Universität Konstanz, Lehrstuhl J. Mlynek, Ufo-Verlag, Allensbach (2002).

[79] J. McClelland, private communication (1999).

[80] NIST, Atomic Spectra Databases (2003), URL `http://physics.nist.gov/\discretionary{-}{}{}PhysRefData/\discretionary{-}{}{}ASD1/\discretionary{-}{}{}choice.html?\discretionary{-}{}{}nist_atomic_spectra.html`.

[81] K. Andersson, *The electronic spectrum of Cr_2*, Chem. Phys. Lett. **237**, 212–221 (1995).

[82] J. Dalibard and C. Cohen-Tannoudji, *Dressed-atom approach to atomic motion in laser light: the dipole force revisited*, J. Opt. Soc. Am. B **2**, 1707–1720 (1985).

[83] B. R. Mollow, *Power Spectrum of Light scattered by Two-Level Systems*, Phys. Rev. **188**, 1969–1975 (1969).

[84] P. O. Schmidt, *Lichtmasken in der Atomlithographie*, diploma thesis, Universit"at Konstanz, Lehrstuhl J. Mlynek (1998).

[85] J. Söding, R. Grimm, Y. B. Ovchinnikov, P. Bouyer, and C. Salomon, *Short-Distance Atomic Beam Deceleration with a Stimulated Light Force*, Phys. Rev. Lett. **78**, 1420–1423 (1997).

[86] J. Dalibard and C. Cohen-Tannoudji, *Laser cooling below the Doppler limit by polarization gradients: simple theoretical models*, J. Opt. Soc. Am. B **6**, 2023–2045 (1989).

[87] R. Gaggl, L. Windholz, C. Umfer, and C. Neureiter, *Laser cooling of a sodium atomic beam using the Stark effect*, Phys. Rev. A **49**, 1119 (1994).

[88] H. L. Bethlem, G. Berden, and G. Meijer, *Decelerating Neutral Dipolar Molecules*, Phys. Rev. Lett. **83**, 15581561 (1999).

[89] H. Metcalf and P. van der Straten, *Laser Cooling and Trapping* (Springer, New York, 1999).

[90] P. D. Lett, W. D. Phillips, S. L. Rolston, C. E. Tanner, R. N. Watts, and C. I. Westbrook, *Optical molasses*, J. Opt. Soc. Am. B **6**, 2084–2107 (1989).

[91] H. Katori, T. Ido, Y. Isoya, and M. Kutawa-Gonokami, *Magneto-Optical Trapping and Cooling of Strontium Atoms down to the Photon Recoil Temperature*, Phys. Rev. Lett. **82**, 1116–1119 (1999).

[92] J. J. Sakurai, *Modern Quantum Mechanics* (Addison–Wesley, Redwood City, CA, 1985), 1 edn.

[93] P. D. Lett, R. N. Watts, C. I. Westbrook, W. D. Phillips, P. L. Gould, and H. J. Metcalf, *Observation of Atoms Laser Cooled below the Doppler Limit*, Phys. Rev. Lett. **61**, 169 (1988).

[94] P. Ungar, D. Weiss, S. Chu, and E. Riis, *Optical Molasses and Multilevel Atoms — Theory*, J. Opt. Soc. Am. B **6**, 2058–2071 (1989).

[95] V. I. Balykin, V. G. Minogin, and V. S. Letokhov, *Electromagnetic trapping of cold atoms*, Rep. Prog. Phys. **63**, 1429–1510 (2000).

[96] M. Barrett, J. Sauer, and M. Chapman, *All-Optical Formation of an Atomic Bose-Einstein Condensate*, Phys. Rev. Lett. **87**, 010404 (2001).

[97] T. Ido, Y. Isoya, and H. Katori, *Optical-dipole trapping of Sr atoms at a high phase-space density*, Phys. Rev. A **61**, 061403(R) (2000).

[98] C. Bradley, C. Sackett, and R. Hulet, *Bose-Einstein Condensation of Lithium: Observation of Limited Condensate Number*, Phys. Rev. Lett. **78**, 985 (1997).

[99] W. H. Wing, *On neutral particle trapping in quasistatic electromagnetic fields*, Prog. Quant. Electr. **8**, 181 (1984).

[100] A. L. Migdall, J. V. Prodan, W. D. Phillips, T. H. Bergeman, and H. J. Metcalf, *First Observation of Magnetically Trapped Neutral Atoms*, Phys. Rev. Lett. **54**, 2596 (1985).

[101] T. Bergeman, G. Erez, and H. J. Metcalf, *Magnetostatic trapping fields for neutral atoms*, Phys. Rev. A **35**, 1535–1546 (1987).

[102] J. Reichel, *Microchip traps and BoseEinstein condensation*, Appl. Phys. B **75**, 469–487 (2002).

[103] Y. V. Gott, M. S. Ioffe, and V. G. Telkovsky, Nuclear Fusion, 1962 Suppl., Pr. 3 (International Atomic Energy Agency, Vienna, 1962) pp. 1045–1049 (1962).

[104] D. E. Pritchard, *Cooling Neutral Atoms in a Magnetic Trap for Precision Spectroscopy*, Phys. Rev. Lett. **51**, 1336 (1983).

[105] L. V. Hau, B. D. Busch, C. Liu, Z. Dutton, M. M. Burns, and J. A. Golovchenko, *Near-resonant spatial images of confined Bose-Einstein condensates in a 4-Dee magnetic bottle*, Phys. Rev. A **58**, R54–R57 (1998).

[106] T. Esslinger, I. Bloch, and T. W. Hänsch, *Bose-Einstein condensation in a quadrupole-Ioffe-configuration trap*, Phys. Rev. A **58**, R2664 (1998).

[107] M.-O. Mewes, M. Andrews, N. van Druten, D. Kurn, D. Durfee, and W. Ketterle, *Bose-Einstein Condensation in a Tightly Confining dc Magnetic Trap*, Phys. Rev. Lett. **77**, 416 (1996).

[108] W. Petrich, M. H. Anderson, J. R. Ensher, and E. A. Cornell, *Stable, Tightly Confining Magnetic Trap for Evaporative Cooling of Neutral Atoms*, Phys. Rev. Lett. **74**, 3352 (1995).

[109] C. Sukumar and D. Brink, *Spin-flip transitions in a magnetic trap*, Phys. Rev. A **56**, 2451 (1997).

[110] U. Ernst, A. Marte, F. Schreck, J. Schuster, and G. Rempe, *Bose-Einstein condensation in a pure Ioffe-Pritchard field configuration*, Europhys. Lett. **41**, 1 (1998).

[111] J. Schoser, A. Batär, R. Löw, V. Schweikhard, A. Grabowski, Y. B. Ovchinnikov, and T. Pfau, *Intense source of cold Rb atoms from a pure two-dimensional magneto-optical trap*, Phys. Rev. A **66**, 023410 (2002).

[112] T. Binhammer, *Verdampfungskühlung ultrakalter Chrom-Atome*, Diplomarbeit, 5. Physikalisches Institut, Universität Stuttgart (2002).

[113] A. Griesmaier, *Aufbau einer kombinierten magneto-optischen Falle für Chrom und Rubidium*, Diplomarbeit, 5. Physikalisches Institut, Universität Stuttgart (2002).

[114] A. Witte, T. Kisters, F. Riehle, and J. Helmcke, *Laser cooling and deflection of a calcium atomic beam*, J. Opt. Soc. Am. B **9**, 1030 (1992).

[115] J. Werner, *Kontinuierliches Laden einer Magnetfalle mit lasergek"uhlten Chromatomen*, Diplomarbeit, Universit"at Konstanz (2000).

[116] L. Ricci, M. Weidemüller, T. Esslinger, A. Hemmerich, C. Zimmermann, V. Vuletic, W. König, and T. W. Hänsch, *A compact grating-stabilized diode laser system for atomic physics*, Opt. Comm. **117**, 541–549 (1995).

[117] R. W. P. Drever, J. L. Hall, F. V. Kowalski, J. Hough, G. M. Ford, A. J. Munley, and H. Ward, *Laser phase and frequency stabilization using an optical resonator*, Appl. Phys. B **31**, 97 (1983).

[118] S. Hensler, *Eine magneto-optische Falle mit Chromatomen*, diploma thesis, Universität Konstanz, Lehrstuhl J. Mlynek (1999).

[119] J. Werner, Phd thesis, 5. Physikalisches Institut, Universität Stuttgart, Pfaffenwaldring 57, 70550 Stuttgart (2004), in preparation.

[120] M. A. Joffe, W. Ketterle, A. Martin, and D. E. Pritchard, *Transverse cooling and deflection of an atomic beam inside a Zeeman slower*, J. Opt. Soc. Am. B **10**, 2257–2262 (1993).

[121] J. Stuhler, P. O. Schmidt, S. Hensler, J. Werner, J. Mlynek, and T. Pfau, *Continuous loading of a magnetic trap*, Phys. Rev. A **64**, 031405 (2001).

[122] P. O. Schmidt, S. Hensler, J. Werner, T. Binhammer, A. Görlitz, and T. Pfau, *Continuous loading of cold atoms into a Ioffe-Pritchard magnetic trap*, J. Opt. B: Quantum Semiclass. Opt. **5**, S170–S177 (2003).

[123] M. Inguscio, S. Stringari, and C. E. Wieman, eds., *Bose-Einstein Condensation in Atomic Gases* (International School of Physics "Enrico Fermi", Varenna, Italy, 1998).

[124] P. R. Berman, ed., *Atom Interferometry* (Academic Press, New York, 1997).

[125] W. Ketterle, D. Durfee, and D. Stamper-Kurn, *Making, probing and understanding Bose-Einstein condensates*, in *Proceedings of the International School of Physics - Enrico Fermi*, edited by M. Inguscio, S. Stringari, and C. Wieman, p. 67 (IOS Press, 1999).

[126] T. Loftus, J. R. Bochinski, and T. W. Mossberg, *Magnetic trapping of ytterbium and the alkaline-earth metals*, Phys. Rev. A **66**, 013411 (2002).

[127] C. C. Bradley, J. J. McClelland, W. R. Anderson, and R. J. Celotta, *Magneto-optical trapping of chromium atoms*, Phys. Rev. A **61**, 053407 (2000).

[128] E. Mandonnet, A. Minguzzi, R. Dum, I. Carusotto, Y. Castin, and J. Dalibard, *Evaporative Cooling of an atomic beam*, Eur. Phys. J. D **10**, 9 (2000).

[129] J. Dalibard, private communication (2001).

[130] E. Andersson, T. Calarco, R. Folman, M. Andersson, B. Hessmo, and J. Schmiedmayer, *Multimode Interferometer for Guided Matter Waves*, Phys. Rev. Lett. **88**, 100401 (2002).

[131] E. A. Hinds, C. J. Vale, and M. G. Boshier, *A Two Wire Waveguide and Interferometer for Cold Atoms*, Phys. Rev. Lett. **86**, 1462 (2001).

[132] A. S. Bell, J. Stuhler, S. Locher, S. Hensler, J. Mlynek, and T. Pfau, *A magneto–optical trap for chromium with population repumping via intercombination lines*, Europhys. Lett. **45**, 156–161 (1999).

[133] A. Görlitz, private communication (2002).

[134] X. Xu, T. H. Loftus, J. L. Hall, A. Gallagher, and J. Ye, *Cooling and trapping of atomic strontium*, J. Opt. Soc. Am. B **20**, 968–976 (2003).

[135] K. Dieckmann, R. J. C. Spreeuw, M. Weidemüller, and J. T. M. Walraven, *Two-dimensional magneto-optical trap as a source of slow atoms*, Phys. Rev. A **58**, 3891 (1998).

[136] J. Dalibard, *Laser cooling of an optically thick gas: the simplest radiation pressure trap?*, Opt. Comm. **68**, 203 (1988).

[137] A. P. Kazantsev, G. I. Surdutovitch, D. O. Chudesnikov, and V. P. Yakovlev, *Scattering, velocity bunching, and self-localization of atoms in a light field*, J. Opt. Soc. Am. B **6**, 2130 (1989).

[138] W. D. Phillips, J. V. Prodan, and H. J. Metcalf, *Laser cooling and electromagnetic trapping of neutral atoms*, J. Opt. Soc. Am. B **2**, 1751 (1985).

[139] B. Steinheil, *Aufbau eines frequenzverdoppelten Dodenlaser-Systems zur Untersuchung ultrakalter Chromatome*, Diploma thesis, 5. Physikalisches Institut, Universität Stuttgart, Pfaffenwaldring 57, 70550 Stuttgart (2003).

[140] W. Ketterle, K. B. Davis, M. A. Joffe, A. Martin, and D. E. Pritchard, *High Densities of Cold Atoms in a Dark Spontaneous-Force Optical Trap*, Phys. Rev. Lett. **70**, 2253 (1993).

[141] L. Santos, F. Floegel, T. Pfau, and M. Lewenstein, *Continuous optical loading of a Bose-Einstein Condensate*, Phys. Rev. A **63**, 063408 (2001).

[142] M. Drewsen, P. Laurent, A. Nadir, G. Santarelli, A. Clairon, Y. Castin, D. Grison, and C. Salomon, *Investigation of sub-Doppler cooling effects in a cesium magneto-optical trap*, Appl. Phys. B **59**, 283 (1994).

[143] C. D. Wallace, T. P. Dinneen, K. Y. N. Tan, A. Kumarakrishnan, P. L. Gould, and J. Javanainen, *Measurements of temperature and spring constant in a magneto-optical trap*, J. Opt. Soc. Am. B **11**, 703 (1994).

[144] S. Chang, T. Y. Kwon, H. S. Lee, and V. G. Minogin, *Laser sub-Doppler cooling of atoms in an arbitrarily directed magnetic field*, Phys. Rev. A **66**, 043404 (2002).

[145] M.Walhout, U. Sterr, and S. L. Rolston, *Magnetic inhibition of polarization-gradient cooling in $\sigma_+ - \sigma_-$ optical molasses*, Phys. Rev. A **54**, 2275 (1996).

[146] M. Walhout, J. Dalibard, S. L. Rolston, and W. D. Phillips, *$\sigma_+ - \sigma_-$ Optical molasses in a longitudinal magnetic field*, J. Opt. Soc. Am. B **9**, 1997 (1992).

[147] K. Helmerson, A. Martin, and D. E. Pritchard, *Laser cooling of magnetically trapped neutral atoms*, J. Opt. Soc. Am. B **9**, 1988 (1992).

[148] F. Schreck, G. Ferrari, K. L. Corwin, J. Cubizolles, L. Khaykovich, M.-O. Mewes, and C. Salomon, *Sympathetic cooling of bosonic and fermionic lithium gases towards quantum degeneracy*, Phys. Rev. A **64**, 011402 (2001).

[149] I. D. Setija, H. Werij, O. J. Luiten, M. W. Reynolds, T. W. Hijmans, and J. T. M. Walraven, *Optical Cooling of Atomic Hydrogen in a Magnetic Trap*, Phys. Rev. Lett. **70**, 2257–2260 (1993).

[150] P. O. Schmidt, S. Hensler, J. Werner, T. Binhammer, A. Görlitz, and T. Pfau, *Doppler cooling of an optically dense cloud of trapped atoms*, J. Opt. Soc. Am. B **20**, 960–967 (2003).

[151] W. Ketterle and N. van Druten, *Evaporative Cooling of Trapped Atoms*, Adv. At. Mol. Opt. Phys. **37**, 181 (1996).

[152] J. R. Anglin and W. Ketterle, *Bose-Einstein condensation of atomic gases*, Nature **416**, 211–218 (2002).

[153] E. A. Cornell and C. E. Wieman, *Nobel Lecture: Bose-Einstein condensation in a dilute gas: the first 70 years and some recent experiments*, Rev. Mod. Phys **74**, 875–893 (2002).

[154] J. Dalibard and C. Cohen-Tannoudji, *Laser cooling below the Doppler limit by polarization gradients: simple theoretical-models*, J. Opt. Soc. Am. B **6**, 2023 (1989).

[155] D. Boiron, A. Michaud, J. M. Fournier, L. Simard, M. Sprenger, G. Grynberg, and C. Salomon, *Cold and dense cesium clouds in far-detuned dipole traps*, Phys. Rev. A **57**, R4106 (1998).

[156] D.-J. Han, S. Wolf, S. Oliver, C. McCormick, M. T. DePue, and D. S. Weiss, *3D Raman Sideband Cooling of Cesium Atoms at High Density*, Phys. Rev. Lett. **85**, 724–727 (2000).

[157] A. J. Kerman, V. Vuletic, C. Chin, and S. Chu, *Beyond Optical Molasses: 3D Raman Sideband Cooling of Atomic Cesium to High Phase-Space Density*, Phys. Rev. Lett. **84**, 439–442 (2000).

[158] D. J. Han, M. T. DePue, and D. S. Weiss, *Loading and compressing Cs atoms in a very far-off-resonant light trap*, Phys. Rev. A **63**, 023405 (2001).

[159] D. Pritchard and W. Ketterle, *Atom traps and atom optics*, in *Laser Manipulation of Atoms and Ions*, edited by E. Arimondo, W. Phillips, and F. Strumia,

Proceedings of the International School of Physics "Enrico Fermi", Course CXVIII, pp. 473–496 (North Holland, Amsterdam, 1992).

[160] N. Newbury, C. Myatt, E. Cornell, and C. Wieman, *Gravitational Sisyphus Cooling of ^{87}Rb in a Magnetic Trap*, Phys. Rev. Lett. **74**, 2196 (1995).

[161] T. Hijmans, O. Luiten, I. Setija, and J. T. M. Walraven, *Optical cooling of atomic hydrogen in a magnetic trap*, J. Opt. Soc. Am. B **6**, 2235 (1989).

[162] Y. Castin, J. Cirac, and M. Lewenstein, *Reabsorption of Light by Trapped Atoms*, Phys. Rev. Lett. **80**, 5305 (1998).

[163] K. Ellinger and J. Cooper, *Many-particle effects in laser cooling of one-dimensional optical molasses*, Phys. Rev. A **55**, 4351–4376 (1997).

[164] G. Hillenbrand, C. J. Foot, and K. Burnett, *Heating due to long-range photon exchange interactions between cold atoms*, Phys. Rev. A **50**, 1479–1489 (1994).

[165] L. Khaykovich and N. Davidson, *Compression of a cold atomic cloud by on-resonance laser light*, J. Opt. Soc. Am. B **16**, 702–709 (1999).

[166] L. Pruvost, I. Serre, H. T. Duong, and J. Jortner, *Expansion and cooling of a bright rubidium three-dimensional optical molasses*, Phys. Rev. A **61**, 053408 (2000).

[167] D. Sesko, T. Walker, and C. Wieman, *Behavior of neutral atoms in a spontaneous force trap*, J. Opt. Soc. Am. B **8**, 946 (1991).

[168] S. Wolf, S. J. Oliver, and D. S. Weiss, *Suppression of Recoil Heating by an Optical Lattice*, Phys. Rev. Lett. **85**, 4249–4252 (2000).

[169] T. Walker and P. Feng, *Measurements of collisions between laser-cooled atoms*, Advances in Atomic, Molecular, and Optical Physics **34**, 125–170 (1994).

[170] R. deCarvalho, C. I. Hancox, and J. M. Doyle, *Enhanced Inelastic Scattering Rates of Cold Atomic Chromium*, J. Opt. Soc. Am. B **20**, 1131–1134 (2003).

[171] C. J. Joachain, *Quantum collision theory* (North-Holland publishing company, Amsterdam, 1975).

[172] W. Nolting, *Quantenmechanik, Teil 2: Methoden und Anwendungen*, vol. 5 of *Grundkurs: Theoretische Physik* (Zimmermann-Neufang, Antoniusstraße 9, D-56766 Ulmen, 1994), 2 edn.

[173] L. D. Landau and E. M. Lifshitz, *Quantum Mechanics*, vol. 3 of *Course of theoretical physics* (Butterworth-Heinemann, Oxford, United Kingdom, 1977), 3 edn.

[174] H. Friedrich and J. Trost, *Phase Loss in WKB Waves Due to Reflection by a Potential*, Phys. Rev. Lett. **76**, 4869–4873 (1996).

[175] J. Trost, C. Eltschka, and H. Friedrich, *Quantization in molecular potentials*, J. Phys. B: At. Mol. Opt. Phys. **31**, 361374 (1998).

[176] P. S. Julienne and F. H. Mies, *Collisions of ultracold trapped atoms*, J. Opt. Soc. Am. B **6**, 2257–2269 (1989).

[177] B. DeMarco, J. Bohn, J. Burke, Jr., M. Holland, and D. Jin, *Measurement of p-Wave Threshold Law Using Evaporatively Cooled Fermionic Atoms*, Phys. Rev. Lett. **82**, 4208 (1999).

[178] H. M. J. M. Boesten, C. Tsai, J. Gardner, D. Heinzen, and B. Verhaar, *Observation of a shape resonance in the collision of two cold ^{87}Rb atoms*, Phys. Rev. A **55**, 636 (1997).

[179] J. P. Burke, C. H. Greene, and J. L. Bohn, *Determination of ^{39}K scattering lengths using photoassociation spectroscopy of the O_g^- state*, Phys. Rev. A **60**, 4417–4426 (1999).

[180] C. J. Williams, E. Tiesinga, P. Julienne, H. Wang, W. C. Stwalley, and P. L. Gould, *Determination of the scattering lengths of ^{39}K from 1_u photoassociation line shapes*, Phys. Rev. A **60**, 4427–4438 (1999).

[181] K. Burnett, P. S. Julienne, P. D. Lett, E. Tiesinga, and C. J. Williams, *Quantum encounters of the cold kind*, Nature **416**, 225–232 (2002).

[182] G. Gribakin and V. Flambaum, *Calculation of the scattering length in atomic collisions using the semiclassical approximation*, Phys. Rev. A **48**, 546 (1993), model potential, critical radius, 75% positive a.

[183] N. F. Mott and H. S. W. Massey, *The Theory of Atomic Collisions*, vol. 1 (Oxford University Press, Oxford, United Kingdom, 1965), 3 edn.

[184] V. V. Flambaum, G. F. Gribakin, and C. Harabati, *Analytical calculation of cold-atom scattering*, Phys. Rev. A **59**, 1998–2005 (1999).

[185] B. Gao, *Quantum-defect theory of atomic collisions and molecular vibration spectra*, Phys. Rev. A **58**, 4222–4225 (1998).

[186] F. Dalfovo, S. Giorgini, L. P. Pitaevskii, and S. Stringari, *Theory of Bose-Einstein condensation in trapped gases*, Rev. Mod. Phys. **71**, 463 (1999).

[187] H. T. C. Stoof, *Atomic Bose gas with a negative scattering length*, Phys. Rev. A **49**, 3824 (1994).

[188] J. James Patrick Burke, *Theoretical Investigation of Cold Alkali Atom Collisions*, Phd thesis, University of Colorado, Boulder, Colorado (1999).

[189] C. J. Pethick and H. Smith, *Bose-Einstein Condensation in Dilute Gases* (Cambridge University Press, Cambridge, United Kingdom, 2002), 1 edn.

[190] R. J. LeRoy and R. B. Bernstein, *Dissociation Energy and Long-Range Potential of Diatomic Molecules from Vibrational Spacings of Higher Levels*, J. Chem. Phys. **52**, 3869–3879 (1970).

[191] C. Chin, A. J. Kerman, V. Vuletic, and S. Chu, *Sensitive Detection of Cold Cesium Molecules Formed on Feshbach Resonances*, Phys. Rev. Lett. **90**, 033201 (2003).

[192] P. S. Julienne, *Ultra-cold Collisions of Atoms and Molecules*, in *Scattering*, edited by E. R. Pike and P. Sabatier, vol. 2 of *Direct and Inverse Scattering in Pure and Applied Science*, chap. 2.6.3, pp. 1043–1067 (Academic Press, New York, 2001).

[193] S. J. J. M. F. Kokkelmans, J. N. Milstein, M. L. Chiofalo, R. Walser, and M. J. Holland, *Resonance superfluidity: Renormalization of resonance scattering theory*, Phys. Rev. A **65**, 053617 (2002).

[194] E. A. Donley, N. R. Claussen, S. T. Thompson, and C. E. Wieman, *Atom-molecule coherence in a Bose-Einstein condensate*, Nature **417**, 529 (2002).

[195] K. Dieckmann, C. A. Stan, S. Gupta, Z. Hadzibabic, C. H. Schunck, , and W. Ketterle, *Decay of an Ultracold Fermionic Lithium Gas near a Feshbach Resonance*, Phys. Rev. Lett. **89**, 203201 (2002).

[196] K. M. O'Hara, S. L. Hemmer, M. E. Gehm, S. R. Granade, and J. E. Thomas, *Observation of a Strongly Interacting Degenerate Fermi Gas of Atoms*, Science **298**, 2179–2182 (2002).

[197] L. D. Landau and E. M. Lifschitz, *Lehrbuch der theoretischen Physik*, vol. IX Statistische Physik, Teil 2 (Akademie–Verlag, Berlin, 1980).

[198] V. Vuletić, A. J. Kerman, C. Chin, and S. Chu, *Observation of Low-Field Feshbach Resonances in Collisions of Cesium Atoms*, Phys. Rev. Lett. **82**, 1406 (1999).

[199] S. Giovanazzi, private communication (2002).

[200] J. Dalibard, *Collisional dynamics of ultra-cold atomic gases*, in *Proceedings of the International School of Physics - Enrico Fermi*, edited by M. Inguscio, S. Stringari, and C. Wieman, p. 321 (IOS Press, 1999).

[201] S. Kotochigova, E. Tiesinga, and P. S. Julienne, *Relativistic ab initio treatment of the second-order spin-orbit splitting of the $a^3\Sigma_u^+$ potential of rubidium and cesium dimers*, Phys. Rev. A **63**, 012517 (2000), second order spin orbit coupling.

[202] F. H. Mies, C. J. Williams, P. S. Julienne, and M. Krauss, *Estimating Bounds on Collisional Relaxation Rates of Spin-Polarized ^{87}Rb Atoms at Ultracold Temperatures*, J. Res. Natl. Inst. Stand. Tech. **101**, 521 (1996).

[203] P. Fedichev, M. Reynolds, and G. Shlyapnikov, *Three-Body Recombination of Ultracold Atoms to a Weakly Bound s Level*, Phys. Rev. Lett. **77**, 2921 (1996).

[204] H. F. Hess, *Evaporative cooling of magnetically trapped and compressed spin-polarized hydrogen*, Phys. Rev. B **34**, 3476 (1986).

[205] O. Luiten, M. Reynolds, and J. T. M. Walraven, *Kinetic theory of the evaporative cooling of a trapped gas*, Phys. Rev. A **53**, 381 (1996).

[206] H. Wu, E. Arimondo, and C. J. Foot, *Dynamics of evaporative cooling for Bose-Einstein condensation*, Phys. Rev. A **56**, 560 (1997).

[207] C. S. Adams, H. Lee, N. Davidson, M. Kasevich, and S. Chu, *Evaporative Cooling in a Crossed Dipole Trap*, Phys. Rev. Lett. **74**, 3577 (1995).

[208] M. D. Barrett, J. A. Sauer, and M. S. Chapman, *All-Optical Formation of an Atomic Bose-Einstein Condensate*, Phys. Rev. Lett. **87**, 010404 (2001).

[209] S. Hensler, Phd thesis, 5. Physikalisches Institut, Universität Stuttgart, Pfaffenwaldring 57, 70550 Stuttgart (2003), in preparation.

[210] M. Arndt, M. B. Dahan, D. Guéry-Odelin, M. Reynolds, and J. Dalibard, *Observation of a Zero-Energy Resonance in Cs-Cs Collisions*, Phys. Rev. Lett. **79**, 625 (1997).

[211] S. A. Hopkins, S. Webster, J. Arlt, P. Bance, S. Cornish, O. Marago, and C. J. Foot, *Measurement of elastic cross section for cold cesium collisions*, Phys. Rev. A **61**, 032707 (2000).

[212] I. Bloch, M. Greiner, O. Mandel, T. W. Hänsch, and T. Esslinger, *Sympathetic cooling of ^{85}Rb and ^{87}Rb*, Phys. Rev. A **64**, 021402 (2001).

[213] N. Newbury, C. Myatt, and C. Wieman, *S-wave elastic collisions between cold ground-state ^{87}Rb atoms*, Phys. Rev. A **51**, R2680 (1995).

[214] K. B. Davis, M.-O. Mewes, M. A. Joffe, M. R. Andrews, and W. Ketterle, *Evaporative Cooling of Sodium Atoms*, Phys. Rev. Lett. **74**, 5202 (1995).

[215] B. DeMarco and D. Jin, *Onset of Fermi Degeneracy in a Trapped Atomic Gas*, Science **285**, 1703 (1999).

[216] G. Roati, W. Jastrzebski, A. Simoni, G. Modugno, and M. Inguscio, *Optical trapping of cold fermionic potassium for collisional studies*, Phys. Rev. A **63**, 052709 (2001).

[217] H. Wu and C. J. Foot, *Direct simulation of evaporative cooling*, J. Phys. B **29**, L321 (1996).

[218] G. Kavoulakis, C. Pethick, and H. Smith, *Collisional relaxation in diffuse clouds of trapped bosons*, Phys. Rev. A **61**, 053603 (2000).

[219] C. Boisseau, E. Audouard, and J. Vigué, *Quantization of the highest levels in a molecular potential*, Europhys. Lett. **41**, 349–354 (1998).

[220] J. M. Gerton, D. Strekalov, I. Prodan, and R. G. Hulet, *Direct observation of growth and collapse of a Bose-Einstein condensate with attractive interactions*, Nature **408**, 692 (2000).

[221] H. Pu, W. Zhang, and P. Meystre, *Macroscopic spin tunneling and quantum critical behavior of a condensate in double-well potential* (2003), arXiv: cond-mat/0203066.

[222] C. Cohen-Tannoudji, J. Dupont-Roc, and G. Grynberg, *Atom-photon interactions* (John Wiley & Sons, 1992), 1 edn.

[223] G. C. Maitland, M. Rigby, E. B. Smith, and W. A. Wakeham, *Intermolecular Forces* (Claredon Press, Oxford, 1981).

[224] R. Cambi, D. Cappelletti, G. Liuti, and F. Pirani, *Generalized correlations in terms of polarizability for van der Waals interaction potential parameter calculations*, J. Chem. Phys. **95**, 1852–1861 (1991).

[225] J. C. Slater and J. G. Kirkwood, *The Van Der Waals Forces in Gases*, Phys. Rev. **37**, 682 (1931).

[226] A. Simoni, private communication (2003).

[227] J. Söding, D. Guéry-Odelin, P. Desbiolles, G. Ferrari, and J. Dalibard, *Giant Spin Relaxation of an Ultracold Cesium Gas*, Phys. Rev. Lett. **80**, 1869 (1998).

Danksagung

Viele Leute haben durch ihre Unterstützung einen Beitrag zum Gelingen dieser Arbeit geleistet.

An erster Stelle möchte ich Tilman Pfau danken, der nicht nur das angenehme und kreative Umfeld für diese Arbeit geschaffen hat, sondern auch stets mit seinem Wissen und neuen Ideen zum Fortschritt des Experiments beigetragen hat. Darüber hinaus gab er mir die durchaus nicht selbstverständliche Freiheit zum eigenständigen wissenschaftlichen Arbeiten und verschaffte mir durch den Umzug nach Stuttgart die Gelegenheit "Sekundärqualifikationen" anzueignen.

Ein besonderer Dank gebührt Axel Görlitz, der mit seinen fundierten — nicht nur experimentellen — Kenntnissen wesentlich zum Fortschritt des Experiments, und damit dieser Arbeit beigetragen hat. Insbesondere unsere physikalischen Diskussionen waren sehr stimulierend und haben mein Wissen über die Physik vertieft.

Diese Arbeit hätte es ohne meine Kollegen so nicht gegeben. Ich möchte mich an dieser Stelle bei allen für die Mit- und Zusammenarbeit bedanken:

- Jürgen Stuhler, der als "Vater" des Chrom-Projekts in der Konstanzer Zeit die treibende Kraft war. Nie werde ich die unzähligen Diskussionen und gemeinsamen Messnächte vergessen! Insbesondere sein Optimismus und sein mitreißendes Wesen haben wesentlich zum Spaß an der Physik und zur hervorragenden Atmosphäre in der Gruppe beigetragen.

- Sven Hensler, der als Dompteur der Diodenlaser Wunder vollbracht hat und das Wagnis auf sich genommen hat, gemeinsam mit mir das Experiment nach Stuttgart umzuziehen. Dafür bin ich ihm sehr dankbar. Neben seinen Fähigkeiten im Labor und beim Entwurf von Vakuumkammern nebst Zubehör, lernte ich auch seine "pädagogische Begabung" als Snowboard-Lehrer zu schätzen. Unvergessen bleiben auch unsere gemeinsamen Bergtouren, besonders die Mondschein-Tour auf die Churfirsten.

- Jörg Werner, unserem Rechner-Guru, der praktisch alle meine Sonderwünsche in sein fantastisches Steuerprogramm integriert hat und die Rechner des In-

stituts am Laufen hielt. Daneben war er maßgeblich am Aufbau des blauen Lasersystems als Teil seiner Diplomarbeit beteiligt.

- Thomas Binhammer, unserem ersten Stuttgarter Diplomanden, der uns beim Wiederaufbau des Experiments in Stuttgart geholfen hat. Durch seinen erfolgreichen Kampf mit Kapton & Kupferrohr konnte er unsere Magnetfalle aufbauen und war an den ersten Messungen damit beteiligt.

- Axel Griesmaier, der im Rahmen seiner Diplomarbeit zusammen mit Sven die neue Chrom/Rubidium Apparatur aufgebaut hat, an der ich die Messungen zu den elastischen Kollisionen machen durfte.

- Bernd Steinheil, der als Diplomand einen wichtigen Beitrag zum Aufbau eines frequenzverdoppelten Diodenlasersystems geleistet hat.

- Jürgen Schoser, der nicht nur meine Schreibtischnachbar sondern auch mein Kletterpartner war und viele schweisstreibende Stunden mit mir in der Kletterhalle oder am Turm verbrachte. Auch die physikalischen Diskussionen mit ihm waren stets eine Bereicherung für mich.

- Karin Otter, die als Institutsassistentin weit über ihre Pflichten hinaus für unser Wohl gesorgt hat.

Daneben möchte ich mich bei meinen Kollegen Jürgen Schoser, Robert Löw, Axel Grabowski, Rolf Heidemann und Jochen Steinmann und Yurii Ovchinnikov vom Rubidium-Team sowie Alexander Batär, Sven Kroboth und Bernd Kaltenhäuser vom Ytterbium-Team für die vielen Diskussionen und die freundschaftliche Zusammenarbeit, sowie den apparativen und den Know-How Austausch bedanken.

Mein besonderer Dank gilt auch den mechanischen und elektronischen Werkstätten der Universitäten Konstanz und Stuttgart, stellvertetend Herrn Möhrle, Herrn Kamella und Herrn Dietrich, die durch ihr Können und ihre Vorschläge zum erfolgreichen Aufbau der Apparatur beigetragen haben.

Ein herzliches Dankeschön auch an Axel Görlitz, Sven Hensler, Jörg Werner, Stefano Giovanazzi und Jürgen Stuhler, die durch das unermüdliches Korrekturlesen dieser Arbeit die Zahl der inhaltlichen und Rechtschreibfehler deutlich reduziert haben.

Ich habe in meiner Zeit als Doktorand viel von den Diskussionen über unser Projekt mit anderen Wissenschaftlern profitiert. An dieser Stelle möchte ich mich daher stellvertretend bei Gora Shlyapnikov, Stefano Giovanazzi und Andrea Simoni für die Unterstützung in theoretischen Fragen zur Bose-Einstein-Kondensation im Allgemeinen und zur Streutheorie im Besonderen, bedanken.

Bei der Studienstiftung des deutschen Volkes möchte ich mich für die finanzielle Unterstützung während meiner Promotion bedanken.

In der Konstanzer Zeit haben mir viele Mitarbeiter des ehemaligen Lehrstuhls Mlynek mit Rat und Tat zur Seite gestanden: Björn Brezger, Thomas Schulze, Dirk Jürgens, Stephan Nowack, Dominik Schneble, Markus Oberthaler, Ute Hentzen, Stefan Eggert, Stefan Hahn und natürlich Herr Mlynek selbst. Daneben haben meine Freunde und WG-Mitbewohnerinnen immer ein offenes Ohr für meine seltsamen physikalischen Probleme gehabt.

In Stuttgart gewährten mir die "Aprikosen" Unterschlupf in ihrem Haus. Ich werde Euch und den Party-Keller vermissen!

Nicht zuletzt möchte ich mich bei meinen Eltern Ute und Fritz, meinen Geschwistern Jan und Anika sowie ganz besonders bei meiner Frau Susanne ganz herzlich bedanken. Eure Unterstützung, den Rückhalt den ihr mir gegeben habt und das Verständnis das ihr meiner Arbeit und mir entgegegebracht habt, haben mir sehr viel bedeutet.